Towards cheap and sustainable energy sources by exploiting self-organized catalyst micro and nanostructures

Inauguraldissertation

zur

Erlangung der Würde eines Doktors der Philosophie

vorgelegt der

Philosophisch-Naturwissenschaftlichen Fakultät

der Universität Basel

von

Roché Marcel Walliser

aus Weil am Rhein, Deutschland

Basel, 2015

Genehmigt von der Philosophisch–Naturwissenschaftlichen Fakultät

auf Antrag von

Prof. Dr. Edwin C. Constable

Prof. Dr. Thomas Pfohl

Basel, den 21.04.2015

_____

Dekan

Prof. Dr. Jörg Schibler

Attribution-NonCommercial-NoDerivatives 4.0 International

(CC BY-NC-ND 4.0)

You are free to: Share — copy and redistribute the material in any medium or format

Under the following terms:

Attribution — You must give appropriate credit, provide a link to the license, and indicate if changes were made. You may do so in any reasonable manner, but not in any way that suggests the licensor endorses you or your use.

NonCommercial — You may not use the material for commercial purposes.

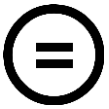

NoDerivatives — If you remix, transform, or build upon the material, you may not distribute the modified material.

Wobei gilt:

- **Verzichtserklärung** — Jede der vorgenannten Bedingungen kann **aufgehoben** werden, sofern Sie die ausdrückliche Einwilligung des Rechteinhabers dazu erhalten.

- **Public Domain (gemeinfreie oder nicht-schützbare Inhalte)** — Soweit das Werk, der Inhalt oder irgendein Teil davon zur Public Domain der jeweiligen Rechtsordnung gehört, wird dieser Status von der Lizenz in keiner Weise berührt.

- **Sonstige Rechte** — Die Lizenz hat keinen Einfluss auch die folgenden Rechte:
  - Die Rechte, die jedermann wegen der Schranken des Urheberrechts oder aufgrund gesetzlicher Erlaubnisse zustehen (in einigen Ländern als grundsätzliche Doktrin des **fair use** bekannt);
  - Die Persönlichkeitsrechte des Urhebers;
  - Rechte anderer Personen, entweder am Lizenzgegenstand selber oder bezüglich seiner Verwendung, zum Beispiel für **Werbung** oder Privatsphärenschutz.

- **Hinweis** — Bei jeder Nutzung oder Verbreitung müssen Sie anderen alle Lizenzbedingungen mitteilen, die für diesen Inhalt gelten. Am einfachsten ist es, an entsprechender Stelle einen Link auf diese Seite einzubinden.

Quelle: https://creativecommons.org/licenses/by-nc-nd/4.0/ Datum: 17.06.2015

Für meine Frau Michaela, meine beiden Söhne Jan und Leon, sowie den Rest meiner Familie.

Vielen Dank für alles.

One Ring to rule them all, One Ring to find them, One Ring to bring them all and in the darkness bind them.

J.R.R. Tolkien

Picture 1*: SEM-FIB nanolithography used to write J.R.R. Tolkiens: One Ring to rule them all, …, in elvish tengwar letters on a gold surface. Text was taken from "The Lord of the Rings".*

Acknowledgements

First of all, I would like to thank *Prof. Dr. Edwin C. Constable* and *Prof. Dr. Catherine E. Housecroft* for giving me the possibility to do my PhD in their research group. During the last almost three years, they did an excellent job in mentoring and supporting me throughout the entire time. Thank you for this not common but very interesting interdisciplinary project. Without the reams of helpful suggestions and the scientific freedom you gave me, the project would not have been half as beneficial as it has become. Thank you.

I would like to thank *Prof. Dr. Thomas Pfohl* for co-examination of this thesis.

Sincere thank is given to *Prof. Dr. Catherine E. Housecroft* for chairing the examination.

I would like to thank the people from the Eidgenössische Materialprüfungs- und Forschungsanstalt (EMPA) Dübendorf, namely *Dr. Artur Braun*, *Dr. Rita Tóth*, *Dr. Jakob Heier* and *Florent Boudoire* for the good and productive collaboration we shared. I especially like to thank *Rita* for the helpful discussions and the very nice and productive collaboration. Without all of you I would not be able to show that many nice results.

I am also very thankful for the collaboration with *Prof. Dr. István Lagzi* who is (in my opinion) one of the leading experts in the fields of self-assembling and self-organizing materials like it occurs in Liesegang type phenomena. Thank you very much for sharing your knowledge, for your helpful suggestions and the possibility to ask and to get an answer whenever I asked.

I would also like to thank all the supporting staff of the Department of Chemistry: *Beatrice Erismann* for her outstanding help in all administrative questions/issues as well as for the nice coffee breaks we shared. *Markus Hauri*, *Markus Ast*, *Andres Koller, Andreas Sohler* and the rest of the workshop team for their help and the nice and productive collaboration. *Dr. Bernhard Jung* for his IT support. It was a great pleasure to work and talk with all of them. I especially like to thank *Bernhard* and *Beatrice* for their deeper friendship.

I am very thankful for the collaboration with the former and all current people from Zentrum für Mikroskopie Basel (ZMB). A special thank goes to *Dr. Markus Dürrenberger*, *Marcel Düggelin* and *Daniel Mathys*, without your help I would not be able to show all these very nice SEM-images, EDX data or videos, of which all were necessary to transform the observation of a band forming process into a useable process with possible applications.

I would like to thank the current and former members of the Constable-Housecroft research group, for the good and productive working atmosphere, especially I would like to thank *Dr. Jonas Schönle*, *Dr. Gabriel Schneider-Joerg*, *Dr. Steffen Müller*, *Dr. Ewald Schönhofer*, *Dr. Nik Hostettler*, *Dr. Sven Brauchli*, *Dr. Iain Wright*, *Dr. Colin Martin*, *Dr. Collin Morris*, *Dr. Markus Willgert*, *Dr. Marketa Smidkova*, *Cathrin Ertl*, *Sarah Keller*, *Annika Büttner*, *Maximilian Klein*, *Frederik Malzner*, *Thomas Müntener* and the Master students *Tatjana Kosmalski*, *Felix Brunner*, *Cedric Wobill, Daniel Ris* and *Emanuel Kohler*.

Special thanks go to *Jonas*, *Gabriel*, *Steffen* and *Cathrin* for their deeper friendship and great time we had in the former Labs 217 and 219. Furthermore I want to thank *Max* and *Sarah* also for their deeper friendship as well as for the great time we had together, especially before, at and after the Singapore conference.

Next, it is a pleasure for me to thank *Kaspar Zimmermann* and *Dr. Heiko Gsellinger* also for their deeper friendship and the great job they did in mentoring me during my Master studies in the research group of *PD Dr. Daniel Häussinger*, whom I like to thank again for the possibility to do my Master in his group and the great time I had with him and his group.

For financial support, the University of Basel, EMPA Dübendorf and the Swiss National Science Foundation (No. 200021-137868) are gratefully acknowledged.

I would like to thank the Swiss Light Source, Villigen, for the allocation of synchrotron radiation beamtime at PolLux endstation.

I also like to thank *Dr. Monica Schönenberger-Schwarzenbach* for her help with the AFM and the laser microscope.

I want to close my acknowledgements with my deepest expressions of gratitude to my family. They supported me throughout my entire life and without them I would not be where I am now. I especially would like to thank my uncle *Wolfgang Barth* who opened my eyes and mind to the fascinating world of science. Special thank goes also to both of my grandfathers (*Heinz* and *Ernst*) who showed me how to realize even complicated ideas, this helped me a lot during my studies. I also thank my parents, my brother and my sisters for their constant support. Last but not least I want to thank my wife *Michaela*, who supported me at any time since I have known her and my two sons *Jan Daniele* and *Leon Fynn Ludwig*. You three greatly enriched my life. Thank you!

Contents

Abbreviations

A.C.S	American Chemical Society
AFM	Atomic force microscopy
AM	Air Mass
approx.	approximately
BSE	Backscattered electrons
CVD	Chemical vapor deposition
e^-	electron
EDX	Energy-dispersive X-ray spectroscopy
E_{photon}	Energy of a photon = $h \cdot \nu$
ETD	Everhart Thornley detector
eV	electron Volt
FTO	Fluorine-doped tin oxide (SnO_2:F)
h	hour
h	Planck constant ($6.62607 \cdot 10^{-34}$ J·s)
h^+	photon
HTS	High throughput screening
Hz	Hertz [s^{-1}]
in	inch
J	Joule
k	kilo
lm	Lumen
M	molar [$mol \cdot L^{-1}$]
mbar	millibar → 1 mbar = 100 Pa
min	minute
MW	Molar weight [$g \cdot mol^{-1}$]
NMR	Nuclear magnetic resonance
Pa	Pascal (pressure)
PDMS	Polydimethoxysiloxane
PECs	Photo electrochemical cells
PMMA	Poly(methyl methacrylate)
PMT	Photomultiplier tube
PP	Polypropylene
PVA	Polyvinyl alcohol

rpm	Rotation per minute
s	second
SE	Secondary electrons
SEM	Scanning electron microscopy
SEM-FIB	Scanning electron microscopy – Focused Ion Beam
Si_3N_4	Silicon nitride
SLS	Swiss light source (at Paul Scherrer Institute, Villigen, Switzerland)
STEM	Scanning transmission electron microscopy
STXM	Scanning transmission X-ray microscopy
TGA	Thermogravimetric analysis
TLD	Through the lens detector
w/w%	weight percentage
WETs	Wet stamping
XPS	X-ray photoelectron spectroscopy
ZMB	Zentrum für Mikroskopie Basel
ν	Frequency of a wave [Hz]

Abstract

Reaction diffusion precipitation processes in hydrogels can result in highly periodic micro- and nano-structured patterns known as Liesegang bands. These structures offer a very simple and cheap way to increase the surface area of certain catalyst materials. However, investigating the chemical origin of the precipitation bands is crucial for understanding and controlling the precipitation process. For this reason, the classical Liesegang system, discovered more than 100 years ago, was investigated in the first place. In this system two types of precipitation band, namely thick primary, and very dense, fine structured secondary bands are observed. Based on the results of the investigations (using STXM, SEM, SEM-FIB and EDX), a model was proposed, which describes the chemical origin of the precipitation bands. In addition, it was found that the fine structured so-called secondary bands originate from a different chemical system than the larger primary precipitation bands. Similarly to the classical Liesegang system, the origin of these fine structured bands was further investigated, resulting in a new Liesegang system containing only fine structured bands. It was found form material analysis using SEM, SEM-FIB, EDX and XPS that these highly periodic and very dense (up to 1 band per μm) bands consist of silver (Ag^0) nano particles. By optimizing the parameters of this system it was also possible to control the precipitation process. It was also found that different hydrogels can be used and the structural design of special shaped precipitation bands and other structures (grids) was achieved. Since silver is known to be the most conductive element we wanted to combine these structures with hematite for solar induced water splitting applications in photo electrochemical cells (PEC). For this purpose, it was necessary to remove the hydrogel without destroying the precipitation structures. A simple sintering protocol was developed, which allows full removal of the hydrogel and full transformation of the particles forming the bands into pure silver bands. Several systems were tested to combine the silver bands with PEC photoanodes containing hematite. Unfortunately it was not possible to obtain an increase in the water splitting efficiency of the PEC cells, further optimization is needed. In addition to these fine structured silver systems, a high throughput screening protocol was developed, which allowed fast screening for new precipitation bands forming systems. By using this technique seven new, Liesegang type precipitation systems have been discovered, of which two consist of catalyst materials, such as $AgMoO_4$ an $AgWO_4$, and the others of iron or ruthenium coordination compounds. To the best of our knowledge this is the first time that it was possible to show that Liesegang type precipitation structures are formed out of more complex materials than metal salts.

1. Introduction

1.1 Motivation and aim

Energy in forms of fossil fuels and electricity are essential to maintain the quality of modern life that we know. During the last decades global energy consumption increased almost exponentially, reaching a value of 523 EJ (1 Exajoule, EJ = $1 \cdot 10^{20}$ J) in 2010 (Figure 1.1).[1,2] It is expected that consumption will increase up to 730 EJ in 2035.[3,4]

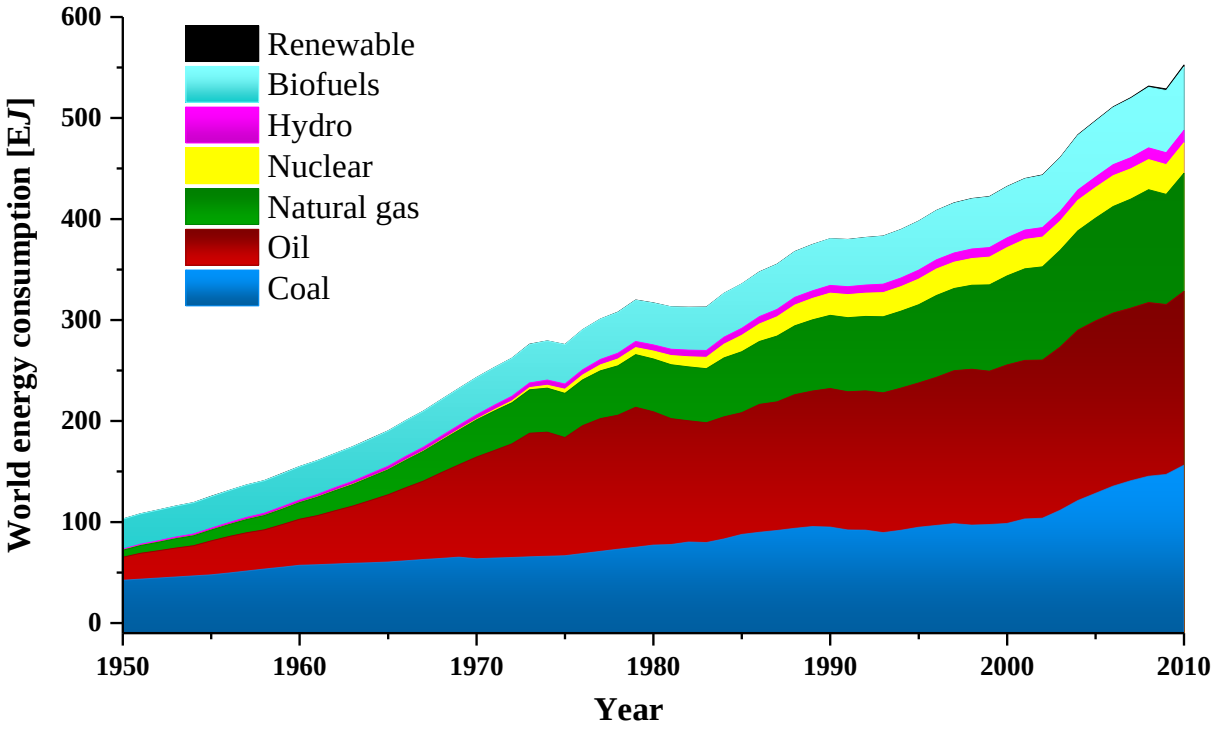

Figure 1.1: Global energy consumption over the last 6 decades, subdivided in to the different energy sources. Data were extracted and combined from several sources.[1–6] Renewable energy sources contain, solar and wind energy.

This increase is caused by several reasons, on the one hand the population of the earth almost tripled within the last 60 years (Figure 1.2).[7–10] This population boom is due to higher agricultural and medicinal standards, in combination with a static decrease in child mortality on the one hand.[7,9,11–13]

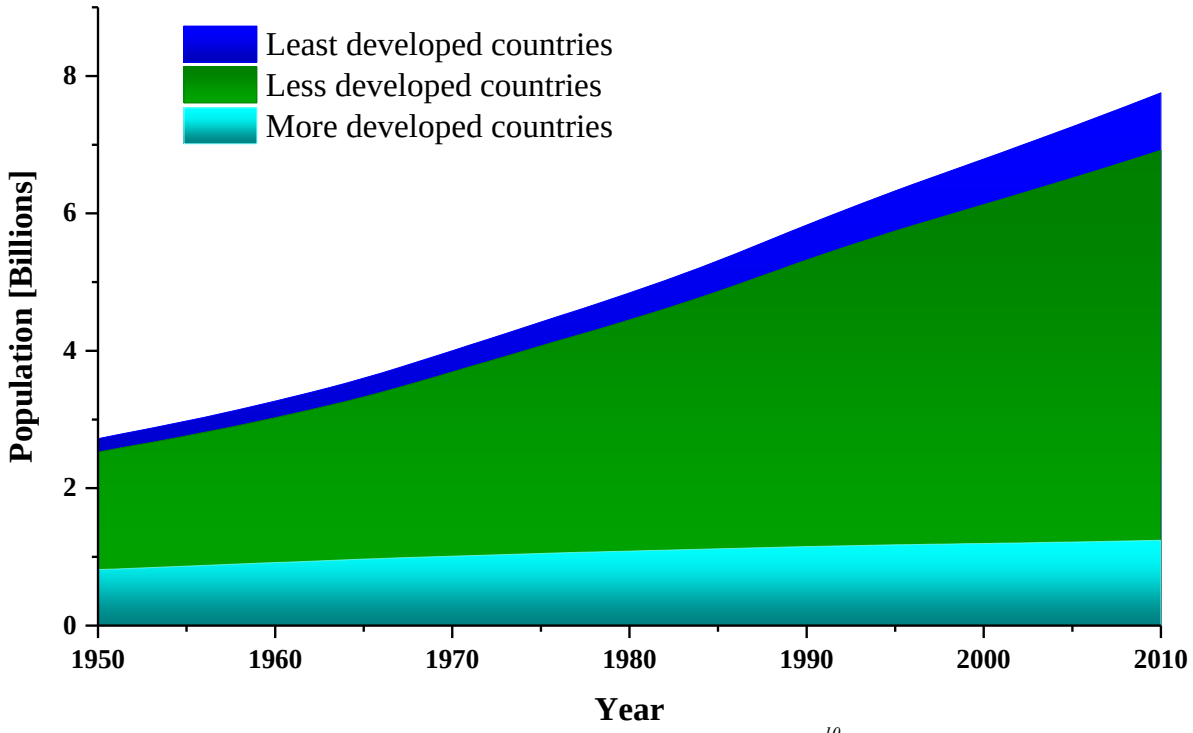

Figure 1.2: Evolution of the world population over the last 6 decades[10] subdivided into UN classified countries. Blue curve: population of "least developed countries"; green curve: population of "less developed countries" and cyan curve: population of "more developed countries". Classification according to UN.[10]

On the other hand, more and more countries have developed from agricultural or pre-industrial economies to modern high technology industrial economy countries. This trend is captured by the Human development index (HDI).[7,14–16] Along with this economic expansion and vitality, which originates also from globalization, a social advancement occurs. In combination with technological advancements this leads to higher mobility (use of vehicles powered by fossil fuels) and the use of more electronic devices and gadgets (smart phones, computers, TVs and many more), which are expected to make our everyday lives much easier. This private lifestyle and the pursuit of happiness increase the global energy consumption additionally. But industrial and lifestyle caused energy consumption represents only about 53% of the global consumption. An additional significant part (approx. 47%)[17] is owed to the generation of heat, in terms of heating and cooling of industrial processes, buildings, domestic water, foods and other consumable goods (Figure 1.3). However, energy used to generate unused heat as side product (e.g. in light bulbs, colocation centers or exhaust gases) was not taken into account. Non-energy use covers the use of fossil energy sources for the production of products such as plastics, solvents, paraffin waxes, bitumen, lubricants and other products.[18]

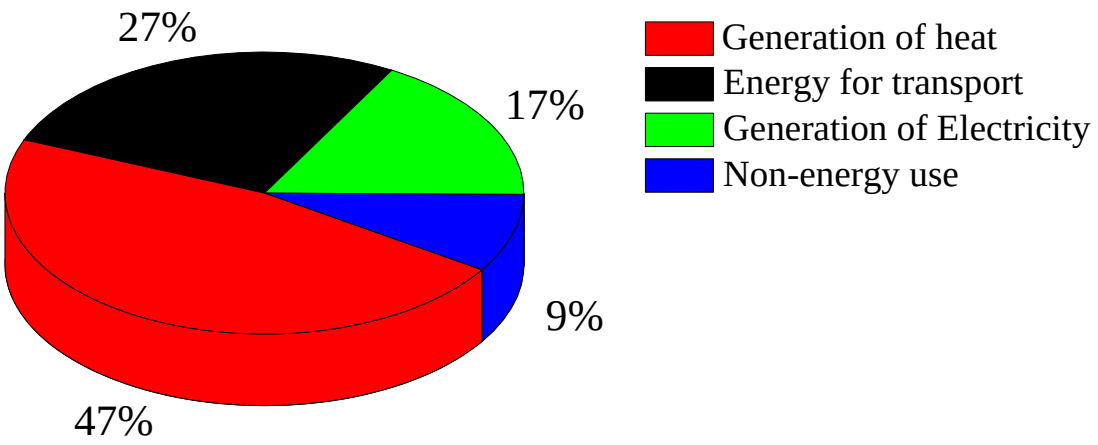

Figure 1.3: Pie chart showing the distribution of the global energy consumption on a percentage basis.[17]

Nowadays, fossil fuels are used to a large extent to generate the required energy (Figure 1.1). But our fossil energy resources are depleting and pollution is increasing.[1,17] Air pollution and smog, often found in megacities like Delhi, Beijing or Paris during hot and dry summer days/weeks, can cause health problems.[19] Nevertheless, other forms of pollutions caused by mining of raw materials (coal, oil and gas)[20–22] can also lead to health problems. In order to minimize these effects and in order to maintain our standards, other forms of energy production are needed. Nuclear energy as a source of pollution free energy[23–25] was the vision of the last century, but since the large core melt accidents of Chernobyl in 1986[26–30] or Fukushima in 2011,[31,32] contaminating large areas and a large part of the population, in addition to the significant problem with radioactive waste, which possesses half-lives of up to several ten to hundred thousand years,[33–36]other more sustainable ways to produce energy are desired[37–40] (especially in Germany,[41] Austria, Switzerland,[42] Italy, Ireland and Sweden).
Depending on the country, their politics, geographic and geological location it is expected that renewable energy sources such as wind, hydro-power, biofuels, geothermal and solar energy can possibly allay more than half of the global needs in the near future.[43,44] In the case of Germany, 24% (638 TWh = $2.297 \cdot 10^{18}$ *J*)[45–47] of the gross energy production was obtained by renewable energy sources of which 5%[48] was produced by solar energy conversion in 2013. In order to further decrease the use of fossil energy sources and to boost technological developments, the German government established a law to increase the amount/percentage of cost-efficient renewable energy on the gross consumption of up to 55-60% by 2035 and up to 80% by 2050.[43] Since the Sun`s radiation reaching the Earth`s surface delivers energy of about 7.3 EJ within one minute,[49–51] less than two hour`s irradiation would in theory deliver enough energy to allay all global energy needs of one year. Therefore it is reasonable to investigate and improve solar to energy conversion techniques, methods and materials.

There are several known possibilities for the conversion of solar energy into other forms of energy. One possibility is the energy conversion in solar thermal power stations,[52–54] by collecting and focusing the sun`s irradiation to produce steam. This is similar to conventional fossil or nuclear driven steam power plants. Another possibility is the use of Si crystal,[55,56] dye-sensitized[57] or perovskite[58,59] based photovoltaic cells, converting sun light directly into electricity (Figure 1.4).

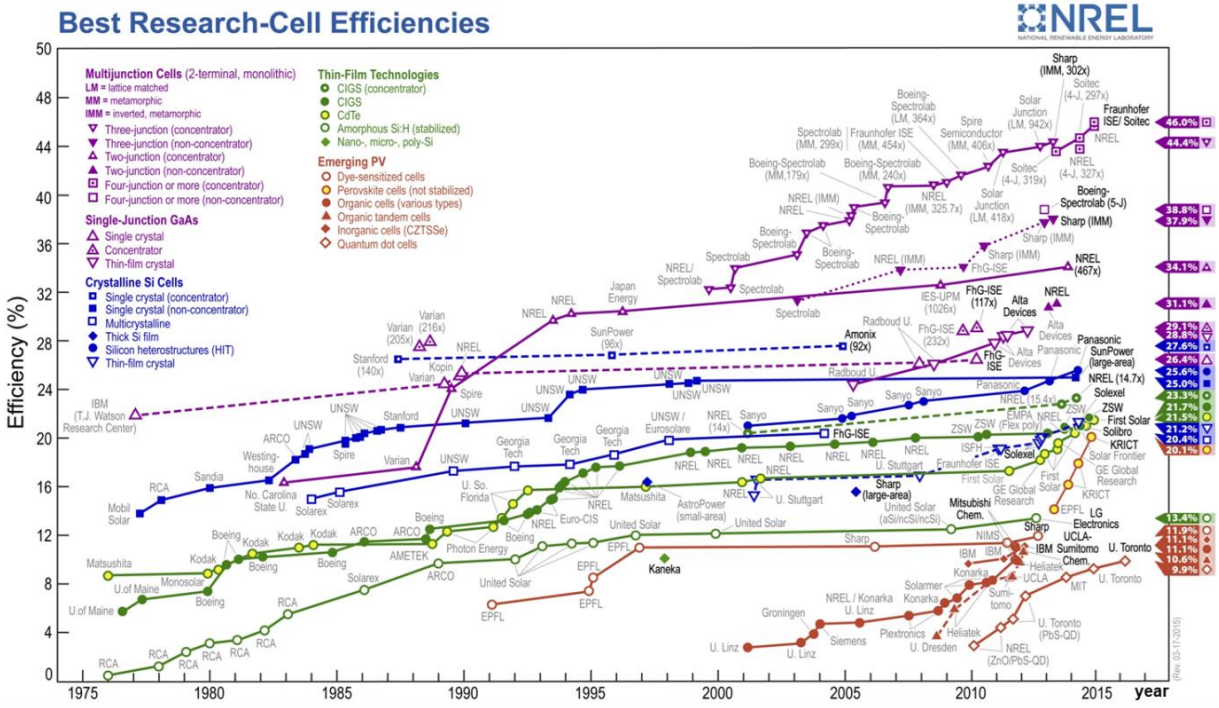

Figure 1.4: Solar cell efficiency table showing efficiency records obtained for research cells under laboratory test conditions.[60]

Highly efficient photovoltaic cells were tested at the Fraunhofer Institute for Solar Energy Systems (Germany) showing an efficiency of up to 44.7%.[61] However, the best commercially available cells have an average efficiency of about 15-25%.[62] Most commonly used photovoltaic cells are silicon based and have a bad life cycle assessment, since their production is resource consuming.[63–66] The silicon needs to be of highest quality and purity and additional elements, such as gallium, arsenic, indium, germanium, cadmium, gold, silver or tellurium are needed for additional parts within these cells.[67] Furthermore, these cells offer a maximal lifetime of 15-25 years[63–66,68] until they need to be replaced. These reasons reduce the environmental sustainability of this type of solar cells. In the case of dye-sensitized solar cells, efficiencies of 11%[69] and in the case of perovskite-sensitized solar cells an efficiency of up to 20%[70] have been observed. In terms of energy transport and storage, direct conversion of solar energy into fuels is of interest. The production of hydrogen fuel by solar induced photocatalytic water splitting in photo-electrochemical cells (PECs)[71–74] represents a

promising way to reach this aim (cf. Chapter 2.3.1). In order to facilitate decomposition of water into oxygen and hydrogen, catalyst materials are needed, showing both corrosion stability and high absorbance in the visible and near-visible region of the sun`s spectrum. Unfortunately, most promising catalyst materials are either very expensive or their efficiency is very low.[75,76] Hematite (α-Fe_2O_3/ rust)[73–75,77–79] as photoanode catalyst for oxygen evolution in the water splitting process, represents one of these weakly efficient materials. Nevertheless, rust as catalyst material has attracted attention, since it represents one of the most corrosion stable and cheapest materials in the world.[77–80] But the biggest drawback of this oxide is its low light absorbance. To overcome this problem, the material needs to be thick to be able to convert photons into electrons and holes. But a thick hematite layer on the photoanode results in a very low conductivity. To circumvent this, the catalyst layer needs to be very thin to separate the photo generated electrons and holes. This conflict reduces the overall efficiency of the hematite system.[71,80,81] One possibility to overcome these difficulties is the use of nano- or microstructures to increase the surface area of the catalyst, without producing thick films (Image 1.1).

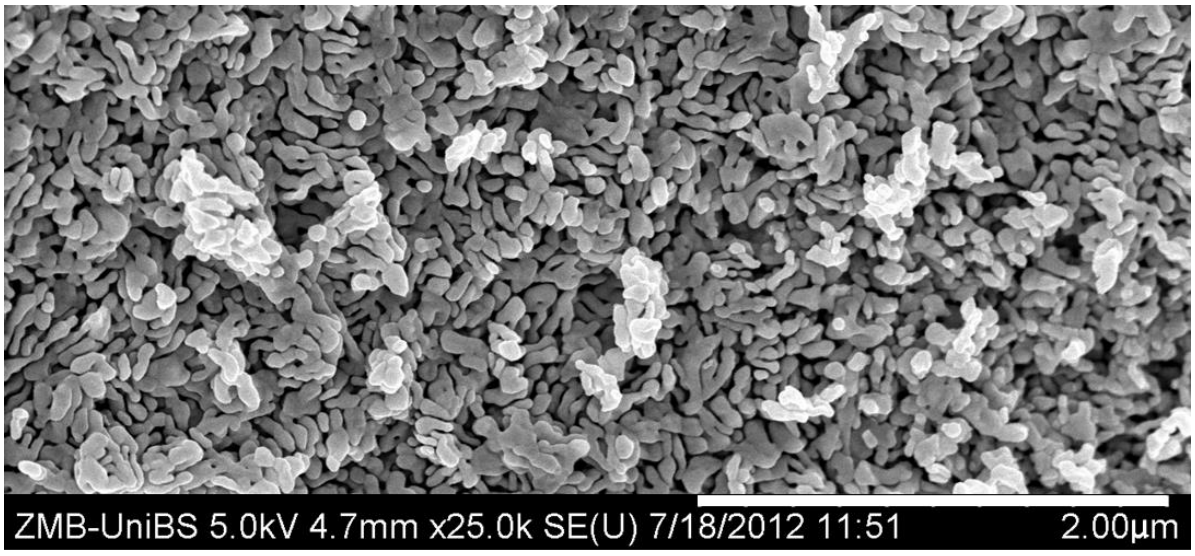

Image 1.1: SEM-Image of hematite nanoparticles on top of FTO-glass prepared as PEC photoanode.

Conventional methods to produce micro- or nanostructured materials are the so-called “top-down” techniques, where the structures are produced by removing parts of the material. Examples of these methods include photo-,[82–84] micro- and nanolithography.[85,86] But a big drawback of these techniques is their complexity and cost. In contrast, so-called “bottom-up” techniques, represent a new, much simpler, lithographic free and inexpensive way to produce micro- and nanostructures, as the structures are made out of building blocks in self-assembling steps. The most promising bottom-up approach is represented by the wet stamping

(WETs) technique.[87–96] In this technique, periodic precipitation processes such as the Liesegang phenomenon are used for the production of micro- and nanostructures.

The major aim[97] of this project was to increase the surface area of such weak, but stable and cheap catalyst materials (such as hematite) without increasing the thickness of the catalyst layer, by exploiting highly periodic reaction diffusion precipitation processes known as Liesegang phenomena. For this reason it was necessary to investigate the Liesegang phenomenon for a controllable use of the precipitation process for the implementation of possible catalyst materials. A secondary target was the screening for new possible catalyst material combinations showing the ability to form periodic precipitation bands.

1.2 About Liesegang phenomena

Precipitation phenomena showing periodic structures and bands in hydrogels (such as gelatin) were first described in 1896 by *Raphael Eduard Liesegang*.[98] In this reported classical system, silver nitrate diffuses into a potassium dichromate containing gelatin matrix, forming periodic precipitation rings like those shown in the Image 1.2.

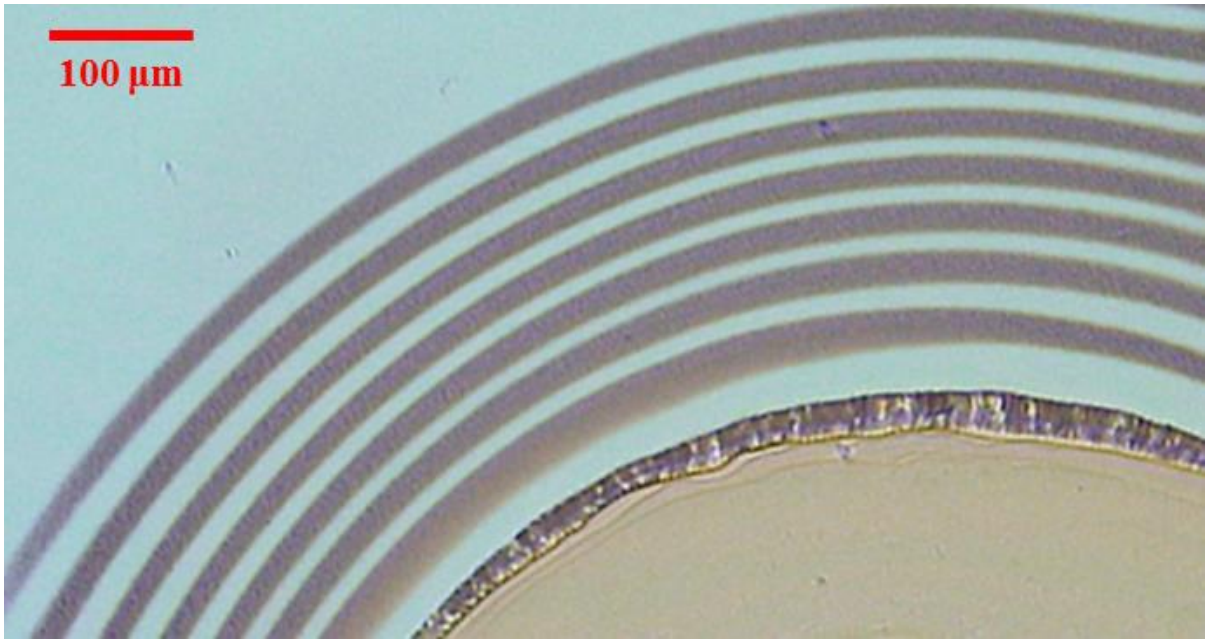

Image 1.2: Optical image of periodic precipitation rings, observed in the classical Liesegang system, containing silver nitrate as outer and potassium dichromate as inner electrolytes.

For this reason, periodic precipitation bands are also-called Liesegang bands or rings. The diffusion direction is controlled by the concentration of the inner and outer electrolytes. Usually the inner electrolyte is of lower concentration than the outer electrolyte. In the classical system, silver nitrate represents the so-called invading or outer electrolyte, because it penetrates the potassium dichromate system, which on the other hand represents the so-called inner electrolyte. In this system, the precipitates forming the bands consist of the reaction diffusion product of the outer (silver nitrate) and the inner electrolyte (potassium dichromate), and the material forming the precipitation bands is believed to be silver dichromate.[90,98,99] In general, this periodic precipitation phenomenon occurs when one, two or more[100] compounds (salts) that are soluble in a hydrogel, diffuse into a certain hydrogel matrix (e.g. gelatin,[87,98,101–105] polyvinyl alcohol (PVA),[106–108] or agarose),[109] containing another charged (ionic) compound. There, the outer electrolyte reacts either with the gel-matrix or with the inner electrolyte, forming insoluble precipitates.

In addition to this, the precipitation pattern (rings or bands) is described as well separated regions containing visible and invisible (cf. Section 4.3.1) precipitation products, while regions between two rings/bands are optically free of such precipitates (Figure 1.5).

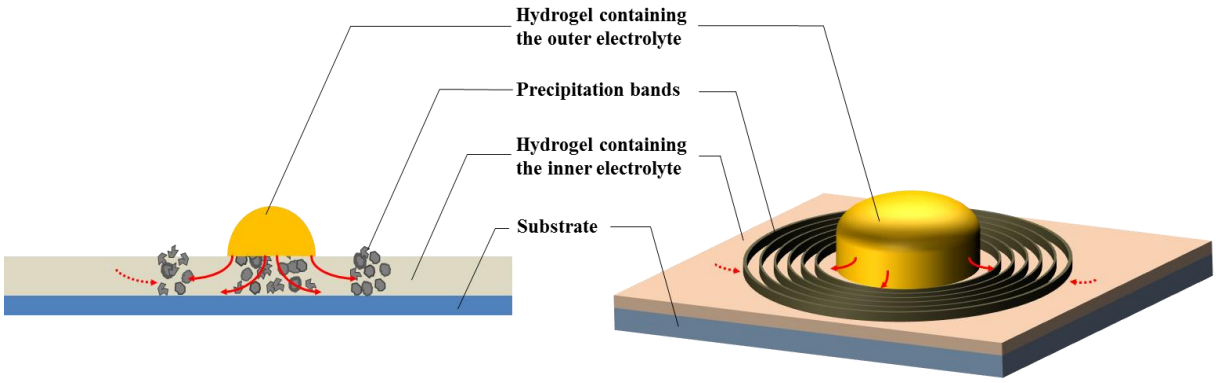

Figure 1.5: 2D cartoon (left) and 3D cartoon (right), illustrating the periodic precipitation process observed in Liesegang-type systems: Outer electrolyte (yellow droplet) diffuses (red full arrows) into the hydrogel containing the inner electrolyte (grey layer). There both electrolytes react with each other (indicated by the dashed red arrow) forming precipitates/bands (dark grey). The band forming process is not fully understood yet. (cf. three theories describing the precipitation process).

Since the discovery of the classical system, many additional systems have been discovered in various fields of research e.g. geology,[100,110–112] medicine,[113–121] biology,[122] and both physics and chemistry.[87,88,90,91,99,101,123–129] Large expanding Liesegang bands (up to several meters) containing iron oxides were observed in sandstones,[110] while very thin and dense bands (0.5 - 2.0 mm) have been observed in banded agate stones.[112] Interestingly, Liesegang structures were also observed in human excretions and tissues, such as urine[116] (of sick persons), damaged eyes[120] and fibroblastic tumors.[121] In addition to that Liesegang structures made out of fungi were observed on the surface of rotten food, such as vegetables.[122,130] All these different examples show how commonly this effect occurs. Nevertheless, chemists and physicists discovered the potential of this phenomenon and its use for the preparation of self-organizing and self-assembling micro- and nanostructures.[90,91,104,106,131] For this reason, several intense experimental and theoretical studies have been carried out over the past 120 years. Depending on the geometry of the system (used hydrogel, pH, concentration of the ionic electrolytes), different types of patterns, including regular band formation, dendrites with fractal structure, revert type Liesegang bands, dynamic precipitation waves, and the coexistence of primary and secondary patterns can be observed.[88–90,99,123–127,132–134] In the latter case two different types of patterns with different frequencies are superimposed.[88] However, in order to understand, to describe and to explain this phenomenon, experimental investigations were mainly focused on the role of the hydrogel, the used electrolytes (salts)

and the control of the band formation (shape and size of the bands), as well as on the material composition of the precipitates and their use in possible applications, while the theoretical analysis dealt with equations and mathematical models to describe the experimental observations. As a result of both experimental and theoretical investigations, several theories, such as the so-called "supersaturation theory", "colloidal coagulation theory" or "phase separation theory" were developed, describing the occurrence of periodically well separated rings.[87,89,91,92,98,103,105,113,116,131,135–145]

The supersaturation theory, proposed by *Wilhelm Ostwald* in 1897 shortly after the discovery of the Liesegang phenomenon represents the simplest model describing the periodic precipitation.[138] In this proposed mechanism it is assumed that the invading outer electrolyte reacts with the inner electrolyte in the hydrogel matrix. The concentration of the reaction products gradually increases until it reaches a value of supersaturation. At this critical point nucleation/band formation starts and large amounts of micro- and nanoparticles are precipitating. Since the concentration is very high, the particles will form very fast. This effect depletes the surrounding area, lowering the concentration of the inner electrolyte. However, the diffusion is ongoing and the outer electrolyte passes over this depleted area in to regions where the concentration of the inner electrolyte is higher. There the whole process is repeated and the next band is formed further afar. This process continues until one of the electrolytes is removed or until the concentration of the outer electrolyte reaches a value where diffusion or reaction with the inner electrolyte stops.[137–140]

In the colloidal coagulation theory it is assumed that the band forming process is divided into two steps. In the first step the sol particles are formed as a reaction product of the outer and inner electrolytes, while the outer electrolyte penetrates the hydrogel matrix containing the inner electrolyte. Elemental for this theory is the assumption that the particles forming the sol in a kind of colloidal suspension are very small (a few nm), so that the hydrogel matrix still allows their diffusion. It is also assumed that the hydrogel stabilizes the sol electrostatically once it is formed. The precipitation/coagulation of the sol occurs when the concentrations of the outer electrolyte and the sol in the hydrogel matrix increase until the ionic strength of the sol reaches the critical coagulation point. This process forms the first precipitation band. However, once a nucleation site is generated, more particles from the sol will accumulate very fast, leading to a depleted zone, where the concentration of the sol particles is reduced.

Since diffusion of the outer electrolyte is ongoing, it passes over this depleted area and reaction of the outer and inner electrolyte starts again leading to an increase in the sol concentration. This starts the sol coagulation process again.[108,109,139,140,142,146–149] This process was supported by experiments from *Hedges* and *Henley*,[141] by *Flicker* and *Ross*,[142] and also by *Kai, Müller* and *Ross*.[142–144] In their experiments the reaction product of the inner and outer electrolyte was prepared first, forming a colloidal sol, which was used to prepare a hydrogel matrix (without an inner electrolyte). Once the outer electrolyte was added, the diffusion process into the hydrogel matrix was started. Interestingly, regular precipitation bands were formed without reaction of an inner and outer electrolyte.

The so-called "phase separation theory" proposed by *Z. Rácz et al.* in 1999[145] represents a more reasonable explanation for the formation of Liesegang bands, since it also explains the occurrence of small precipitation particles between two bands. In this theory, the band formation is described as spinodal decomposition scenario, where it is assumed that the outer and inner electrolytes form an intermediate compound (*I*) in the hydrogel matrix. Based on the Cahn-Hilliard dynamics, the intermediate compound *I* is located as a homogeneous precipitate behind the moving chemical front (invading outer electrolyte). When the local concentration of the precipitate reaches a critical value, the precipitate segregates into high- (c_h) and low- (c_l) concentration regions. The high- (c_h) concentration regions are forming the precipitation bands, while low- (c_l) concentration regions are responsible for the depletion zones between two adjacent bands.[88,106,124,134,139,147,150–152] This theory was also used for the mathematical model in Section 3.4.4.

However, although the Liesegang phenomenon was extensively studied for more than a hundred years, leading to various theories and mathematical models, none of these models can explain all the experimental observations. For this reason a proper mechanism explaining the occurrence of Liesegang bands is still under discussion. Nevertheless the broad occurrence of this phenomenon suggests the assumption that it is possible to find many other systems showing this behavior. In combination with the possibility to control the shape and size of the precipitation bands, by using several experimental techniques (such as the WETs technique), this opens a wide range of possible applications of different materials. For both reasons, finding a proper model and possible applications, it is necessary to investigate the Liesegang phenomenon further.

2. Methods and materials

2.1 Introduction

In this chapter every essential analytical technique used to analyze the observed micro- and nanostructures as well as the techniques and methods for sample preparation are briefly described. In the first part all used analytical tools and methods are described, which were used to analyze the surface and the material of the micro and nano particles forming the Liesegang precipitation bands. The second part is about the photo electrochemical cells (PECs) setup used to evaluate the water splitting properties of some of the prepared samples. The third part describes the used techniques for sample preparation, while the last part is about the used chemicals and other materials.

2.2 Analytical tools and techniques

2.2.1 Surface and material properties

2.2.1.1 Light/optical and Laser microscopy

Optical microscopy represents one of the simplest analytical methods used. The specimen can be magnified by a simple optical lens system. Therefore light is applied, shining onto the specimen. This light is then either transmitted by the specimen or reflected from its surface (depending on the used microscope technique). The light leaving the specimen is than magnified in the lens system, giving a large scale image.[153,154] The resolution (d) of a light microscope is limited by the wavelength (λ) of the used light and the numerical aperture (NA) (Equation 1).

$$d = \frac{\lambda}{2\,NA} \qquad (1)$$

With the best optical microscopes available at the ZMB, a maximal resolution of 200 nm (and 50 nm in darkfield) can be obtained.

In Stereomicroscopes the light is directed onto a specimen and reflected from its surface. The reflected light passes the lens system of the microscope and a magnified image of the surface is generated (Figure 2.1 left). In case of transmitted light microscopes the light ray is tuned and focused onto the specimen by a condenser lens before transmitting the specimen. After transmission the light passes the lens system, generating a magnified image of the specimen (Figure 2.1 right). 3D laser profile images were acquired using a 3D Laser Scanning

Microscope (*Keyence VK-X200*),[155] which has in principle the same lens system as a stereomicroscope (Figure 2.1 right). Here a violet laser (408 nm at 0.95 mW) is used as the light source. This technique allows a maximal resolution of 24000 which means that the resolution for the profile (height) measurements is 0.5 nm. In the 3D profile mode, a laser beam is used to prepare several images of a specific focus point. During one measurement, this focus point is varied by changing the distance between the specimen and the laser. The data are digitalized; all images are superimposed and corrected with the height change during the measurements, resulting in very precise 3D profiles. These profiles are then further analyzed with special software. The drawback of this technique is the maximal resolution which is lower compared to atomic force microscopy (AFM). But for objects in the micro- and nano-region the 3D laser profiling offers a much faster technique delivering the same profile information.

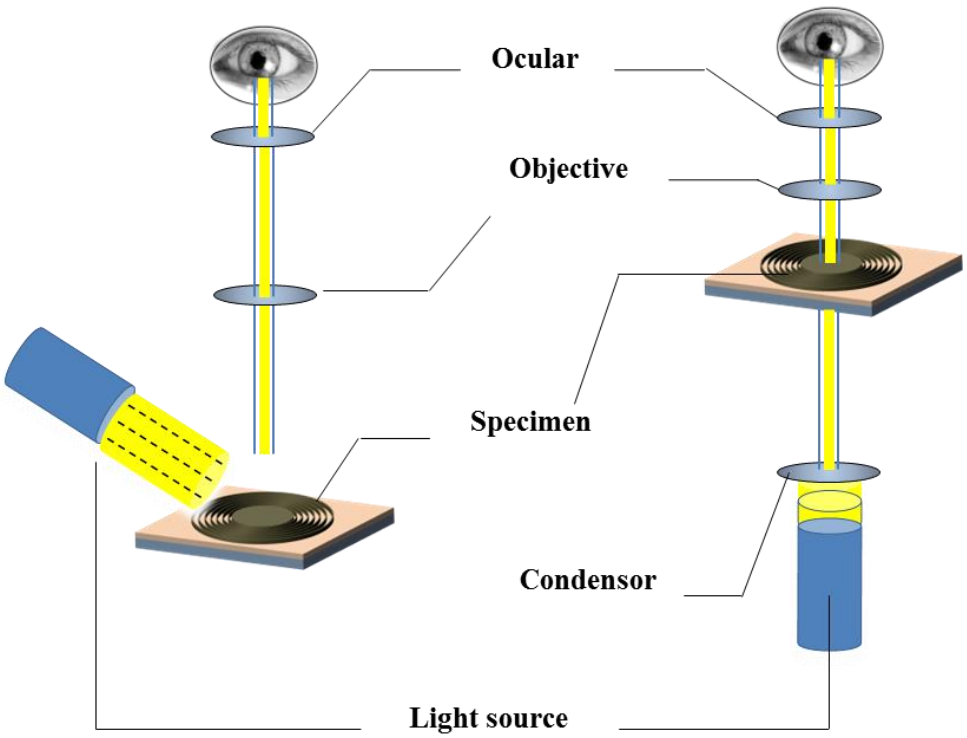

Figure 2.1: Schematic setup of a stereo microscope (left) and a transmitted light microscope (right).

2.2.1.1.1 Electron microscopy

Electron microscopy was used for sample and structure analysis in the micro- and nanoscale. The differences between the used electron microscopes (TEM, STEM and SEM) can be found in *Figure 2.2*. A detailed description about the working principle of each can be found in the following section.[156,157]

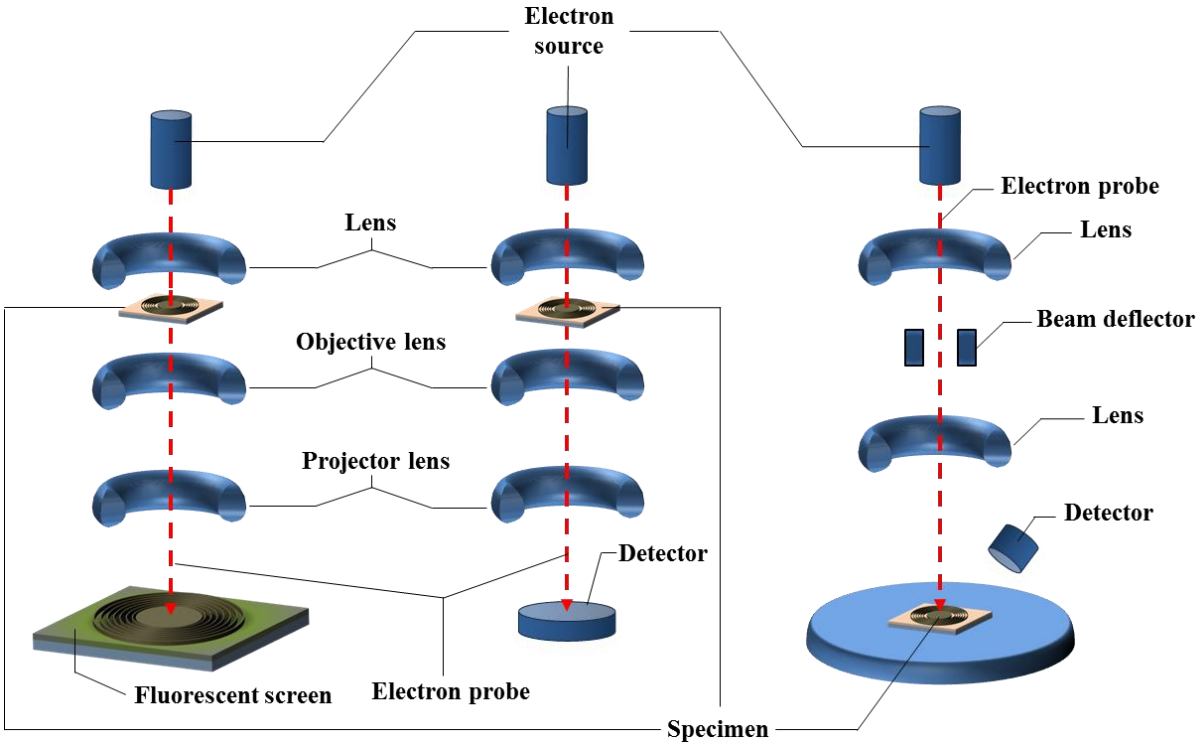

Figure 2.2: Schematic setup of a transmission electron microscope (TEM) (left), a scanning transmission electron microscope (STEM) (middle) and a scanning electron microscope (SEM) (right).

2.2.1.1.2 Scanning electron microscopy (SEM)

2.2.1.1.2.1 General

Scanning electron microscopy (SEM) (Figure 2.2 right) is used to obtain high resolution information of the structure and state of a specimen. For this reason, an electron beam (primary electrons) prepared by a cold field emission electron gun is used which scans the sample line by line. In contrast to light microscopy, the resolution is only limited by the diameter of the electron beam and the vacuum in the ray path which results in a much higher resolution and a very high depth of focus.[156–158] Different information about the specimen can be gained depending on the power range (eV-keV) of the beam (Figure 2.3 left). A weak electron beam up to 50 eV[156,157,159] generates secondary electrons (SE) in the specimen which are collected in a detector and converted into images. Those are used to obtain topographic information. A stronger primary electron beam (up to approx. 40 keV) penetrates further into the sample and produces secondary and backscattered electrons (BSE). BSE are used to obtain material contrast. The information gained by BSE originates from a much larger area than those from SE (Figure 2.3 right).[156,157,159]

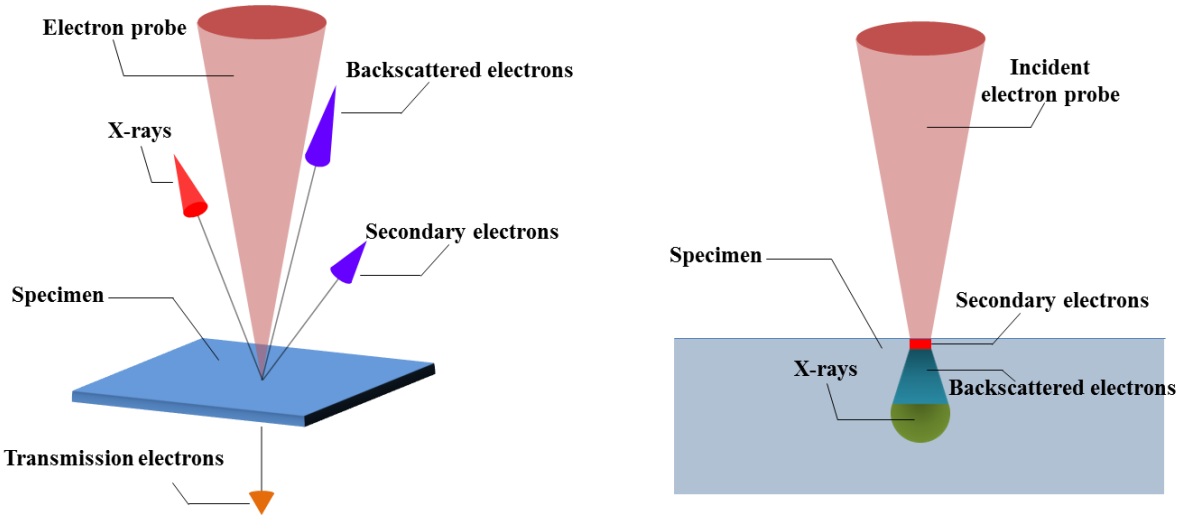

Figure 2.3: Infographic of the material information, which can be obtained by electron microscopy (left). The right infographic shows how deep the primary electron beam penetrates the specimen and how big the area is from where the material information is collected.

2.2.1.1.2.2 Secondary electrons (SE)

SE can be detected either by an Everhart Thornley detector (ETD) or an In-Lens detector, which is also known as Through the Lens detector (TLD). The ETD is laterally located in the microscope. This leads to images with an uneven chiaroscuro contrast (i.e. strong contrast between black and white or dark and light). Regions facing the detector appear brighter compared to those on the averted side. This generates a vivid impression of the sample surface. The TLD as the name implies is found directly in the lens/electron column of the microscope. One big advantage of this is the proximity of the detector towards the specimen, leading to more secondary electrons being received at the detector which increases the resolution limit of the microscope. Another advantage of the central location of the detector is the increase of the material contrast leading to an increase in the depth of focus.

2.2.1.1.2.3 Backscattered electrons (BSE)

As mentioned before, BSE, which are created in the specimen by stronger primary electrons, are detected in the backscattered electron detector. This detector is usually located beneath the TLD to increase the uniformity of the distance towards all collected BSE creating high quality material contrast images. As the signal of BSE depends on the chemical composition, the method is used to obtain information about elements in the specimen. In other words, high atomic number elements appear bright and low atomic number elements darker.

2.2.1.1.2.4 Energy dispersive X-ray spectroscopy (EDX)

More precise data about the chemical composition of a specimen are gained by EDX spectroscopy.[160–163] The EDX detector monitors characteristic X-ray emission form the specimen. These emissions are generated after the sample is irradiated with a high-energy beam of charged particles (e.g. electrons) (Figure 2.4).

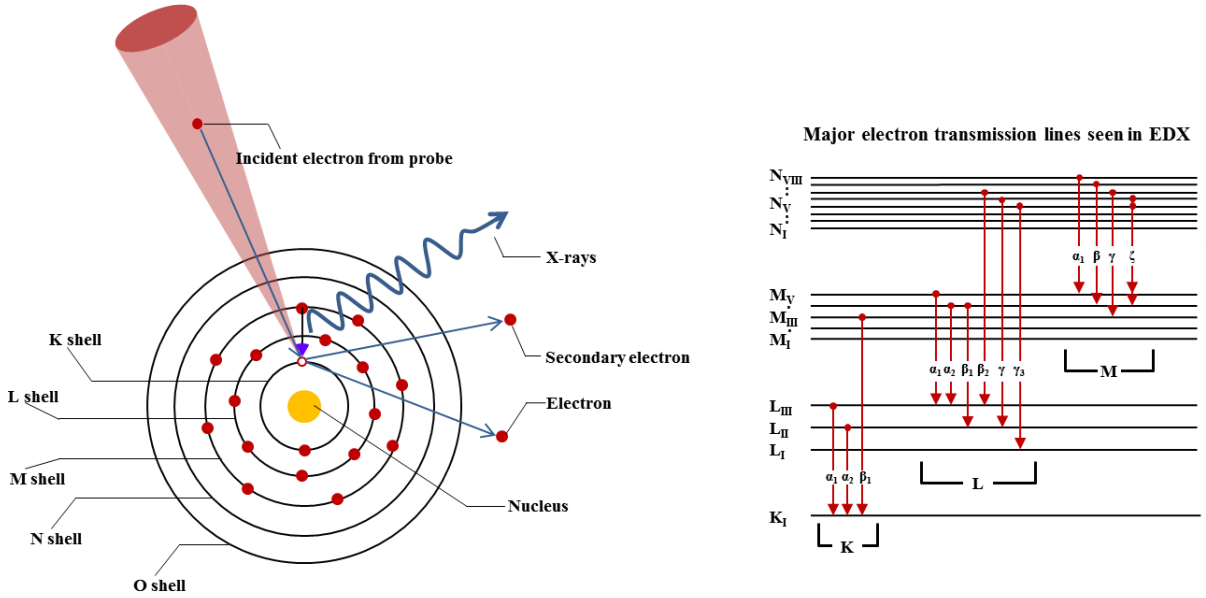

Figure 2.4: Physicochemical origin of the information, which can be obtained by EDX spectroscopy. According to JEOL periodic table for EDS analysis.[164]

The missing subshell electrons are replaced by electrons from the outer shell to get back to a more stable electron configuration. As electrons in the outer shell possess more energy as subshell electrons, the energy difference (outer – subshell electron) is emitted as X-ray irradiation, which is specific for each element. The collected X-ray data are digitalized and visualized in a spectrum showing the elemental composition of the specimen. It has to be mentioned that the energy (keV) of the primary electron beam has to be at least twice as high as the energy which can be visualized in the analysis later. In the case of silver for example, the primary electron beam has to have 6.0 keV at the minimum to obtain Lα at 2.984 keV. But one has to be aware of the fact the information gained by X-rays originates from a much larger area than that gained by secondary electrons (Figure 2.3 right). This can lead to problems if particles less than 20 nm in diameter need to be analyzed.

2.2.1.1.2.5 SEM sample preparation (for FEI Nova Nano SEM 230)

In order to prevent the specimen from charging while measuring and to get high resolution images with an excellent quality, the sample has to be made conductive. The specimen was therefore put onto a special conductive carbon containing sticker which was connected to a conductive object slide. Depending on the desired resolution and purpose of the SEM measurement the whole sample was then covered either with a 30 nm carbon (C), 20 nm gold (Au) or 30 nm platinum (Pt) sputtering layer (Figure 2.5).

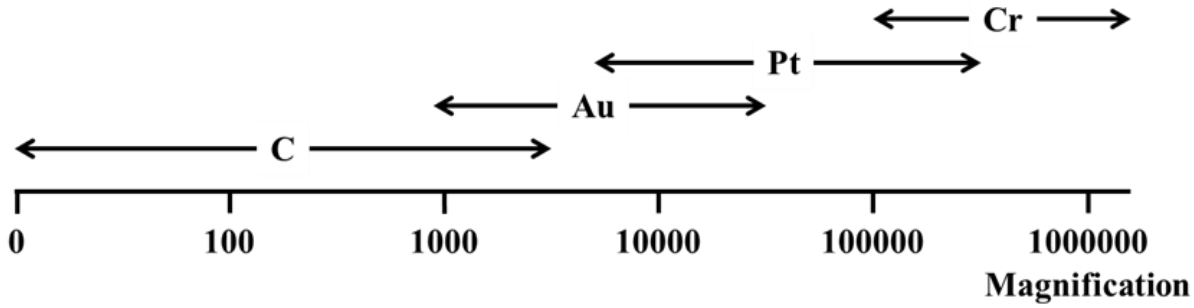

Figure 2.5: Sputter coating material according to the desired resolution in the SEM.

All samples were sputtered either in a *Leica EM ACE600* high vacuum coater or a *BalTec MED020* sputter coating unit. If a sample is not sputtered, the specimen charges and objects in the SEM images appear very bright and out of focus.

2.2.1.1.3 Scanning electron microscopy – focused ion beam (SEM-FIB)

2.2.1.1.3.1 General

All SEM-FIB experiments were performed on a *FEI Helios Nano Lab 650* which is a dual beam instrument combining the advantages of two techniques, field emission scanning electron microscopy and focused ion beam. Generally an SEM-FIB can deliver the same information as a standard SEM, but also offers the possibility to manipulate the specimen with the FIB. In all the SEM-FIB images and SEM-FIB EDX data, presented in this thesis, the FIB was used to cut/mill the specimen and SEM as well as EDX were used for imaging and analysis. This offered the possibility to obtain high resolution information about the material composition and arrangement inside the specimen.

2.2.1.1.3.2 SEM-FIB sample preparation (before and in SEM-FIB)

In order to obtain information about the inner part of the specimen the sample has to be milled in the FIB. During the milling process the sample is tilted by 54° in the SEM-FIB vacuum chamber to receive a proper cut. For this reason, the specimen is fixed very tightly to the conductive objective slide by using conductive silver paste. After drying the samples at room temperature for 20 minutes, they were sputter coated with a 30 nm platinum (Pt) layer (*Leica EM ACE600*). This was also done to prevent the specimen from charging during measuring and milling (Image 2.1 left).

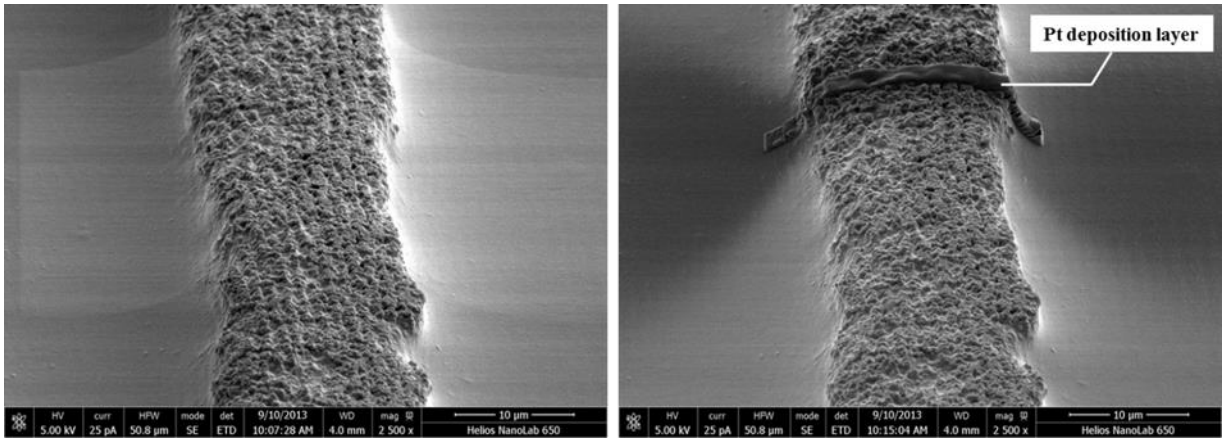

Image 2.1: SEM images of the SEM-FIB process. Left: image of a fine structured primary and secondary Liesegang band (classical Liesegang system) with a 30 nm sputter coated Pt layer. Right: Same place as the left image but with an additional Pt deposition layer, before the milling process was started.

As mentioned before, the sample is tilted by 54° in the vacuum chamber due to the technical arrangement of the SEM magnetic lens system. The SEM has to be perpendicular to the ground otherwise earth gravitation would influence the primary electron beam. After tilting, the specimen is covered by an additional 0.8 µm thick platinum layer (Figure 2.6). For this, an automated gas injection needle is brought very close to the specimen (100 µm distance to the desired protection place). Trimethyl(methylcyclopentadienyl)platinum(IV) ($MeCpPtMe_3$) is used as platinum containing gas. By scanning with a weak gallium ion beam (1-10 $pA/\mu m^2$), the precursor gas starts to decompose into volatile and non-volatile parts. The volatile compound is removed by the vacuum system of the SEM-FIB chamber and the non-volatile part remains on the sample surface as a highly conductive platinum deposition layer (Image 2.1 right). This is done to protect the observation area from destruction through gallium ions during the milling process. After addition of the deposition layer the gas injection needle is removed and the milling/etching process is started. For this process the ion beam current density is increased (1-100 $nA/\mu m^2$).[165,166] The gallium ion beam which is directed towards

the Pt deposition layer mills material off while scanning over the surface (Figure 2.6 right and Image 2.2 left).

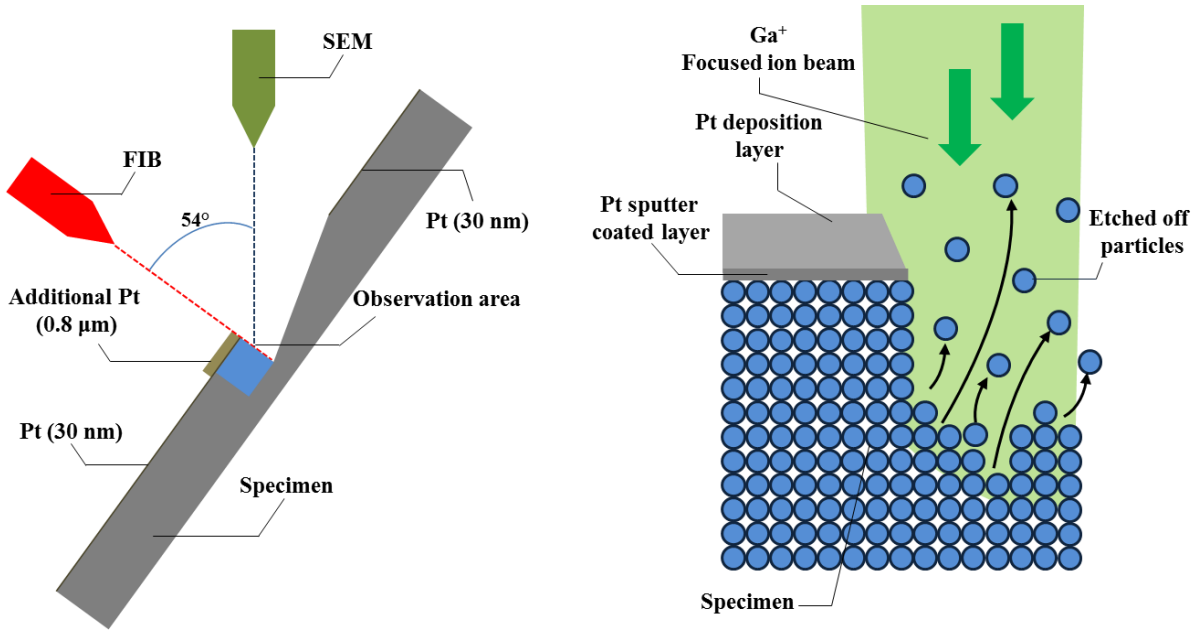

Figure 2.6: Schematic working principle of the Dual Beam SEM-FIB instrument. Left: instrument arrangement of the SEM and FIB. Right: surface etching process induced by the Ga ions.

If the gallium ions have too much energy during the milling process, it is possible that some of the etched material is redeposited at the etching zone, seen as white stripes in Image 2.2 left. For a proper cut and a clean surface (Image 2.2 right), the specimen has to be polished with a weaker gallium beam afterwards. After etching and polishing the samples were further analyzed by SEM and EDX.

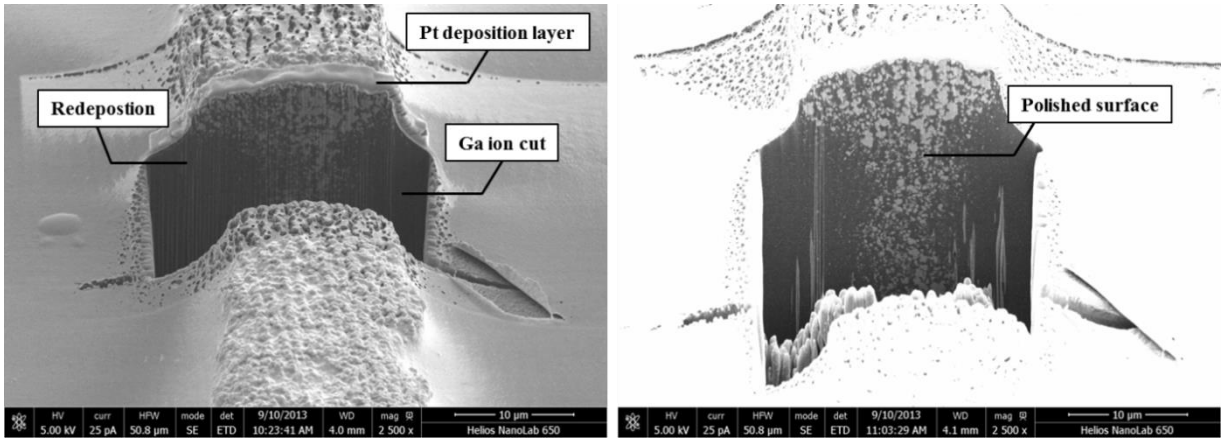

Image 2.2: Same sample as in Image 2.11. Left: image taken shortly after the milling process was started. Sample contains some artefacts from redeposited material. Right: Image taken after the etching and polishing process of the FIB was finished.

2.2.1.1.4 Scanning transmission electron microscopy (STEM)

2.2.1.1.4.1 General

STEM measurements were performed on a *FEI Helios Nano Lab 650*. As the scanning transmission electron microscope offers nano- and sub-nanoscale resolution, it was used for additional specimen analysis. The instrument setup of STEM is almost the same as for a Transmission Electron Microscope (TEM) (Figure 2.2 left). Primary electrons emitted by a field emission electron gun are focused by a set of electromagnetic lenses onto the specimen. The higher the accelerating voltage, the smaller the wavelength of the primary electron beam which increases the maximal theoretically available resolution. But this is also limited by the quality of the lens system as well as by the specimen. Heavier elements in the specimen lead to a better deflection of the transmitted electrons resulting in higher material contrast. In contrast to SEM, the electron detector in STEM is located below the specimen. For this reason, the specimen needs to be thin to be transparent enough for electrons to go through. The samples had to be therefore less than 200 nm thick.

2.2.1.1.4.2 STEM-EDX combination mode

As the EDX spectra from the SEM-FIB samples also included background information from the gelatin matrix used in almost all experiments, it was not possible to obtain highly accurate material composition information from the specimen. For this reason, EDX measurements were performed using the STEM mode and microtome cuts. The advantage of the microtome cuts lies in their thickness, leading to EDX spectra with almost no background noise.

2.2.1.2 Atomic force microscopy (AFM)

Atomic Force Microscope (AFM) (*Bruker Dimension 3100*) images and profiles were obtained in contact and tapping mode. The sample is mounted on an XYZ sample stage which can be moved under the cantilever for measurements. During the measurement a laser beam is adjusted to the backside of the cantilever and is reflected towards the photodiode detector. While the very sharp tip (< 5 nm width) is rastered over the sample, it is tilted by the shape of the surface (Figure 2.7 left).
Depending on the AFM mode (Figure 2.7 right), the reflected laser beam generates a signal which is translated by a computer into an image. In the contact, mode the cantilever tip is

moved up and down only by the height differences in the sample surface. In the tapping mode, the cantilever oscillates above the sample surface, minimizing the sample penetration of very soft surfaces such as gelatin.[167,168]

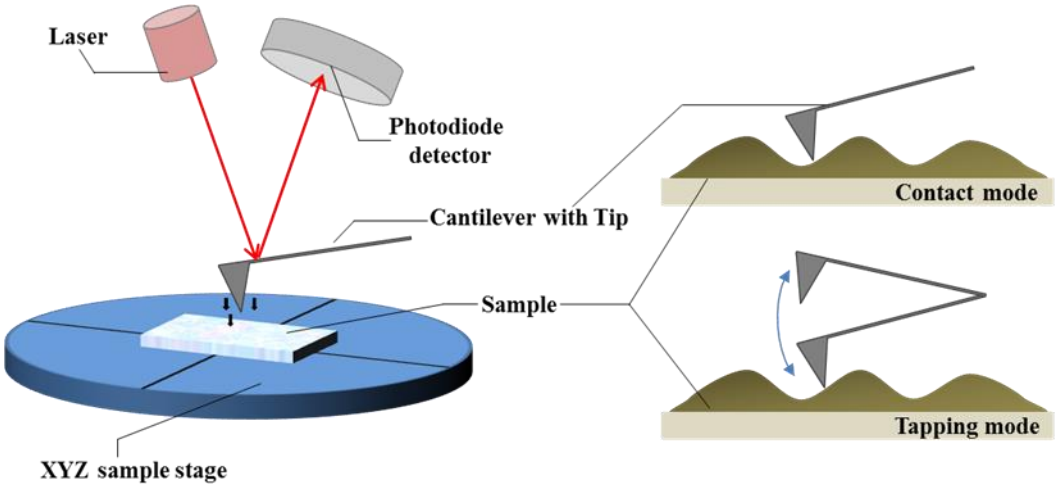

Figure 2.7: General working principle of an atomic force microscope (left) and simplified working scheme of the contact and tapping modes (right).

2.2.1.3 X-ray photoelectron spectroscopy (XPS)

This analytical technique was used for a quantitative analysis of the elemental composition of the Liesegang bands in the silver system (Section 4.3.5, p. 71). For XPS analysis, an X-ray beam (monochromatic Al Kα excitation) is directed onto the sample surface in a high vacuum chamber (~10^{-8} mbar) to excite photoelectrons. These excited photoelectrons can be produced by different processes in the sample while X-ray photons are absorbed (Figure 2.8 left).

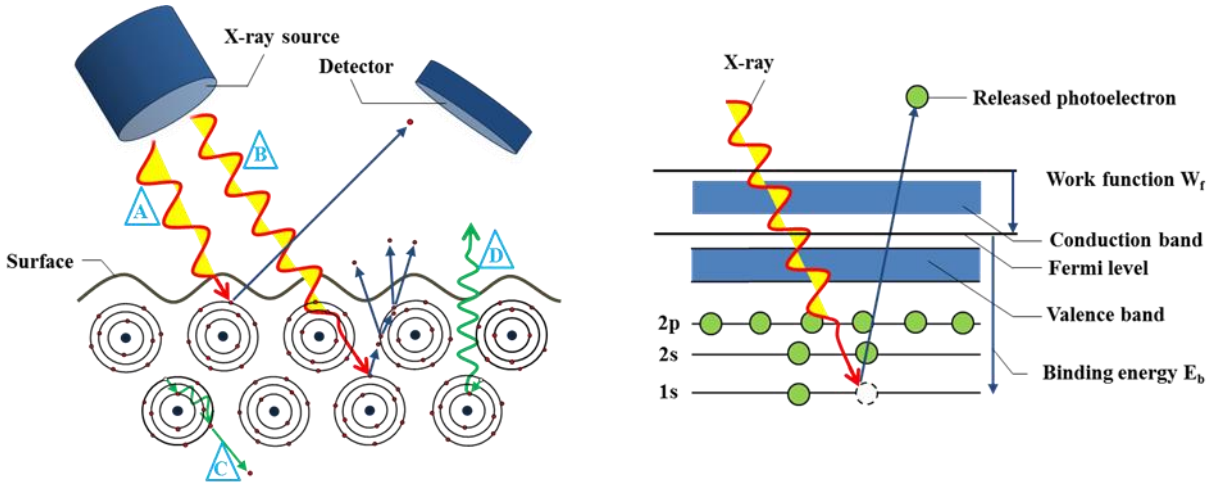

Figure 2.8: Schematic representation of the working principle of an X-ray photoelectron spectroscopy measurement. Sources for emitted photoelectrons (left). Relevant binding energy Eb. levels (right).

In the first case (A), photoelectrons are directly emitted (without scattering). In the second case (B), the emitted photoelectrons are scattered at other surface atoms/molecules. This either elastic or inelastic scattering leads to the release of additional electrons, which are seen in the spectrum as background noise. In the third case (C), so-called Auger electrons are produced by electrons jumping from an outer shell into the electron hole consigned by previously emitted electrons. In the fourth case (D), fluorescence is observed, emitted by outer shell electrons which also jump into the empty electron holes like in C, but without emission of additional electrons.[169–171] Based on the energy levels of the released photoelectrons (case A-C), which are specific for each element, XPS is used to obtain information about the elemental composition and binding energy of atoms/molecules in the specimen (Figure 2.8 right). The specific binding energy E_b depends on the chemical environment and can be calculated by Equation 2 where $E_{Photon} = h \cdot v$ (Energy of the excited X-ray photons), E_{Kin} = kinetic energy of the released photoelectron and W_f = work function.

$$E_b = E_{Photon} - E_{Kin} - W_f \quad (2)$$

2.2.1.4 Synchrotron based scanning transmission X-ray microscopy

Near edge X-ray absorption fine structure (NEXAFS), which is measured in the soft X-ray range (100-2000 eV) provides information about the chemical speciation of the material in a specimen. Combination of synchrotron-based scanning transmission X-ray spectro-microscopy (STXM) and NEXAFS allows high resolution mapping on the nanometer ($\geq$ 20 nm) scale.[172–176] STXM was performed at the *PolLux beamline* of the *Swiss Light Source* (SLS) (*Paul Scherrer Institute, Villigen, Switzerland*).[172–174,176]As all STXM samples had to be X-ray transparent, they were prepared on 100 and 200 nm thick Si_3N_4 membranes. Images were acquired covering length scales from 250 µm to 20 nm at photon energies covering the chromium L-edge (565 eV to 800 eV), the oxygen K-edge (500 eV to 600 eV) and the silver M-edge (340 eV to 420 eV). The silver energy range also contains the nitrogen K-edge (395 eV to 403 eV), which causes some interference due to nitrogen present in the gelatin and the silicon nitride membranes supporting the samples and the Fresnel zone-plate focusing optic of the STXM instrument. For the STXM measurements and image preparation, the X-ray beam is focused on the sample by Fresnel lenses. While the X-ray beam scans over the sample, the intensity and the change of the transmitted X-rays are detected in a photomultiplier tube (PMT) (Figure 2.9). There the raw data are translated into images and

data sets, which can be compared with reference samples and spectra to obtain information about the elemental composition as well as chemical bonding (of the material) in the samples.

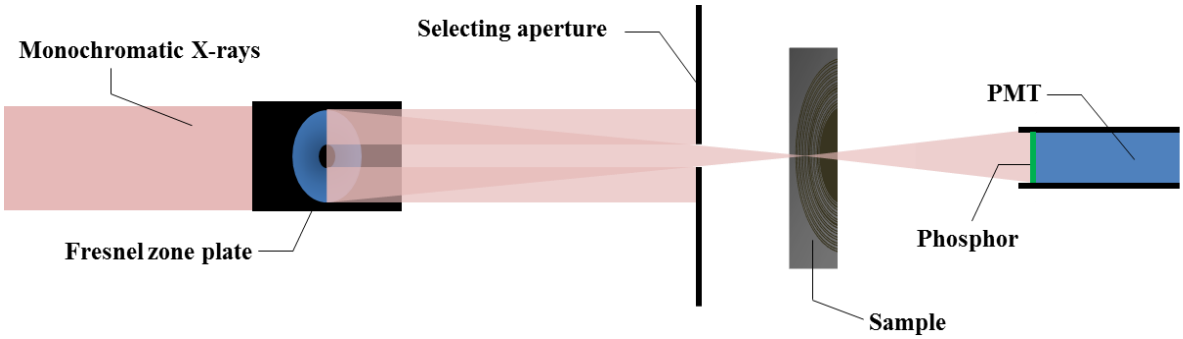

Figure 2.9: Working principle of STXM measurements. The monochromatic X-rays are obtained from the synchrotron line.

2.2.1.5 Live observation of the precipitation process

2.2.1.5.1 General

The live observation of the precipitation process taking place in the classical Liesegang system was necessary in order to see how the precipitation bands are formed. For this reason live observation and digital video recording of the precipitation process was done using a stereo microscope (*Leica MZ16)*, connected to a high definition digital video camera and a pure white (6000 K) LED light source. The most critical point in the monitoring setup was the light source, which had to fulfill the following criteria: On the one hand, the energy of the light beam has to be weak, since silver nitrate, used as outer electrolyte, is light sensitive and would be reduced to elemental silver. This would stop the precipitation process. In addition this would lead to a darkening of the sample, making it impossible to see the process. On the other hand, the light needs to be bright enough to facilitate the monitoring and the digital video recording. Another critical point was the temperature of the observation area. If the temperature was too high, the stamp as well as the gelatin layer would dry and the precipitation process would stop. For these reasons a ringlight (*Scott VisiLED LED Brightfield Ringlight S80–55*) with a light flux of 100 lm was used for indirect illumination of the specimen.

We had to choose this setup and the lower resolution because it was not possible to monitor the precipitation process with a transmitted light microscope. There, the involved light source is a mercury vapor lamp, which would have heated and therefore dried the observation area. Another problem of this type of microscopes was the maximal available working distance between the objective lens and the specimen, which was too short for our setup.

2.2.1.5.2 Sample preparation and monitoring setup

0.5 mL of a hot gelatin solution (10 w/w%, *type 0*, 60°C, 0.03 w/w% NH_4OH) containing potassium dichromate (0.01 M) as inner electrolyte was doctor-bladed onto a microscope cover slip (60 x 24 x 0.16 mm). After drying for 24 h, the cover slip was mounted onto an adapter, with the gelatin layer pointing downward. The agarose stamp containing 0.3 M $AgNO_3$ as inner electrolyte was prepared according to standard procedures (Section 2.4.2.1). After drying on a dust free paper for 10 minutes, the stamp was placed on a clean microscope slid with the pins bound upwards. The monitoring and precipitation process was started, while the cover slip was placed on the stamp, with the gelatin layer pointing towards the stamp pins (Figure 2.10 left). The cover slip adapter was necessary to stabilize the thin slip during the observation process.

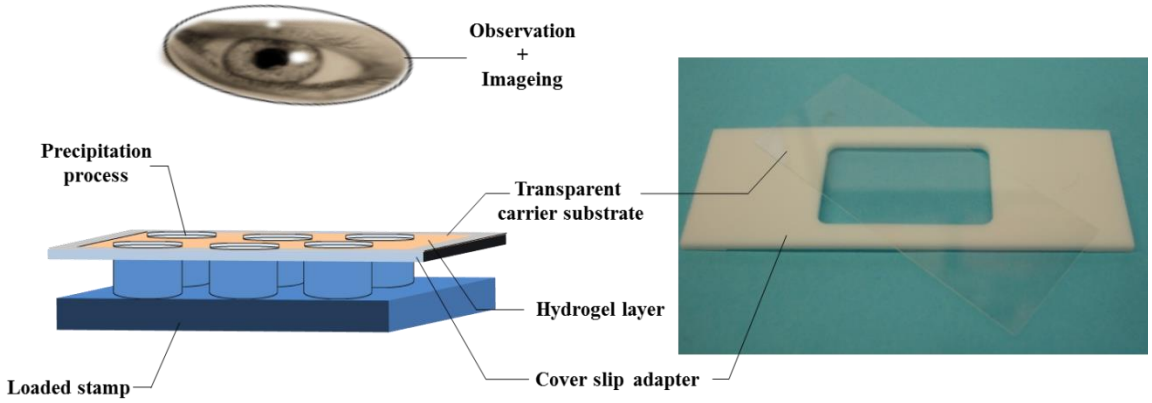

Figure 2.10: Sample setup for real time observation of the precipitation process under a stereo microscope. Schematic representation of the setup (left) and a photograph of the cover slip adapter (right).

2.2.1.5.3 Video processing

After two hours, the precipitation process was finished and the monitoring process was stopped. The recorded video was then reworked using a video editing freeware (*Microsoft Movie Maker*) to prepare a time lapse movie of the precipitation process where 1 s equals 1 min in real time. In this video it is easy to see that the location of the bands is fixed once they are formed. It is also possible to observe that a white precipitate is formed first before the first bands appear. For visualizing purpose the video clip was uploaded to the internet.

2.2.1.6 pH measurements

Two types of pH meter were used to measure the pH values of the samples. The measurements in the gelatin solutions were performed using the standard pH meters (*Metrohm 696 pH Meter* with a *Metrohm 6.0220.100 (pH 0-14 …80°C 3 M KCl) pH electrode*). Therefore the electrode was put into a tempered (22°C) gelatin solution. For pH measurements on the sample surface a 50 µm and a 100 µm thin pH micro electrode (*Unisense pH-50 and pH-100*) and a Unisense pH meter (*pH/redox measuring system 1 CH6849*) was used. As these electrodes are very fragile they were mounted to an XYZ stage. During the measurements the electrodes were carefully put onto the sample surface. The pH on the surface was for all measured samples in the same range as the pH values (differences of 0.05-0.1) measured with the Metrohm electrode. For this reason it was decided to measure all values directly in the liquid to speed up the measurements.

2.2.1.7 Thermogravimetric Analysis (TGA)

Thermogravimetic analysis (*Mettler Toledo TGA/SDTA851*) was used to obtain information about the decomposition point of gelatin. In the TGA the sample is heated to a defined temperature. A high precision microbalance records the mass change during the heating process. This mass change is then plotted versus time and the temperature at this time.

2.2.1.8 Nuclear Magnetic Resonance (NMR) Spectroscopy

Nuclear magnetic resonance spectroscopy was used for analysis of the ligands used for the coordination compounds. NMR spectra were either recorded on a *Bruker Avance III Ultrashield 400 MHz-Spectrometer* with a *PABBO BB-1H/D Z-GRD Z116098/0013 –probe* or on a *Bruker Avance III Ultrashield 500 MHz-Spectrometer* with a *Bruker 5 mm 500 MHz BBI probe with Z Gradient (p/n Z810701)*.

2.3 Watersplitting properties

2.3.1 Photoelectrochemical cells (PECs)

2.3.1.1 General

All measurements and setups concerning PECs were performed at EMPA Dübendorf by *Dr. Rita Tóth*. As some of my samples were used as photoanodes in cells measured at EMPA the technique is briefly described to explain the working principle. For artificial photosynthesis, i.e. solar water splitting experiments, photoelectrochemical cells were used. PEC cells utilize solar energy to electrolyze water to hydrogen and oxygen. The PEC cell consists of a photoanode, a metal counter electrode and a reference electrode immersed in an aqueous electrolyte and connected to an external circuit. The first solar water splitting using this technique was reported by Fujishima and Honda in 1972.[177] In their setup a TiO_2 photoanode was used which was irradiated with UV light to facilitate water oxidation (oxygen evolution) (Equation 3).

$$2H_2O \longrightarrow 4e^- + O_2 + 4H^+ \quad (3)$$

The general working principle of a PEC cell can be seen in Figure 2.11 and Image 2.3.

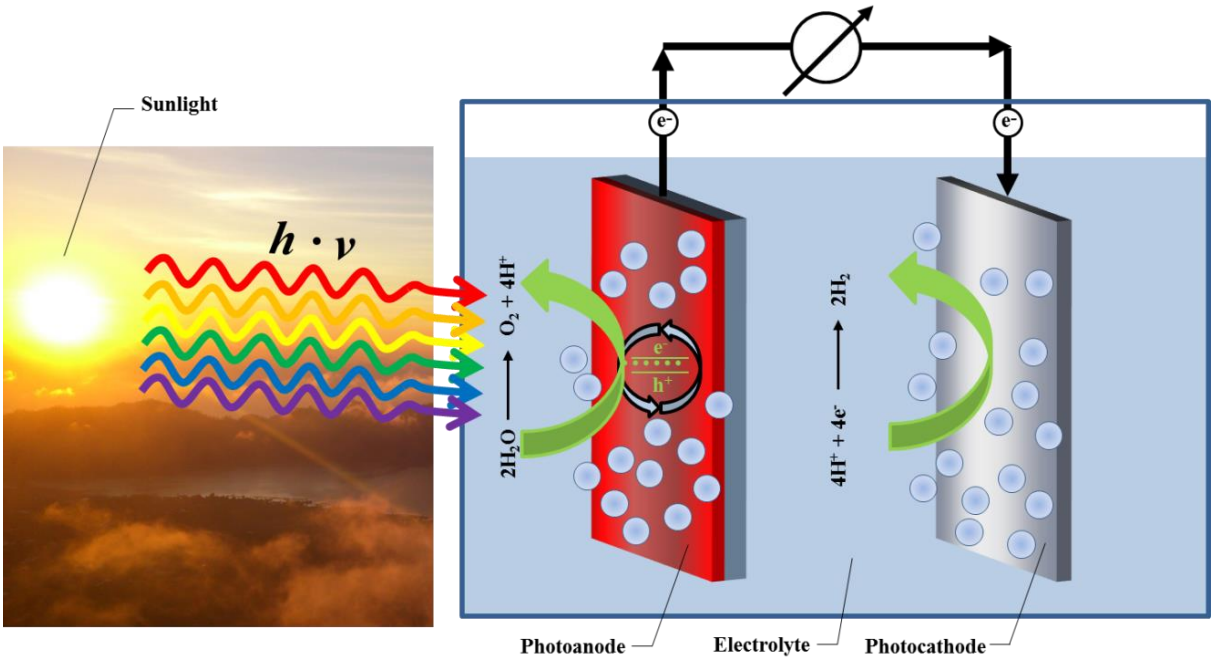

Figure 2.11: Working principle and preparative setup of a photoelectrochemical cell.

When light irradiates a semiconductor (usually a metal oxide) on top of a transparent conductive substrates, such as indium tin oxide (ITO) or fluorinated tin oxide (FTO) coated glass, electron-hole pairs are generated. The holes diffuse to the anode surface and oxidize water to form oxygen. The electrons generated in this process migrate to the cathode surface

where protons are reduced and hydrogen is evolved. Metals such as platinum as well as metal oxides such as Cu_2O are used as the electrode material for the photocathode.[71,76,79,80,178–184] Usually, an external electric bias is needed to drive the electrons from the anode to the cathode.

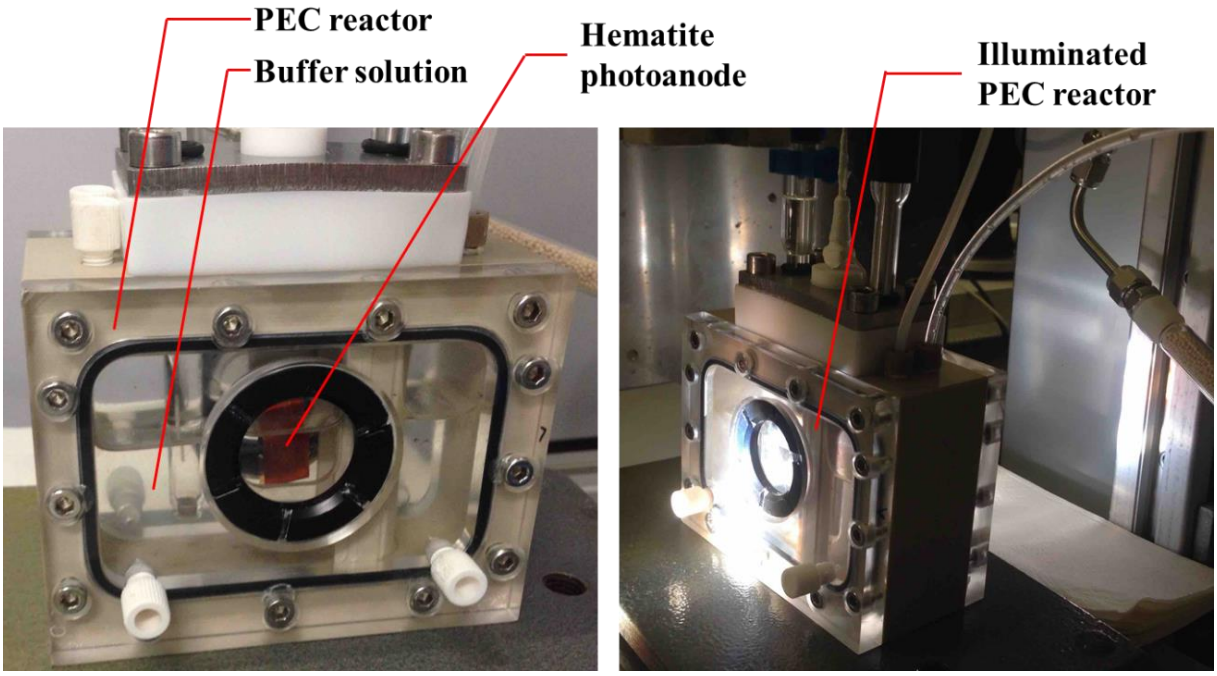

Image 2.3: Setup of a PEC reactor containing a hematite PEC photo anode (left). Image of a working PEC reactor (right). Images were taken at EMPA Dübendorf.

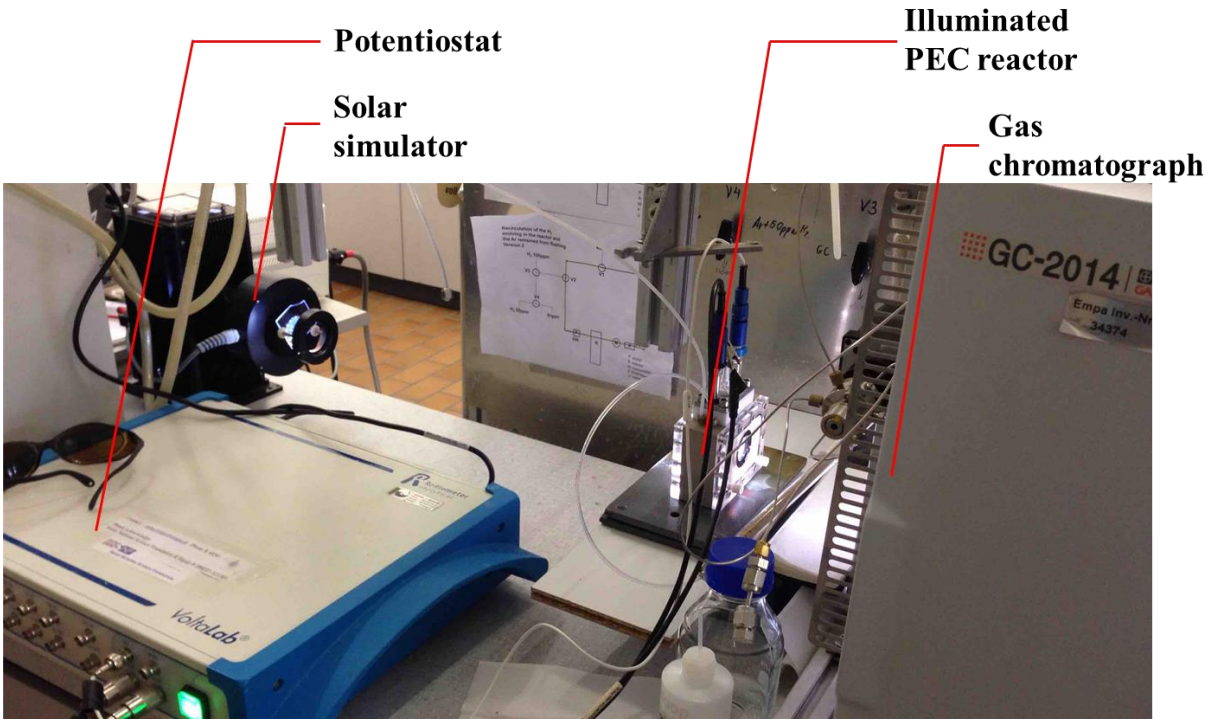

Image 2.4: The PEC test station at EMPA Dübendorf.

2.3.1.2 PEC cell measurements

In the PEC test station at EMPA (Image 2.4) a sun simulator (1.5 AM) is used as a standardized light source. For hydrogen quantification and to provide the external bias potential a potentiostat with an impedance analyzer (*Voltalab80 Radiometer Analytical*) is connected to the PEC cell. The evolved gas is measured *in situ* with a gas chromatograph (*Shimadzu*) which is also connected to the PEC cell. The evolved gas is recirculated and 200 µL samples are injected periodically (every 10 - 30 minutes). The gas chromatograph is calibrated with two reference gases containing 50 and 100 ppm H_2 in argon. A 1.0 M KOH solution is used as electrolyte in the PEC cell. As photoanode different samples containing hematite on fluorine doped tin oxide (FTO) were used. The system also contains a Pt photocathode and Ag/AgCl reference electrode. The quality of the photoelectrode is analyzed by measuring the photocurrent as a function of the applied voltage.

2.4 Sample preparation

2.4.1 Spin-coating

For spin-coating, a spin module (*SAWATEC SM-180-BT*) was used. In the first step all carrier substrates were cleaned by high ultrasonication with milliQ water, followed by sonication in ammonia (2.0 w/w%) and distilled ethanol. The substrates were then dried under a dust free nitrogen gas stream. The following materials were used as carrier substrates: FTO-glass (*Solaronix*), ultrapure microscopy glass (*Menzel*), Thermowax (*Thermanox*), pure and aluminum coated silicon wafers (*Sigma-Aldrich*), silicon nitride (*Silson Ltd.*), polypropylene (*Maagtechnic AG*) and poly(methyl methacrylate) (*Acros-Organics*). Only the 100 nm and 200 nm thin Si_3N_4 membranes used for STXM experiments were spin-coated without a previous cleaning step because of their fragility. For coating, the substrates are placed on a special vacuum chuck in the top center of the rotation motor. Vacuum is applied to keep the carrier in the center of the rotation axis while coating. In the next step the hydro fluid matrix was poured onto the carrier and the spinning module was started (one second acceleration up to the desired coating speed). Depending on the setup, coating speeds between 200-3000 rotations per minute (rpm) were used. This speed was then kept constant for 58 seconds. After that, the rotation was stopped within one second and the vacuum was turned off. The samples were removed and dried at ambient temperature. In case of the small ($3 \cdot 10^{-3}$ x $3 \cdot 10^{-3}$ x $1 \cdot 10^{-7}$ m) Si_3N_4 membranes, a special vacuum chuck (Image 2.5) was manufactured which applies

the vacuum only at the edges of the membrane surrounding silicon frame, to minimize the mechanical stress and sample damage.

Image 2.5: Special vacuum chuck for Si_3N_4 membranes, which applies the vacuum only on the Si-frame edges (black).

2.4.2 Wet Stamping (WETs)

The wet stamping technique adopted from established protocols by *B. Grzybowski et al.*[93] was used for downsizing the Liesegang bands from centimeter- and millimeter- to micro- and nano-scale (Figure 2.12).

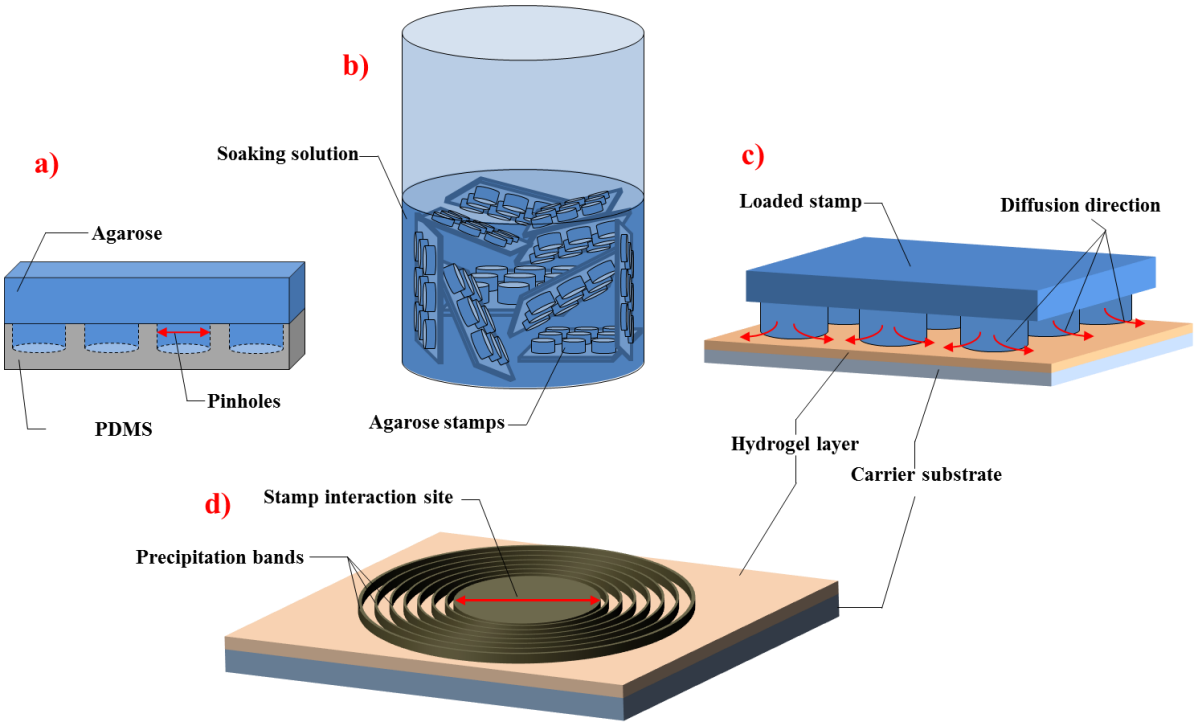

Figure 2.12: Wet stamping principle. a) stamp preparation, b) stamp loading process, c) precipitation reaction while the stamp is on top of the hydrogel layer and d) precipitation rings or bands after removing the stamps.

2.4.2.1 Stamp preparation

An aqueous agarose solution (6 w/w%) (*OmniPur Agarose*) was prepared by mixing degassed milliQ water with agarose. The solution was then heated in a household microwave oven (700 W) (10 times for 30 seconds). For a stable concentration, the evaporated water was replaced and the solution was stirred after every heating step. After the last heating step the hot solution was poured on a preformed polydimethylsiloxane (PDMS) mould. The mould is the negative of the desired stamp, featuring an array of small holes (25 holes·cm^{-2} and a diameter of 0.5 mm). The gel on the negative was then quickly but gently degassed to increase the amount of agarose filling the holes of the mould (Figure 2.12 a). After the gelation process was finished, the raw agarose stamp was removed and cut into smaller stamps (0.4 x 0.4 cm with 3 x 3 pins).

2.4.2.2 Loading and stamping

The stamps were soaked in the outer electrolyte **A** containing solution for 48 hours in the dark (Figure 2.12 b). Before stamping, the stamps were removed from the solution and dried for 3 minutes on a dust free paper. Used electrolytes were water soluble metal salts or metal coordination compounds. For the stamping process the pre dried stamps were placed on a thin and dried hydrogel layer (e.g. gelatin, agarose or PVA) containing the inner electrolyte **B**. The diffusion direction is controlled by the concentration of the electrolytes **A** and **B** (Figure 2.12 c). During the interaction of the stamp and the hydrogel film, **A** diffuses into the **B** containing system, where reaction occurs, forming precipitation bands in the hydrogel matrix. This so-called reaction diffusion process is either finished when the concentration of the salt in the stamp reaches the same concentration as the salt in the hydrogel, or when the stamp dries out or when the stamp or the hydrogel are removed. Depending on the salt combinations, the precipitates form regular structures, rings or bands (Figure 2.12 d).

2.4.3 STEM sample preparation (for FEI Helios Nano Lab 650)

2.4.3.1 Microtome cut

In order to produce very thin samples (~ 90-150 nm) microtome cuts of the specimen are produced (Figure 2.13) and mounted on a copper TEM grid. For this purpose the samples were prepared on a special Thermowax which is used as carrier substrate. After mounting the

sample onto a sample holder, it is sliced by a diamond blade into small sections. These so-called microtome cuts are placed on the TEM grids.

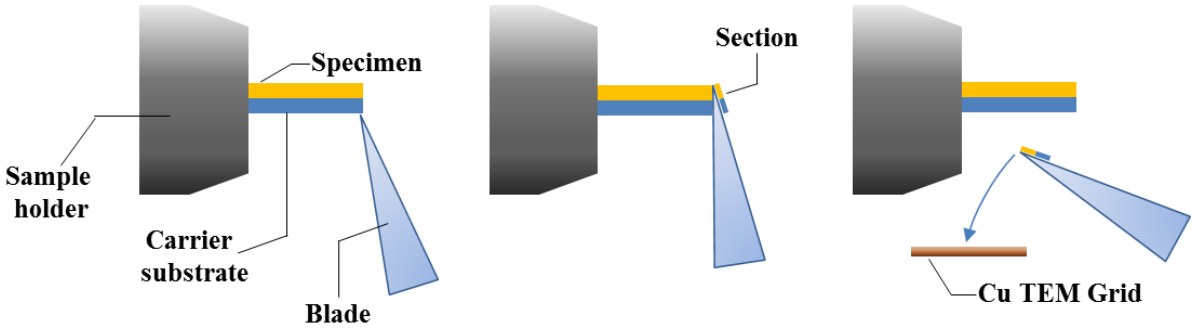

Figure 2.13: Preparative setup for the production of microtome cuts used for STEM measurements.

2.5 Chemicals and materials

2.5.1 Gelatin

As gelatin (CAS: 9000-70-8) is a natural product made out of denaturized collagen collected from slaughterhouse waste (bones, offal and skin) it usually contains approx. 90% denaturized protein and some minerals and water.[185] Depending on the manufacturing method and source this has an influence on the type (Type A: acidic fusion of the raw material, Type B: basic fusion of the raw material), the gelatinization temperature, the jelly consistency (measured in Bloom) and the natural pH which is 4.2-6.8 for a 10 w/w% gelatin solution at 20°C. In order to test these influences in the precipitation system different types of gelatin (*type 0-type 7*) and other hydro fluids (e.g. PVA and agarose) were tested.

Gelatin *type 0*: gelatin for analytics granular (*Acros-Organics*), *type 1*: from porcine skin, gel strength 90-110 g Bloom, Type A, Sigma-G6144 (*Sigma-Aldrich*), *type 2*: from cold water fish skin Sigma-G7041 (*Sigma-Aldrich*), *type 3*: from porcine skin, gel strength 300 g Bloom, Type A, Sigma-G2500 (*Sigma-Aldrich*), *type 4*: from bovine, gel strength 336 g Bloom, Type B, Sigma-G9382 (*Sigma-Aldrich*), *type 5*: from bovine + porcine bones, for ballistic analysis Type A, 250-290 g Bloom, Fluka-53028 (*Sigma-Aldrich*), *type 6*: from porcine skin, gel strength ~175g Bloom, Type A, Sigma-G2625 (*Sigma-Aldrich*), *type 7*: Kitchen gelatin, from porcine, (*RUF*).

2.5.2 Other chemicals

Agarose	OmniPur Agarose, CAS: 9010-36-6 (*EMD chemicals/Merck*).
$AgNO_3$	Silver nitrate, extra pure 99.85% for analysis, CAS: 7761-88-8 (*Acros-Organics*).
$K_2Cr_2O_7$	Potassium dichromate, extra pure 99.5%, CAS: 7778-50-9 (*Acros-Organics*).
K_2CrO_4	Potassium chromate, ACS reagent, ≥99.5%, CAS: 7789-00-6 (*Sigma-Aldrich*).
NH_4OH	Ammonium hydroxide, for analysis, 28-30 w/w% solution of NH_3 in water, CAS: 1336-21-6 (*Acros-Organics*).
$Fe(NO_3)_3 \cdot 9H_2O$	Iron(III) nitrate nonahydrate, 99+%, for analysis, CAS: 7782-61-8 (*Acros-Organics).*
L-Methionine:	L-Methionine, 98+%, CAS: 63-68-3 (*Merck*).
PVA	Polyvinyl alcohol, MW 95000 g/mol, CAS: 9002-89-5 (*Acros-Organics*).
$FeCl_2 \cdot 4H_2O$	Iron(II) chloride tetrahydrate, 99+%, CAS: 13478-10-9 (*Acros-Organics*).
TEOS	Tetraethoxysilane, ≥98%, CAS: 78-10-4 (*Sigma-Aldrich*).
bpy	2,2'-Dipyridyl, 99+%, CAS: 366-18-7 (*Acros-Organics*).
pytpy	4'-(4-pyridyl)-2,2':6',2''-terpyridine was prepared according to literature procedures.[186]
PMMA	Poly(methyl methacrylate), MW 15000 g/mol, CAS: 9011-14-7 (*Acros-Organics*).
$MeCpPtMe_3$	Trimethyl(methylcyclopentadienyl)platinum(IV), CAS: 94442-22-5 (*Sigma-Aldrich*).
K_2PtCl_4	Potassium tetrachloroplatinate(II), CAS: 10025-99-7 (*Sigma-Aldrich*).
$PdCl_2$	Palladium(II) chloride, CAS: 7647-10-1 (*Sigma-Aldrich*).
$RuCl_3 \cdot xH_2O$	Ruthenium(III) chloride hydrate, CAS: 14898-67-0 (*Oxen Ltd.).*
$FeSO_4 \cdot 7H_2O$	Iron(II) sulfate heptahydrate, CAS: 7782-63-0 (*Acros-Organics*).
$NaWO_4 \cdot 2H_2O$	Sodium tungstate dihydrate, CAS: 13472-45-2 (*Acros-Organics*).
$NaMoO_4 \cdot 2H_2O$	Sodium molybdate dihydrate, CAS: 10102-40-6 (*Acros-Organics*).
$KAuCl_4$	Potassium tetrachloroaurate(III), CAS: 13682-61-6 (*Sigma-Aldrich*).
$FeCl_3 \cdot 6H_2O$	Iron(III) chloride hexahydrate, CAS: 10025-77-1 (*Riedel-de Haën*).
$(NH_4)_2C_2O_4 \cdot H_2O$	Ammonium oxalate monohydrate, CAS: 6009-70-7 (*Acros-Organics*).

$Na_2C_2O_4$	Sodium oxalate; CAS: 62-76-0 (*Merck*).
NH_4PF_6	Ammonium hexafluorophosphate, CAS: 16941-11-0 (*Fluka*).
$CuSO_4 \cdot 5H_2O$	Copper(II) sulfate pentahydrate, CAS: 7758-99-8 (*Sigma-Aldrich*).
$Cu(CO_2CH_3)_2 \cdot H_2O$	Copper(II) acetate monohydrate, CAS: 6046-93-1 (*Sigma-Aldrich*).
$[Fe(pytpy)_2]Cl_2$	Bis(4′-(4-pyridyl)-2,2′:6′,2″-terpyridine)iron(II) dichloride was prepared according to literature procedures.[187]
$[Fe(bpy)_3]Cl_2$	Tris(2,2'-bipyridine)iron(II) dichloride was prepared according to literature procedures.[188]
$[Ru(bpy)_3]Cl_2$	Tris(2,2'-bipyridine)ruthenium(II) dichloride was prepared according to literature procedures.[188]

2.5.3 Used materials

Si_3N_4	Silicon nitride, membranes (*Silson Ltd.*).
Microscope slide	76 x 26 x 1 mm, (ISO Norm 8037/I) (*Menzel*).
Silicon wafer	Single side polished, N-type, contains no dopant, diameter × thickness 3.0 in. × 0.5 mm, CAS: 7440-21-3 (Sigma- Aldrich).
FTO	Fluorine-Doped Tin Oxide (SnO_2:F) glass was used for PECs as well as for SEM/ SEM-FIB samples. Specification data: *Solaronix,* TCO22-7 2.2 mm thick glass substrate with a conductive FTO layer which has a surface resistivity of 7 ohm/sq.) and a transmission of more than 80% between 400 to 700 nm.
PP	Poly propylene, plate PP-H, extruded, CAS: 9003-07-0 (*Maagtechnic AG*).
Pressure tubes	Round-bottom tubes, 14 mL, PP (*BD Falcon*).
TEM-Grid	Copper TEM grid (*Stork Veco Eerbeek*).
Thermowax	Thermowax polymer (*Thermanox*).

3. Investigating the classical Liesegang system

One aim of my research is the fabrication of low cost, environmentally friendly nano-scale surfaces and systems which show catalytic properties. Therefore understanding the periodic precipitation process in the classical Liesegang system (silver nitrate/ potassium dichromate), [98] as a model and template for a controllable use of periodic precipitation bands in applications was necessary.

3.1 Introduction

To be able to use the Liesegang phenomenon for increasing the active surface area of photoanode catalysts in photoelectrochemical cells and other purposes, it is essential to understand the physico-chemical origin and the factors which control the frequency of the self-organizing and self-assembling band forming processes. As mentioned in the introduction (Section 1.2, p.7), different types of precipitation patterns, depending on the characteristics of the system, including regular band formation, dendrites with fractal structure, revert type Liesegang bands, dynamic precipitation waves, and the coexistence of primary and secondary patterns can be observed.[87–90,99,123–127,132–134] To the best of our knowledge, no experimental study, providing a chemical mechanism for the formation of so-called primary and secondary precipitation patterns, has been carried out so far. For these reasons, we decided to lay our initial focus on the classical periodic precipitation phenomenon. To be able to determine the chemical and spatial speciation of the primary and secondary bands and to formulate a mechanism for their formation we needed a method which could deliver quantitative chemical information with a spatial resolution better than 100 nm. In the past it was shown by *Lagzi* and *Grzybowski*[91,93] that it is possible to downsize the primary and secondary precipitation bands of the potassium chromate/silver nitrate system to the micro and nano-scale by using wet processing (e.g. WETs technique). By adopting this technique, (Section 2.4.2, p.28) we were able to prepare small enough bands for scanning transmission X-ray microscopy (STXM) measurements. STXM was used to spatially map the electronic structure and chemical state of the pattern via near-edge X-ray absorption fine structure (NEXAFS) spectroscopy in the mesoscopic size range. The obtained NEXAFS data were then compared with the data gained by SEM-FIB and EDX to obtain a quantified model describing the chemistry of the precipitation process.

3.2 General

In aqueous solution we expect a chemical equilibrium (Equation 4) between chromate and dichromate which can be controlled by the pH of the medium (hydrogel).

$$2CrO_4^{2-}(aq) + 2H^+(aq) \rightleftharpoons Cr_2O_7^{2-}(aq) + H_2O \qquad (4)$$

For this reason the experiments were carried out using both potassium dichromate and potassium chromate as inner electrolytes in the gelatin film (cf. Section 1.2).

3.2.1 pH effects

As this equilibrium (Equation 4) was deemed to be a necessary parameter for the periodic precipitation band formation in the classical Liesegang system, we decided to start our experimental investigations by analyzing the influence of the pH. The effect of the pH on the pattern formation was carried out by systematically varying the initial ammonia concentration of the hydrogel containing the inner electrolyte (potassium chromate (0.01 M) or potassium dichromate (0.01 M)) (Appendix B, Table 1, p. 144). The solutions were than heated at 65°C in a pressure stable tube (*BD Falcon*) for 4 h. In the next step the hot solutions were spin-coated onto a glass substrate (3 x 3 x 0.1 cm) (Figure 3.1 and Figure 3.2).

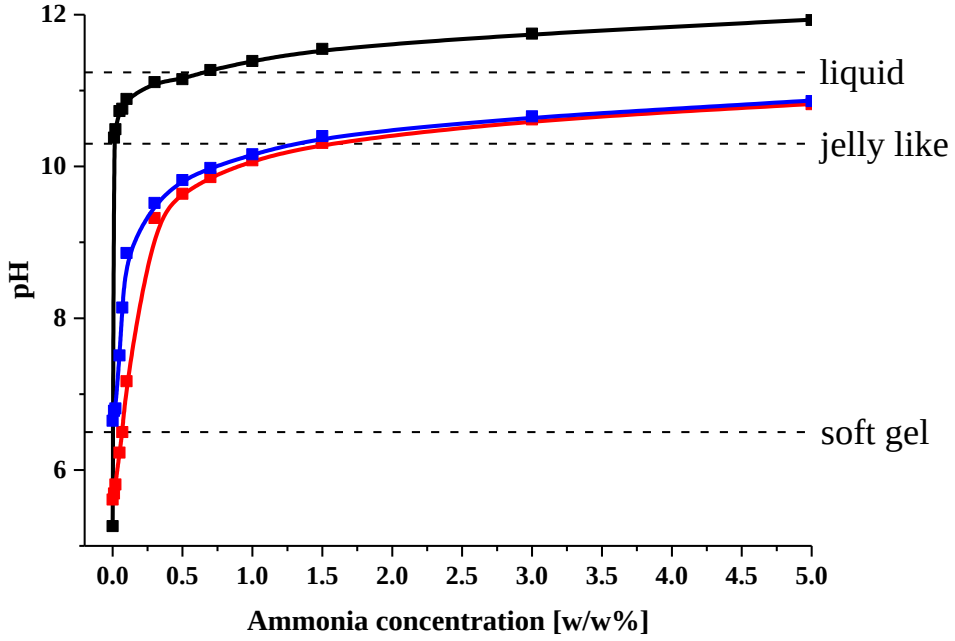

Figure 3.1: Gelatin properties (soft gel, jelly like, liquid) depending on the amount of added ammonia, respectively on the pH of the gelatin solution. Black curve: gelatin (*type 0*) (no additive). Blue curve: gelatin (*type 0*) with K_2CrO_4 (0.01 M). Red curve: gelatin (*type 0*) with $K_2Cr_2O_7$ (0.01 M).

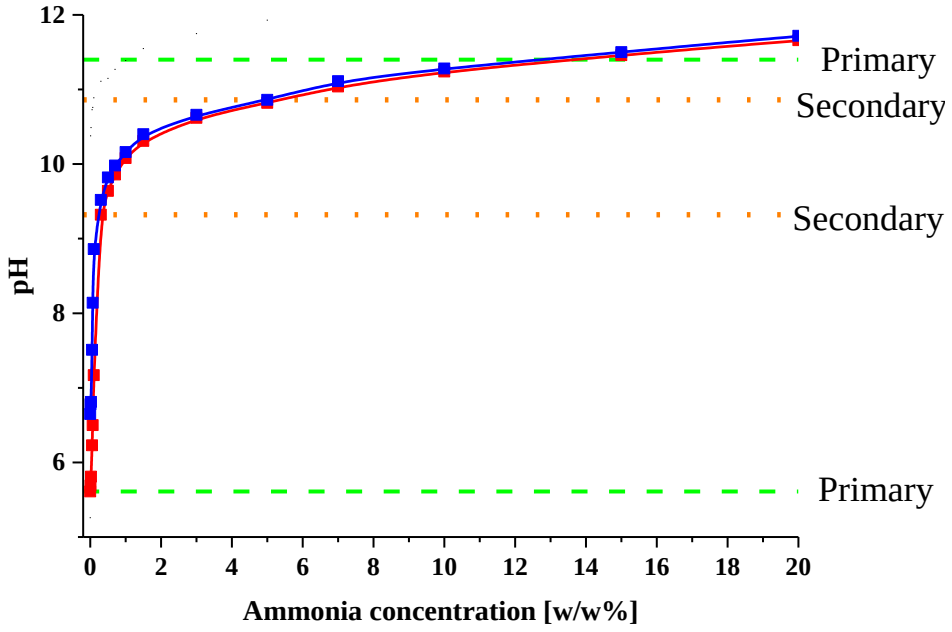

Figure 3.2: Occurrence of precipitation bands depending on the pH of the gelatin solution. Blue curve: gelatin with K_2CrO_4 (0.01 M). Red curve: gelatin with $K_2Cr_2O_7$ (0.01 M). Green dashed lines: upper and lower pH range where primary bands were observed; orange dotted lines: upper and lower pH range where secondary bands were observed in addition to the primary bands.

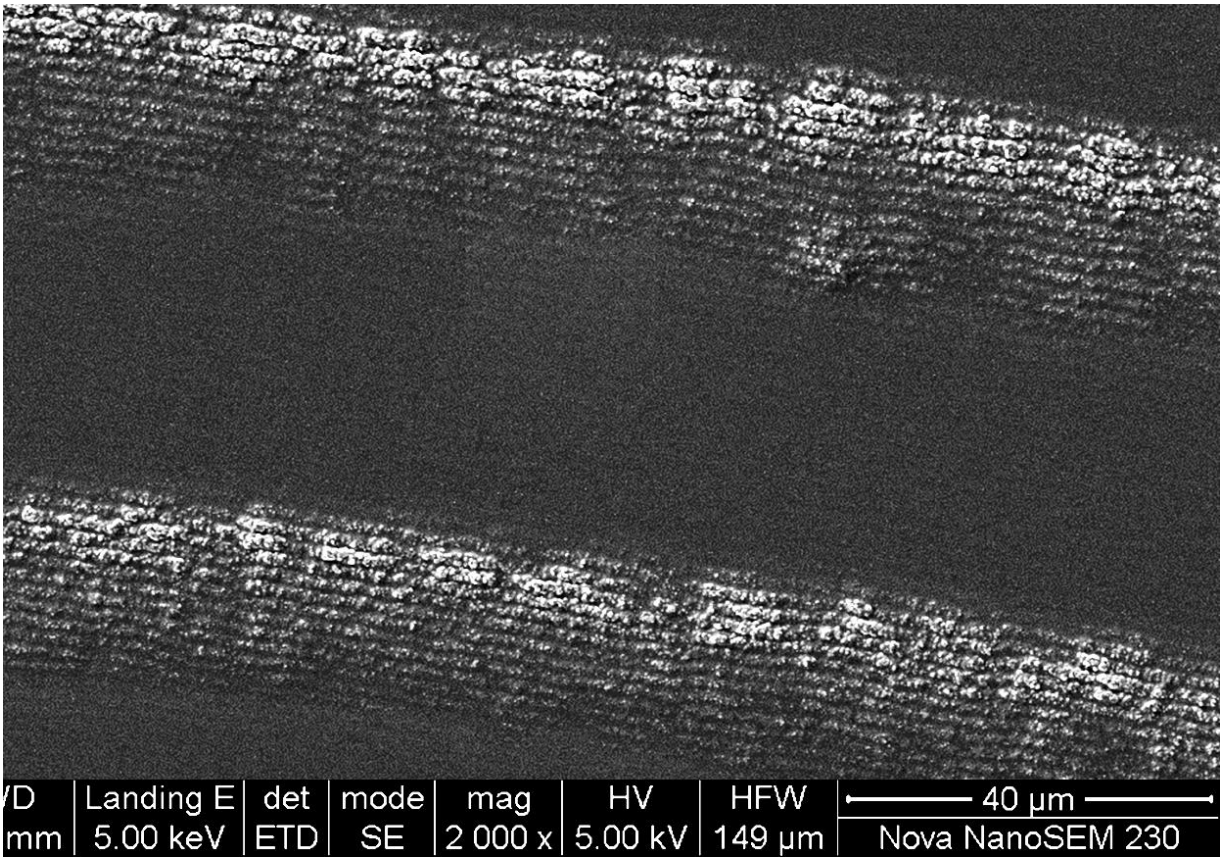

Image 3.1: SEM image, showing the occurrence of both fine structured secondary bands between and on top of the larger primary bands.

Since the pH measurements on the substrate surface were very difficult and the obtained values were similar to those measured in the cold (25°C) gelatin solutions, it was decided to measure all values directly in the gelatin solutions. For proper statistics and good reproducibility, a set of 4 gelatin films of each solution at four spin-coating speeds (300, 500, 750, 1000 rpm) were prepared. After drying the gelatin films, the WETs technique was used and a silver nitrate (0.3 M) loaded stamps were placed on the gelatin layers. The stamps were removed after 90 minutes and the formed patterns were analyzed by optical microscopy. Two kinds of Liesegang bands were observed (Image 3.1): wide bands with a large frequency (primary bands) and very thin bands with high frequency (secondary bands) between and on top of the primary bands.

3.2.1.1 STXM/SEM-FIB samples preparation

The WETs technique[91] was adopted for the preparation of Liesegang rings containing STXM samples. Gelatin was used as a hydrogel and carrier matrix for the inner electrolyte, while agarose was used as a carrier system for the outer/invading electrolyte. As we were interested why two different types of precipitation bands can occur in the classical system, a set of samples containing only primary bands and a set with containing both primary and secondary bands were needed.

Samples with primary and secondary pattern

A 65°C hot gelatin solution (10 w/w%) in aqueous ammonia (0.3 w/w%) containing potassium dichromate (0.01 M) was spin coated onto small (3.0 mm x 3.0 mm x 100 nm) Si_3N_4 windows. Spin coating rotation speeds between 1000-2000 rpm were needed to produce a gelatin film thickness of approximately 400-500 nm. The invading electrolyte was introduced into the thin gelatin by an agarose-gel stamp (6 w/w%) containing silver nitrate (0.3 M). When the stamp is placed on the film the invading electrolyte diffuses into the gelatin forming precipitation rings around the stamp contact location.

Samples with only primary pattern

The pH dependence study (Figure 3.2) showed it is possible to obtain samples with only primary bands by decreasing the amount of ammonia used. Therefore, samples with only primary bands were prepared by a slight modification of the above system, in which the amount of ammonia was changed to 0.01 w/w%.

Reference samples

A set of reference samples was prepared by placing a small crystal of the compounds ($K_2Cr_2O_7$ (Cr^{VI}), K_2CrO_4 (Cr^{VI}) and $AgNO_3$ (Ag^{I})) onto the Si_3N_4 membrane and a second set was prepared by solvent evaporation of the aqueous compound which was placed as droplets on top of the membranes. An empty hole of the sample holder and a silver (Ag^0) sample were provided by the PolLux beamline of the SLS. An additional silver (Ag^0) sample was prepared by *Dr. Rita Tóth* at EMPA using chemical vapor deposition (CVD) methods. Pure gelatin films were prepared by spin-coating (2000 rpm) a hot (65°C) gelatin solution (10 w/w%, *type 0*) in aqueous ammonia (0.01 respectively 0.3 w/w%) onto Si_3N_4 membranes.

3.3 Analytics

3.3.1 STXM measurements

STXM measurements and analysis was done in cooperation with *Dr. Rita Tóth, Florent Boudoire, Prof. Dr. István Lagzi*, *Dr. Artur Braun* and *Dr. Benjamin Watts*.

Images were recorded at the chromium $L_{3,2}$ edges (576.2 eV and 584.9 eV) (Image 3.2), the oxygen K edge and the silver M edge. The spectra were acquired on secondary bands in and between the primary bands (Image 3.2, positions A and C), in the area between the secondary bands at these two locations (Image 3.2, positions B and D), and in and between primary bands when secondary bands were not present (image not shown).

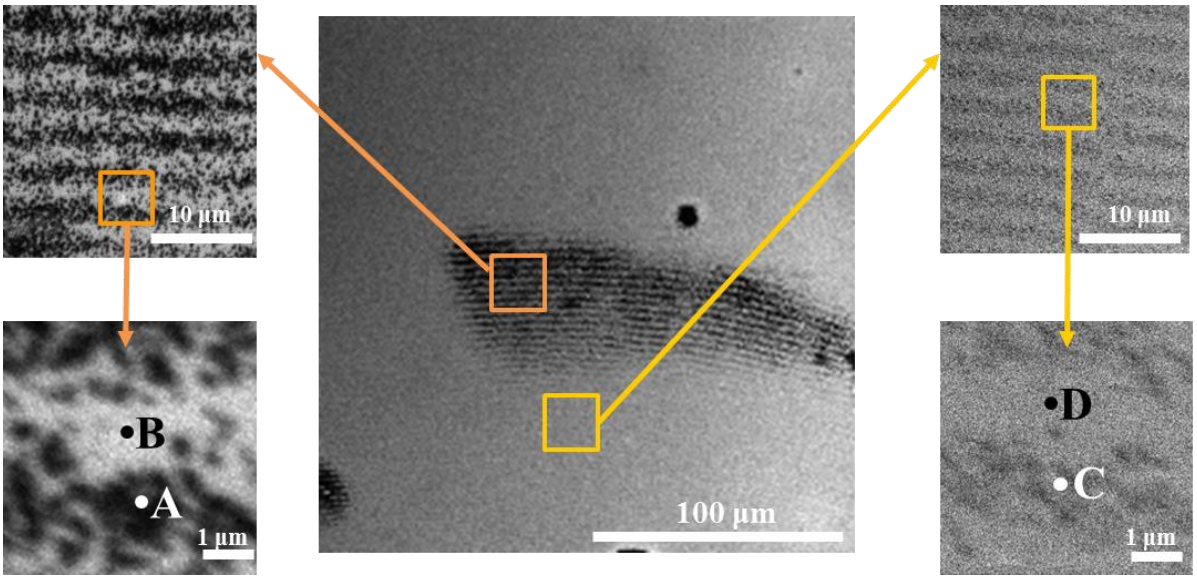

Image 3.2: STXM images of the precipitation bands. The images were measured at 576.2 eV (corresponding to the absorption of Cr). In the middle: Image of the periodic bands and their surrounding area (1.25 µm pixels). Left: Detailed images of bands (top: 125 nm pixels, bottom: 50 nm pixels). Right: Detailed images of an area between two primary bands (top: 125 nm pixels, bottom: 50 nm pixels).

3.3.2 Live observation of the precipitation process

Real time band formation was visualized and monitored by *in situ* digital video recording of the precipitation process occurring in the classical Liesegang system. The experimental setup of this can be found in Section 2.2.1.5, p. 22. The time lapse photographs taken from the video can be found in optical images (Image 3.3).

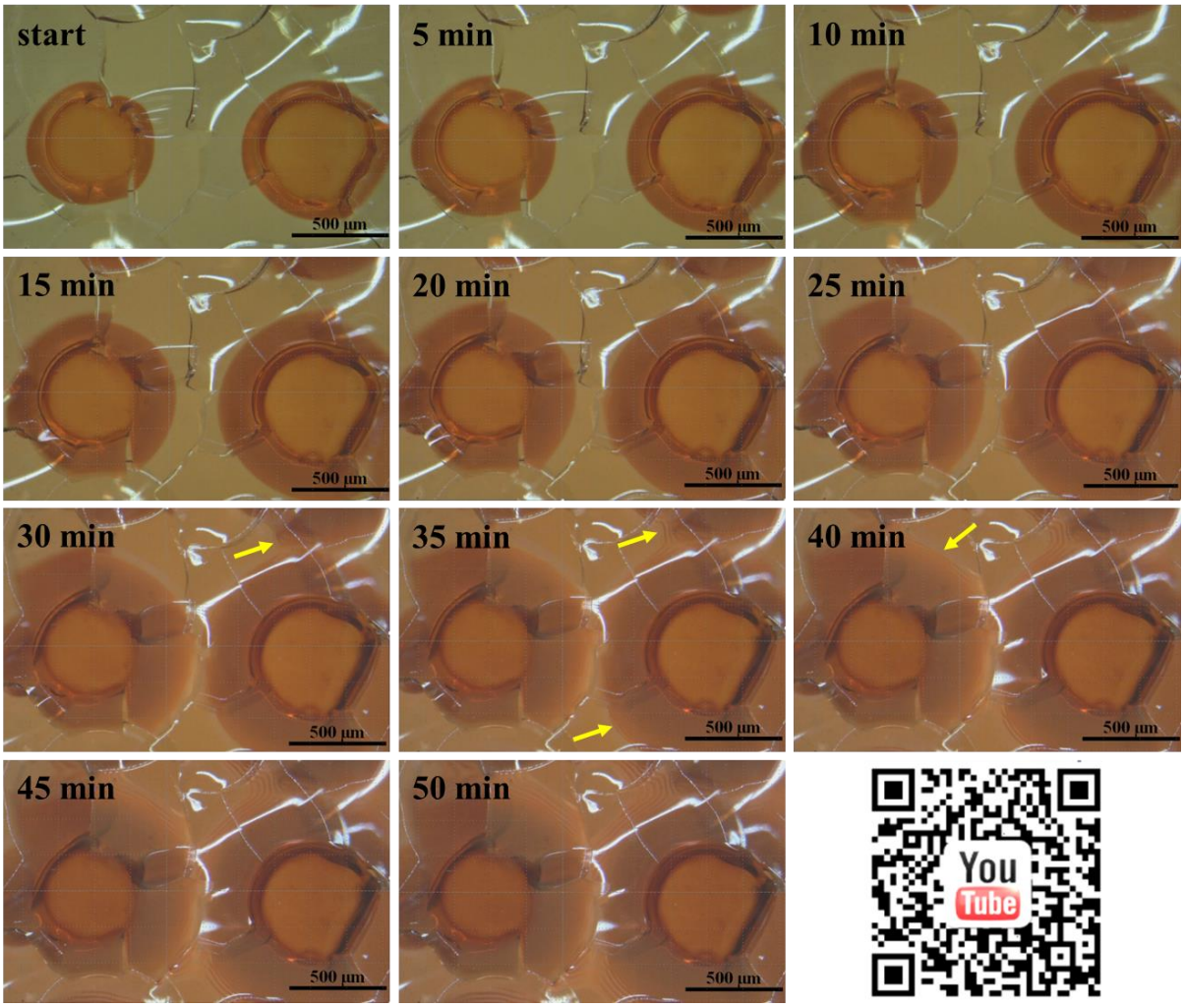

Image 3.3: Time lapse photographs taken from the monitored precipitation process occurring in classical Liesegang system. Yellow arrows indicate the formation of the precipitation bands. The QR code can be used to access the video online. Also available at: https://www.youtube.com/watch?v=oj0FRvxEyEI.

3.3.3 SEM-FIB and EDX measurements

For comparable results, SEM-FIB and EDX measurements were performed on the same samples which have been analyzed before by STXM. For this reason the STXM sample holder was mounted onto a SEM sample holder. The whole setup was then sputter-coated with a 30 nm platinum layer to increase conductivity. The implementation of the vapor deposited

platinum protection layer and the gallium-ion driven milling process was carried out as previously described (Section 2.2.1.1.3, p. 16). After polishing the samples, EDX measurements were performed on the particles forming the bands (10 keV).

3.4 Results and Discussion

3.4.1 STXM measurements

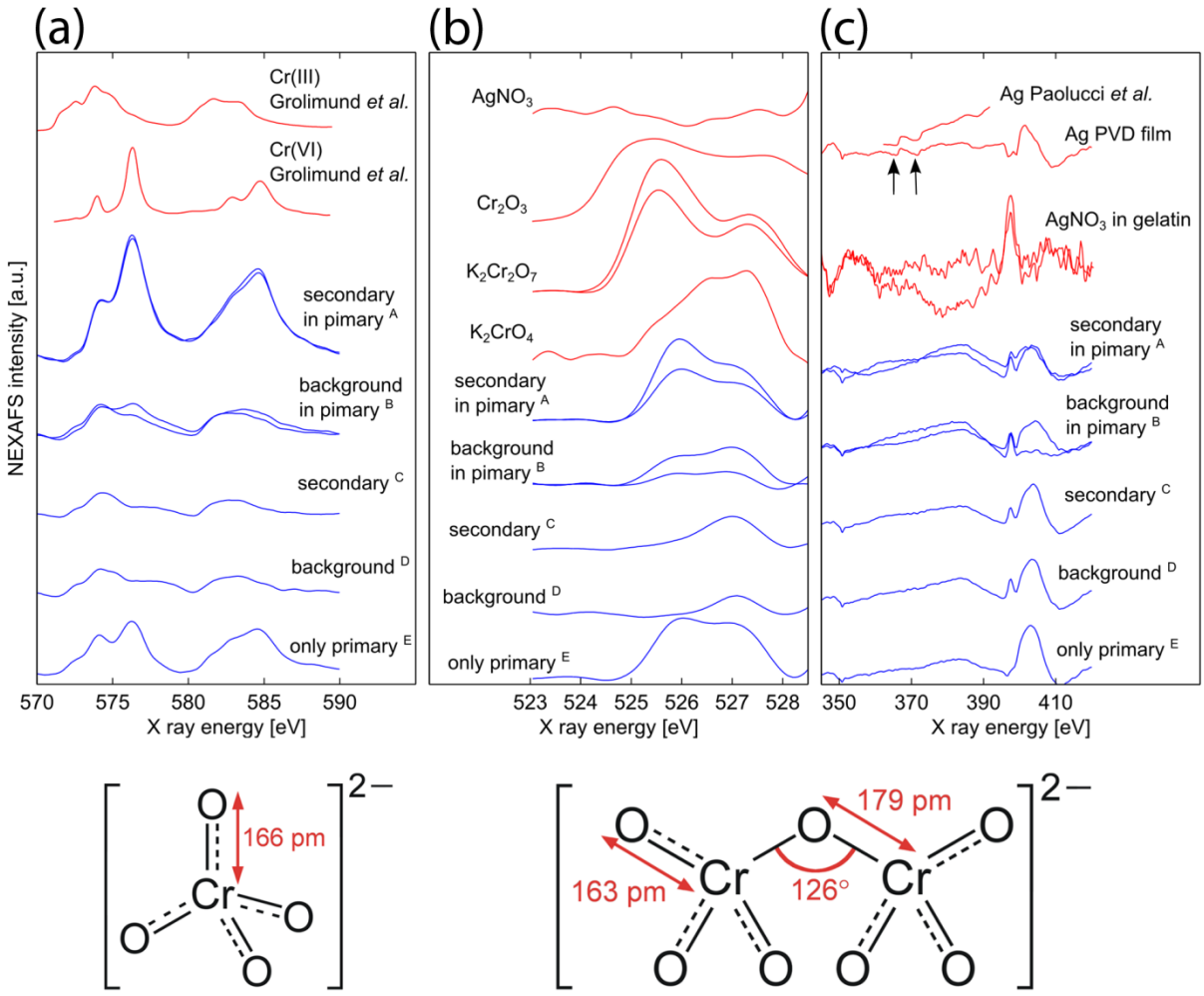

Figure 3.3: STXM spectra of a) chromium $L_{3,2}$-edges, b) oxygen K-edge and c) silver M-edge average spectra of 10 square areas (20 nm x 20 nm). A) measured on the fine structure of a band, B) on the background between the fine structure in the band, C) on the fine structure between two bands, D) on the background at two different positions where no precipitation occurred, E) on a band where no fine structure was visible, plus the reference spectra (red).

Additional reference spectra were taken from *Grolimund et al.*[189] and from *Paolucci et al.*.[190] Starting with the Cr $L_{2,3}$ spectra of the measured samples we can see the Cr 2p multiplet in the L_3 region (570-579 eV) and in the L_2 region (580-590 eV) (Figure 3.3a). The strong similarity of spectra A and E to the reference Cr(VI) spectrum[189] reveals that the chromium in the

precipitation bands is present as Cr(VI). As the L_2 (~584 eV) peak in spectra B, C and D is shifted slightly towards lower energy, the peaks are similar to the Cr(III) reference spectrum,[189] which means that Cr(III) is present in the background between the precipitation bands. In this respect it is essential noting that the X-ray beam contains spectral Cr(III) contamination from the synchrotron beamline optics. Moreover, it has to be taken into account that the gelatin which was the carrier substrate for all samples containing precipitation bands, could act as reducing agent, converting some of the Cr(VI) to Cr(III). In the background very small amounts of precipitate are present. From these data it seems reasonable that the precipitate contains mainly Cr(VI), but when very small amounts of precipitate are present the Cr(III) "contamination" becomes prevalent. As both chromate and dichromate are Cr(VI), the data do not clarify the material composition (chromate or dichromate) of the primary and secondary bands, but the spectra indicate a different coordination geometry for the Cr in the two compounds. To address this problem, the oxygen K-edge spectra (523-529 eV), reflecting the valence band to a large extent, was studied. Figure 3.3b shows the oxygen 1s spectra of regions measured in and around the primary and secondary bands, as well as spectra of several compounds (i.e. Cr_2O_3, $K_2Cr_2O_3$, and K_2CrO_4) which were recorded as reference spectra. For Cr_2O_3, the Cr is in octahedral coordination, while chromates have structures made of tetrahedral CrO_4 units sharing an O corner. The presence of two peaks in spectra A, B and E indicates that the precipitate in the primary bands contains $Cr_2O_7^{2-}$ ions. The narrowly defined peaks compared to the $K_2Cr_2O_7$ reference spectrum are possibly due to bonding with Ag^+ ions. The peaks in spectra C and D match very well with the K_2CrO_4 reference, indicating that the main material forming the secondary bands is CrO_4^{2-}. To elucidate the question if silver is coordinating to chromate or dichromate in the bands, the silver $M_{4,5}$-edge spectra (Figure 3.3c) were recorded. The NEXAFS scan showing the silver spectra of the precipitation bands contains also the nitrogen K-edge peak around 405 eV. The peaks corresponding to the $M_{4,5}$-edges at 368 eV and 374 eV are clearly visible in the Ag reference spectra, but they are not discernible in any of the precipitate spectra (A-E). The broad, flat peak in the range of the Ag $M_{4,5}$-edges suggests that silver is present throughout the entire pattern. The information gained from the nitrogen K-edge at 405 eV are weak, since nitrogen is present in the gelatin matrix, the substrate (Si_3N_4 window) and the outer electrolyte $AgNO_3$. It is possible (but not reasonable) that all three components contribute to the spectral weight in the nitrogen spectrum. It is most likely that the nitrogen comes from the gelatin which consists of denaturized proteins. The additional peak around 398 eV in spectra A-D, which is also present in the $AgNO_3$ reference, most likely corresponds

to an Ag–N bond. It is interesting to note that this peak is not present in a sample with only primary bands (spectrum E). This observation suggests that this Ag–N bond signature is specific to the secondary bands. At higher ammonia concentrations diamine silver(I),[191] ($Ag(NH_3)_2NO_3$ (aq)), can be formed by the reaction of $AgNO_3$ and NH_4OH, causing the peak at 398 eV. If this is true, bands should not be formed when there is no ammonia present in the system. Therefore experiments using KOH instead of ammonia were performed. As both primary and secondary bands are formed in the KOH system, the formation of diamine silver can be ruled out. A more reasonable explanation for the Ag-N bond signature is that this signal originates from the amino groups in gelatin which coordinate silver in an alkaline milieu.

3.4.2 SEM-FIB imaging and EDX measurements

From the STXM data we expected silver dichromate to be the material forming primary bands and silver chromate to be the material forming the secondary bands. In order to verify these observations SEM-FIB and EDX measurements were performed on the same samples measured in the STXM (Image 3.4).

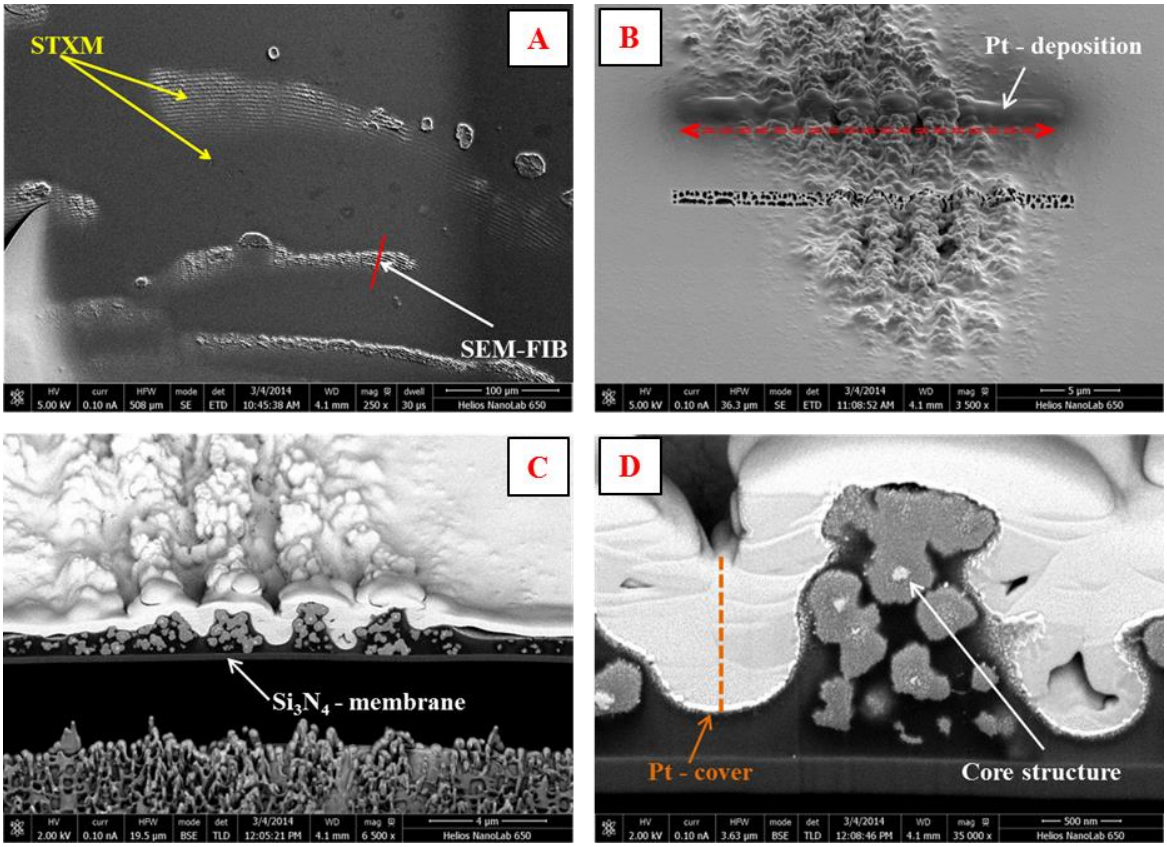

Image 3.4: A): (overview) with marks where the STXM and SEM-FIB measurements were performed. B): SEM-image showing a band with fine structures before the FIB was started. C): SEM-FIB cross section through a band and D): higher resolution of C.

As one can see from the material contrast in the backscattered electron images (Image 3.4), the particles forming the bands have a core structure containing heavier elements than the surrounding material. The same observation was made for the secondary bands between the primary bands (image not shown). Taking the different composition of the band forming particles into account, EDX measurements were carried out at different sample locations, to obtain material information about the core structure and the surrounding material. The EDX measurements performed on the core structures as well as on the surrounding material (Figure 3.4) support our findings from the BSE images. The amount of silver in the core structure is much higher compared to the amount of silver found in the surrounding material. The observed values for silver and chromium can be found in the EDX material analysis next to the EDX spectra (Figure 3.4 right).

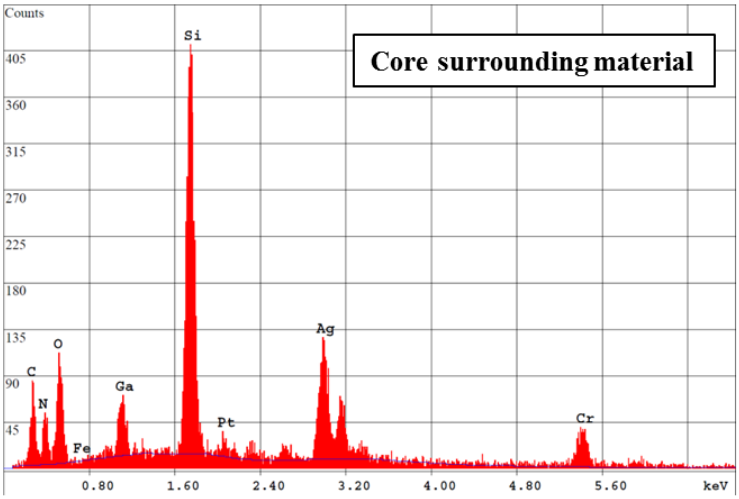

EDX quantification

Element	w/w%	At%
C K	3.27	11.03
N K	3.93	11.35
O K	4.65	11.75
Ga L	4.04	2.34
Si K	21.59	31.11
Pt M	3.08	0.64
Ag L	35.89	13.46
Cr K	23.55	18.32
Total	100.00	100.00

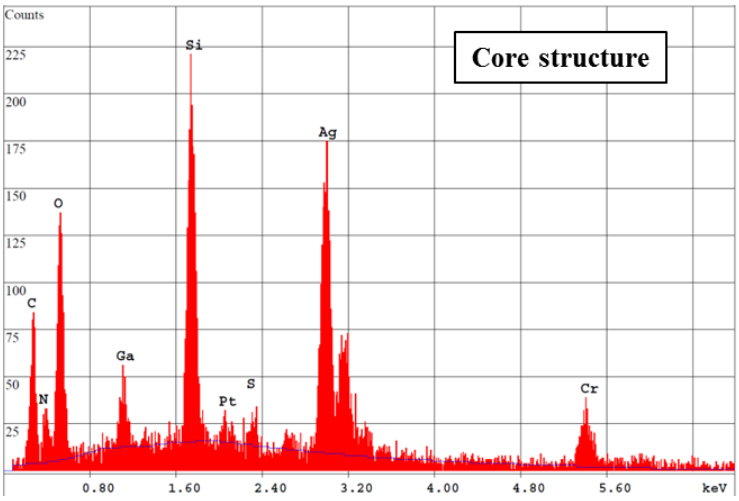

Element	w/w%	At%
C K	2.96	11.46
N K	2.32	7.68
O K	6.62	19.23
Ga L	2.60	1.73
Si K	10.82	17.89
S K	1.13	1.63
Pt M	2.25	0.54
Ag L	51.56	22.21
Cr K	19.74	17.63
Total	100.00	100.00

Figure 3.4: EDX measurements of the particles forming the bands. Top spectrum: measurement on the surrounding material of the core structure. Bottom spectrum: measurement directly on the core structure. Material analysis/quantification of the EDX measurements can be seen on the right side of the corresponding spectrum.

The values for carbon, nitrogen, oxygen and sulfur can be neglected as these are the main elements of the gelatin matrix, which is necessary to facilitate the band forming process. An EDX spectrum of gelatin can be found in the appendix (Appendix C, p. 163). As the sulfur peak overlaps with parts of the platinum peak, it was sometimes a problem to detect sulfur in the specimen. The gallium peak arises from the gallium-ion beam which contaminates the sample weakly during the milling process. The silicon signal and parts of the nitrogen signal are due to the Si_3N_4 membranes which were used as carrier substrates. The platinum peak originates from both the platinum sputter coating layer and the deposition layer. For these reasons only the silver and chromium peaks were useable to obtain a hint about the material composition of the nano-particles forming the Liesegang rings/bands.

3.4.3 pH effects

When potassium dichromate is the inner electrolyte the pH dependency experiments showed that only primary band form below pH = 9.3, for samples prepared at 300 rpm spin coating speed. If the pH is changed towards higher values, the probability of secondary band formation increases, while the number of primary bands decreases. The higher the pH (the more base is added) the more the equilibrium is shifted towards the chromate side, i.e. more secondary bands can form and less dichromate ions remain to form primary bands. Above pH = 10.8 the gelatin does not gelatinize anymore. For this reason the gelatin matrix is not able to support the band forming precipitation process any longer. The influence of the pH on the precipitation process can also be used to control and manipulate the formation of the bands e.g. the number of formed bands at a given pH (Figure 3.5).

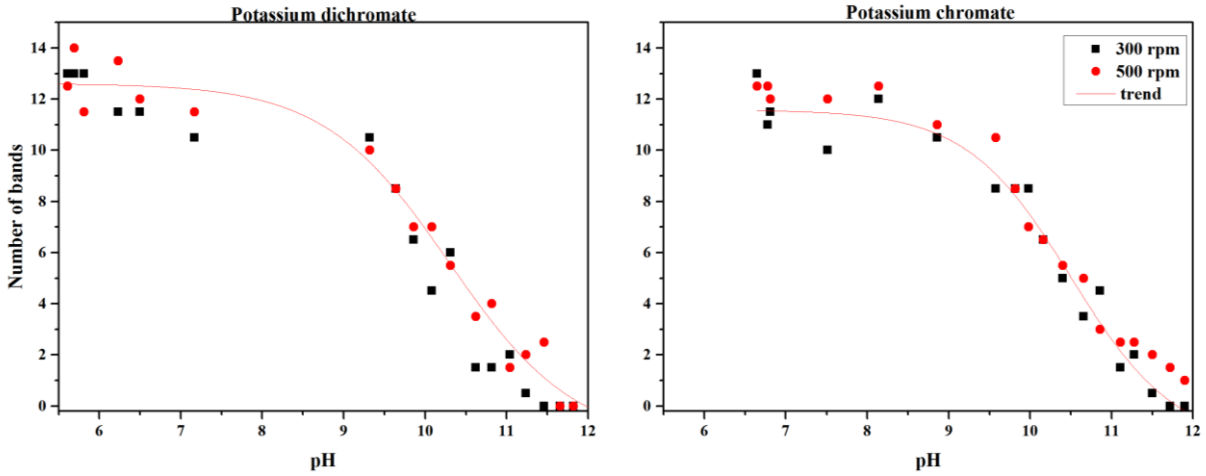

Figure 3.5: Influence of the pH on the number of formed primary bands for both tested systems with potassium dichromate 0.01 M (left) and potassium chromate 0.01 M (right) as inner electrolyte.

The same trends were observed, when the thickness of the gelatin layer was reduced, caused by sample preparation at higher coating speeds (500 rpm). The red curve fit was done with the origin function "connect lines; B-Spline" where the points are weighted equally in the least squares fit. As the number of bands also correlates with the time the stamp was on the hydro gel, the stamping time was kept constant for all experiments. The spacing of primary bands (space between two bands) increases with increasing pH. The spacing can be illustrated by the so-called spacing law (Equation 5).[99,124]

$$P = \frac{X_{n+1}}{X_n} \quad (5)$$

Where the spacing coefficient P is defined by X_n and X_{n+1}, which are the positions of the (n^{th}) and ($n+1$)th bands, respectively, measured on the hydrogel film. In addition, it was found that the occurrence of fine structures (secondary bands) also increases with increasing pH. The formation of secondary bands started at pH 9.32 and was observed up to a pH of 10.86. Even higher pH values might also lead to the formation of fine structures, but above pH 10.86 the gelatin lost its consistency (did not form a gel anymore) (Figure 3.1).In case of the control experiment, where the gelatin contained potassium chromate instead of the traditional potassium dichromate, we expected to see only secondary band formation, since in this case the equilibrium is already shifted towards the left-hand side of Equation 4. But both primary and secondary bands were observed, showing the same characteristics as those in the dichromate system (Figure 3.5 right). Only the pH values of the gelatin solutions are shifted slightly (Figure 3.1 and Figure 3.2). The reason for this is that the gelatin acts as buffer, shifting the pH of both systems to ~6. The pH values of 0.01 M $K_2Cr_2O_7$ and 0.01 M K_2CrO_4 solutions without gelatin and NH_4OH are 4.22 and 8.66 respectively. However, when 10% gelatin (*type 0*) is added, the pH change to 5.6 and 6.6, respectively. For the formation of secondary bands/fine structures it is crucial to work in the alkaline pH region (Image 3.6).

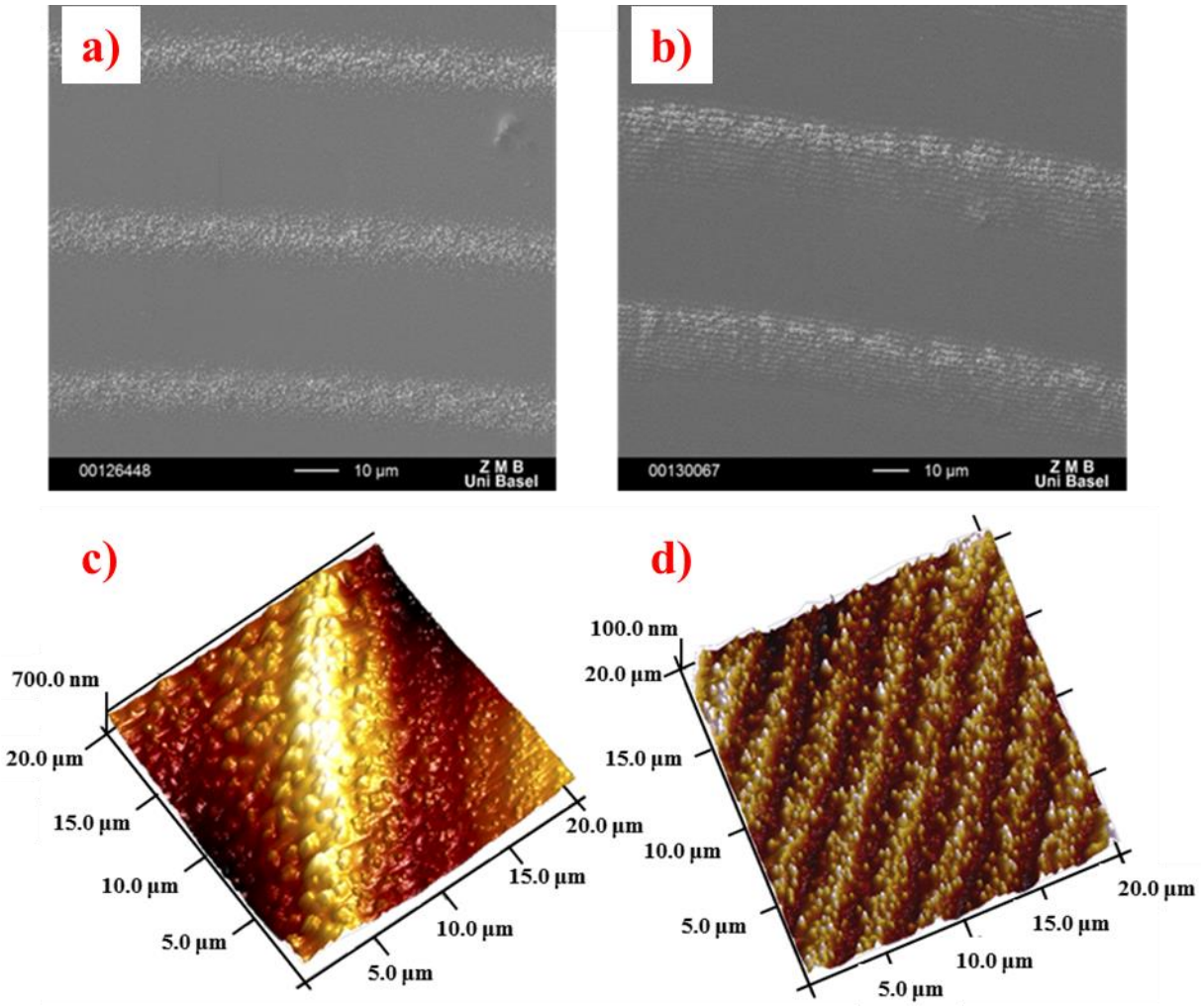

Figure 3.6: Dependence of pattern formation on the pH of the gelatin film. SEM images: a) Primary bands without fine structure (pH = 5.7) and b) Primary bands containing fine structures (pH = 10.1). AFM surface profile images: c) of a primary band without fine structures and d) of secondary bands between primary bands.

3.4.4 Mathematical Modeling

Prof. Dr. István Lagzi developed a reaction-diffusion model based on the Cahn-Hilliard phase separation scenario which supports and illustrates the findings of the STXM measurements. The kinetic model contains $AgNO_3$ (A), K_2CrO_4 (B_1), $K_2Cr_2O_7$ (B_2), and two precipitates, Ag_2CrO_4 (C_1) and $Ag_2Cr_2O_7$ (C_2):

$$B_1 \underset{\kappa_2}{\overset{\kappa_1}{\rightleftharpoons}} B_2 \tag{6}$$

$$A + B_1 \xrightarrow{k_1} C_1 \tag{7}$$

$$A + B_2 \xrightarrow{k_2} C_2 \tag{8}$$

κ_1, κ_2 and k_1, k_2 are the chemical rate constants for the equilibrium between chromate and dichromate and for the precipitation reactions, respectively. Pattern formation occurs in the wake of a diffusively moving reaction front resulting from the inhomogeneous initial distribution of the outer and inner electrolytes. The reaction-diffusion equations describing the pattern formation and the details of the model are shown in appendix B, p.146).

3.5 Conclusion

As a conclusion of the NEXAFS results, the analysis of the Cr 2p multiplet spectra shows that the secondary and primary bands consist generally of $Cr^{(VI)}$. The oxygen K pre-edge results reveal that the secondary bands contain CrO_4^{2-} ions, while the primary bands contain $Cr_2O_7^{2-}$ ions. Since the Ag M edge results show that silver is present in both precipitate bands we can conclude that the secondary bands contain silver chromate whilst the main precipitation product of the primary bands is silver dichromate and propose that the precipitation process is controlled by the chromate-dichromate equilibrium reaction. Three chemical equilibria ***(4)***,[192] ***(9)***[193] and ***(10)***[193] are relevant to the precipitation processes, of which ***(4)*** is directly related to the pH defined by the ammonia concentration:

$$2CrO_4^{2-}(aq) + 2H^+(aq) \rightleftharpoons Cr_2O_7^{2-}(aq) + H_2O \qquad \log K = 13.8 \quad (4)$$

$$2Ag^+(aq) + CrO_4^{2-}(aq) \rightleftharpoons Ag_2CrO_4(s) \qquad K_{sp} = 9.0 \times 10^{-12} \quad (9)$$

$$2Ag^+(aq) + Cr_2O_7^{2-}(aq) \rightleftharpoons Ag_2Cr_2O_7(s) \qquad K_{sp} = 2.0 \times 10^{-7} \quad (10)$$

Returning to the effect of the used base (ammonia), it is worthy of note that the probability of secondary band formation increases with increasing pH, (Figure 3.2) while fewer and fewer primary bands are formed (Figure 3.5). The higher the initial pH, the more the equilibrium is shifted towards the chromate side, resulting in more secondary bands and fewer dichromate ions and primary bands. Figure 3.5 illustrates how pH can be used to control and tailor the formation and frequency of the precipitation bands. We also studied systems where the gelatin contained potassium chromate instead of potassium dichromate. In this case, the equilibrium is already shifted to the left hand side of Equation 4 and we expected to see only secondary band formation. However, both primary and secondary bands were observed, due to the buffering effect of the gelatin in the absence of ammonia. The pH of 0.01 M $K_2Cr_2O_7$ and 0.01 M or 0.02 M K_2CrO_4 solutions without gelatin or ammonia are 4.22 and 8.66 respectively. But if gelatin (10 w/w%) is added, the pH changes to 5.6 and 6.6.

With the video studies (Section 3.3.2, p. 38) we were able to demonstrate that the bands are fixed at their location once they are formed. Another remarkable finding/observation from the monitoring process is that a milky/off-white precipitate is formed at the propagation wave front before primary bands are formed (Image 3.5 and Image 3.6).

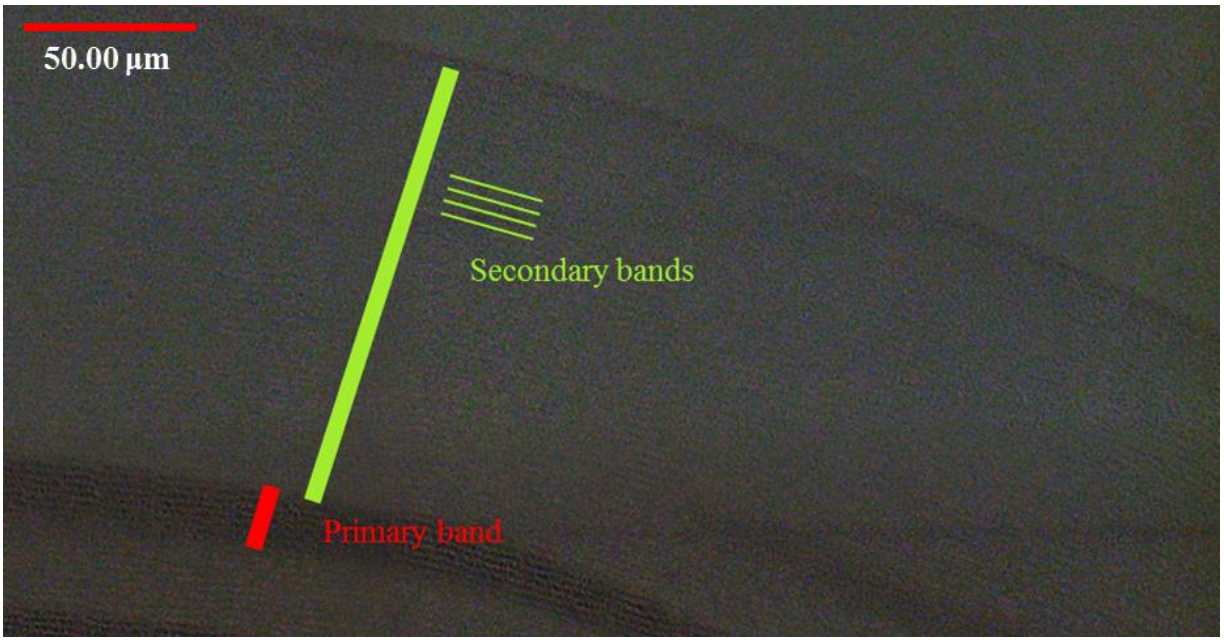

Image 3.5: High resolution Laser microscope photograph showing secondary bands at the end of the precipitation front. The thick red line indicates the primary bands, while the green dotted lines indicate the secondary bands.

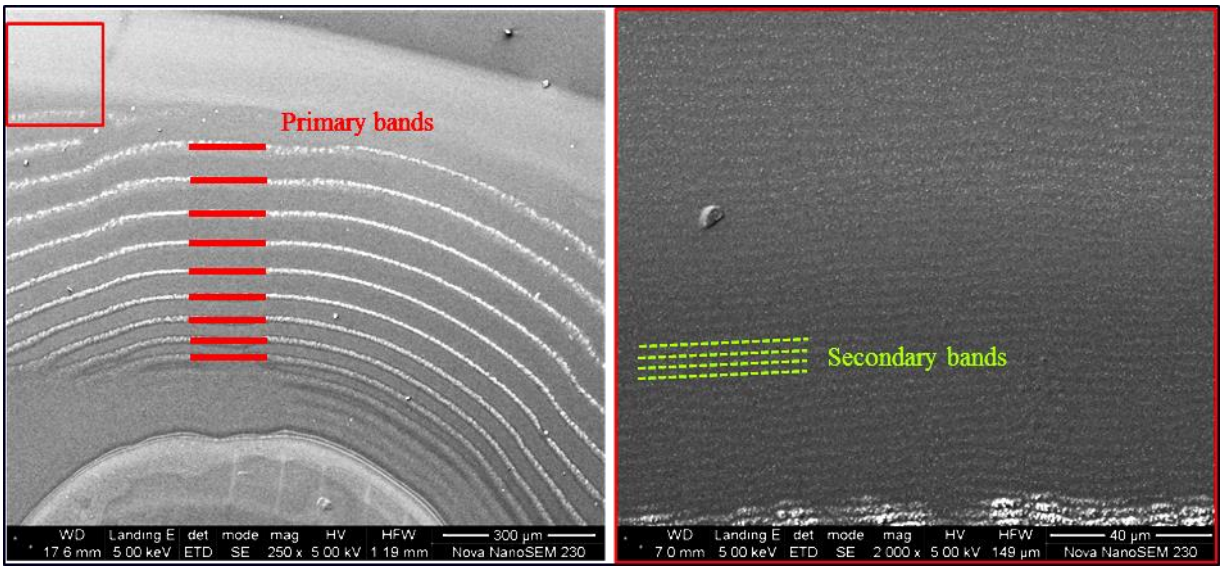

Image 3.6: SEM images showing secondary bands at the end of the precipitation front. Left image: overview, with indicate the place for the higher resolution SEM image on the right. The thick red lines indicate the primary bands, while the green dotted lines indicate the secondary bands.

If we now combine this with the fact that secondary bands are always seen at the front of the precipitate propagation direction (Image 3.5 and Image 3.6), it is possible that these white precipitates observed in the video (3.3.2) are secondary bands.

If we take into account the information gained from the SEM-FIB images and the EDX analysis of the core structures, it is more likely that the white precipitation front seen in the video are silver containing nanoparticles which are formed out of the invading outer electrolyte on a different time scale (faster), before the precipitation reaction between the inner and outer electrolyte occurs. As these core structures were found in all SEM-FIB samples prepared by using the classical Liesegang setup, it seems reasonable that $Ag_2Cr_2O_7$ and Ag_2CrO_4 need the silver containing nanoparticles as nucleation site for the formation of the particles which later form the primary and secondary bands. As Ag_2CrO_4 precipitates are more stable than $Ag_2Cr_2O_7$ (cf. chemical Equations p. 46), the two precipitates can form consecutively and both of them can be present at the same time.

It has already been suggested by *Holba*[101], *Ramaiah*[128] that secondary precipitation band formation precedes the primary band growth, but it was thought that the latter is a result of the coarsening and strengthening of the secondary bands. However, from our results it is clear that the chemical composition of the two types of precipitation bands is different; therefore they must form independently from each other.

Another possibility is that the white precipitates formed first are the fundamental structure of the primary and secondary bands, before silver chromate/dichromate is formed around the silver containing core structures. But this can neither be measured by any of the used methods nor be visualized by SEM or optical microscopy, since the necessary time scale for the sample preparation and measurement is much longer (hours) than the reaction time of the materials in the samples (seconds). But if this was true it should be possible to prepare samples where only secondary bands are formed (cf. Section 4.2, p.50).

In our publication[90] about the “Growth of Nanoparticles and Microparticles by Controlled Reaction-Diffusion” we describe how the particle size (of the particles forming the bands) in the investigated classical Liesegang system is increasing with increasing distance to the stamping center.

This observation is fundamental for the analysis of Liesegang systems and their use in possible applications, also with respect to Liesegang systems presented in the following chapters.

4. About new silver containing Liesegang structures

Understanding and controlling the formation of new, silver containing Liesegang precipitation systems.

4.1 Introduction

From our investigations concerning the classical Liesegang system (Section 3.3, p.37), it was found that the particles forming the bands have a high amount of silver in their core structure. The additional video also showed that a white precipitate is initially formed before bands are visible. The resolution of the monitoring process was not high enough to see if this white precipitate consisted of secondary bands or the material forming the core structures found in the band forming particles. However it is possible that the material (i.e. silver dichromate or silver chromate) forming the particles of the primary and secondary bands needs the silver-containing core as a nucleation site. Together with the fact that secondary bands are always found at the end of the periodic precipitation propagation zone (Image 3.5 and Image 3.6), these findings imply that it is possible that the so-called secondary bands are formed first from a silver (but not chromate) containing material. After these structures are formed, the chromate/dichromate equilibrium (Equation 4) facilitates the accumulation of silver chromate or silver dichromate found in primary and secondary bands. If this is true, we assumed that it should also be possible to form these dense and highly periodic precipitation rings/bands in the absence of chromate or dichromate. In this chapter we show how it is possible to form fine structured bands containing only a silver precipitate showing the same pattern characteristics (spacing, height and the width of the bands) as the so-called secondary bands, observed in the classical Liesegang system. We also demonstrate how it is possible to control specific parameter of these fine structures (i.e. spacing between two bands, band thickness, particle size …). Our analytical measurements (STEM-EDX, XPS, EDX, SEM-FIB, AFM) on these particles forming the bands allow us to propose a possible chemical equilibrium which is necessary to facilitate band formation. Additionally, we found that it is possible to use other hydrogels than gelatin, such as agarose or PVA, simplifying the system parameters which are necessary for band formation. This also proves that gelatin is not needed for band formation.
This system was of special interest since the density and the material composition of the bands open a wide field of possible applications (cf. Chapter 5).

4.2 Formation of highly periodic mesoscale silver containing patterns

From our investigations on the classical Liesegang system, we found that there is a pH region where the secondary band formation is visible (pH 7.2 – 10.8) (Figure 3.2). Below pH 7.2 we only observed primary bands and above pH 10.8 the gelatin does not jellify properly anymore (Figure 3.1). We also learned that using ammonia as the base was very simple to handle compared to the other tested alkaline solutions. As we assumed that the core structures of the secondary bands originate from a chemical system other than the chromate/dichromate system, we decided to start our investigations in the above mentioned characteristic pH range using ammonia, gelatin and silver nitrate without additional additives.

4.2.1 Preparation of the gelatin solutions (and sample preparation)

10 mL of a 10 w/w% gelatin (*type 0*) solution was prepared for each ammonia concentration (using either: 0.1, 0.3, 0.7, 1.0, 1.5 or 3.0 w/w% ammonia solutions). The mixtures were then vigorously shaken for 1 minute and heated (65°C) in a pressure stable tube (*BD Falcon*) for 4 h. During the heating process, the solutions were shaken every 30 minutes to obtain homogeneous gelatin-ammonia solutions. In the next step, the hot solutions were spin-coated onto a glass substrate (3 x 3 x 0.1 cm). For each solution a set of 20 samples at each coating speed (300 and 500 rpm) was prepared. After drying the gelatin films overnight at ambient temperature, the WETs technique (Section 2.4.2 p. 28) was used and a silver nitrate loaded stamp (48 h in a 0.3 M $AgNO_3$ solution) was placed on the gelatin layer. For proper statistics the stamps were removed on 4 samples of each setup after 30, 60, 90, 120 and 180 minutes. For verification that an alkaline milieu is needed for the band formation, a set of gelatin solutions containing HCl (0.01 M, 0.1 M and 1.0 M) and citric acid (0.01 M, 0.1 M and 1.0 M) instead of ammonia was tested. All samples were analyzed by optical microscopy (*Leica DMLP*) and by Laser profiling (*Keyence VK-X200*).

4.2.2 Results and discussion

On the first sets of samples we were not able to see any bands by optical microscopy. But while measuring the sample using the laser microscope, we observed very weak bands in the

measured profiles (Figure 4.1). After profile measurements samples were analyzed again by optical microscopy. This time bands were also observed by optical microscopy (Image 4.1).

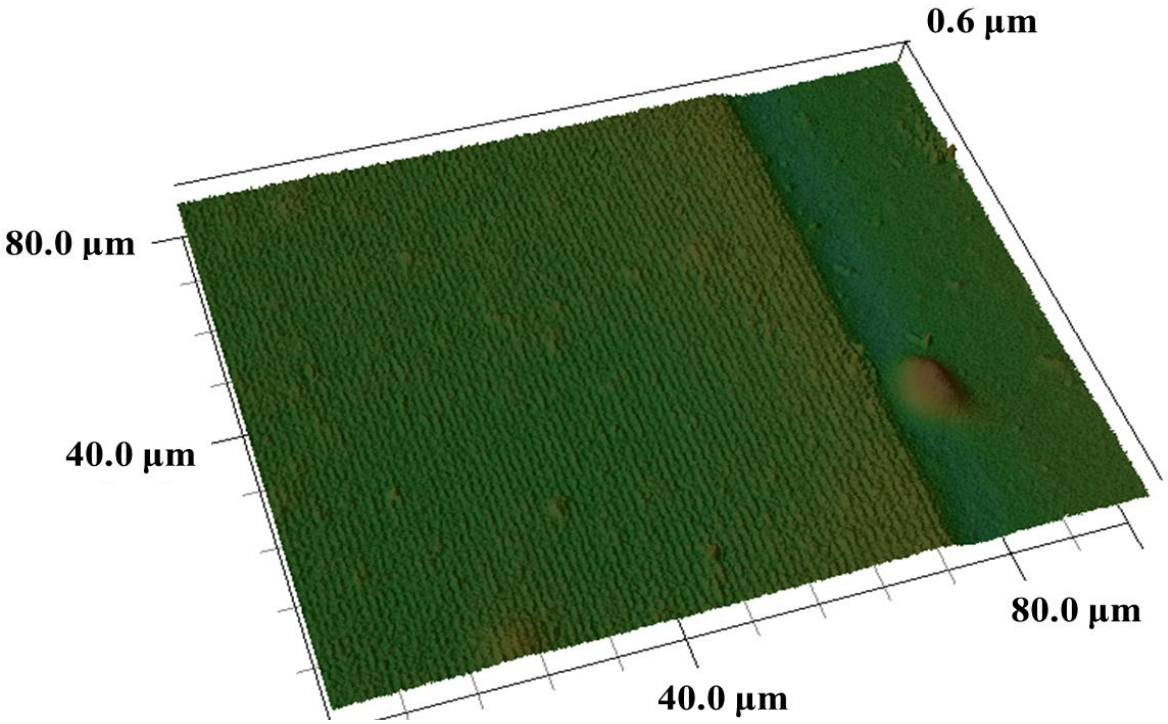

Figure 4.1: 3D Laser profile measurement at the end of the precipitation propagation zone. Sample: 10 w/w% gelatin (*type 0*) in 0.3 w/w% ammonia at 300 rpm and a stamping time of 90 minutes.

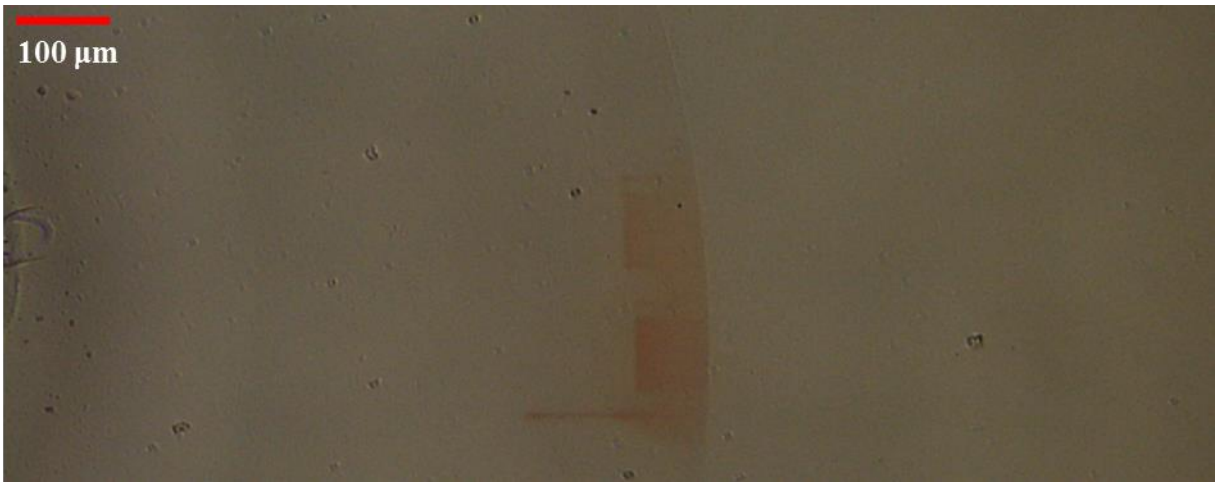

Image 4.1: Optical image after laser profiling: Middle left: stamp interaction site, middle brown: end of precipitation zone and place where the laser irradiated the sample.

Form these observations we concluded that the energy of the laser beam used for the profiling process somehow changed the material in the gelatin film. As the laser used in the microscope is a violet laser with 408 nm at 0.95 mW, we decided to irradiate all samples for 30 minutes with UV-light before optical measurements. A UV-A/UV-C hand lamp (*Dr. Gröbel*) was used for UV-irradiation (256 and 365 nm, 6 W). In the verification experiments using acid

solutions no band formation was observed. If we compare the shape and sizes of the highly periodic mesoscale pattern in the alkaline milieu with those of the secondary bands found in the classical system (Figure 4.2), we can see that they are almost identical.

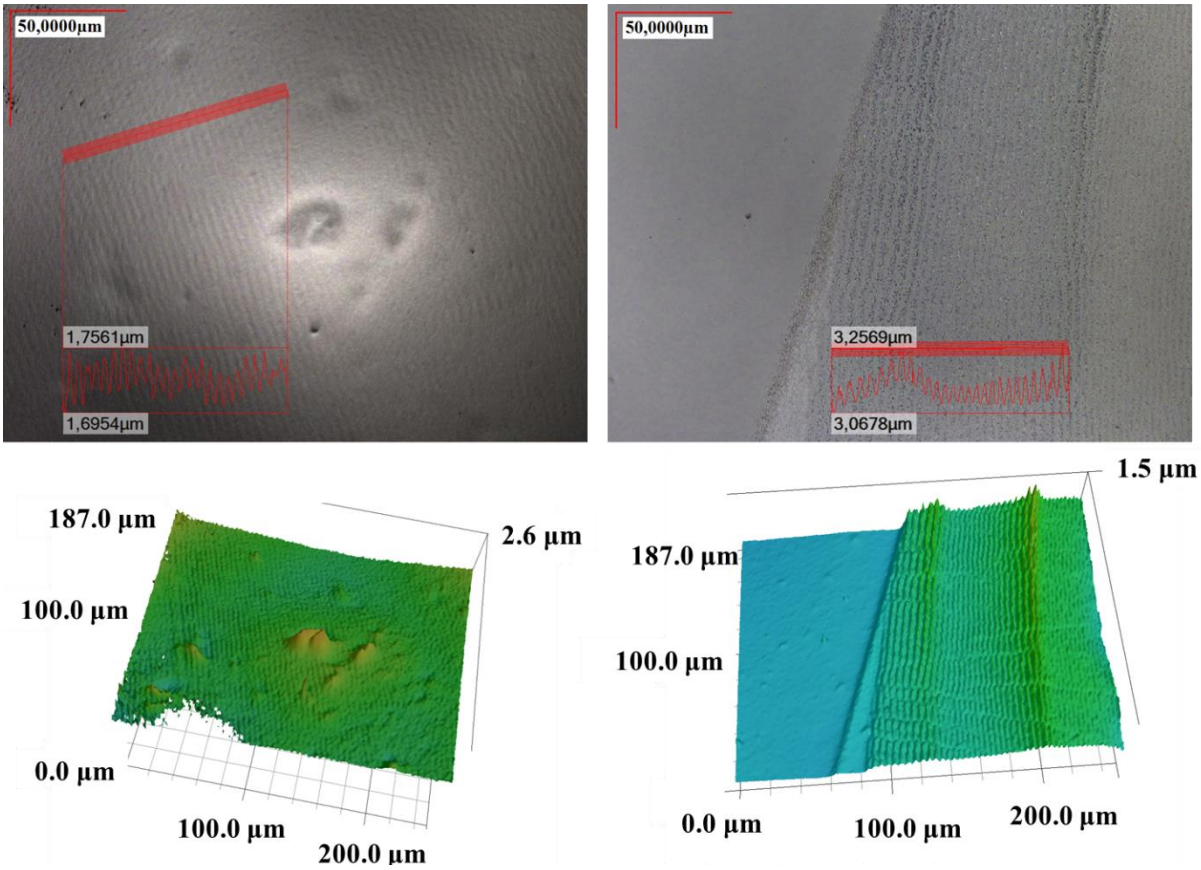

Figure 4.2: Comparison of the new silver system (left) and the classical Liesegang system (right). Top images: optical images with measured surface profiles (average of 10 lines). The different height values originate from different starting values (Z-axis). Only the difference between the upper and lower value are of interest. Bottom images: 3D laser profiles showing the fine-structures observed in both systems.

For this comparison we used the same amount of gelatin (10 w/w%, *type 0*), base (0.3 w/w% ammonia), and silver nitrate in the stamps and identical stamping times (45 min). The only difference between the two systems was that no potassium dichromate was added to the gelatin solution in the new system. The SEM-FIB cross sections were made at approximately the same distance (350 µm) from the stamping core. In the new system (Figure 4.2 left) we found an average band height of 40-90 nm, a FWHH of 2.0 µm and a space between two bands of 3.15 µm (measured from the maximum of one peak to the maximum of the neighbouring peak). For the bands of the classical system (Figure 4.2 right) we found an average band height of 40-80 nm, a FWHH of 2.1 µm and as average space between two bands 3.4 µm. Moreover, it was found that not only the shape of the bands is identical but also the size of the nanoparticles forming the precipitation bands. By using SEM-FIB, it was possible to compare the particle size of the nanoparticles of both systems.

Interestingly it was also found that the particle size of the core structures in the classical system (Image 4.2 B and D) are almost identical in shape and size to the nanoparticles found in the new system (Image 4.2 A and C).

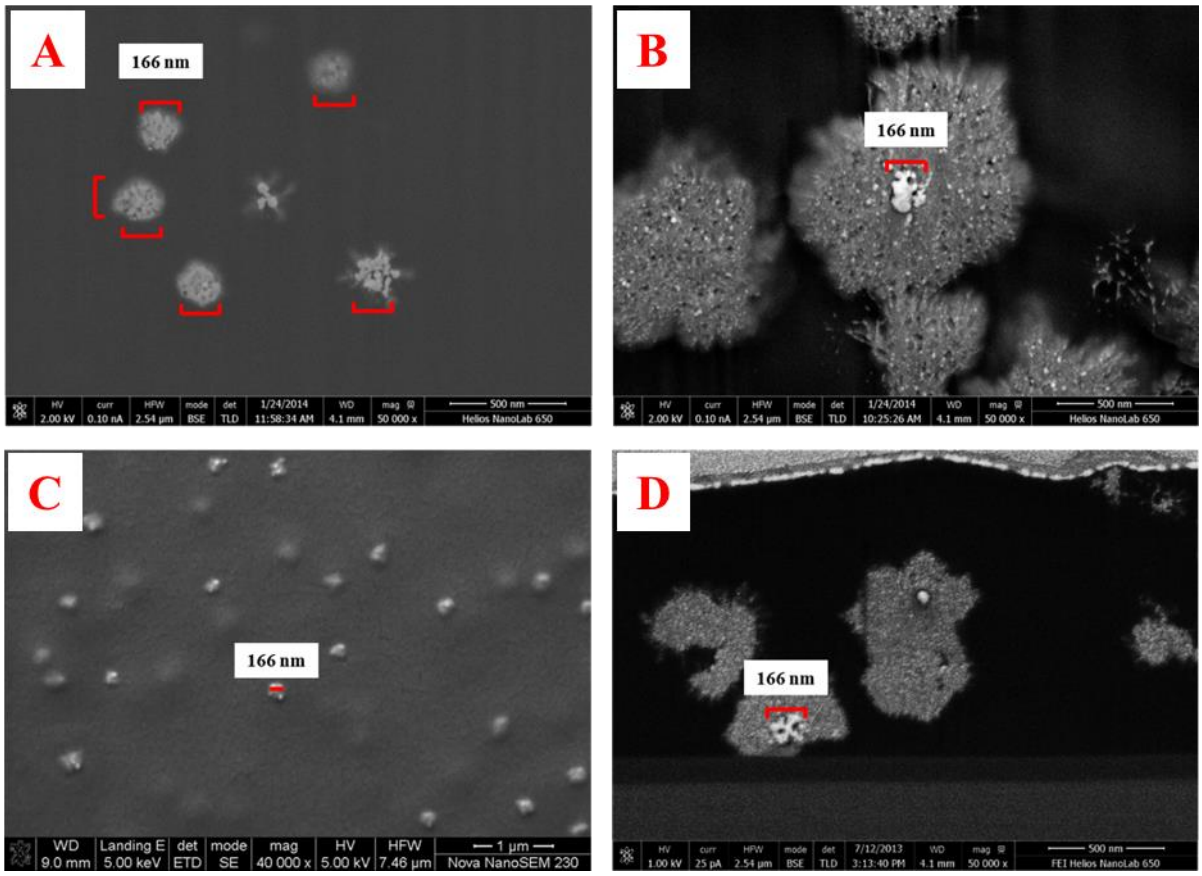

Image 4.2: SEM images from the top and SEM-FIB cross section images showing the size and shape of the nanoparticles forming the bands. SEM-FIB image (A) and SEM image (C): Nanoparticles, forming the bands in the new silver system. SEM-FIB images (B and D): Nanoparticles forming the primary bands in the classical Liesegang system. White core structures (in B and D) show the same size and shape as the nanoparticles found in the new silver system (red scale bar equals 166 nm).

4.2.3 Conclusion

In the described system it is possible to prepare Liesegang fine-structures very similar to the so-called secondary bands observed in the classical Liesegang system. The bands must be formed from a silver containing material, since there was only gelatin, silver nitrate and ammonia (no chromate or dichromate) in the system. Our findings raised new questions about the necessity for UV-illumination, the role of the base as well as the role of the hydrogel and also about the material composition of the particles forming the bands.

4.3 Further investigations of the fine structured system

4.3.1 About the role of UV-irradiation

Previously (Section 4.2.2, p. 50) we showed that UV light was necessary to make the fine structured bands visible. This opened the question whether the bands were already there before UV-irradiation or they formed from light sensitive silver containing nanoparticles during illumination. To address this question, special in situ AFM measurements were performed.

4.3.1.1 Sample preparation and AFM studies

The samples were prepared in the dark to avoid possible influences of the illumination. For the WETs process a special black box (Appendix B, p. 147) was designed, to protect the samples as efficiently as possible during the manufacturing process.
20 mL of a 10 w/w% gelatin (*type 0*) solution was prepared using ammonia (0.3 w/w%). The mixture was than heated (70°C) in a pressure stable tube (*BD Falcon*) for 4 h. During the heating process the solutions were shaken every 30 min. In the next step the hot solution (0.4 mL) was spin-coated onto a glass substrate (3 x 3 x 0.1 cm) at 300 rpm. After coating and drying the gelatin films in the dark overnight at ambient temperature, the WETs technique (Chapter 2.4.2) was used and a silver nitrate loaded stamp (48 h in a 0.6 M $AgNO_3$ solution) was placed on the gelatin layer. After 60 minutes the precipitation process was stopped and the samples were directly transferred into the AFM. A set of four identical samples was prepared to ensure reproducible statistics/results. First the samples were analyzed by AFM measurements (*Bruker*). Therefore the prepared samples were mounted onto the XYZ stage of the AFM in the dark and the AFM was used in contact mode (Section 2.2.1.2). After the first measurements, the samples were irradiated (256 nm) for 30 minutes. After illumination the samples were measured again at the same place (Image 4.3). An optical image was also taken on the AFM measured area on another sample, before and after UV-treatment (Image 4.4). After the AFM studies had been carried out, the samples were further analyzed by optical microscopy (*Leica DMLP*) and by Laser profiling (*Keyence VK-X200*).

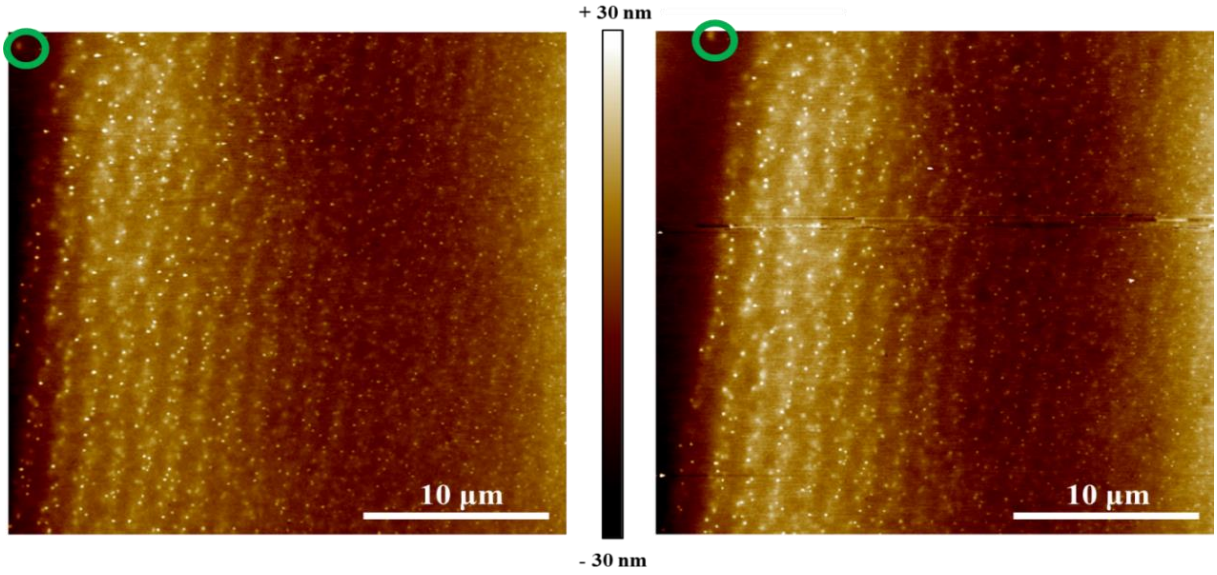

Image 4.3: AFM profiles before (left) and after (right) UV-irradiation (256nm). The green marker in both images shows the same particle. If the images are superimposed at that place it is found that there is no change in the surface structure after illumination. Measurements in contact mode (30 x 30 µm).

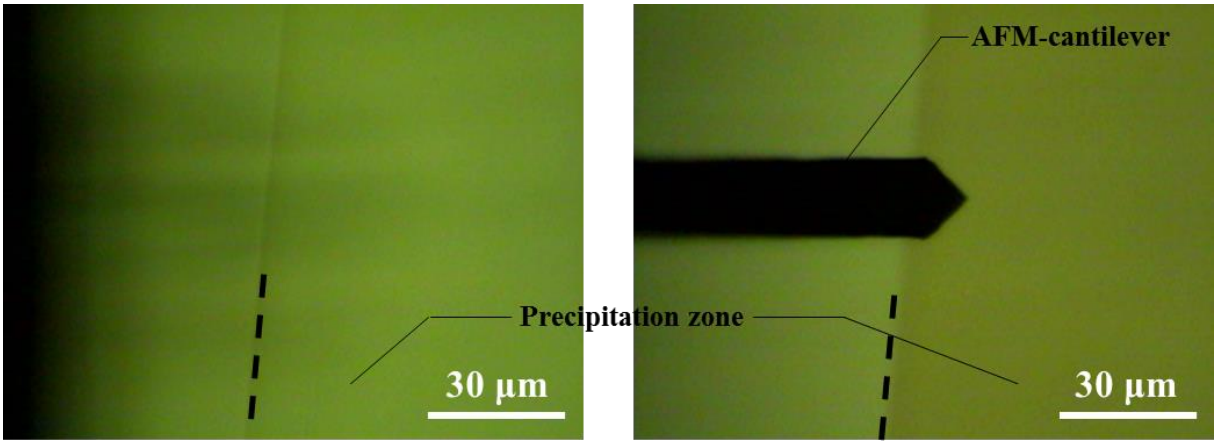

Image 4.4: AFM surface profile studies, measured before (left) and after (right) UV-irradiation (256 nm). Photographs were taken with an exposure time of 4 min. The dashed lines indicate the precipitation propagation front (precipitation bands were on the right side).

4.3.1.2 Results and discussion

From the AFM-profile measurements (Image 4.3 and Image 4.4) it is clear that the precipitation bands are formed without light treatment. Furthermore it was also found that UV-irradiation has no influence on the shape/structure of the bands. This can be seen, if the AFM surface profiles (Image 4.3) are superimposed at the green circles. Therefore, the observations imply that the darkening during the UV-irradiation is caused by a pure photographic effect,[194,195] where the silver species in the bands are reduced to silver(0).

4.3.2 The role of base on the formation of the silver containing bands

The observations from both previously described experiments open questions about the role of the base for the pattern formation. It is known that silver nitrate reacts with ammonia forming a diamine-silver complex $Ag(NH_3)_2^+$ (also known as Tollens` reagent),[196] which is light sensitive and can be reduced to silver(0) by irradiation. If this is true and the formation of this silver complex causes the band formation, no bands should be formed if ammonia is replaced by other alkaline solutions. For this reason the role of the used base was investigated by exchanging ammonia by other alkaline solutions.

4.3.2.1 Sample preparation and analytics

Tested alkaline solutions: 0.1, 0.3 and 1.0 w/w% diethylamine (Et_2NH)
0.1, 0.3 and 1.0 w/w% triethylamine (Et_3N)
0.01 M and 0.1 M potassium hydroxide (KOH)
0.01 M and 0.1 M sodium hydroxide (NaOH)

10 mL of a 10 w/w% gelatin (*type 0*) solution was prepared for each of the above mentioned alkaline solutions. All samples were then prepared according to the previously described procedures (Section 4.2.1 page 50). Images of the most beautiful samples of each setup can be found in Appendix B, Image 1-4).

4.3.2.2 Results and discussion

The pH range, in which fine structured bands were observed in the NH_4OH containing system was found to be pH 8.1 – 11.4. For all tested systems containing other alkaline solutions, fine structured Liesegang rings/bands were observed. For this reason it can be ruled out that the precipitation process is governed by the formation of a silver-diamine complex. A more likely explanation for this periodic precipitation process is that silver ions are stabilized under alkaline conditions and reduced to silver(0) by gelatin, which acts as reducing agent. The reduction occurs during the whole precipitation process in the gelatin, which prevents the silver particles from sedimentation, until the silver concentration reaches a point of supersaturation. At that point the silver nanoparticles form precipitates, resulting in the observed fine structured precipitation bands. For the verification of this statement additional investigations were needed.

4.3.3 About the role of the used hydrogel

A very similar system showing silver containing bands in the micro- to millimeter scale was recently published by *Nabika et al.*[104] In their system, gelatin was used as the hydrogel and silver nitrate as the invading outer electrolyte, but in contrast to our system they worked under acidic conditions and used methionine as an additive in the hydrogel. They concluded from their observations that the precipitation process is governed by the formation of a silver methionine complex. This raised the question if the amino acids which are abundant in gelatin (90-95 w/w%) or especially methionine (0.7-3 w/w%),[197–199] are responsible for the band formation in our system as well. To address this, experiments testing different types of gelatin as well as other hydrogels (agarose, PEG, agar-agar and PVA) were carried out.

4.3.3.1 Different types of gelatin

4.3.3.1.1 General and sample preparation

As mentioned before (Section 2.5.1), gelatin is a natural product made out of denaturized proteins, some minerals and water. Depending on the source and manufacturing process the mechanical and chemical properties of gelatin differ. Therefore 8 different gelatins (*type 0-7*) were tested.

A set of acidic, neutral and alkaline 10 w/w% gelatin solutions was prepared by mixing 1.0 g gelatin (*type 0-7*) with 9.0 g of 0.01 M or 0.1 M aqueous citric acid, milliQ water, or 0.3 w/w% ammonia (0.176 M). All samples were then prepared according to the previously described procedures (Section 4.2.1). After spin coating 4 samples of each solution (300 and 500 rpm), drying overnight and wet stamping (0.3 M $AgNO_3$) for 60 minutes, the samples were analyzed by optical microscopy and Laser profiling.

4.3.3.1.2 Results of the experiments with different types of gelatin

Only alkaline gelatin films showed band formation, except gelatin *type 4* where band formation was also observed under neutral conditions. This can be explained with the manufacturing process, since t gelatin Type-B is obtained from alkali-treated raw materials. For the other neutral and acidic samples precipitates were found but without a specific shape/pattern (bands).

4.3.3.2 Agarose as hydrogel

4.3.3.2.1 General and sample preparation

Agarose, a polysaccharide, was firstly tested as hydrogel because it is used in applications as gel matrix e.g. in agarose gel electrophoresis for the electrophoresis of DNA or proteins.
A set of acidic, neutral and alkaline 5, 10 and 15 w/w% agarose solutions was prepared by mixing either 0.5 g, 1.0 g or 1.5 g agarose with 9.0 g of 0.01 M or 0.1 M aqueous citric acid, milliQ water, 0.3 w/w% ammonia (0.174 M) or 0.1 M KOH. The mixtures were then vigorously shaken for 1 minute and heated (90°C) in a pressure stable tube (*BD Falcon*) for 6 hours. During the heating process the solutions were shaken every 20 minutes to obtain homogeneous solutions. In the next step the hot solutions were spin-coated (500 rpm) onto glass substrates (3 x 3 x 0.1 cm). After spin coating, drying overnight and WETs (48 hours loaded agarose stamps (0.3 M $AgNO_3$)) for 30 minutes, the precipitation process was stopped. Half of the samples were directly analyzed by optical microscopy and laser profiling, the rest were treated with UV-light (30 minutes at 365 and 256 nm) before analyzing. This was done for all other experiments presented in this section as well.

4.3.3.2.2 Results

Band formation was observed only in some of the alkaline samples (Image 4.5), but as the reproducibility of this was very low (3:30 samples), further investigations and optimization on the system are needed. For most of the samples, uniformly spread micro- and nanoparticles were found in the diffusion propagation zone.

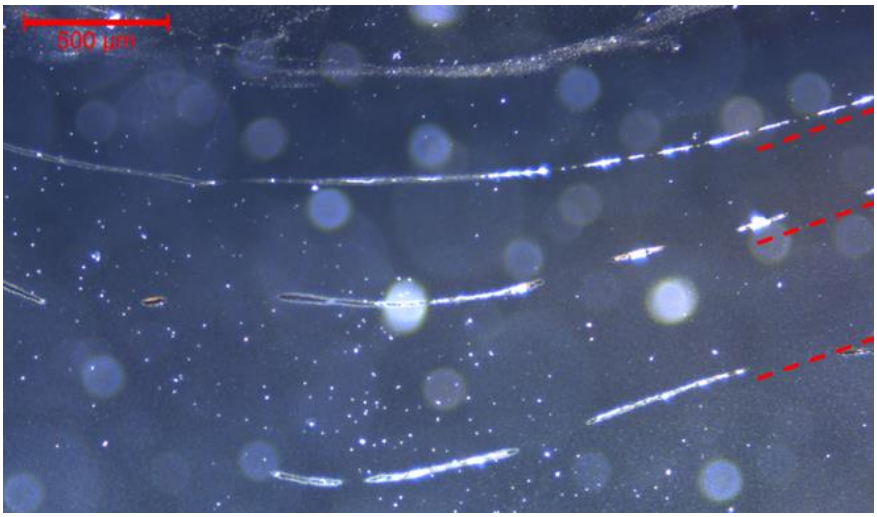

Image 4.5: Precipitation bands (indicated by the red dashed lines) observed in a system with 6 w/w% agarose, 0.3 w/w% NH_4OH, 0.3 M $AgNO_3$ loaded stamp and a stamping time of 40 min.

4.3.3.3 Agar-agar as hydrogel

4.3.3.3.1 General and sample preparation

Agar-agar, which is a mixture of agarose and agaropectin, was also tested.
A set of acidic, neutral and alkaline 5 and 10 w/w% agar-agar solutions was prepared with the same set of acidic, neutral and alkaline solutions as used in the agarose experiment. After heating (85 °C for 5 h) and shaking several times, the solutions were spin coated (500 rpm for 1 min) on to glass substrates. The samples were allowed to dry for 12 hours at ambient temperature before the WETs technique was used (0.3 M $AgNO_3$ loaded stamps). The WETs process was stopped after 90 minutes.

4.3.3.3.2 Results

No band formation was observed (Image 4.6). All samples looked like the agarose samples where the particles were equally dispersed within the propagation zone. The main difference between the agar-agar and agarose system was the propagation speed of the precipitation front, which was three times longer in agar-agar.

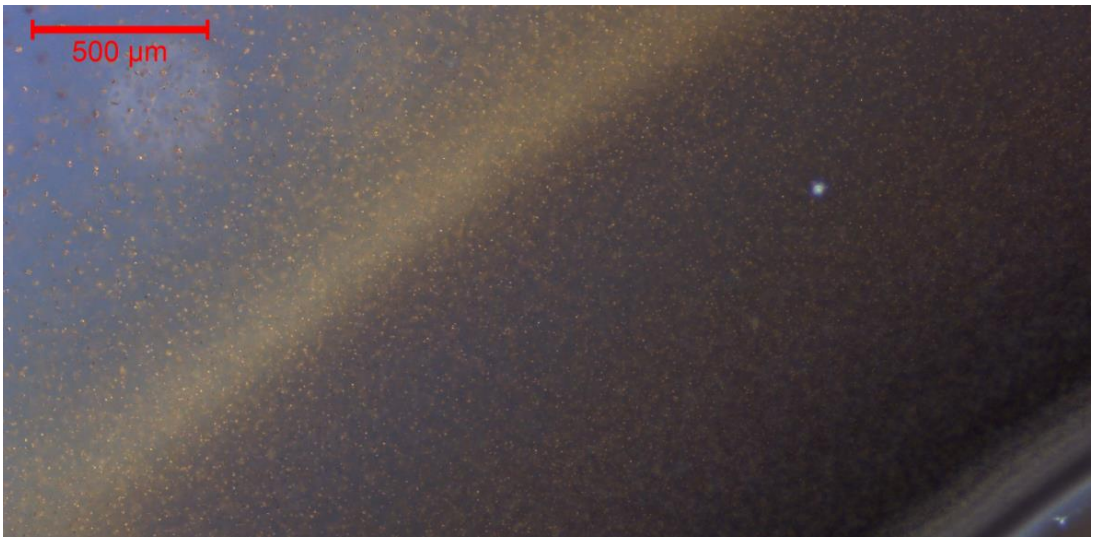

Image 4.6: Optical image of well distributed particles found in a sample prepared with an alkaline (0.1 M NaOH) agar-agar (10 w/w%) solution.

4.3.3.4 Polyethylene glycol as hydrogel

4.3.3.4.1 General and sample preparation

Polyethylene glycol 4000 was used for sample preparation, since all other tested PEGs (e.g. PEG 1500 or PEG 8000) were not suitable for homogeneous film preparation or WETs. The samples were either too liquid or too stiff, so that no precipitation was observed at all.
A set of acidic, neutral and alkaline 15, 25, 40 and 50 w/w% PEG solutions was prepared with the same set of acidic, neutral and alkaline solutions as used in previously described experiments. After heating (60 °C for 3 h) and shaking several times, homogeneous solutions were obtained, which were directly spin coated (300 rpm for 1 min) on to glass substrates. The samples were allowed to dry at ambient temperature for 16 h before the WETs technique was used (0.3 M and 0.6 M $AgNO_3$ loaded stamps) for 40 min.

4.3.3.4.2 Results

Only uniformly spread micro- and nanoparticles, increasing in diameter with increasing distance from the stamp interaction were observed, but none of the tested PEG-solutions led to band formation (Image 4.7).

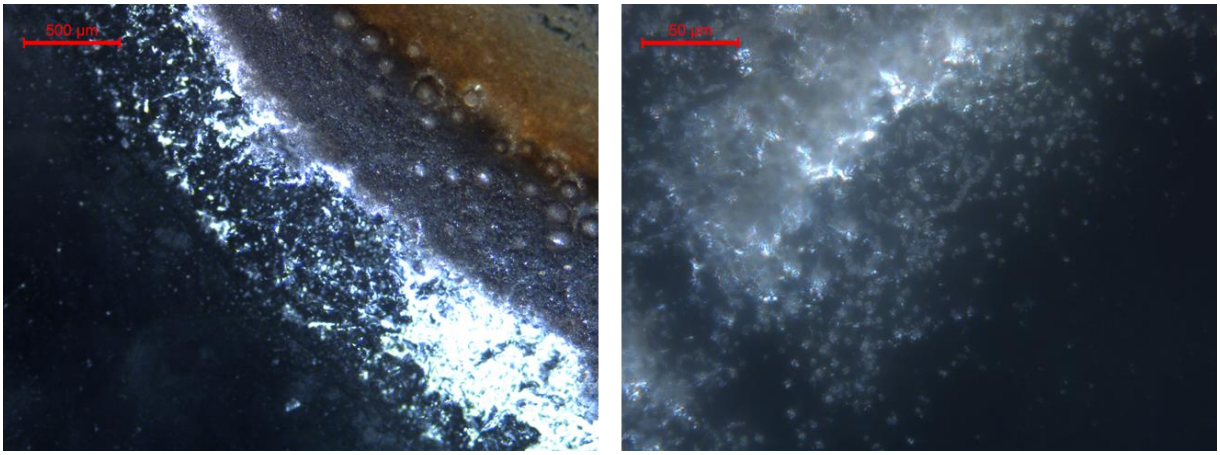

Image 4.7: Optical image of uniformly spread particles found in a sample prepared with an alkaline (0.1 M NaOH) PEG-4000 (40 w/w%) solution. Overview image (left), zoomed image at the precipitation front (right).

4.3.3.5 Polyvinyl alcohol (PVA) as hydrogel

4.3.3.5.1 General and sample preparation

Polyvinyl alcohol was also tested because it was shown by *Péter Hantz et.al.*,[106,107,139] that Liesegang type precipitation band formation could be observed for several systems using this hydrogel.

A set of acidic, neutral and alkaline PVA solutions (5, 10, 15 and 20 w/w%) was prepared in either 0.1 M citric acid, degassed milliQ water, 0.1 M KOH or 0.3 w/w% ammonia. After mixing, the solutions were heated at 70 °C for 7 h. During the heating process the solutions were vigorously shaken several times and the homogeneous solutions were then spin coated (300 and 500 rpm) on to glass substrates. After coating, the samples were allowed to dry at ambient temperature for 24 h before the WETs technique was used (0.3 M and 0.6 M $AgNO_3$ loaded stamps). The precipitation process was stopped after 90 min.

4.3.3.5.2 Results

Most of the samples from the described system showed uniformly spread micro and nano-particles, only one sample with potassium hydroxide showed band formation. Better developed bands have been observed in the system containing PVA (10 w/w%) and KOH (0.1 M). For this reason a second PVA experiment (Section 4.3.3.6) was started using only potassium hydroxide as additive.

4.3.3.6 Additional PVA experiment

4.3.3.6.1 Sample preparation

100 mL of a 10 w/w% aqueous PVA solution were prepared. The solution was heavily shaken every 20 min while heating at 75°C for 6 h. After additional heating at 80°C for 24 h, the homogeneous mixture was portioned (10 x 10 mL samples) and KOH (s) was added to obtain one neutral and a set of alkaline PVA solutions (0.01 M, 0.05 M, 0.1 M, 0.5 M, 1.0 M, 2.0 M, 3.0 M, 4.0 M and 8.0 M KOH). The hot alkaline solutions were then stirred for 2 h at 80°C, before spin coating (300, 500, 750, 1000, 1250 rpm) onto glass substrates. After drying the PVA-films at ambient temperature overnight, the WETs technique was used (0.3 M and 0.6 M $AgNO_3$ loaded stamps) for the precipitation process, which was stopped after 40 min.

4.3.3.6.2 Results

Band/ring formation was observed for 0.5 M, 1.0 M and 2.0 M KOH samples (Image 4.8). At higher (≥ 2.0 M) KOH concentrations the PVA films turned completely black after stamping, and it was impossible to observe bands with optical microscopy or laser profiling. Below 0.5 M KOH, uniformly spread micro- and nanoparticles were observed as in the previously described PVA experiments.

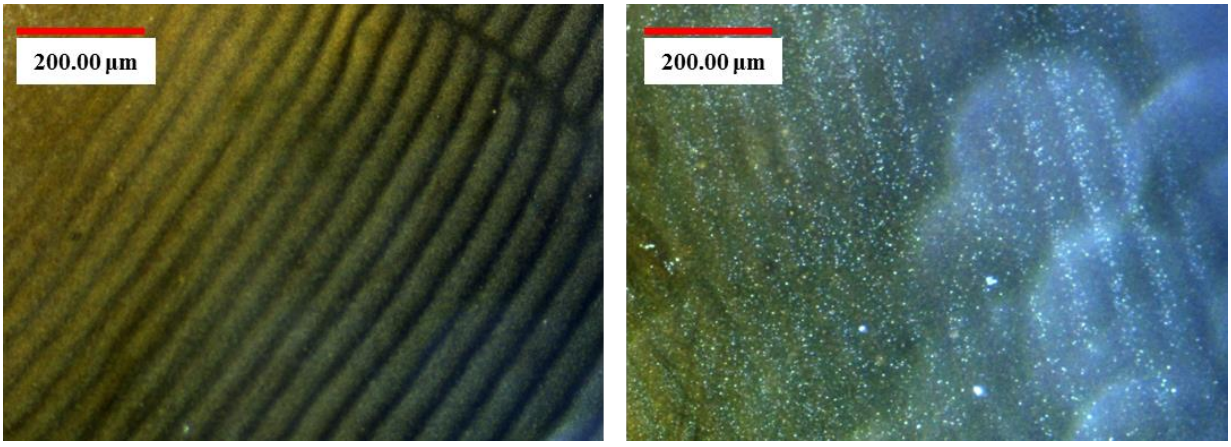

Image 4.8: Optical images of precipitation bands observed in alkaline PVA (10 w/w%) films. Left: 0.5 M KOH, right: 2.0 M KOH.

4.3.3.7 Methionine as hydrogel additive

4.3.3.7.1 General and sample preparation

In the past it was proposed by *Nabika et al.*[104] that methionine as additive is necessary to facilitate precipitation band formation. For this reason the role of methionine was investigated as well. Therefore methionine was added to 3.0 mL all before mentioned and tested hydrogel solutions to obtain a set of 0.1 and 0.5 w/w% methionine hydrogel solutions. Methionine-hydrogel films were prepared according to the procedures described for each hydrogel before.

4.3.3.7.2 Results

Interestingly, not a single of the tested solutions showed precipitation bands after applying the WETs technique, even though band/ring formation was observed in agarose and PVA films when no methionine was present. Both of these hydrogels do not contain sulfur. For this reason methionine or other possible sulfur-silver interactions seem not to be involved in the band forming process.

4.3.3.8 Conclusion of hydrogel dependency experiments

Precipitation was observed in varying degrees in all samples, but fine structured Liesegang-type band/ring formation described at the beginning of this chapter was only observed in alkaline gelatin films, alkaline agarose films and alkaline PVA films. The kind of base had no influence; the only critical point was a pH above 7.2. In addition to that, methionine used as amino acid additive did not help to increase the band formation in gelatin as it was proposed by *Nabika et al.*[104] or any other tested hydrogel system. For this reason, silver-sulfur intermediates which could possibly be formed in gelatin or other hydrogel solutions (containing sulfur compounds), can be ruled out as being involved in the band/ring forming process.

4.3.4 Material analysis using electron microscopy

In order to obtain information about the material composition of the nanoparticles forming these fine structured bands and about the band forming process in general, STEM-EDX, SEM-EDX and SEM-FIB-EDX studies were carried out.

4.3.4.1 STEM-EDX measurements

STEM measurements were performed to obtain reduced EDX background information on the particles forming the bands compared to standard SEM-EDX. Another advantage of STEM-EDX to SEM-FIB-EDX is that there was no sample alteration due to invading gallium ions. However, for STEM the samples need to be very thin (approximately 300 nm) to be transparent enough for transmitting electrons. Thicker samples reduce the penetration rate/transparency of the specimen, leading to increased scattering of the electrons from the electron beam. This causes a large degree of excitation in the sample, generating much background noise/information. However in very thin samples (300 nm or less), the electrons easily penetrate the specimen, leading to a much smaller ionization volume, compared to standard SEM-EDX. This leads to an increase in the resolution. In order to obtain very thin samples ($\leq$ 300 nm) a special setup was needed to perform microtome cut.

4.3.4.1.1 Sample preparation

5 mL of a 10 w/w% gelatin (*type 0*) ammonia (0.3 w/w%) solution was prepared according to previous procedures (Section 4.3.1.1). The hot solution (0.3 mL) was spin-coated onto Thermowax (4 x 4 x 0.04 cm) at 300 rpm. After coating and drying the gelatin films overnight at ambient temperature, the WETs technique (cf. Section 2.4.2) was used and a silver nitrate loaded stamp (48 h in a 0.3 M $AgNO_3$) was placed on the gelatin layer. After 45 min the precipitation process was stopped and the samples were irradiated at 256 nm for 30 min. This was necessary to visualize the bands (Image 4.9) for the later microtome cuts, described in Section 2.4.3.1.

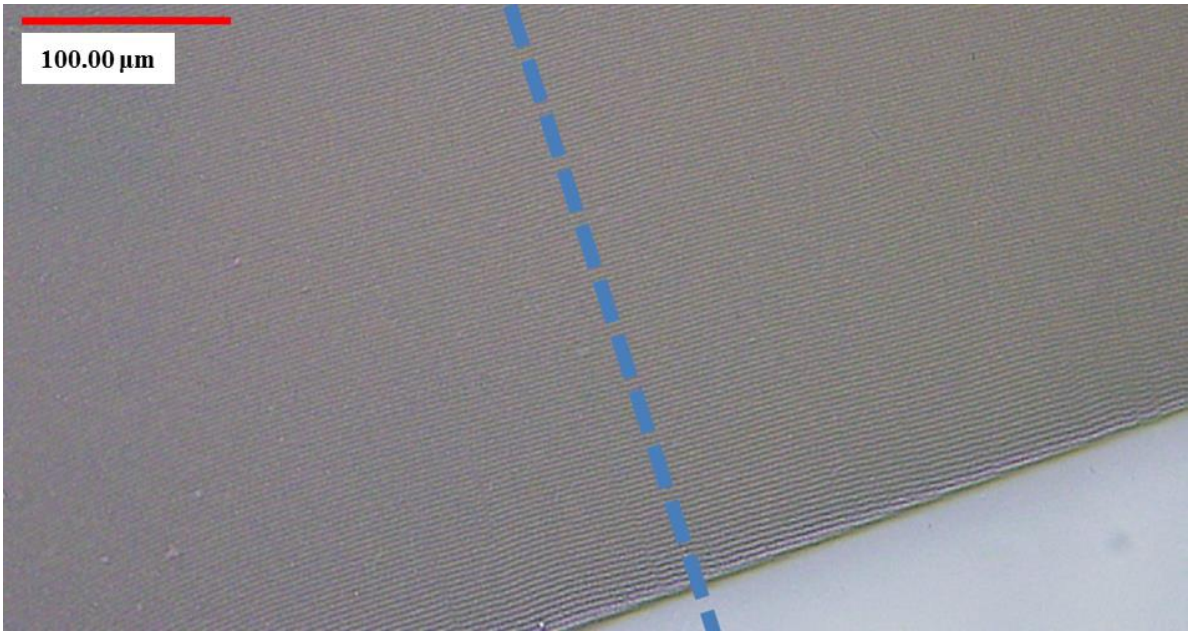

Image 4.9: Optical image: Sample used for microtome cut. Microtome cut along the blue dashed line.

4.3.4.1.2 Analytics

The microtome cuts (profile cross sections) were measured at the *FEI Helios Nano Lab 650* in STEM mode. Procedure described in Section 2.2.1.1.4. In the STEM-mode the measurements were performed on one particle from a band (Image 4.11 black dots). The different contrast in brightness of the particles is caused by their location in the thin cut. Brighter appearing particles are located closer to the electron beam while the dark particles are located closer to the detector. The brightening is owed to the thickness of the cut, because the gelatin layer blocked some of the transmitted electrons.

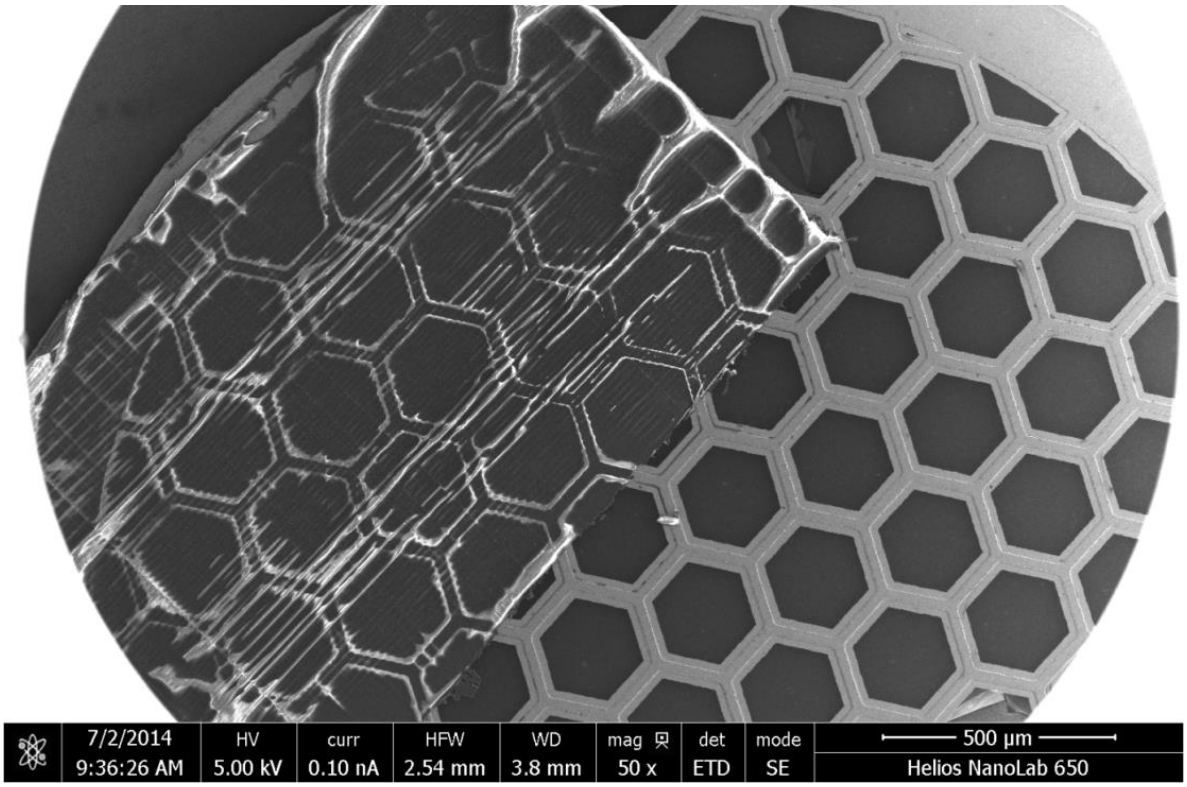

Image 4.10: SEM image showing the microtome cut on a TEM grid.

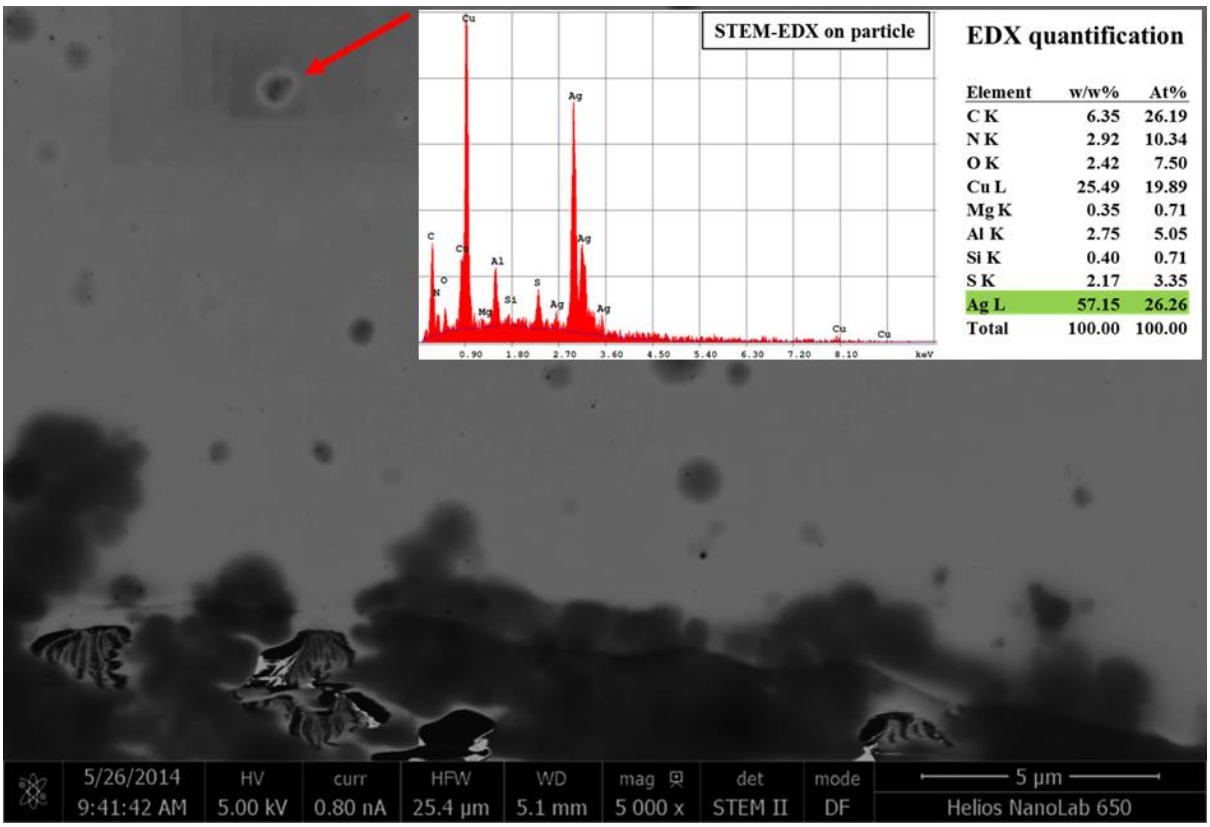

Image 4.11: STEM image of the microtome cut. EDX measured on the particle on the top left (red arrow) and STEM-EDX measurements of the material in the particle forming the bands (top right).

4.3.4.1.3 Results

The obtained EDX spectrum (Image 4.11) shows signals for carbon, nitrogen, oxygen, copper, magnesium, aluminum, silicon, sulfur and silver. The Al and Cu signals originate from the TEM-grid and the sample holder in the vacuum chamber. The amounts of carbon, nitrogen, oxygen and sulfur are comparable to the values found in the gelatin reference investigated in the classical Liesegang system (Section 3.4.2). The high values for silver indicate that the main material forming the particles consists of silver. However this technique does not give any information about the possible oxidation state of the silver species.

4.3.4.2 SEM measurements

4.3.4.2.1 General

For verification purposes the same sample was measured again in SEM and SEM-EDX mode. The white circular dots (Figure 4.3) are the nano-particles forming the bands, located on the copper frame (indicated by the red lines) of the TEM-grid. This location was chosen because the microtome cut cracked during the observation in the SEM mode on the place where no substrate was beneath.

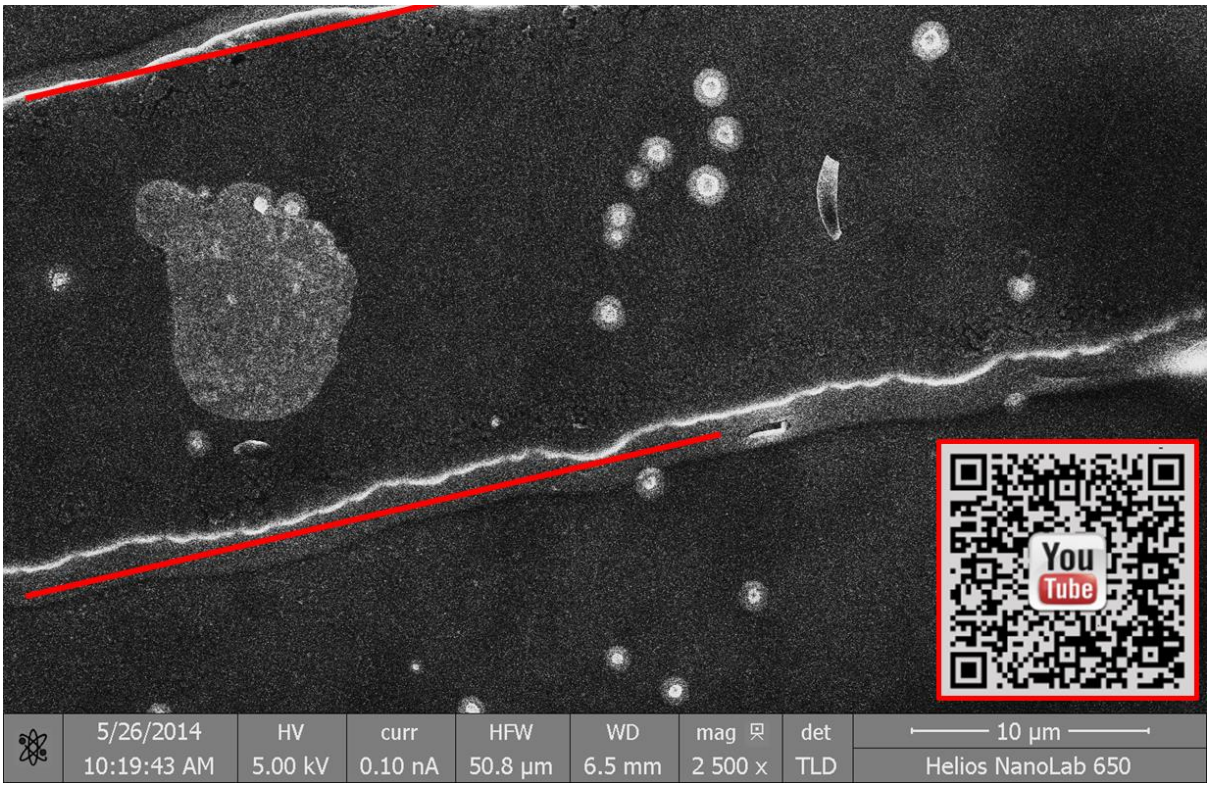

Figure 4.3: SEM image of the microtome cut containing a QR code, which can be used to watch the described process online. The red lines indicate the structure of the Cu-grid. White particles were analyzed by EDX.

The EDX measurement was monitored to show how the energy of the incident electron beam can change the structure of the particles. A video of this this can be found online, by using the QR code or : ***https://www.youtube.com/watch?v=3wIDShkrkCw&list=WL&index=144***
However it was also possible to record some images of the nanoparticles forming the bands where only small amounts of gelatin were surrounding the particles. In Image 4.12 it is possible to see that these particles consist of an accumulation of smaller particles.

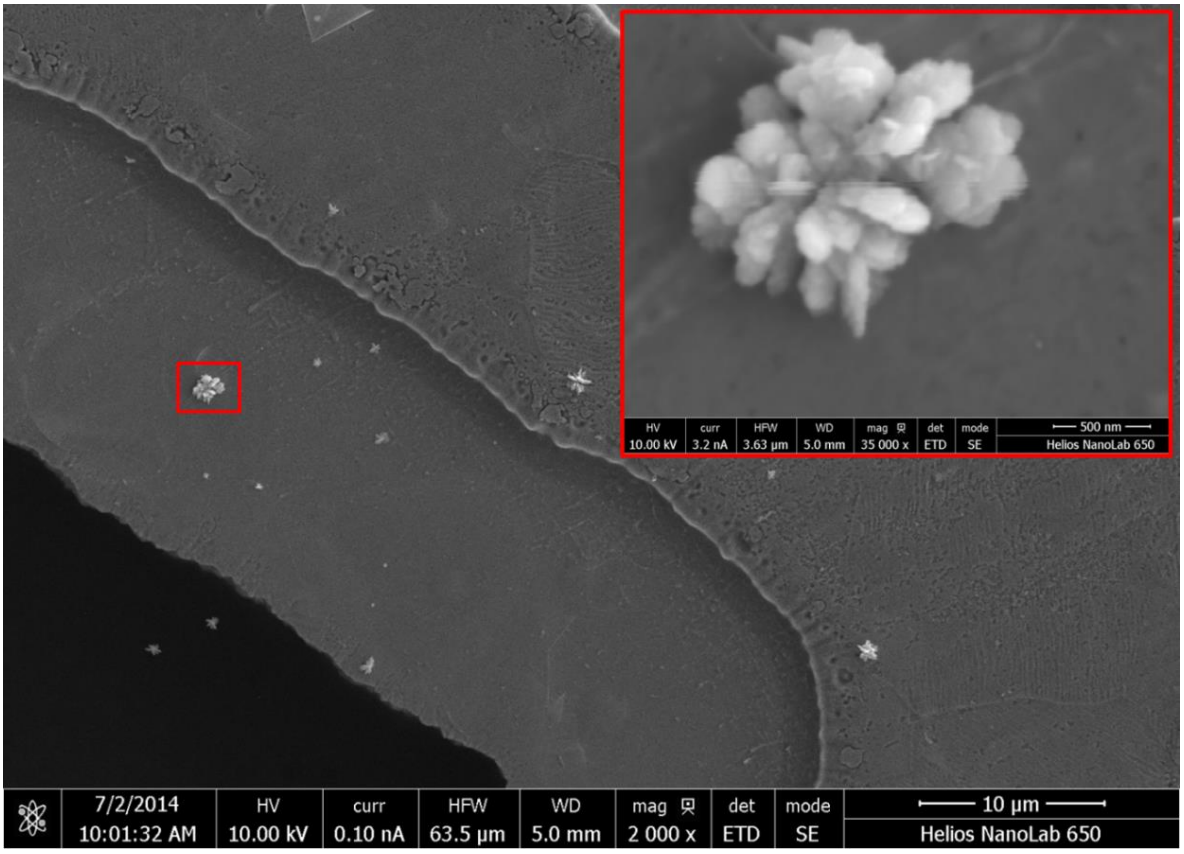

Image 4.12: SEM image, showing the construction of the particles in the sample. The red square in the large image indicates the location of the zoomed in image (top right).

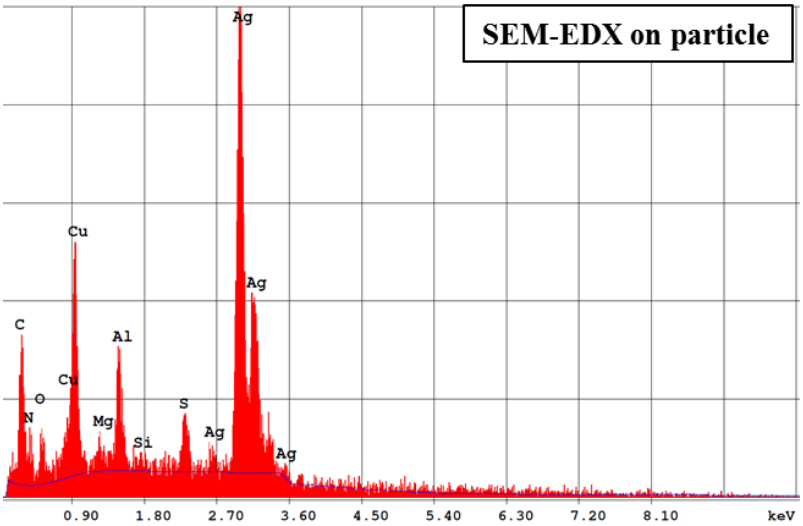

EDX quantification

Element	w/w%	At%
C K	5.13	22.12
N K	3.11	11.48
O K	3.44	11.13
Cu L	11.77	9.59
Mg K	0.81	1.73
Al K	3.19	6.13
Si K	0.41	0.76
S K	2.14	3.45
Ag L	70.00	33.60
Total	100.00	100.00

Figure 4.4: EDX spectrum and material quantification of the particles shown in Image 4.12.

In the SEM-EDX measurement (Figure 4.4) the same elements were observed as in the STEM-EDX measurement (Image 4.11). Here the Al and Cu signals are also caused by the TEM-grid and the sample holder in the vacuum chamber, and the amounts of carbon, nitrogen, oxygen and sulfur are comparable.

4.3.4.2.2 Results

The obtained results from both EDX measurements (STEM and SEM) are very comparable. The differences in the silver values might occur from the change in particles, where it seems possible that the growing material contains a higher amount of silver than the material below.

4.3.4.3 SEM-FIB-EDX measurements

4.3.4.3.1 General

As it is possible that the shear forces applied while preparing the microtome cut might have changed the silver containing nano-particles (possibly silver-oxide was reduced, which leads to a higher silver content), the results from the microtome cuts were compared with SEM-FIB measurements on new samples.

4.3.4.3.2 Sample preparation

For sample preparation the same solution was taken as for the microtome cuts, but instead of thermowax a standard glass substrate was used as carrier. The hot solution was spin coated at 300 rpm, the samples were dried (24 h) and the WETs technique (0.3 M $AgNO_3$ loaded stamp) was used to initialize the precipitation process in the hydrogel.

4.3.4.3.3 Results

Since it was easier to analyze larger particles in EDX and due to the fact that largest particles were always found close to the precipitation front, SEM-FIB cross sections were performed at the precipitation border (Image 4.13). After polishing the surface of the cross section, the sample was tilted towards the EDX detector to obtain better signal to noise ratios. EDX was then measured (Figure 4.5) on several particles found in the cross section through the bands (Image 4.14).

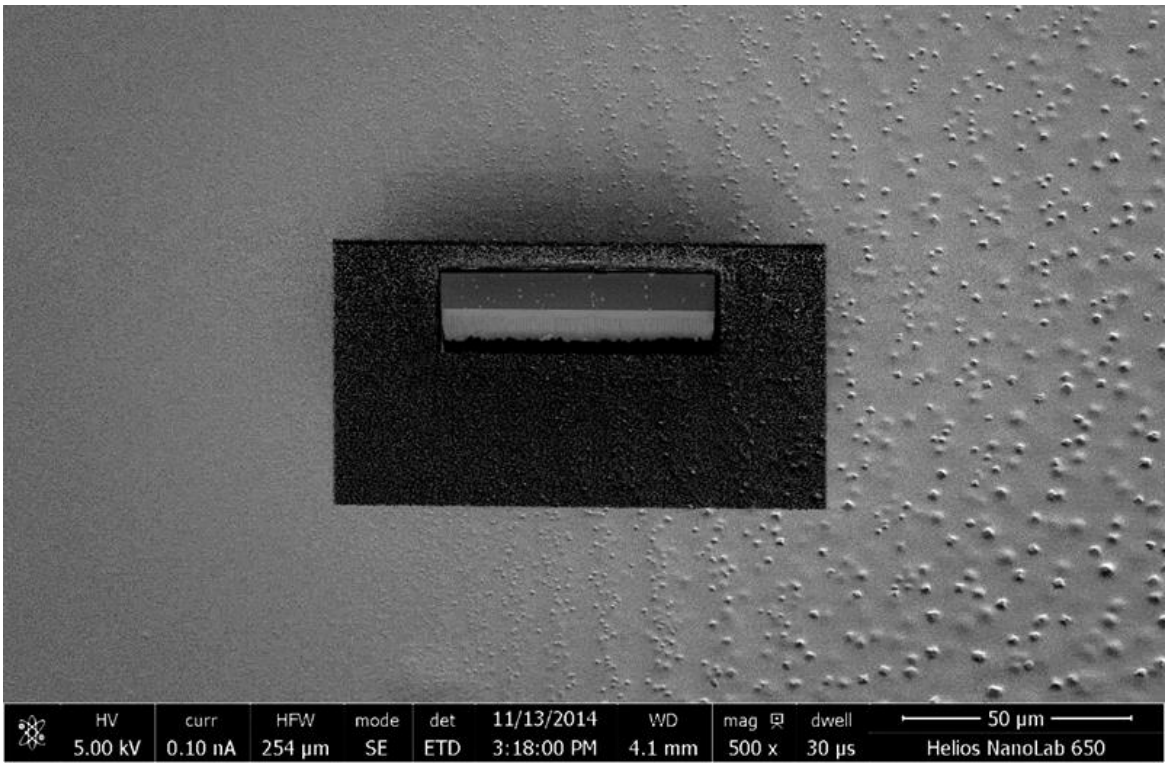

Image 4.13: SEM-FIB cross section at the end of the precipitation zone. The contrast of the cross section was changed to visualize the precipitation bands.

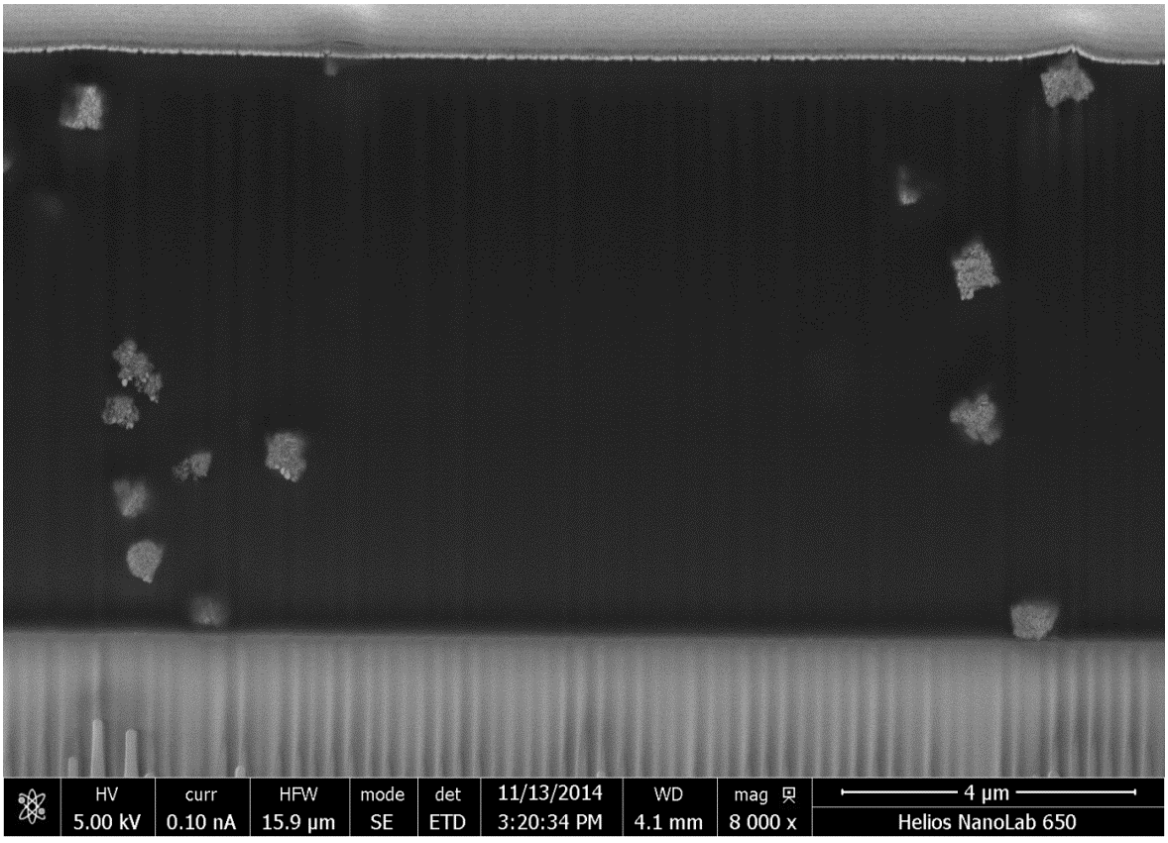

Image 4.14: SEM-FIB image of the cut though the fine structured bands. Particles are well separated, forming the bands, without particles between.

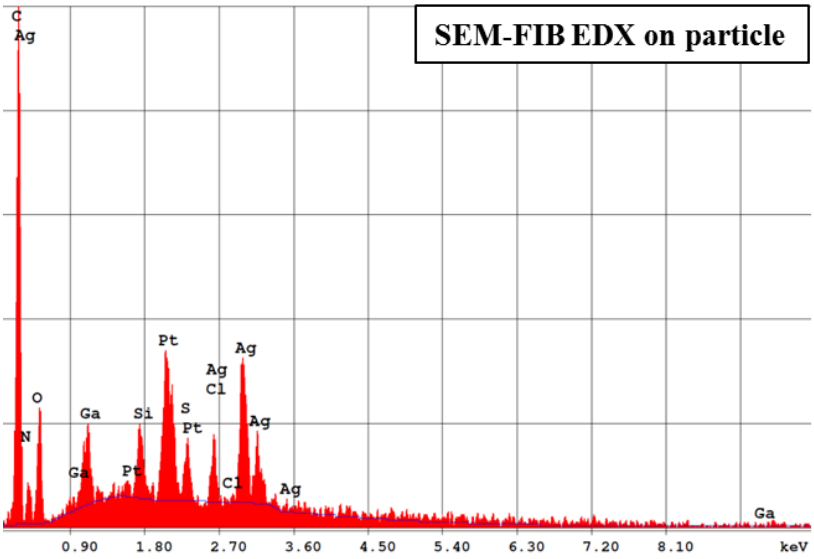

EDX quantification

Element	w/w%	At%
C K	24.90	54.67
N K	6.94	13.08
O K	8.92	14.70
Ga L	4.54	1.72
Si K	2.79	2.62
Pt M	21.23	2.87
S K	2.47	2.03
Cl K	2.83	2.11
Ag L	25.37	6.20
Total	100.00	100.00

Figure 4.5: EDX spectrum and quantitative analysis of the particles forming the fine structured bands.

From the EDX results it is clear that the main material forming the bands consists of a silver species, since all other elements originate either from gelatin (C, O, N, S), from the glass substrate (Si, O, Pt) or from the FIB process (Ga). Interestingly, chlorine was found as well. For this reason the experiment was repeated with a new gelatin solution. In the EDX measurements performed at particles in these samples no chlorine was detected. Therefore it is most likely that chlorine was a contamination in the sample introduced by the used water.

4.3.4.4 Conclusion STEM, SEM, SEM-FIB and EDX measurements

The performed EDX measurements clearly show the elements present in the particles forming the bands. The high values for silver indicate that the main component of the particles is a silver containing species. Since the EDX-technique does not provide any information about the oxidation states of the components in the specimen, no further information can be gained from the measurements. In order to address the oxidation state of the silver component, other analytical techniques such as XPS are needed. However, the SEM-FIB cross section images clearly show how the micro- and nanoparticles form well developed and distinguishable bands inside the gelatin layer and on top of it. If we compare the shape and the size of the particles with the particles forming the core structure in the classical system, we can see that these are almost identical. This is an additional indication that the core-structure found in the classical system originates from the fine structured silver Liesegang system.

4.3.5 Material analysis using X-ray photoelectron spectroscopy

As mentioned before it is not possible to use the EDX measurements to get information about the oxidation state of the material forming the particles and bands. However all investigations performed on this system point to the fact that the particles consist of either pure silver(0), a silver oxide/silver(0) mixture, pure silver(I)oxide or another silver species (without sulfur or nitrogen). In order to get additional data concerning the oxidation state of the silver species in the particles, XPS measurements were performed.

4.3.5.1 Sample preparation

The samples containing a 10 w/w% gelatin (*type 0*) solution, in 0.3 w/w% or 0.6 w/w% ammonia were prepared according to previously described procedures (Section 4.2.1). The hot solution was then spin coated at 500 or 750 rpm onto precut silicon wafers (2.0 x 2.0 x 0.1 cm). After drying (24 h, r.t.) the WETs technique (0.3 M $AgNO_3$ loaded stamp) was used to obtain samples shown in Figure 4.6. The stamping zone was set to one corner of the silicon-wafer to have enough material at the rest of the wafer for background measurements. The precipitation process was stopped after 40 min and the samples were dried at high vacuum ($1.0 \cdot 10^{-3}$ mbar) for 24 h. This step was needed to protect the sample from cracking through fast water loss in the high vacuum chamber of the XPS system. As the special resolution of the measuring point in the used XPS system was 0.3 x 0.3 cm, the measurements were performed within the red window (Figure 4.6). For this reason we did not only obtain information about the particles forming the bands, but also information about the material between the bands and background information from the gelatin film. This fact had to be taken into account when the data were analyzed.

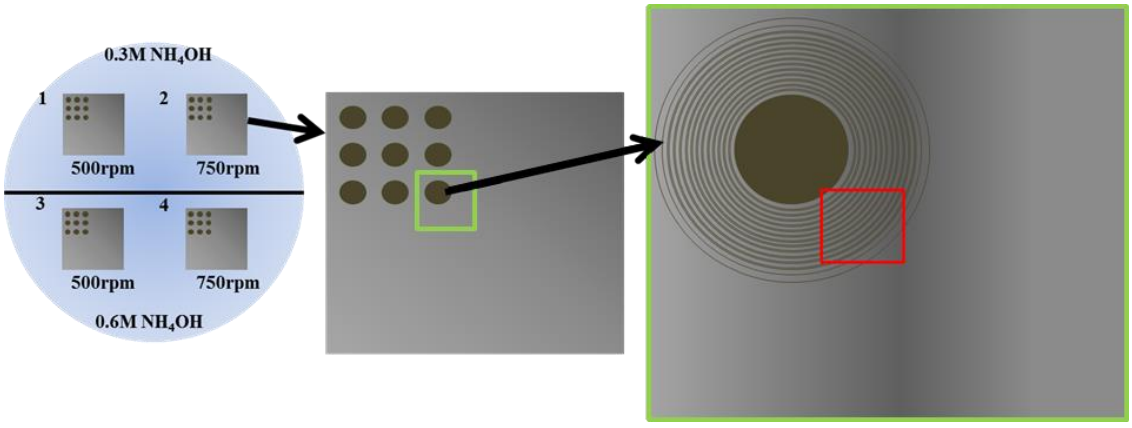

Figure 4.6: Cartoon describing the preparative setup of the samples prepared for XPS measurements. The red window (right) indicates the size of the measured area in XPS.

4.3.5.2 Results and discussion

XPS measurements were performed at the Department of Physics, University of Basel, by *Dr. Laurent Marot*.

As mentioned before, the measured area contains information about the background (gelatin), the fine structured rings/bands, and the material between the bands. Several spectra were measured and compared. In Figure 4.7, one can see an overlaid spectrum of two identical measurements on one sample. If we compare the obtained results with the measurements on another sample and the gelatin background (Figure 4.8), we find the same specific peaks for silver (blue spectrum) which were not present in the background measurement (red spectrum). A table with the corrected values (according to C 1s) for each measurement can be found in the appendix (Appendix B, p. 152). Interestingly, in the samples additional nitrogen (N 1s around 400 eV) and oxygen (O 1s around 530 eV) peaks were also observed which were not present in the gelatin background measurements. The nitrogen peak was only further investigated for gelatin, since there were no reference values available for possible amino acid-silver species. The C 1s reference shift was difficult to determine, because the different amino acids in gelatin produce a very broad carbon shift. Silicon as reference was not useable since we were not able to detect it in all measurements. In addition to that it is also known that the XPS core levels are influenced by the particle size.[200,201] This means that differently sized nanoparticles can lead to very broad peaks. Taking the information from the SEM investigations into account where most of the particles forming the bands are an accumulation of nano particles with different sizes (Image 4.14) and that the size of the particles forming the bands increases along the propagation direction of the precipitation process (Image 4.15), the influence of the particle size is one of the major problems of our XPS investigations. For these reasons the XPS data were difficult to interpret, and the results obtained from this technique can only be used as an additional clue about the chemical composition of the micro- and nanoparticles forming the fine structured bands/rings. However, most of the values fit to pure silver (Ag^0), as well as to silver(I) oxide (Ag_2O). The broader and slightly shifted Ag 3d in the spectra when sample 2 was measured a second time (Figure 4.7), can be explained by the fact that the used X-ray beam in the XPS system was strong enough to change the particle size/shape as was shown in the video of the EDX measurements. However, to make a more precise statement about the chemical nature of the material forming the nanoparticles, additional measurements including PVA or agarose as hydrogels instead of gelatin need to be performed.

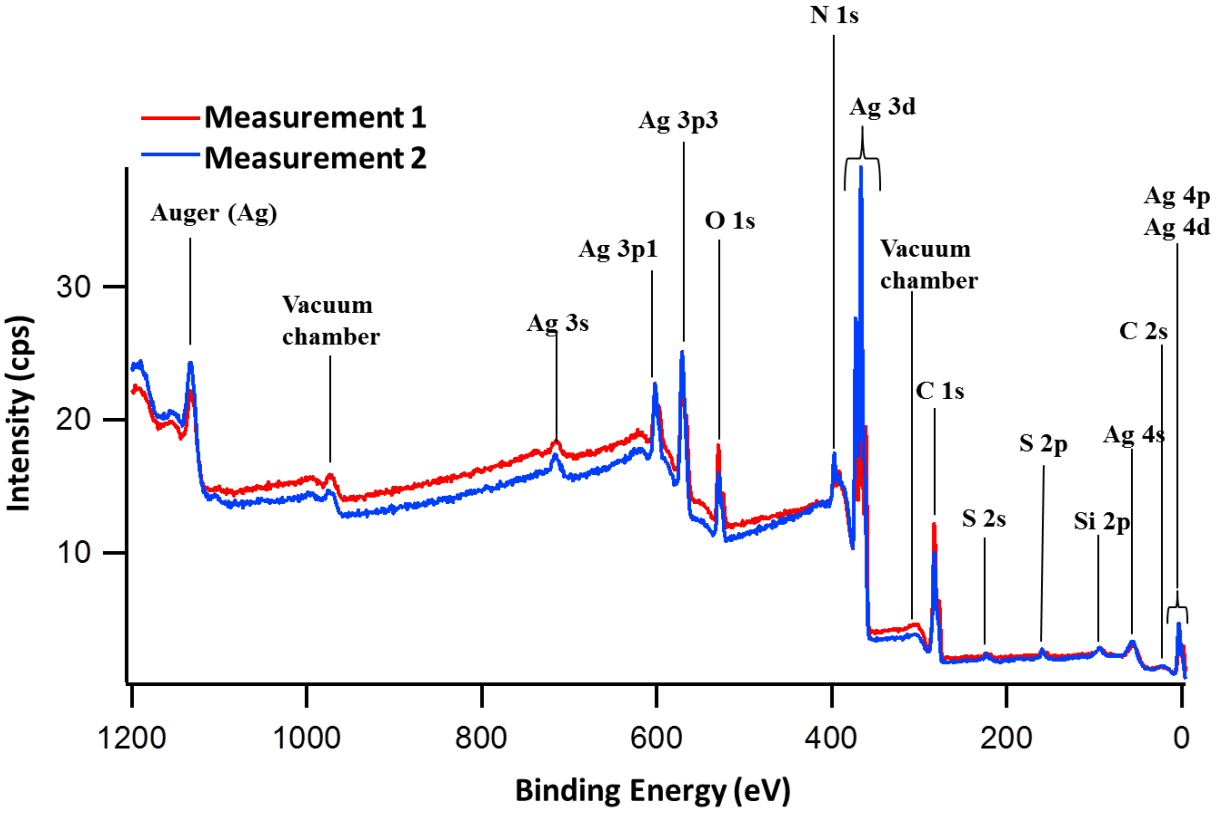

Figure 4.7: Binding energies measured in XPS: Sample 2 (0.6 w/w% NH_4OH, 500 rpm), at 8V Flood gun.

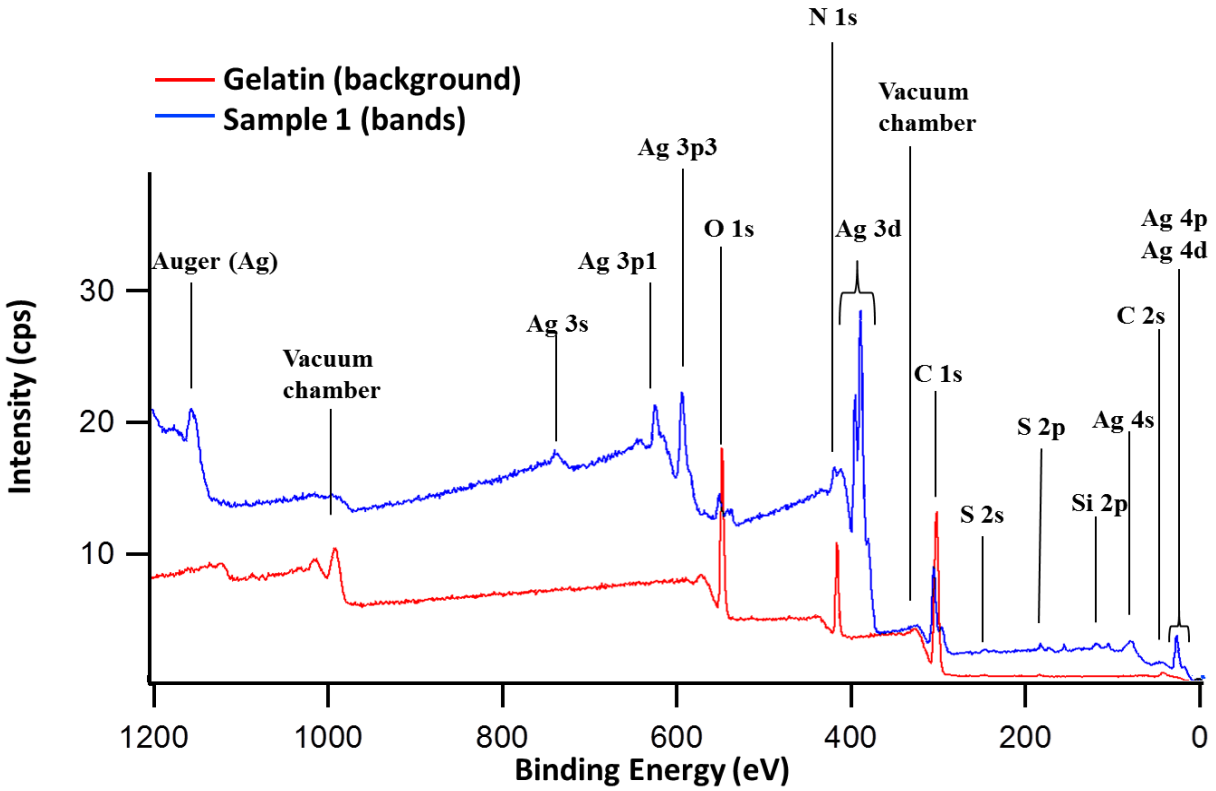

Figure 4.8: Binding energies (eV) measured with XPS. Spectra of a sample containing bands (blue) and the gelatin reference (red).

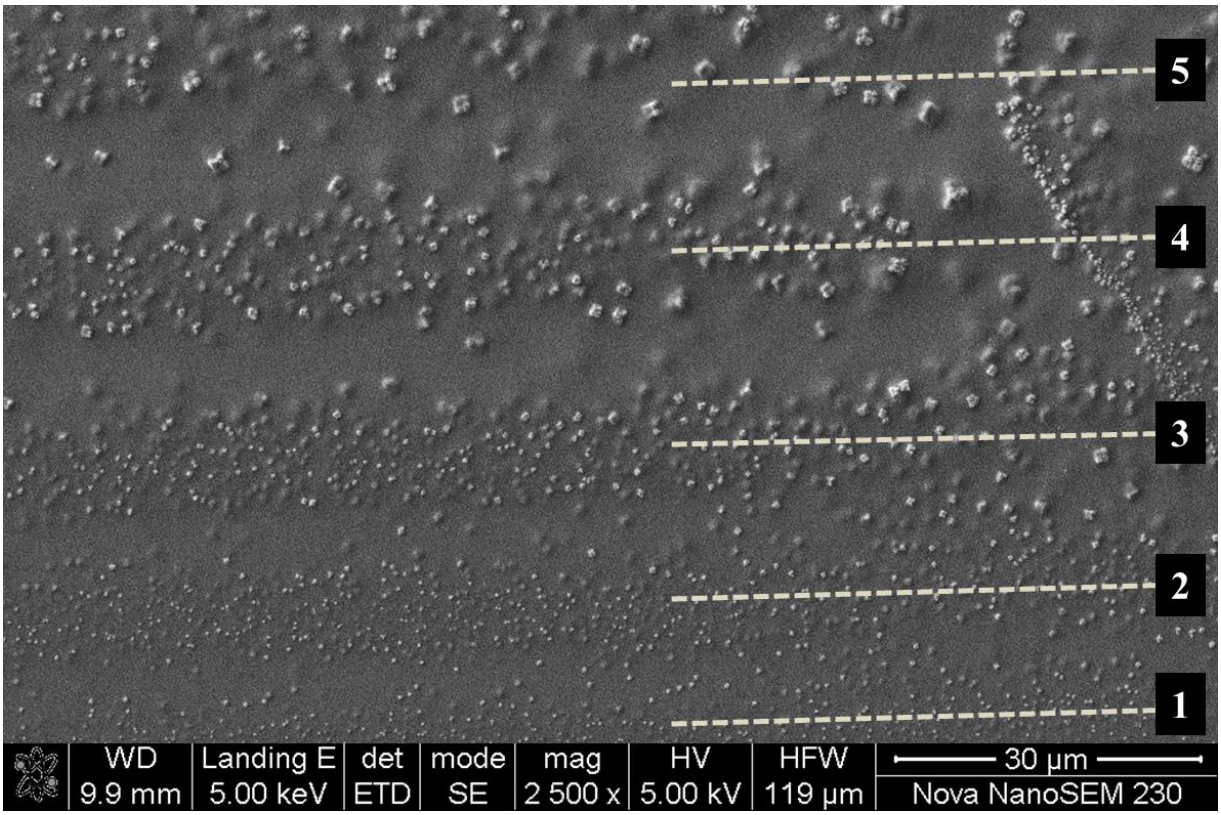

Image 4.15: SEM image showing the difference of the particle size with increasing distance to the stamping center (band 1: close to the center; band 5: close to the end of the precipitation zone).

4.3.6 Silver(I) carbonate control experiments

Since silver(I) oxide was found in the XPS measurements, it was decided to perform material studies concerning some properties of silver(I) oxide. In aqueous solutions silver(I) oxide is in equilibrium with silver hydroxide anions which can react with carbon dioxide (from air) forming silver carbonate (Ag_2CO_3) as pale yellow precipitate. [202–207] In that case the color would fit, because it is not possible to see that color in the gelatin film, since gelatin itself is also pale yellow. From literature it is also known that silver carbonate darkens while irradiated with UV light,[208] which would also fit to the observations from the previous experiments (Section 4.3.1, p. 54), where the bands became visible after illumination. However if this occurs in our system, no band formation should be observed under CO_2 free conditions. Therefore the precipitation experiments (Section 4.2, p. 50) were repeated in a glove box (N_2 atmosphere). Interestingly after removal of the stamps and irradiation with UV light, a black precipitate became visible (in the glove box). For analysis with optical microscopy the sample was removed from the glove box. As the sample shows bands, the theory of a possible silver carbonate reaction can be ruled out.

4.4 Conclusions

If we now combine all observed information from the hydrogel investigations and the material composition studies (STEM; SEM; SEM-FIB; EDX; XPS) with the fact that it is possible to form these fine structured bands only in alkaline hydrogels like gelatin, PVA or agarose, the data can be used to formulate a reasonable chemical process responsible for the precipitation in a Liesegang type manner in hydrogel films.

$$Ag^+(aq) + 2OH^-(aq) \rightleftharpoons [Ag(OH)_2]^-(aq) \quad (11)$$

$$[Ag(OH)_2]^-(aq) + Ag^+(aq) \rightleftharpoons Ag_2O(s) + H_2O \quad (12)$$

$$[Ag(OH)_2]^-(aq) \longrightarrow Ag^0(s) \quad (13)$$

$$2Ag_2O(s) \xrightarrow{\Delta} 2Ag^0(s) + O_2(g) \quad (14)$$

Silver nitrate dissociates in aqueous and hydrogel solutions. Under basic conditions silver hydroxide anions can form (Equation 11), which either react to silver(I) oxide (Equation 12) or are reduced in presence of a reducing agent such as the hydrogel to elemental silver (Ag^0) (Equation 13). However, silver(I) oxide can also be reduced to elemental silver (Ag^0) by thermal treatment (>160°C)[209] or through interaction/reaction with the hydrogel.[208,210–214] From the *in situ* AFM investigation it was found that the precipitation bands are almost colorless (Section 4.3.1, p. 54) before irradiation with light. This would speak against the possibility that the nanoparticles consist of Ag_2O, because it is known that silver oxide has a black color, which turns to brown when it is hydrated ($Ag_2O \cdot xH_2O$).[194,195,208,210,212] All observations like the fact that band formation was observed only in alkaline milieus, or the coloring effect of the bands, which became visible after UV irradiation, or the occurrence of both silver(0) and silver(I) oxide in the XPS measurements, or the band stability found in the *in situ* AFM measurements, would fit to all proposed equilibria (Equations 11-14) if it is assumed that the material forming the particles (5-500 nm diameter) is elemental silver.

There are several possible explanations for the darkening occurring during the illumination with UV light (within 10-30 minutes). One possibility is the formation of a very thin silver(I) oxide layer on top of the silver particles surface, which is a kind of passivation effect comparable to the passivation found in aluminum. Another possibility is the formation of silver(I) sulfide which is a reaction product of atmospheric abundant H_2S with elemental silver.[215] This effect for example causes the darkening of sterling silver over time. Remarkably, in the *in situ* AFM studies no change in the size of the particles as well as in the

spacing, size or height of the bands has been observed. This implies that the possible passivation occurs on a very small scale (0.5-5 nm) on top of the silver particles. More likely the darkening is caused by a purely photographic effect, where Ag^+ ions which are abundant in the hydrogel/bands are reduced while absorbing photoelectrons. From classical silver photography[194,195] it is known that this photoelectron induced reduction takes place at silver nucleation sites are (silver particles in the bands), this would explain why only the bands darken during UV irradiation, while the region between the bands does not change. Concerning the role of the hydrogel, especially for gelatin it is well known that silver nanoparticles can be formed from silver nitrate, where gelatin acts as reducing agent.[214,216] In other words, silver nanoparticles can be formed directly in the hydrogel films out of Ag^+ ions, which also occurs in other hydrogels, e.g. PVA or agarose.[210,213,214,216] But one has to be aware to the fact that silver nanoparticles can be easily oxidized (Equation 13). This will occur to some extent at the surface of the formed silver nano particles, since our system is not closed and air oxygen can react with the particles forming silver(I) oxide.[217–219] This would also explain why both silver(0) and silver(I) oxide was found in the XPS measurements. However, for a more precise model additional spectroscopic measurements are required. But to the best of our knowledge there was no such high resolution method available which could be used to detect the change of the silver oxidation state in the nanoparticle themselves. In our available or used methods there was either a spectral overlay or it was not possible to investigate the samples without a radiation source. Like in case of the silver NEXAFS, where the nitrogen K-edge overlays with the silver $M_{4,5}$-edges, shown in the investigation on the classical Liesegang system (Chapter 3) or in case of the XPS measurements (Section 4.3.5, p. 71), where the resolution was too low to distinguish between the bands and the particle size differs for each band leading to a broadening of the spectral lines, making it difficult to interpret the data. However in all analytical methods (STEM, SEM, FIB, EDX or XPS) except AFM a radiation source was used to investigate the samples. As seen in the video (Section 4.3.4.2, p. 66) irradiation can influence and change the structure of the particles, which would explain some errors in the collected data.

All things considered, this means that a new silver containing fine structured Liesegang-type precipitation system was discovered and all preparative parameters were optimized to obtain high reproducibility. In addition, a chemical model was proposed, which most likely explains the formation and the material composition of the fine structured silver Liesegang precipitation bands.

5. Control and use of the silver Liesegang system

5.1 Introduction

This chapter is about the structural control of fine structured silver systems and their use for possible applications. For a possible application of the silver system, controlled design of the bands, rings and other structures is necessary. Therefore, it is crucial to control the parameters of the precipitation and band forming process. Parameters of interest were the size of the particles forming the bands, the spacing between two bands, the height of the bands, the number of the bands (including the density within a given region), the thickness (FWHH) of the bands, the reproducibility, as well as the removal of the hydrogel without destroying the predefined structures.

5.2 Structural design

From previous investigations on the silver containing Liesegang system (Chapter 4) it was found that samples were most and simply reproducible in gelatin as a hydrogel. For this reason we decided to use this hydrogel for further investigations concerning the structural control/design of the precipitation bands/structures. The simplest ways to control the parameters (e.g. nano-/microparticle size, spacing between two bands, the height of the bands, the number of the bands (including the density within a given region) and the thickness (FWHH) of the bands), of the precipitation bands in the system were found to be the following:

- varying the amount (w/w%) of the gelatin,
- changing the initial pH of the gelatin,
- changing the thickness of the gelatin layer,
- varying the amount of used silver nitrate in the WET stamps.

5.2.1 Sample preparation

5.2.1.1 Gelatin films

A set of 18 different gelatin solutions containing either 3, 5, 7, 9, 10, 11, 13, 15 or 17 w/w% gelatin (*type 0*) were prepared using 0.3 w/w% (0.176 M) and 1.0 w/w% (0.587 M) aqueous ammonia. Each of the solutions was vigorously shaken for 1 minute and heated (65°C) in a pressure stable tube (*BD Falcon*) for 6 hours. During heating, the solutions were shaken every

60 minutes. In the next step, the hot solutions were spin-coated onto glass substrates (3 x 3 x 0.1 cm). For each solution a set of 4 samples at each coating speed (300, 500 and 750 rpm) was prepared, leading to a set of 216 samples.

5.2.1.2 Stamps

The unloaded stamps were prepared according to previously described procedures (Section 2.4.2, p. 29). One set of stamps was loaded (48 h) in 0.01 M $AgNO_3$. Additional 3 sets were either loaded (48 h) in 0.06 M $AgNO_3$, 0.3 M $AgNO_3$ or 0.6 M $AgNO_3$. Higher loadings (>1.0 M) led to a precipitation in the loading solution, whereas lower loadings did not lead to the formation of precipitation bands/rings in gelatin films. The loading was performed in the dark to prevent reduction of silver nitrate. As 864 stamps were needed in total, 240 stamps were prepared for each silver nitrate solution (100 mL).

5.2.1.3 WET stamping

To obtain comparable results, each sample was stamped with 4 different stamps containing different amounts of silver nitrate. One stamp was placed on top of the gelatin film at each corner of the substrate (Figure 5.1). For each spin coating speed 4 samples were prepared this way. For proper statistics, it was ensured that the stamping time was equal for all samples. All stamps were removed after 40 minutes reaction diffusion time.

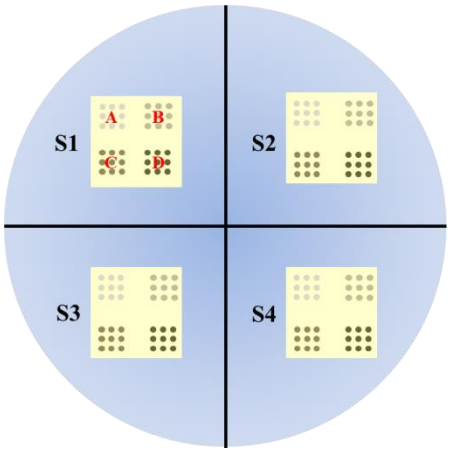

Figure 5.1: Sample preparation: S1-S4 stands for sample 1-4, prepared at one specific spin coating speed. The red letters A-D stand for the used silver nitrate loaded stamps (A: 0.03 M, B: 0.06 M, C: 0.3 M, and D: 0.6 M $AgNO_3$).

5.2.2 Analytics

All samples were analyzed by optical microscopy and laser surface profiling. The optically best samples of each setup (54 samples) were further analyzed by SEM to get precise information about the particle size and the size distribution of the particles according to the location of the bands. Images of the measured samples can be found in the appendix (Appendix B, p. **Fehler! Textmarke nicht definiert.**).

5.2.3 Results and discussion

From the optical analysis of these experiments it is possible to show how the amount of added base (ammonia) and gelatin, the spin coating speed and the amount of silver nitrate in the stamps influence the specific properties of the system. The results shown in the graphs (Figure 5.2-Figure 5.9 except Figure 5.6) are from samples prepared at 300 rpm.

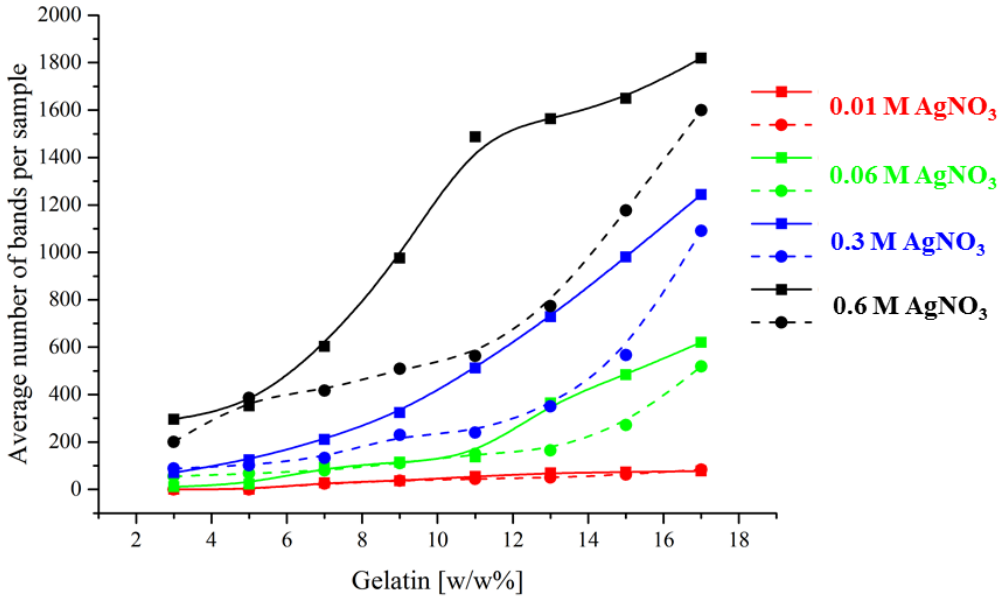

Figure 5.2: Average number of formed bands per sample depending on the amount of gelatin, added base (squares and solid lines: 0.3 w/w% ammonia; circles and dashed line: 1.0 w/w% ammonia) and the silver nitrate concentration (red: 0.01 M. green: 0.06 M. blue: 0.3 M. black: 0.6 M).

Same trends were observed for samples prepared at higher coating speeds. All curve fits were done using the software Origin[220], function "connect lines; B-Spline" where the points are weighted equally in the least squares fit. The elasticity of gelatin is controlled by the amounts of used gelatin and added base. The more base is added the more flexible (more liquid) the gelatin is, resulting in a decreasing number of bands found in the gelatin films (compared to samples with less base) for a given silver nitrate concentration in the stamps. But the more

gelatin is added, the weaker becomes the influence of the base (ammonia), the more dense becomes the gelatin film, resulting in an increasing number of formed bands for a given silver nitrate concentration (Figure 5.2). In the case of some samples, the bands are very dense and they are spread over a range of more than 3000 μm, making it difficult and time consuming to count them manually. For this reason the height, the space between two bands and their density (bands per micron) was measured at 4 different places within one sample (Image 5.1).

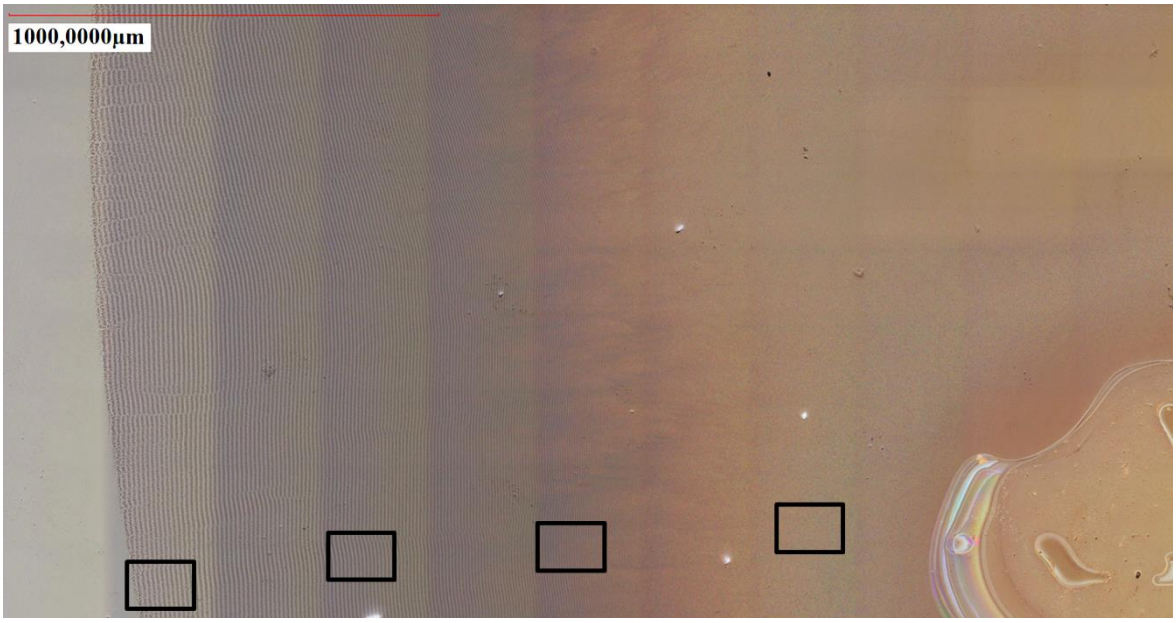

Image 5.1: Optical image showing the measured places (black boxes), used to calculate the average number of bands per sample. First measurements were very close to the stamping zone (right), two were in the middle and one was at the end (left) of the propagation zone.

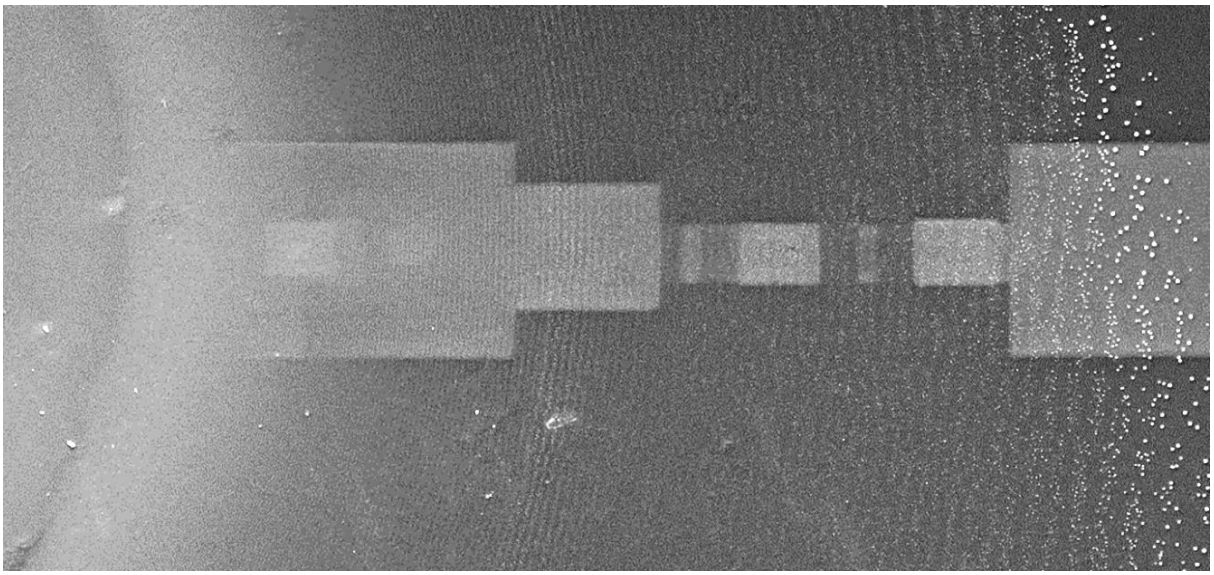

Image 5.2: SEM image showing where SEM measurements were performed (bright quarters). Left part: close to the stamping core, right part: close to the precipitation propagation front.

For some samples the density of the bands was higher than the resolution of the optical microscope. Therefore SEM was used to gain information about the thickness of a band and the space between two adjacent bands, especially for measurements close to the stamping core (Image 5.2). These measurements were used to obtain the average number of bands per micron (Figure 5.3) which was multiplied by the length of the precipitation propagation zone (Figure 5.4) to obtain an average value of bands per sample (Figure 5.2).

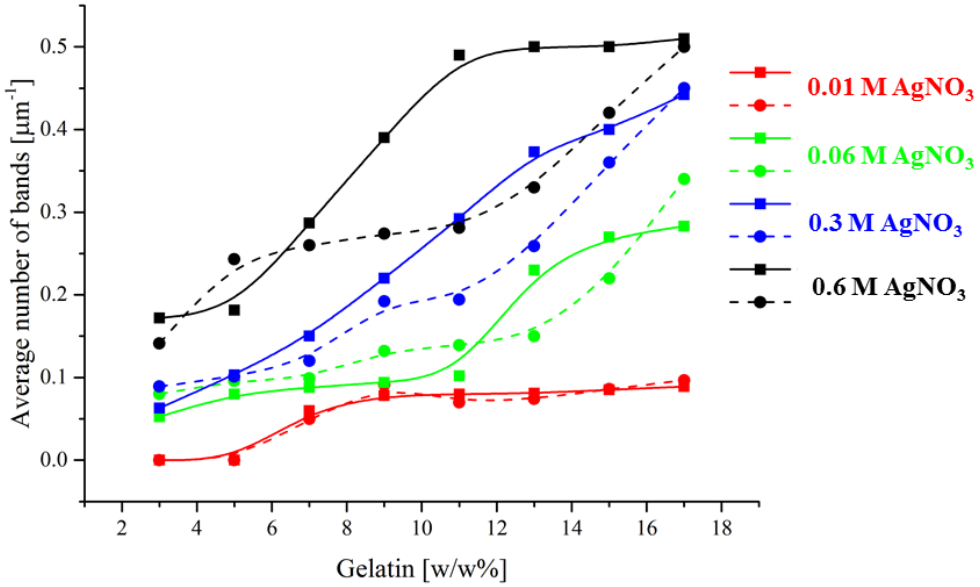

Figure 5.3: Average number of formed bands per micro meter depending on the amount of gelatin, added base (squares and solid lines: 0.3 w/w% ammonia, circles and dashed lines 1.0 w/w% ammonia) and the silver nitrate concentration (red: 0.01 M. green: 0.06 M. blue: 0.3 M. black: 0.6 M).

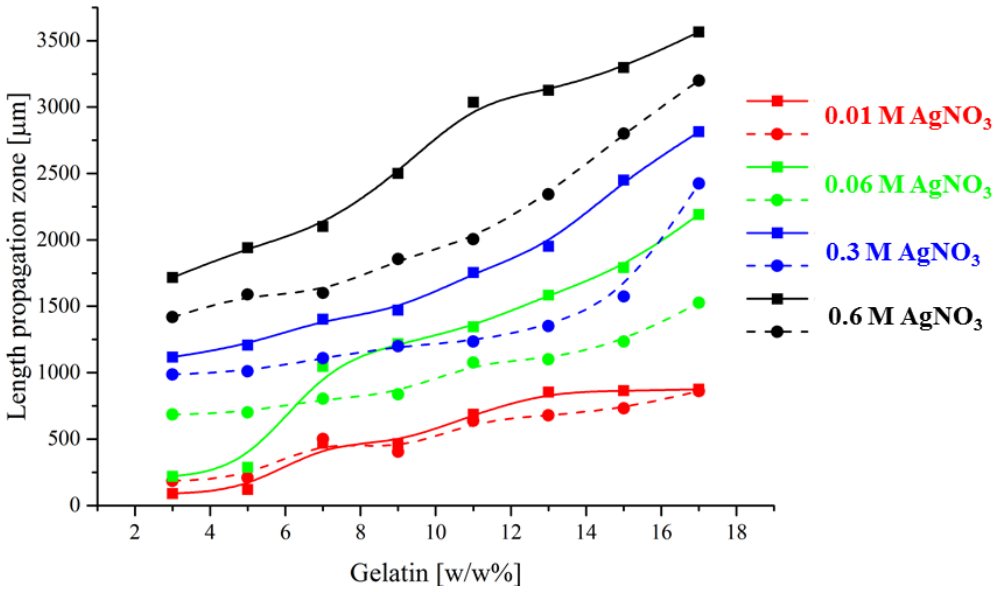

Figure 5.4: Length of the precipitation zone depending on the amount of used gelatin (x-axis), the amount of used ammonia (0.3 w/w% ammonia: square and solid line or 1.0 w/w% ammonia: circle and dashed lines) and the silver nitrate concentration (red: 0.01 M. green: 0.06 M. blue: 0.3 M. black: 0.6 M).

In addition, it was found that a change in the concentrations of the initial parameters influences the density/spacing of the bands. In general, this means that the lower the concentration of the added base, the higher the amount of gelatin and the higher the silver nitrate load in the stamp, the denser the bands that are formed during the precipitation process (Figure 5.5).

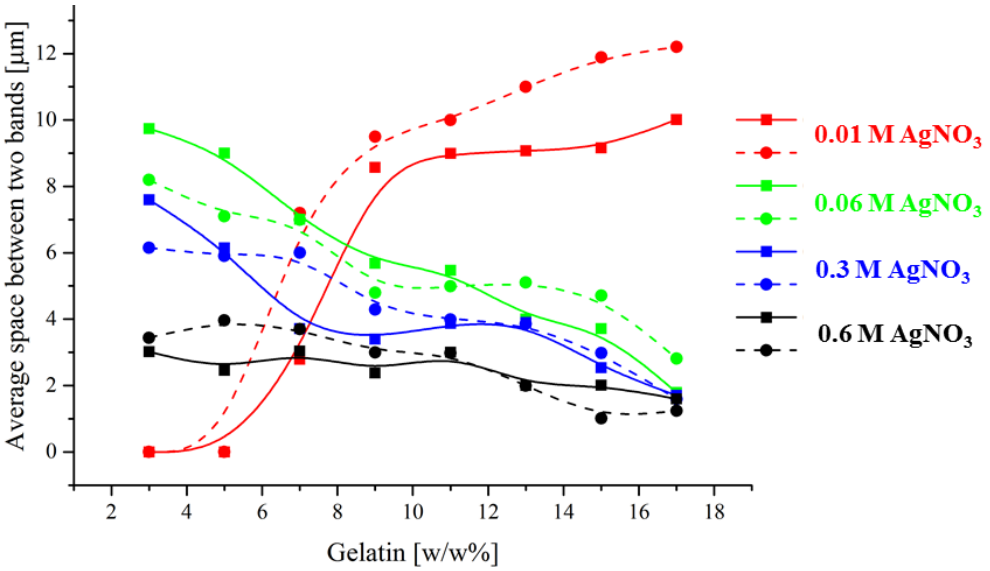

Figure 5.5: Average space between two bands depending on the amount of gelatin, amount of added base (squares and solid lines: 0.3 w/w% ammonia; circles and dashed line: 1.0 w/w% ammonia) and the silver nitrate concentration (red: 0.01 M. green: 0.06 M. blue: 0.3 M. black: 0.6 M).

Samples prepared with a silver nitrate loading <0.06 M show the opposite trend to samples with a higher silver nitrate loading, shown in the graph above (Figure 5.5). It seems that the average space between two bands increases with increasing amount of gelatin. However this is not true because this statistical error arose due to the fact that no bands were observed for low concentration gelatin films (≤7 w/w%) and that the number of formed bands increased with increasing amount of gelatin. Moreover, it is a known [88,90,92,104,146] that the spacing between two bands increases with increasing distance from the stamping center. In case of the samples prepared at <0.06 M $AgNO_3$ the precipitation propagation zone is very small (Figure 5.4). For this reason the increase of the spacing carries much more weight compared to the other samples (≥0.06 M $AgNO_3$), where the distance between the stamping zone and the end of the precipitation zone is much larger. In addition, it was found that the elasticity (defined by the amount of base and the amount of gelatin) of the gelatin hydrogel influences the thickness of the gelatin film at a given spin coating speed. This means that the more elastic the gelatin and/or the higher the coating speed, the thinner the gel films (Figure 5.6).

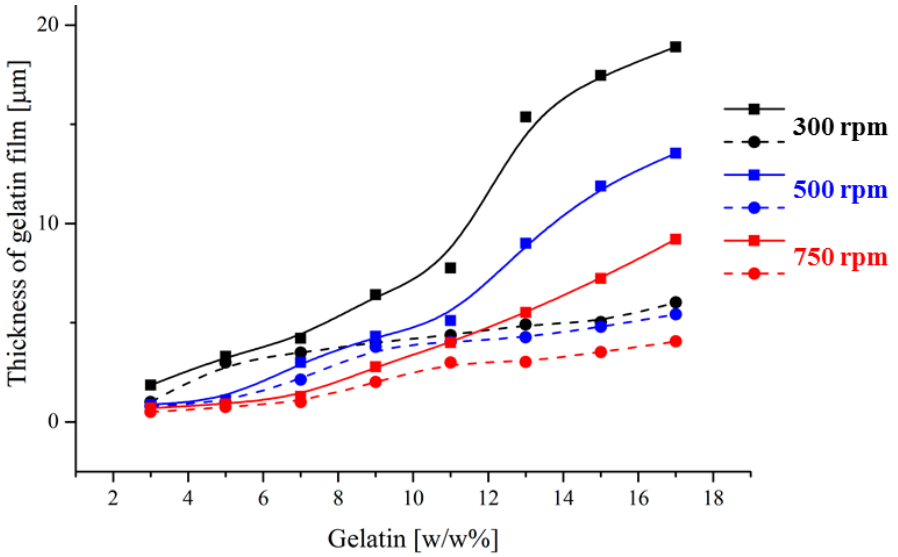

Figure 5.6: Average thickness of the gelatin layer depending on the amount of used gelatin (x-axis), the amount of used ammonia (0.3 w/w% squares and solid lines; 1.0 w/w% circles and dashed lines) and the spin coating speed (black: 300 rpm, blue: 500 rpm and red: 750 rpm).

In order to obtain information about the thickness of the bands formed under predefined conditions the average FWHH of the bands was determined by surface profile analysis (*Keyence VK-200*). The thickness measurements (Figure 5.7) indicate that the thickness (FWHH) of a band can be controlled by changing the amounts of added base, gelatin and silver nitrate.

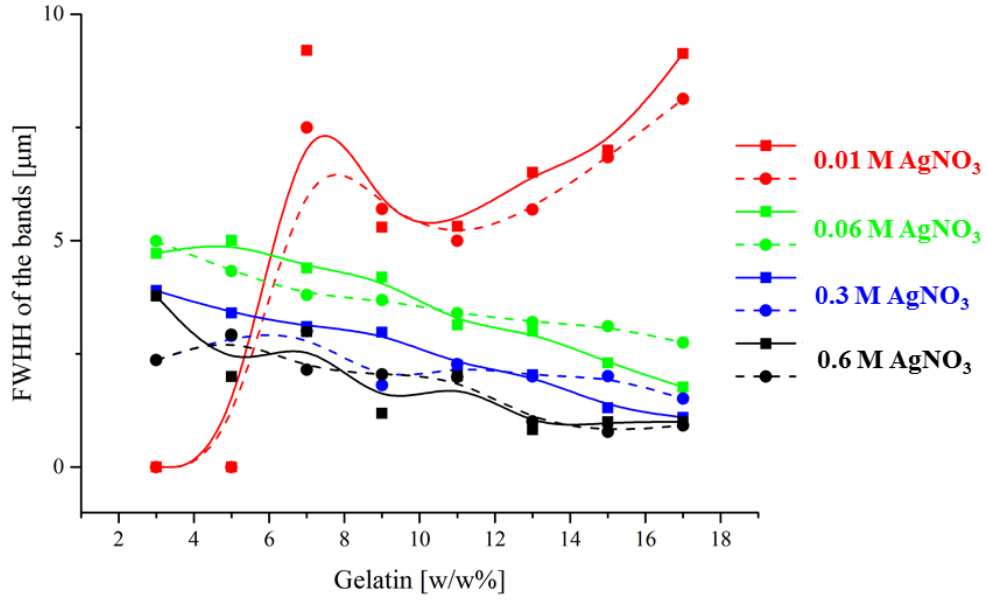

Figure 5.7: Average thickness (FWHH) of the bands depending on the amount of gelatin, ammonia concentration (0.3 w/w% squares and solid lines; 1.0 w/w% circles and dashed lines) and the silver nitrate concentration (red: 0.01 M. green: 0.06 M. blue: 0.3 M. black: 0.6 M).

The higher the initial silver nitrate concentrations in the stamps and the less base there is in the system, the thinner and the denser the bands are at a given gelatin concentration. The shape fit of the red curve (0.01 $AgNO_3$) shows opposite behavior to the other curve fits for higher silver nitrate concentrations. This would lead to the misleading conclusion that the thickness of the bands increases with increasing amount of gelatin. This is not true, since this error is caused by the same effects as the error found for the average space between two bands. From SEM-FIB measurements (Image 4.14) it was found that height of the bands measured in the surface profiles only shows the tip of the iceberg, because the main part is hidden in the gelatin film. If the gelatin is removed (cf. annealing experiments, Section 5.3, p. 87), the height of the hidden bands in the gelatin film is added to the height of the bands found in the surface profile measurements. This means the thicker the gelatin layer, the more silver particles are necessary to form the bands and the higher are the later bands in the sintered samples. However, as mentioned before, the spin coating speed can be used to control the thickness of the gelatin layer. Combined with the observations from SEM-FIB, the coating speed and the amount of added gelatin and base can be used to fine tune the overall height of the bands (Figure 5.8). Furthermore one can see that the amount of added silver nitrate has only a minor influence on the band height.

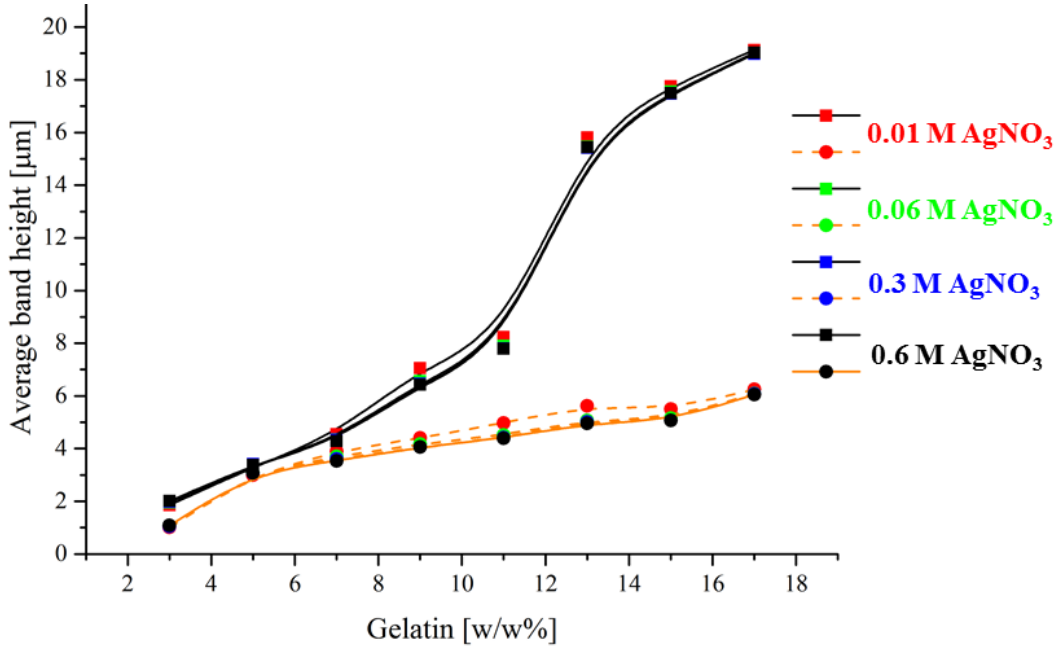

Figure 5.8: Average band height (thickness gelatin layer and height from surface profile measurements) depending on the amount of gelatin, added base (black solid line: 0.3 w/w%; orange dashed line: 1.0 w/w%) and the silver nitrate concentration (red: 0.01 M. green: 0.06 M. blue: 0.3 M. black: 0.6 M).

The coating speed influences not only the height of the gelatin films or the height of the formed bands but also the propagation speed of the precipitation front and therefore, the

amount of bands formed in a specific time. The thinner the gelatin layer, the slower the propagation speed of the precipitation front and the lower the number of formed bands. The same is true for the amount of gelatin; the less gelatin there is in the system, the thinner the layers and the fewer bands can be formed (Figure 5.9). For this reason the variation of the coating speed can be used as additional factor for the structural control and design of the precipitation bands.

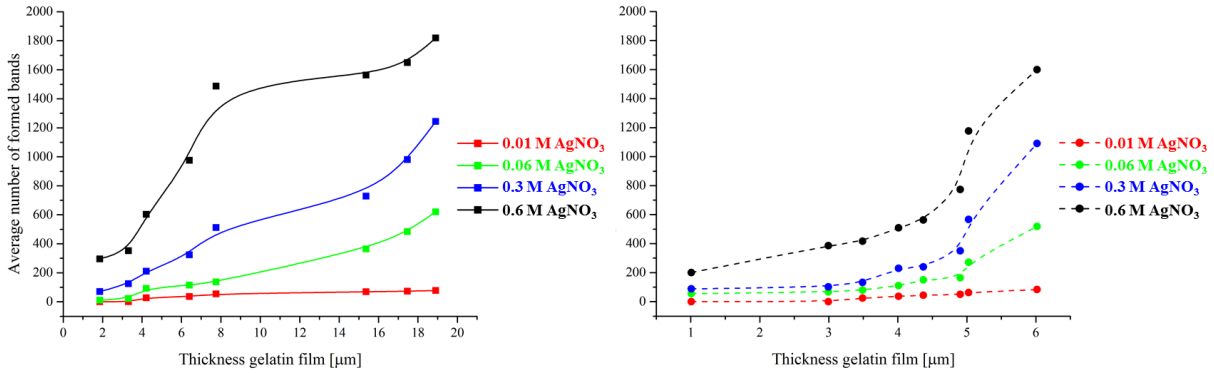

Figure 5.9: Average number of formed bands depending on the thickness of the gelatin layer, the concentration of silver nitrate in the stamps (red: 0.01 M. green: 0.06 M. blue: 0.3 M. black: 0.6 M).) and the amount of base (ammonia) 0.3 w/w% left and 1.0 w/w% right.

As mentioned in Section 4.3.5, it was found that the size of the particles forming the bands increases with increasing distance from the stamping center. This behavior is similar to the particle size increase found in the case of the classical system.[90] In addition, it was also found that this effect directly correlates with the increasing space between two bands which also increases with increasing distance from the stamping center (Image 5.3 and Image 5.4).

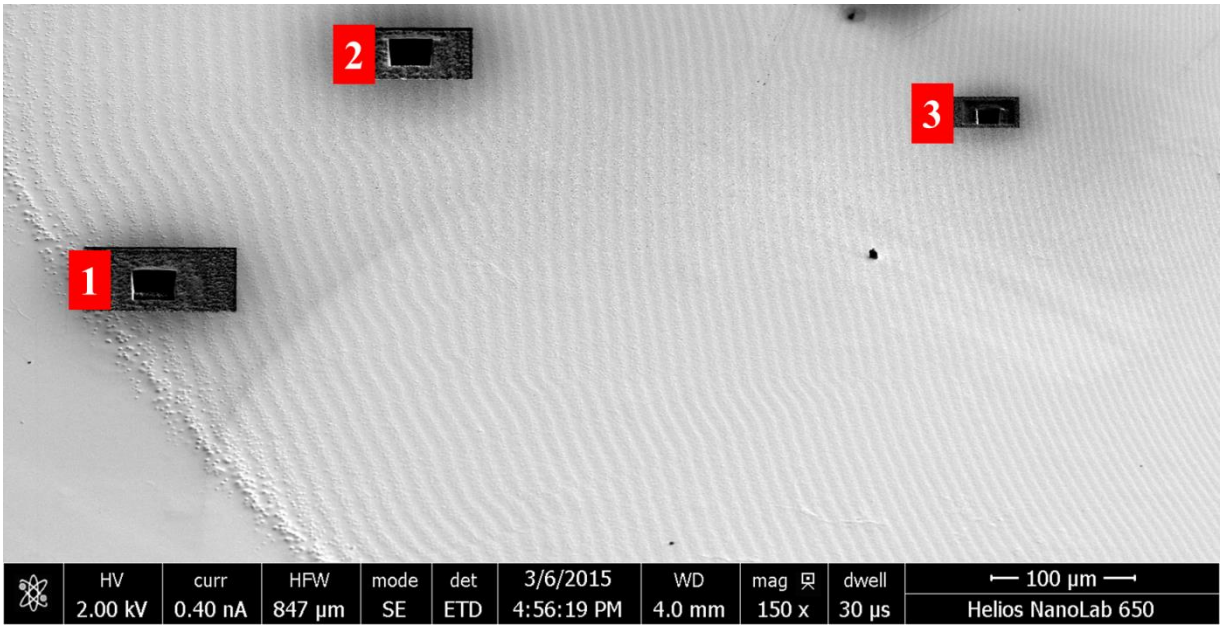

Image 5.3: SEM image showing the places for cross sections. 1: close to the precipitation front, 2: in the middle of the precipitation zone and 3: close to the stamping center.

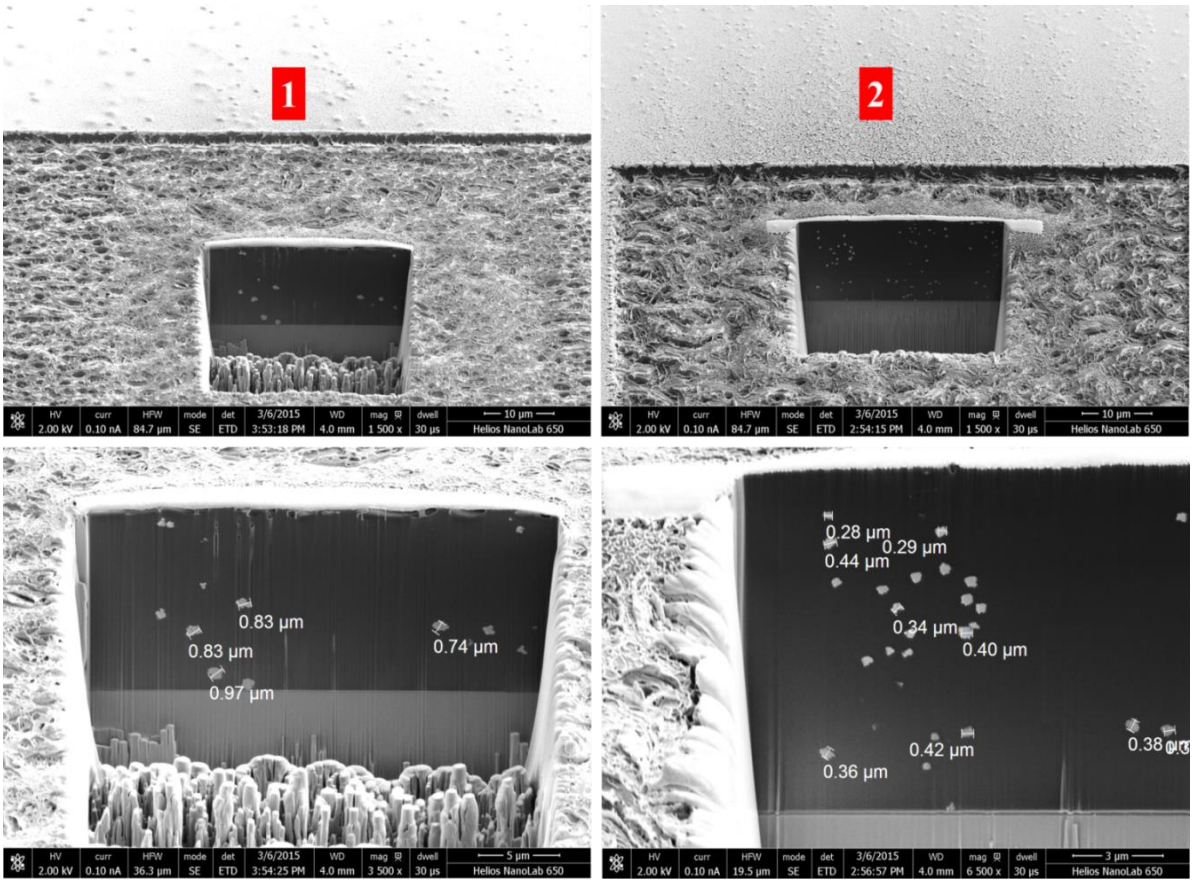

Image 5.4: SEM-FIB cross sections for particle size analysis. 1: At the end of the precipitation zone. 2: Middle of precipitation zone. Numbering according to the SEM-FIB cross sections (Image 5.3).

In the shown system (15 w/w% gelatin, 0.3 w/w% NH_4OH, 300 rpm, 0.01 M $AgNO_3$) one can clearly see how the particle size, the thickness (FWHH) and the space between the bands directly correlate with the distance from the stamping center. Largest particles (≥70 nm) were found close to the end of the precipitation zone (**1**), medium sized particles (≥40 nm) in the middle (**2**) and smallest particles (≥10 nm) were found very close to the stamping area (image not shown). However, it has to be mentioned that this drastic increase is only found in samples prepared with $AgNO_3$ (≤0.01 M). With increasing amount of silver nitrate this effect is decreasing.

5.2.4 Conclusion

By changing several initial parameters in the system, i.e. the concentration of the base, the hydrogel (gelatin), and the outer electrolyte (silver nitrate load in the stamps), and the thickness of the hydrogel film, we are able to produce bands with predefined structural properties.

5.3 Removal of the gelatin

For possible applications of the fine structured silver containing bands it is crucial to remove the gelatin. For example, during photoelectrochemical treatment gelatin would dissolve in the electrolyte and as a consequence, the bands would be dissolved as well. Another critical point is to be able to remove the gelatin without destroying the fine structured precipitation bands. In Section 4.4, it was suggested that the particles forming the bands consist most likely of elemental silver and small amounts of silver(I) oxide, which decomposes by thermal treatment (>160°C).[221–224] For these reasons it was decided to investigate the removal of gelatin and the decomposition of the silver-containing bands by thermal treatment.

5.3.1 TGA analysis

Thermogravimetric analysis was needed to get precise data about the decomposition point of gelatin. For this reason three different samples were tested (Figure 5.10): **Sample 1**: dry gelatin granular (*type 0*). **Sample 2**: dried gelatin, peeled off from a glass substrate (prepared equally to sample 3). **Sample 3**: 10 w/w% gelatin (*type 0*) in ammonia (0.3 w/w%), heated at 65°C for 4 h, and cooling at ambient temperature overnight.

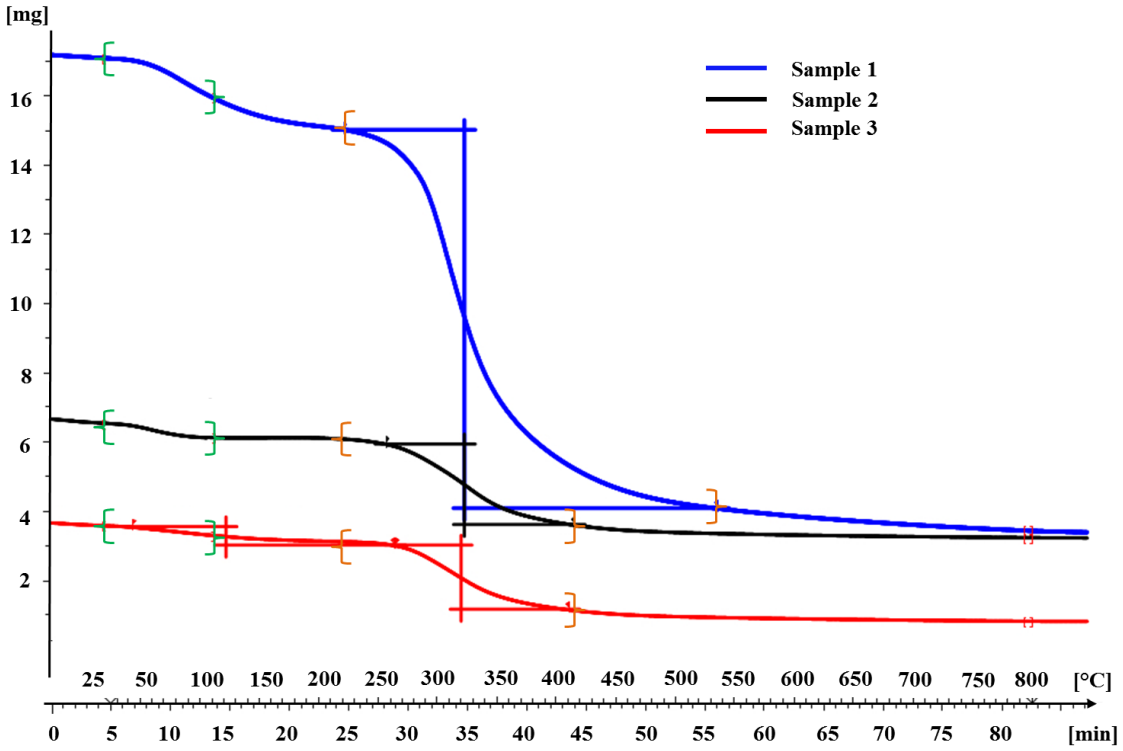

Figure 5.10: Thermogravimetic analysis of gelatin (type 0): Water loss between 50-115°C (green brackets). Decomposition between 220-400°C (orange brackets), starting decomposition at 220-230°C and finished decomposition between 410°C (sample 2+3) up to 520°C (sample 1).

From thermogravimetric analysis it was shown that gelatin decomposes between 220-410°C when only small amounts of gelatin are present as in samples 2 and 3. If higher amounts of gelatin are present (e.g. sample 1), higher temperatures (up to 520°C) are needed to facilitate full decomposition of the gelatin. This has to be taken into account for the thicknesses of the gelatin films. The thicker the gelatin film, the more heat is needed.

5.3.2 Sintering process

5.3.2.1 General and sample preparation

For annealing/sintering a muffle furnace (*Nabertherm*) was used. Each sample was treated separately to avoid contamination or sample loss due to possible problems during the heating process.

A 10 w/w% gelatin solution was prepared by mixing 1.0 g gelatin (*type 0*) with 9.0 g of 0.3 w/w% ammonia (0.176 M). The freshly prepared mixture was shaken vigorously and heated for 6 hours at 65°C. During the heating process the solution was shaken several times. After spin coating (300 rpm, 1 min) the hot solution onto small glass and FTO-glass substrates (1.0 x 1.0 x 0.1 cm) the samples were allowed to dry at ambient temperature overnight. For WETs, a standard (3 x 3 pins) agarose stamp loaded in 0.3 M $AgNO_3$ (48 h) was used. After 40 minutes the stamps were removed and the samples were allowed to dry for 2 hours, before they were treated with UV (256 nm) light for 40 minutes. All samples were further analyzed by optical microscopy, in order to see if and how the temperature/the annealing process influences the shape of the fine structured Liesegang bands.

5.3.2.1.1 Setup 1

In the first experiment the annealing/sintering process was started at room temperature (22°C) and the furnace was continuously heated up to 440 °C within 3 hours. After an additional 2 hours at 440°C, the sample was removed from the furnace. Unfortunately the sample was completely black and the remaining material vanished after treating the sample with a stream of nitrogen (0.05 bar). This was repeated for another 2 samples.

5.3.2.1.2 Setup 2

Since a continuous increase of the temperature up to a desired value destroys the gelatin layer as well as the precipitation bands, a stepwise heating procedure was tested, where the furnace was preheated to a desired temperature. The sample was then annealed/sintered at that temperature for a certain time. As mentioned before, silver(I) oxide starts to decompose at 160°C and gelatin at around 220°C. For these reasons the stepwise sintering process was started at 200°C. The samples were left in the furnace for 3 hours or more. The used sintering times and temperatures can be found in *Table 5.1*. For proper statistics the sintering process was repeated three times for each temperature.

Table 5.1: Sintering temperature and time for the samples shown in Image 5.5.

Sample	1	2	3	4	5	6	7	8	9	10	11	12	13	14	15	16	17	18
Temperature [°C]	200	220	240	240	260	280	300	300	320	340	360	360	360	380	380	400	420	420
Time [h]	3	3	3	o/n	3	3	3	o/n	3	3	o/n	6	3	3	o/n	3	3	o/n

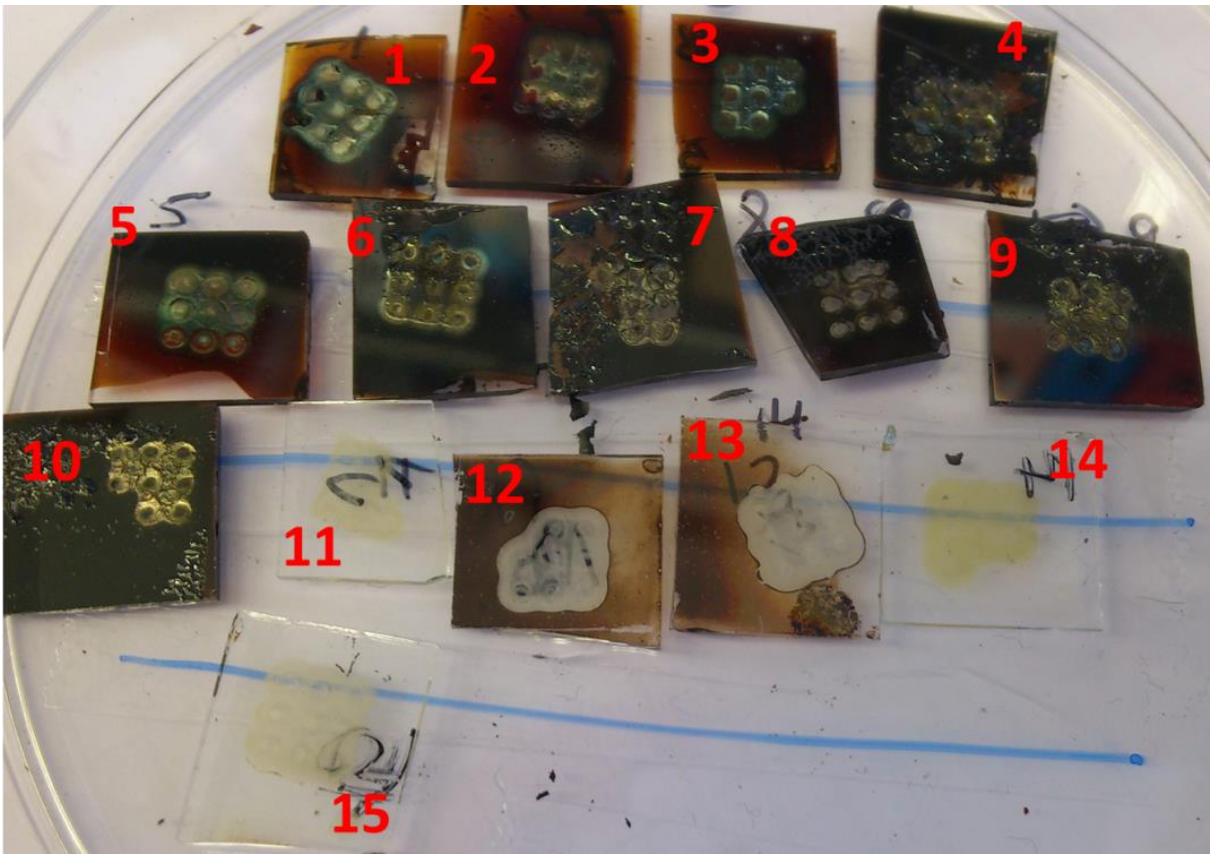

Image 5.5: Optical image of sintered samples. Sintering parameters can be found in Table 5.1.

After sintering (200-340°C), the samples 1-10 were analyzed by optical microscopy. Samples (11-18) sintered at higher temperatures (≥360°C) were also further investigated by SEM, SEM-FIB and EDX.

5.3.2.2 Results and discussion

Proper gelatin removal was observed for sintering temperatures starting at 360°C. For this temperature a sintering time of 12 h (overnight) was needed for full gelatin removal. For higher temperatures (≥380°C) a full removal of gelatin without destruction of the fine structures (sample 11) was observed after 3 h (Image 5.6).

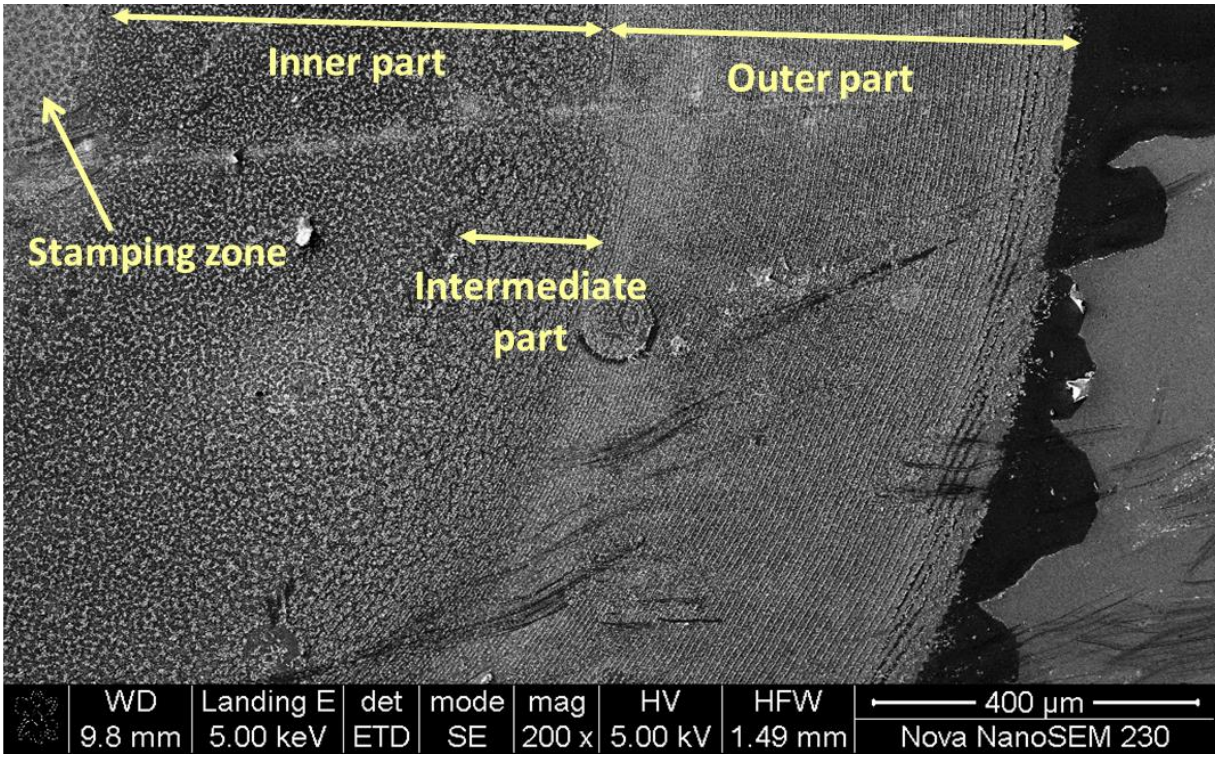

Image 5.6: SEM image of sample 11, sintered at 360°C for 12 hours with indicated delimitation of areas.

However, the fine structures were only stable when the spacing between the bands was larger than 7 µm (Image 5.7). For bands which were denser, as in the case of the intermediate (Image 5.8) or inner part (Image 5.9), the fine structured bands disappeared and equally dispersed nanoparticles were observed.

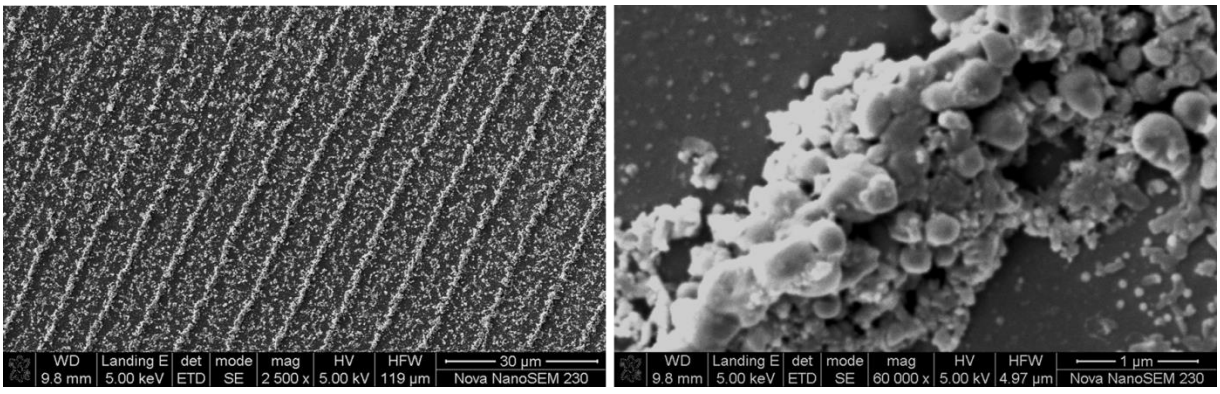

Image 5.7: Zoomed SEM image of the outer part shown in the SEM Image 5.6. Overview image of the sintered bands (left), high resolution image on top of a band (right).

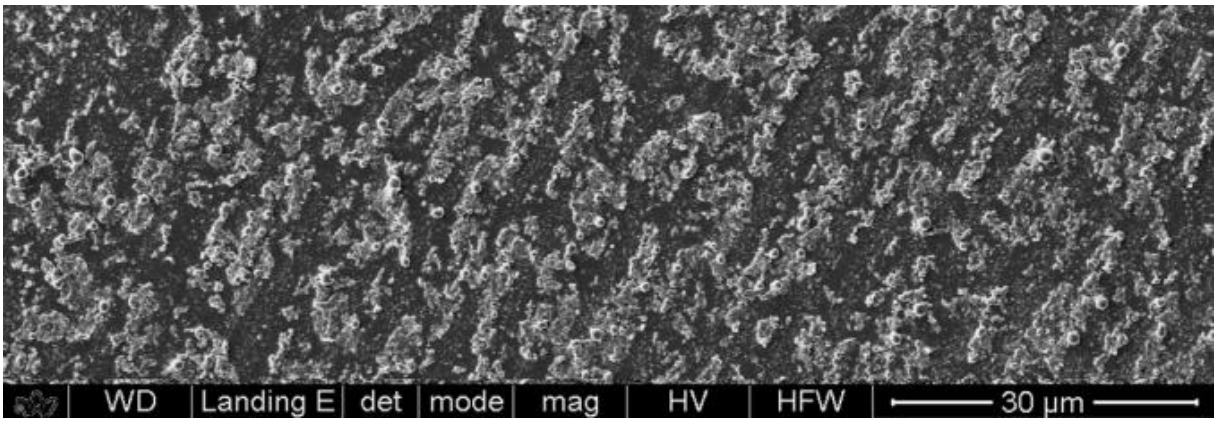

Image 5.8: Zoomed SEM image of the intermediate part shown Image 5.6.

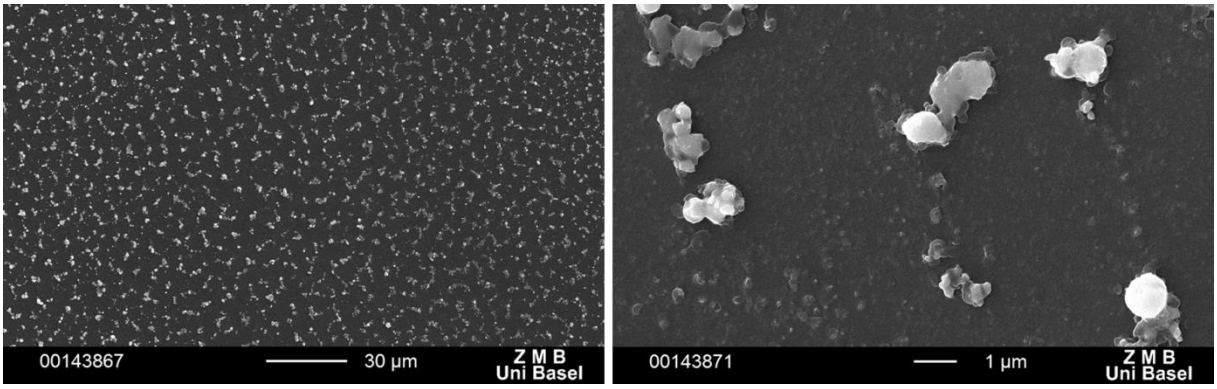

Image 5.9: Zoomed SEM image of the inner part shown in the SEM (Image 5.6). Overview (left) and high resolution image (right).

On some of the prepared samples the fine structured bands disappeared completely and a new self-organized structure (Image 5.10) was observed. This can be explained by the decomposition of gelatin. Especially for thicker gelatin films (1-2 mm) the gelatin sometimes bubbles up during the sintering process, leading to a rearrangement of the nanoparticles.

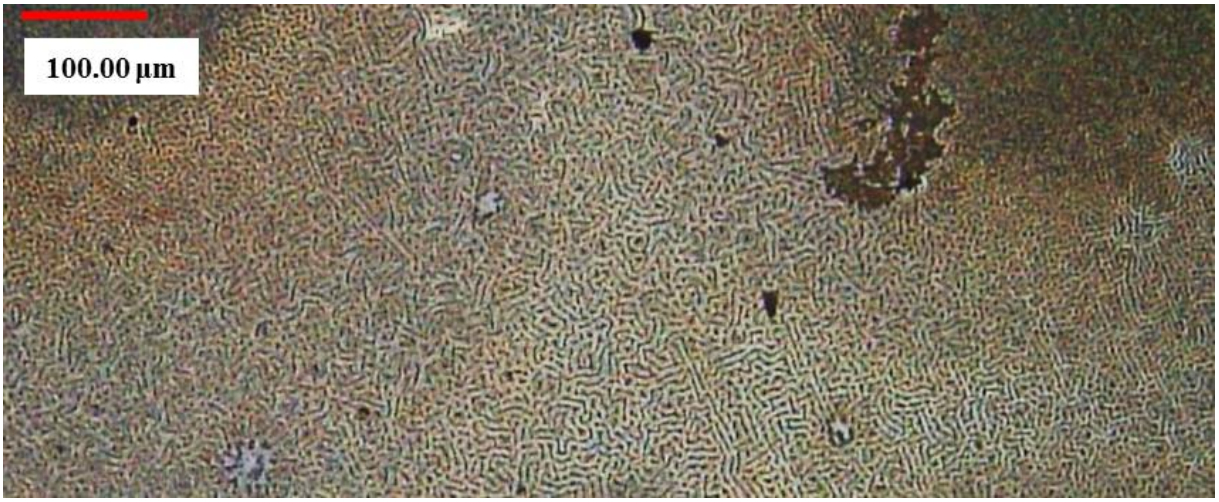

Image 5.10: Optical image of a sample also sintered at 360°C for 12 h, where rearrangement was observed.

For the properly sintered samples, SEM-FIB (Image 5.11) was used to map the silver particles on top of the substrate (FTO-glass). The particles forming the bands are close to each other within the bands but well separated between the bands. In addition, one can see how close the particles are to the FTO surface and how they bind to this. The binding of the particles to FTO is likely to be caused by small molten silver particles (Image 5.11 bottom).

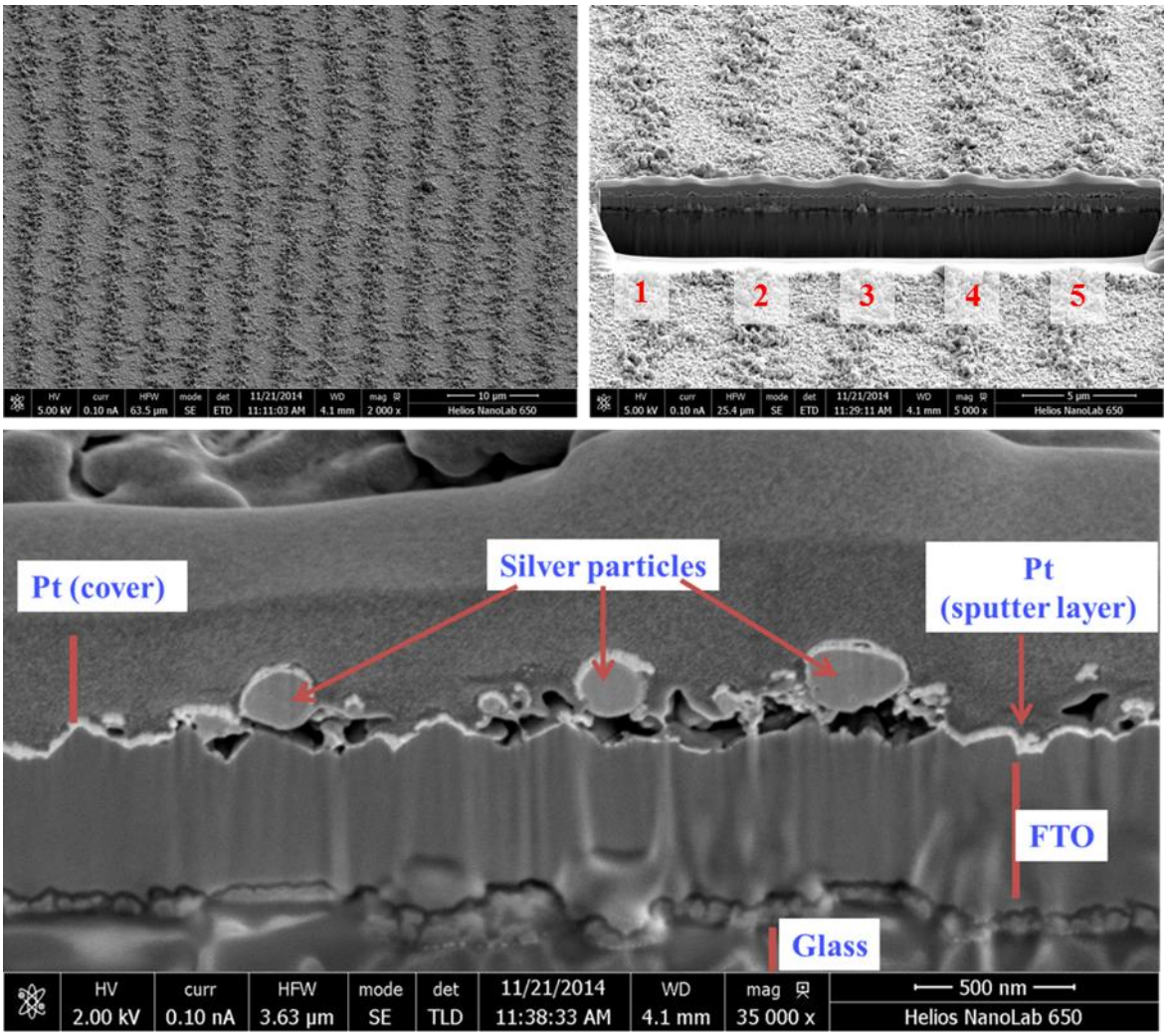

Image 5.11: FIB image: Top left image (before), top right image (after) FIB cross section through five sintered bands. Bottom image: high resolution SEM image of the 4th band. Labels indicate the different materials found in the cut.

5.3.2.3 Conclusion

The annealing/sintering experiments showed how simply the gelatin can be removed from temperature stable substrates (e.g. glass, FTO-glass) without destroying the structures. In addition, full conversion of the nanoparticles to elemental silver as side benefit has been observed. This observation is an additional proof for the proposed chemical model, describing the origin of the material forming the fine structured silver bands (Section 4.4, p. 75).

Another benefit was that the sintering led to the fixation of the nanoparticles/bands on top of the substrates, which increases the number of possible applications. The only two disadvantages of the sintering process were the problems with the band stability if the space between two bands was less than 7 µm, and the formation of dispersed particles between two bands. However, the precise silver bands and the additional inter-band particles can be used to increase the active surface area of hematite in PEC photoanodes (cf. Section 5.4.3). In summary this means that the positive aspects of the sintered silver system dominate over negative aspects.

5.4 Investigated Applications

5.4.1 Application as scattering/light absorbing layers

The light scattering and/or light absorbing properties of the fine structured silver Liesegang bands were investigated using a water soluble iridium(III) coordination compound in gelatin. The used iridium complex (Figure 5.11) was prepared in our group by *Dr. Gabriel Schneider* for applications in light-emitting electrochemical cells (LECs).

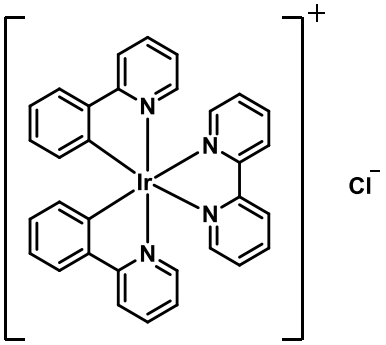

Figure 5.11: Iridium(III) coordination compound GES-165.

5.4.1.1 Sample preparation

A 10 w/w% gelatin solution (*type 0*) in ammonia (0.05 w/w%) was prepared according to previous protocols (Section 4.2.1). The iridium coordination compound (0.005 M) was added to the hot (65°C) solution and the mixture was shaken vigorously. After additional heating for 1 h (65°C) the solution (300 µL) was spin coated (1 min at 300 rpm) onto standard glass slides (3 x 3 x 0.1 cm). After drying the samples overnight at room temperature, a 0.3 M $AgNO_3$ loaded (48 h) agarose stamp (3 x 3 pins) was used for WETs.

After the reaction diffusion process was stopped (40 min) the sample was irradiated with UV light and investigated using the laser microscope.

5.4.1.2 Results and discussion

Silver bands/rings formed in the gelatin-iridium coordination compound mixture. Interestingly the sample shows lighting properties during irradiation with the laser (408 nm) from the laser microscope. However if the sample is moved and the laser beam is directed onto the silver bands the lighting of the compound stops (Figure 5.15). This implies a possible light absorbing effect caused by the silver bands.

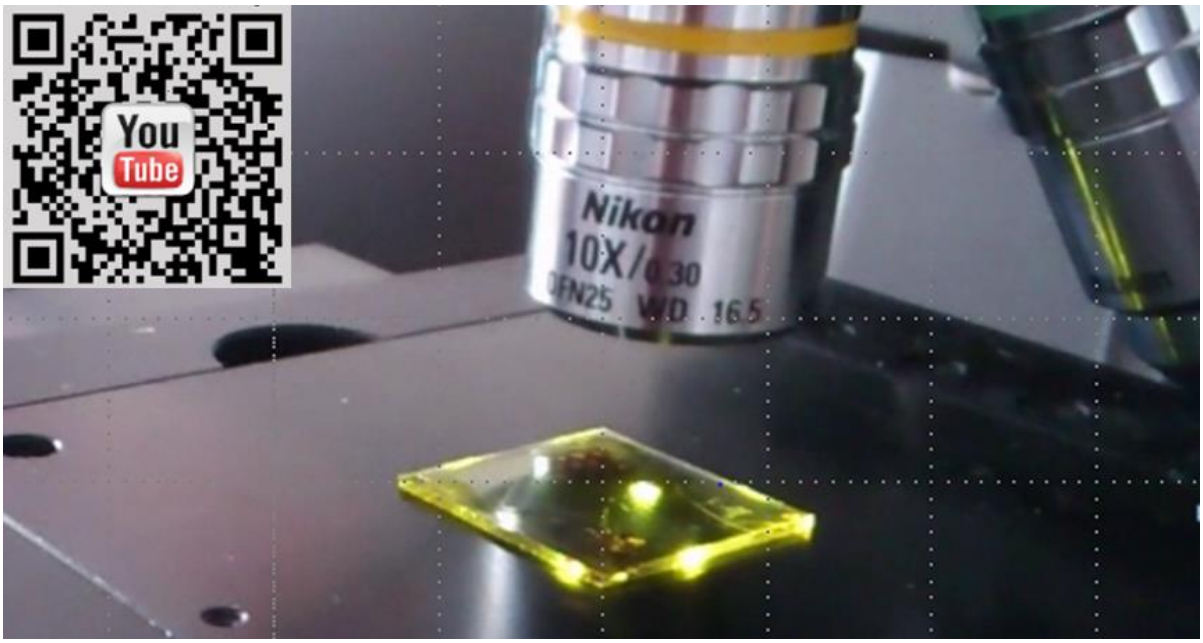

Image 5.12: Optical image showing the lighting of the iridium compound in the gelatin film when irradiated with the laser (408 nm) and the light absorbtion of the fine structured silver bands. The QR code (top left) is linked to *www.youtube.com/watch?v=q7xZaINLafM*.

5.4.1.3 Conclusion

By implementation of the silver rings onto a light emitting iridium coordination compound it was shown how strong the silver structure absorbs the light from the laser beam. This observation can be used to tune other systems, e.g. hematite containing photo anodes.

5.4.2 Applications as mesoscale grids, meshes or sieves

The density of the bands, the material composition and the possibility to remove gelatin by annealing/sintering open possible applications of the silver Liesegang system as mesoscale grids, meshes or sieves. To observe grid-like structures, special sample preparation was needed. From the structural design experiments (Section 5.2), it was shown how it is possible to control parameters, such as spacing, height and the FWHH of the bands in the silver Liesegang system. This knowledge is necessary to generate grid-like structures with precise sizes. The following setup was used as a proof-of-principle. This should also work for other Liesegang systems.

5.4.2.1 Stamp preparation

For the preparation of grid like structures, the shape of the stamp had to change to observe more parallel bands instead of ring like bands. From the literature[87,91,125] it is known that the bands adopt the predefined shape of the stamps. For this reason rectangular (cuboid) agarose stamps were prepared (3 x 0.2 x 0.3 cm). The agarose solution was prepared in the same way as for all the other stamps (Section 2.4.2, p. 29). However, for this type of stamps no predefined mask was needed. After pouring the hot agarose (6 w/w%) solution into a petri dish, the gel was allowed to cool to ambient temperature before it was cut into rectangular solid forms. 40 agarose cuboids were then loaded in 0.3 M $AgNO_3$ (30 mL) for at least 24 h.

5.4.2.2 Sample preparation

In the first step a 10 w/w% gelatin solution (*type 0*) was prepared in 0.3 w/w% ammonia (0.176 M). The following heating, spin coating, drying, WETs (Figure 5.12 A, B) and UV treatment was performed according to previously described procedures (Section 5.2), to obtain a set of 10 samples (Figure 5.12 C). After analyzing the samples by optical microscopy, a second gelatin layer was spin coated (400 rpm) on top (Figure 5.12 D). The used gelatin had a temperature of only 35°C, to prevent the first layer from dissolution. The higher coating speed was needed to compensate the higher viscosity due to the lower temperature. After drying the samples overnight the WETs technique (Figure 5.12 E) was used to prepare a second band on top of the bands in the first layer.

In the final step the stamps were removed (Figure 5.12 F), the samples were irradiated with UV-light (256 nm) and analyzed by optical microscopy.

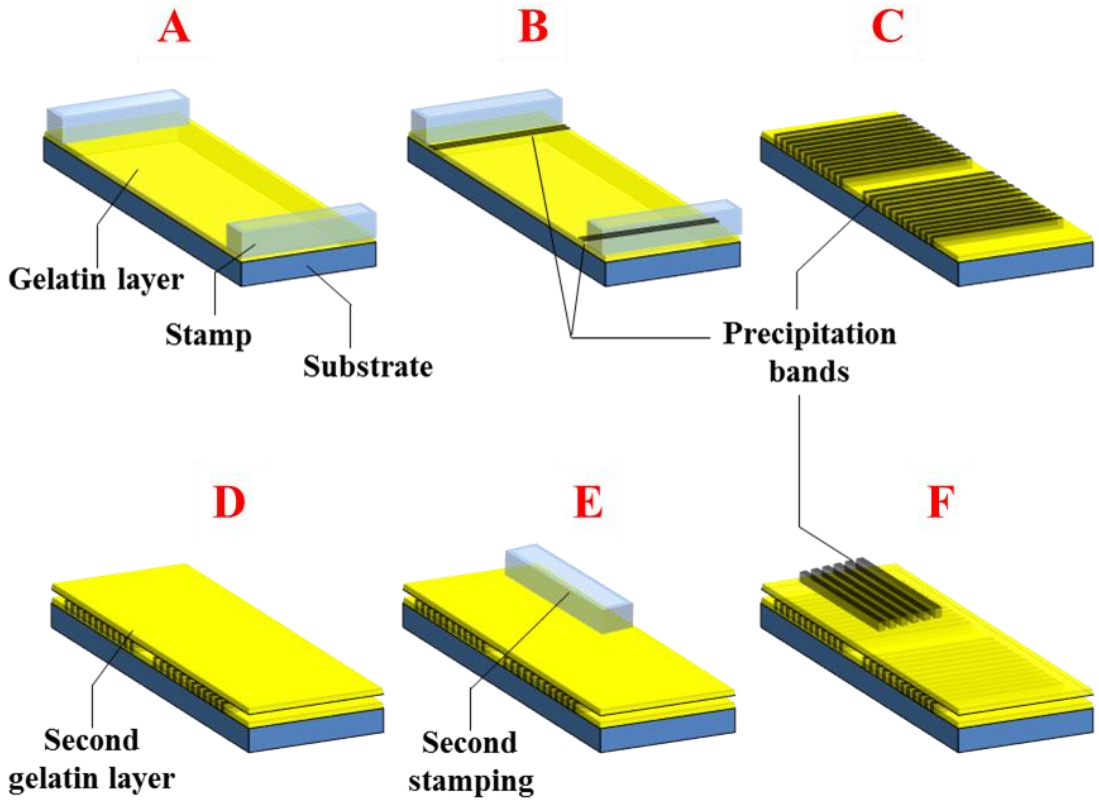

Figure 5.12: Scheme of the preparative setup using fine structured silver Liesegang bands for the preparation of grid-like structures.

5.4.2.3 Results and discussion

All 10 tested samples showed mesoscale grid-like structures. The best results were obtained when the stamp on the second layer was placed perpendicular to the propagation direction of the bands in the first layer beneath (Image 5.13). From repetition experiments it was shown that several parameters are crucial for a successful formation of mesoscale grids. First, interactions between the two gelatin layers have to be kept as small as possible; otherwise the particles forming the bands in the first layer would be dissolved and rearranged during the WETs process in step 5 (Figure 5.12 E). For this reason the primary gelatin layer containing the first set of fine structured silver bands needs to be very dry before a second gelatin layer is added. A pretreatment at high vacuum (10^{-3} mbar) for at least 3 hours after step 3 (Figure 5.12 C) is enough to stop interactions between the two layers.

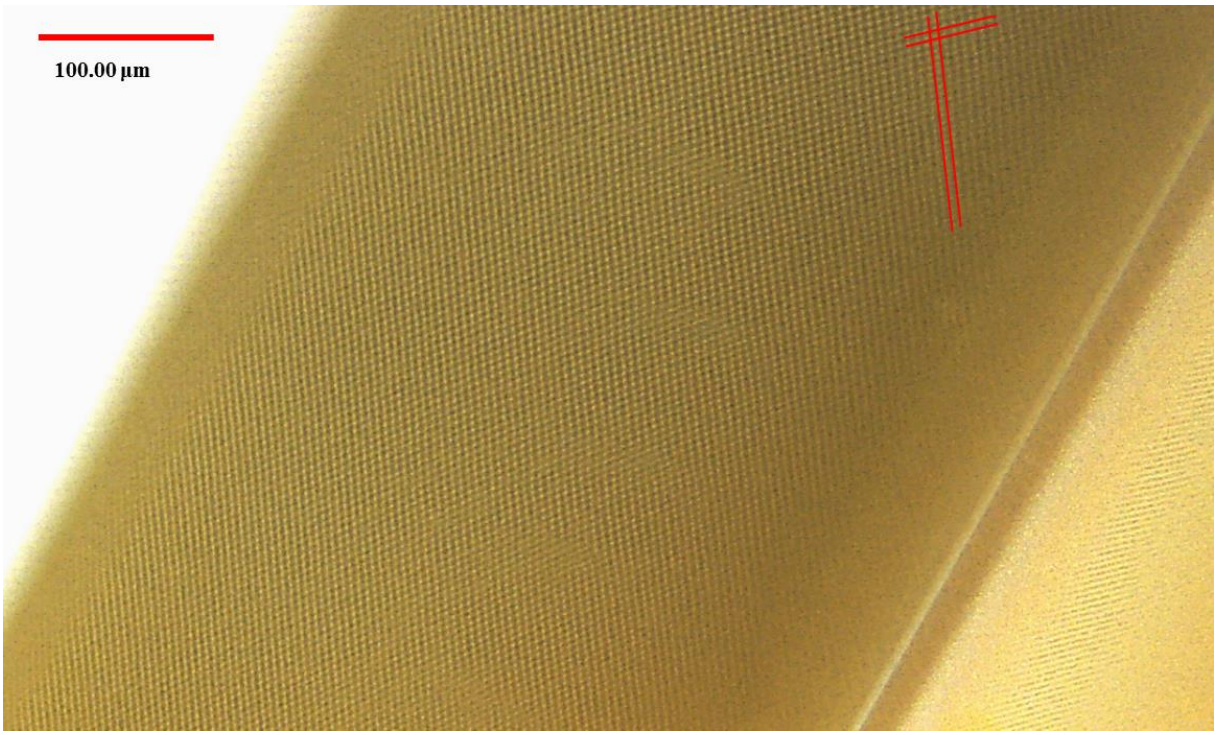

Image 5.13: Optical image of a meso scale grid prepared by using the new fine structured silver Liesegang precipitation system.

Another crucial factor is the temperature of the gelatin solution for the second layer. The best results were obtained for cold (35°C) but still liquid gelatin. An additional significant factor is the wetness of the agarose stamp. If the stamps were not allowed to dry enough before stamping, the water in the stamps led to a swelling of the gelatin layers and therefore to an interaction between the two layers. This would again lead to dissolution, causing a change of the predefined band structures, which means that the particles forming the bands lose coherence and start to disperse.

5.4.2.4 Conclusion

If the above described setup is now combined with the before showed possibility to control the parameter of the bands, e.g. spacing between two bands and/or the possibility to remove gelatin without destroying the structures, the silver Liesegang system can be used for the controllable production of mesoscale silver grids/meshes or sieves. Since all the components are cheap and commercially available and the silver nitrate loaded stamps can be reused (up to 10 times if reloaded), this method can be described as a green, environmentally friendly, simple and low cost way for the production of mesoscale grids.

5.4.3 Application in PEC cells

As mentioned in the introduction one aim of this project was to increase the efficiency of hematite containing photoanodes in photoelectrochemical cells (PECs). Hematite (α-Fe_2O_3/ rust) is a suitable material to be used for water oxidation (oxygen evolution) and therefore for the production of hydrogen fuel by solar water splitting. But it was also described why hematite shows weak efficiencies (cf. Chapter 1). Spatial and material properties of the fine structured silver Liesegang rings/bands make them an ideal candidate to overcome the efficiency problems. The fine structured silver Liesegang bands were investigated from two aspects. Firstly, to increase the active surface area of hematite, and secondly, to increase the conductivity between the hematite layer and the FTO-glass, since silver is known to be the most conductive metal/element.[212,225,226] Additionally, possible light scattering/harvesting properties of the silver rings/bands, (cf. Section 5.4.1, p. 93) were expected to lead to an additional increase in efficiency.

5.4.3.1 Hematite nanoparticle preparation

Si-doped hematite was prepared according to modified literature procedures. From the literature it was also known that the amount of dopant influences the efficiency of the anode material.[78–80,182] For this reason the amount of added TEOS used as the silicon dopant source was varied between 3.7, 1.5, 1.0 and 0.5 w/w%.

5.4.3.1.1 Silicon doped hematite

0.5 w/w% dopant

After combining oleic acid (3.00 g, 10.6 mmol, 6.0 eq.) and TEOS (0.025 g, 0.12 mmol, 0.068 eq.) the mixture was heated at 90°C. After 30 minutes iron(III) nitrate (5.0 g, 12.4 mmol. 7.0 eq.) was added and the homogeneous molten mixture was heated at 130°C until a reddish-brown viscous mass was observed (within 30-70 min). This reddish mass was subsequently treated with tetrahydrofuran (THF), the resulting solution was stirred with a glass rod for 10 min and the reddish precipitate was separated from the solution by centrifugation (6 min at 3000 rpm). After centrifugation, the supernatant was recovered either for the dip coating or for direct preparation of hematite nanoparticle powder by annealing at 450°C (4 h).

The same procedure was used for the other desired dopant rates, simply changing the amount of added TEOS.

1.0 w/w% Si dopant: TEOS (0.050 g, 0.240 mmol, 0.14 eq.)

1.5 w/w% Si dopant: TEOS (0.075 g, 0.360 mmol, 0.20 eq.)

3.7 w/w% Si dopant: TEOS (0.184 g, 0.884 mmol, 0.50 eq.)

5.4.3.1.2 Results and discussion

The hematite nanoparticles and the implementation of the dopant in the prepared powder were investigated by SEM, Raman spectroscopy and XPS.

During the annealing process of the supernatant, iron oxide is formed. Depending on the temperature, different iron(III) oxide species like maghemite (γ-Fe_2O_3) and hematite (α-Fe_2O_3) (differing in their properties and lattice structures/morphology) can be formed.[227] For this reason it was necessary to determine the material composition of the powder by Raman spectroscopy and X-ray powder diffraction (XRD).[228]

5.4.3.1.2.1 SEM analysis

SEM analysis of the hematite powders shows how the amount of added dopant influences the surface of the material. The more dopant is added, the higher/larger the surface area (Image 5.14-Image 5.17 left) and the larger the hematite particles (Image 5.14-Image 5.17 right).

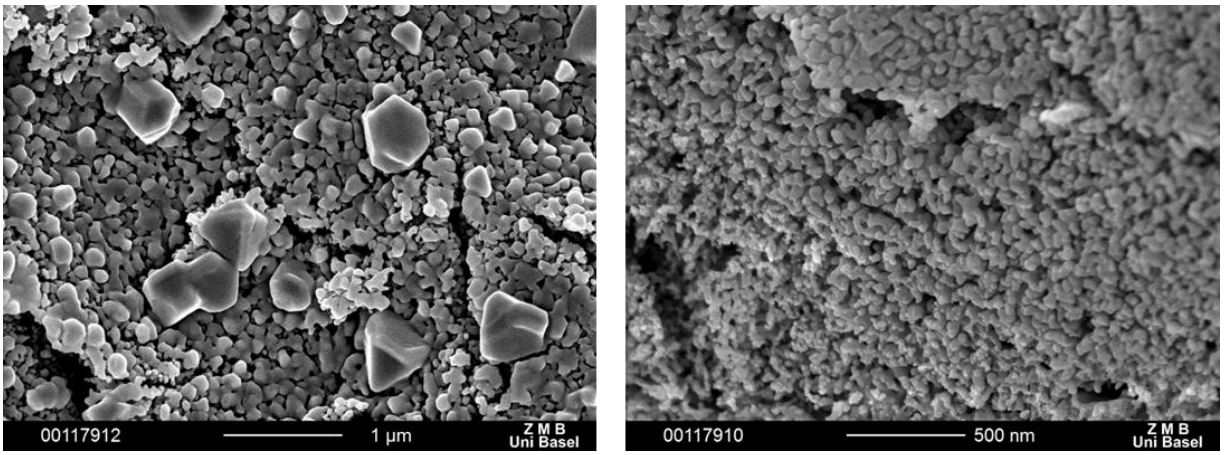

Image 5.14: Sintered hematite nanostructures prepared with 0.5 w/w% Si dopant (TEOS). Left: silicon implementation, right: hematite nanoparticle size.

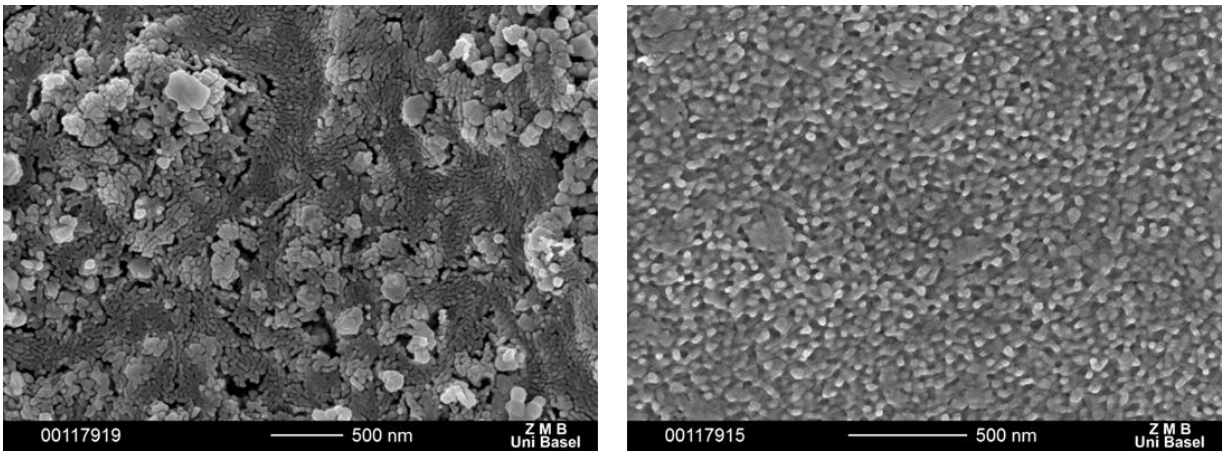

Image 5.15: Sintered hematite nanostructures prepared with 1.0 w/w% Si dopant (TEOS). Left: silicon implementation, right: hematite nanostructures size.

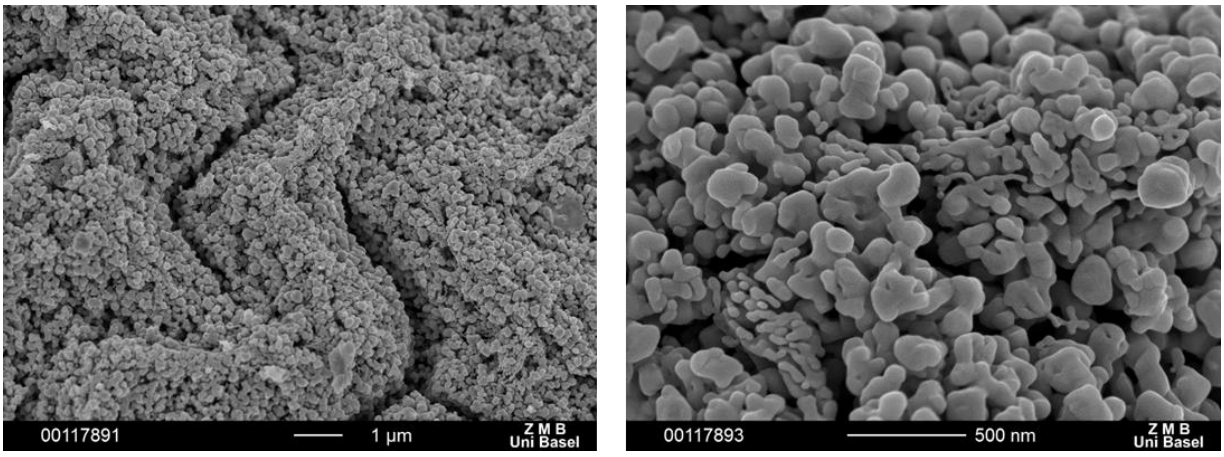

Image 5.16: Sintered hematite nanostructures prepared with 1.5 w/w% Si dopant (TEOS). Left: silicon implementation, right: hematite nanostructures size.

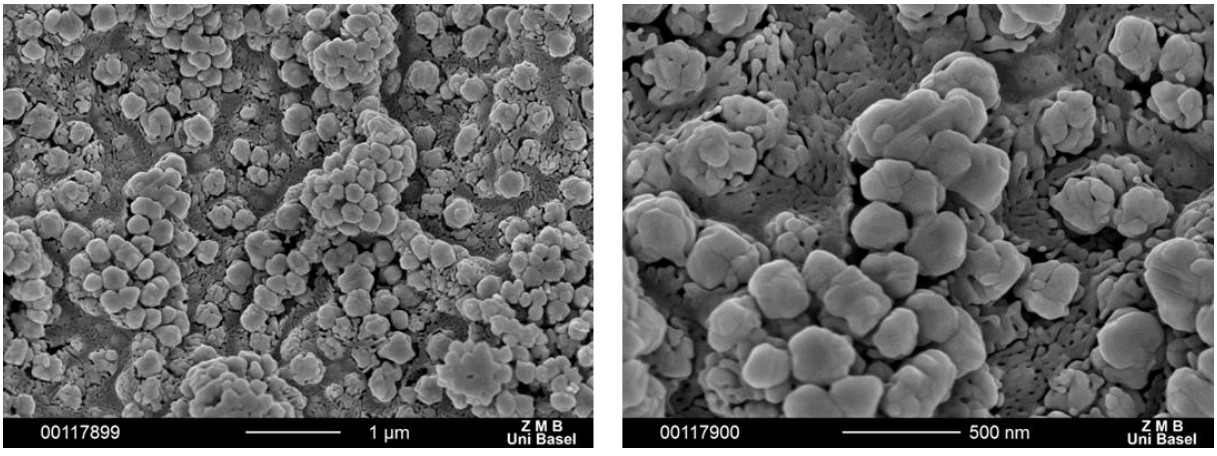

Image 5.17: Sintered hematite nanostructures prepared with 3.7 w/w% Si dopant (TEOS). Left: Si-implementation, right: hematite nanostructures size.

Some of the SEM images were colored to show how the silicon dopant is implemented into the hematite (Image 5.18). However, if no dopant is added, the hematite layers are almost flat and the particles are around 10-20 nm thin (Image 5.19).

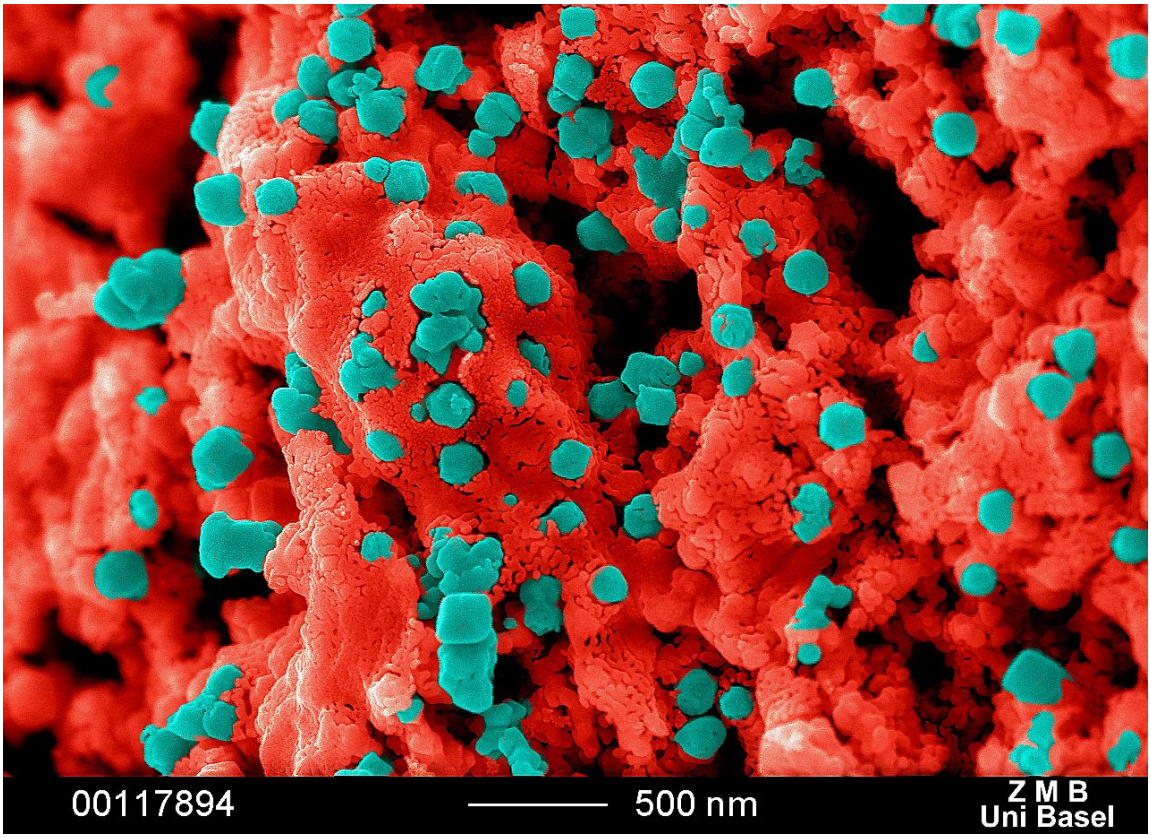

Image 5.18: Colored SEM image of Si-doped hematite. Si-dopant (cyan), hematite (red).

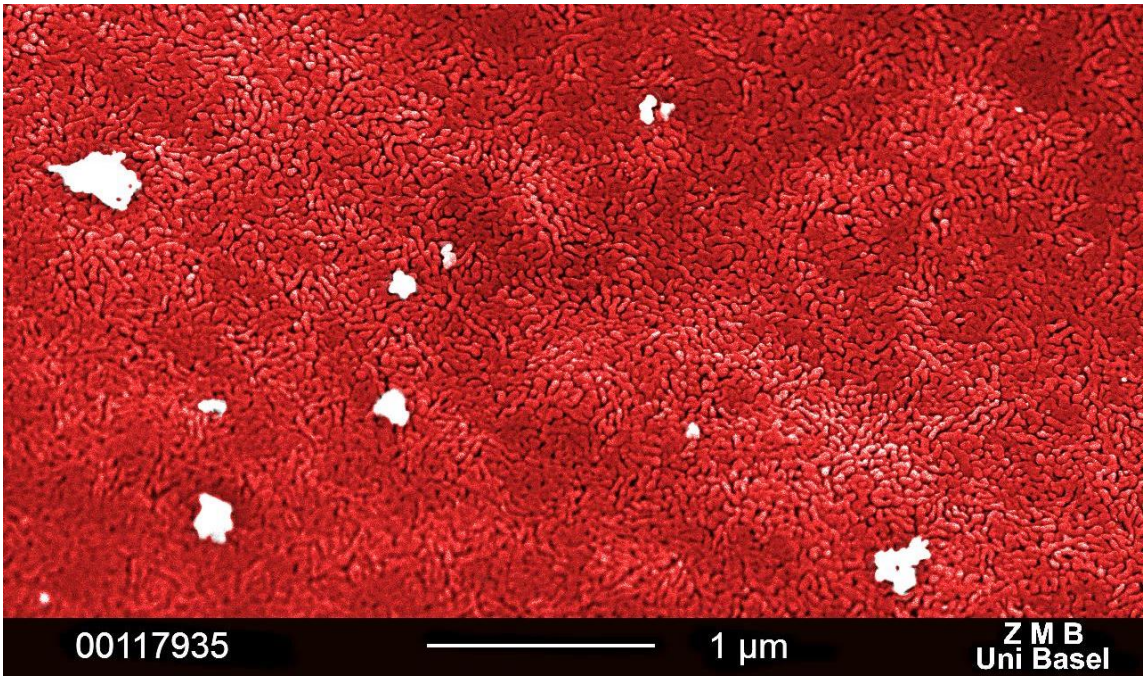

Image 5.19: SEM image of hematite without dopant (red), white parts: charging effect on hematite nanoparticles due to loss of platinum sputter layer.

5.4.3.1.2.2 Raman spectroscopy

The three Raman shifts (Figure 5.13) at 225, 293 and 395 cm^{-1} are characteristic for hematite, if maghemite would have been present additional strong and broad shifts around 350, 500 and 700 cm^{-1} would have been observed.[228,229]

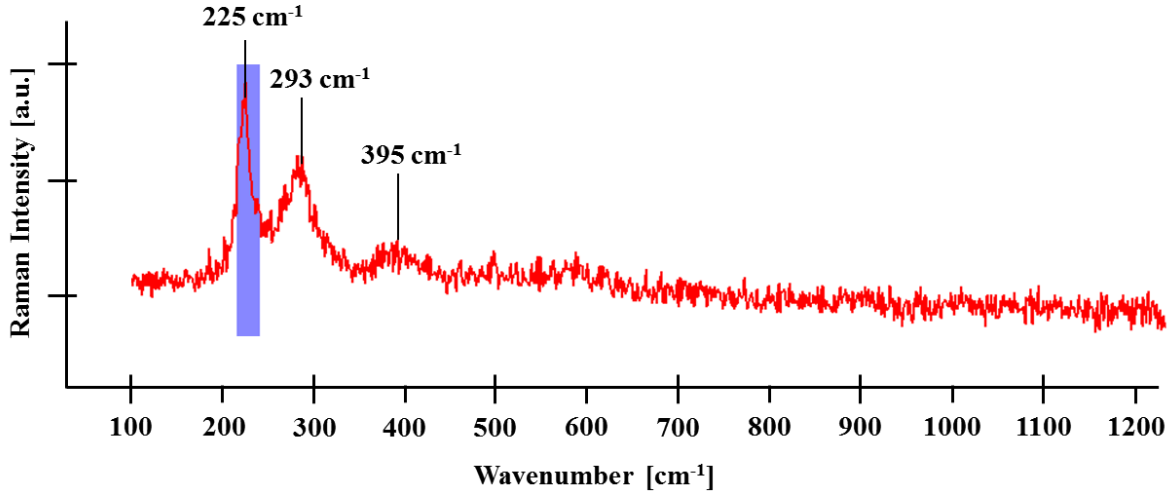

Figure 5.13: Raman spectrum of 0.5 w/w% silicon doped hematite.

5.4.3.1.2.3 X-ray powder diffraction (XRD)

The results from the XRD measurements of 0.5 w/w% Si-doped hematite, shown in the X-ray diffractogram (Figure 5.14) were compared to literature values[80,228,230] of Si-doped hematite and pure hematite. Interestingly no pattern of the Si-dopant was observed in the diffractograms. This might be due the low amount of added dopant (0.5-3.7 w/w%).

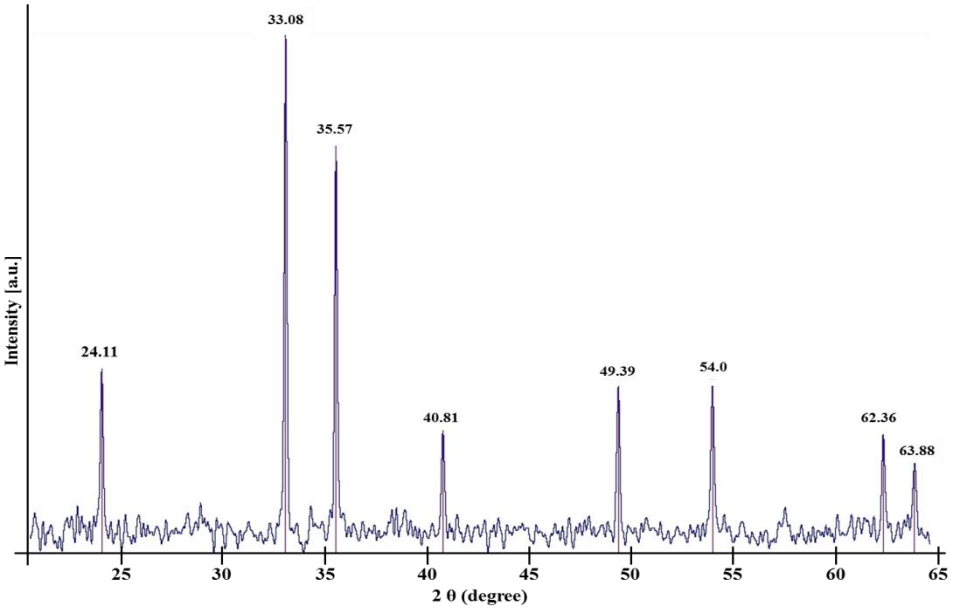

Figure 5.14: X-ray powder diffractogram of 0.5 w/w% silicon doped hematite.

5.4.3.1.3 Conclusion

The setup for the preparation of hematite films and nanoparticles was successfully adopted and modified for our needs.[80] Both Raman and XRD show full conversion to hematite for annealing/sintering temperatures above 450°C.

5.4.3.2 PEC photoanode preparation

5.4.3.2.1 Introduction

Four different setups combining hematite with the fine structured silver Liesegang system were proposed to investigate influences of the bands/rings on the water oxidation efficiency of the anode (Figure 5.15). For transparency and conductivity reasons FTO-glass was used as substrates for all prepared PEC-anodes containing hematite.

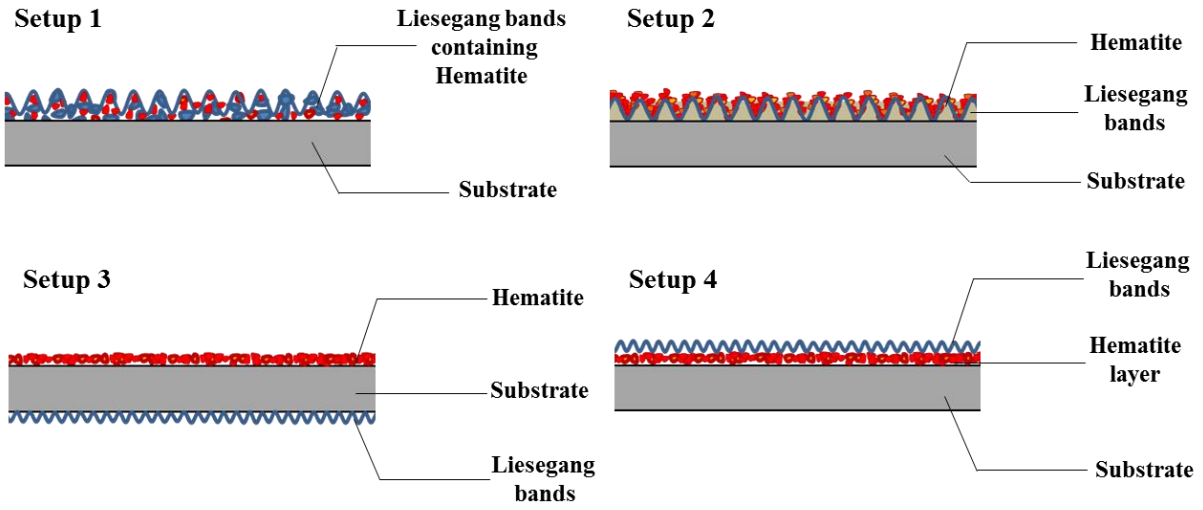

Figure 5.15: Scheme showing the setup used for PEC photoanode preparation. Blue lines: fine structured silver Liesegang bands; red: implementation of hematite; grey: substrate (FTO-glass).

5.4.3.2.2 Experimental and results

In the work of my colleague *Florent Boudoire*,[231] it was shown that it is possible to prepare very thin hematite layers by annealing/sintering iron nitrate. For this reason this technique was adopted and tested in my systems as well. In setup **1** and **2** the silver Liesegang system was used to increase the surface and conductivity of the hematite photoanode. In setup **3** and **4** the silver Liesegang system was used as scattering or light absorbing/harvesting layer, to increase the amount of light absorbed at the surface of the photoanode.

5.4.3.2.2.1 Setup 1: Using the silver Liesegang system as hematite carrier

Si-doped (3.7 w/w% dopant) hematite (1.0 w/w%) was added to a previously prepared 10 w/w% gelatin solution (*type 0*) in 0.3 w/w% ammonia (0.176 M). Heating, spin coating, drying, WETs and UV treatment was performed according to sample preparation described in previous sections (Section 5.2), to obtain a set of 8 samples (4 x 300 rpm and 4 x 500 rpm). For wet stamping a 0.3 M $AgNO_3$ (48 h) loaded standard (3 x 3 pin) agarose stamp was used (Figure 5.15 top left).

5.4.3.2.2.2 Setup 2: Using the silver Liesegang system as hematite carrier substrate

A set of 24 samples containing fine structured silver Liesegang bands in gelatin was prepared according to previous experimental setups (Section 5.2) using 10 w/w% gelatin (*type 0*) in 0.3 w/w% ammonia, a coating speed of 300 rpm and 0.3 M $AgNO_3$ (48 h) loaded agarose stamps (3 x 3 pins). After UV-treatment and optical analysis half of the samples were sintered at 380°C according to the procedure described in Section 5.3.2.1.1. The second half was used without further treatment (Figure 5.15 top right).

5.4.3.2.2.3 Setup 2a: hematite on top of the silver bands in gelatin

Using annealed hematite nanoparticles (setup 2a-1)

Annealed hematite nanoparticle powder (3.7 w/w% dopant) was dissolved in water to obtain a 50 w/w% hematite solution. This solution (0.3 mL) was spin coated (200 rpm) on top of the gelatin films containing the silver bands, resulting in a set of 4 samples. One sample was used for stability tests in water. The second sample was analyzed by SEM-FIB, to obtain information on whether the hematite nanoparticles were incorporated inside the gelatin. The remaining two samples were sintered at 400 °C for 4 hours. One of these samples was also analyzed by SEM-FIB to obtain information about the distribution of the hematite. The second annealed sample was tested in PECs.

Results and discussion (setup 2a-1)

Sample 2a-1/a was dissolved in water after 50 minutes. Sample 2a-1/b showed no difference between a hematite loaded and a non-loaded sample. Sample 2a-1/c showed also no difference. Sample 2a-1/d did not work in PEC cells.

Using the THF-hematite precursor solution (setup 2a-2)

The THF containing hematite (3.7 % dopant) solution was drop coated (200 µL) on top of the silver bands in the gelatin, resulting in a set of 4 samples. One sample was analyzed by SEM-FIB to observe information if and how much hematite nanoparticles were incorporated by the gelatin. The remaining samples were sintered at 400 °C for 4 hours. One of these samples was also analyzed by SEM-FIB and another will be tested in PECs.

Results and discussion (setup 2a-2)

From optical microscopy no change of the bands was observed after adding the THF solution. In both FIB samples no change was observed either. However, PEC measurements have yet to be done.

Using iron(III) nitrate in EtOH (setup 2a-3)

A 0.5 M $Fe(NO_3)_3$ solution was prepared in ethanol and 400 µL were spin coated (300 rpm) on top of the silver bands in the gelatin.

Results and discussion (setup 2a-3)

Unfortunately, after addition of the iron(III) nitrate solution, the gelatin layer cracked and all bands vanished. The cracking might be due to water loss of the gelatin layer after addition of ethanol. However the vanishing of the bands can be explained by a possible silver etching process[232,233] in iron nitrate. The pH of the $Fe(NO_3)_3$ solution prepared in EtOH and water were was 0.41 and 1.12, respectively.

5.4.3.2.2.4 Setup 2b: hematite on top of the sintered silver bands

Same sample preparation as for setup 2a. The only change was the use of sintered silver bands (no gelatin in the system). Hematite was implemented either by solution coating of aqueous (5.0 w/w%) preannealed hematite nanoparticles, by dip coating using the THF-iron(III) nitrate/fatty acid solution or by spin coating (300 rpm) an 0.5 M iron(III) nitrate solution (aqueous, or in EtOH) on top of the sintered silver bands. After addition, the samples were sintered again at 450 °C for 6 h (Figure 5.15 top right).

Results and discussion

Using pre annealed hematite nano particles

No change in the samples was observed in the FIB measurements, meaning that no hematite structure was found on top of the bands. For this reason the samples were not tested in PEC.

Using the THF-hematite precursor solution

Only a few very spread hematite particles have been observed in SEM and SEM-FIB measurements. For this reason no PEC measurements were performed.

Using iron(III) nitrate in EtOH (for later sintering and conversion to hematite)

Same observation was made as for silver bands in gelatin, where the nanoparticle vanished after addition of the iron(III) nitrate (Image 5.20).

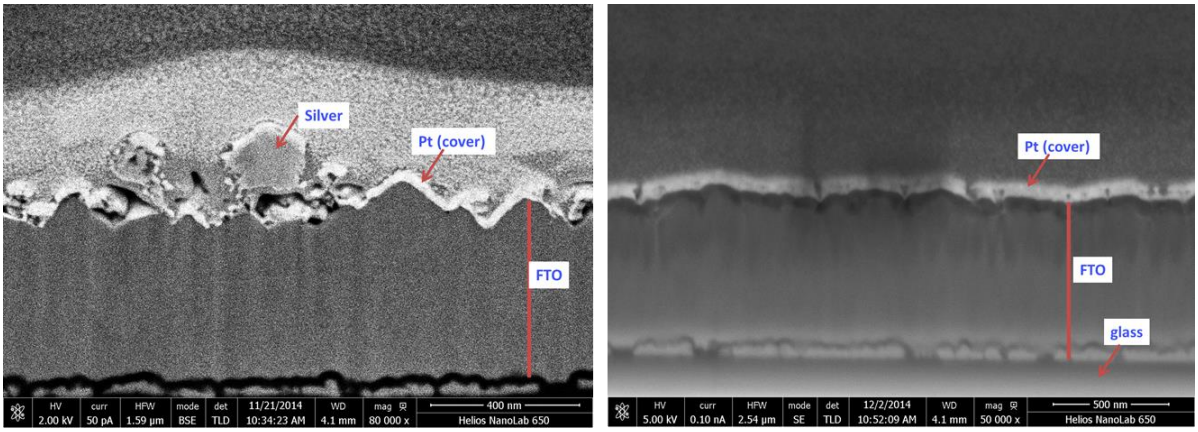

Image 5.20: SEM images of a FIB cross section. Left image: cross section through a sintered fine structured silver Liesegang band (before addition of the iron(III) nitrate solution). Right image: cross section of a sintered silver bands containing sample after addition of the iron(III) nitrate solution. Materials found in the cross sections are indicated.

5.4.3.2.2.5 Setup 3 and 4: Using the silver Liesegang system as scattering or light absorbing/harvesting layer

The anode was prepared by dip coating (4 times) FTO-glass into the Si-doped (3.7 w/w% dopant) hematite-THF solution. After sintering at 450°C, the samples were washed with milliQ water until the hematite layer on the glass site of the FTO-glass disappeared. After drying, the samples were measured in PECs (at EMPA). After PEC measurements the samples were covered with a gelatin layer. The gelatin layer was added by spin coating (300 rpm) a hot (65°C) 10 w/w% gelatin solution containing 0.3 w/w% ammonia on top of either the glass

side (Figure 5.15 setup 3) or on top of the FTO-hematite side (Figure 5.15 setup 4). The samples were allowed to dry at ambient temperatures overnight before the WETs technique was used for formation of silver bands. For wet stamping a 0.3 M $AgNO_3$ (48 h) loaded standard (3 x 3 pins) agarose stamp was used and the stamps were removed after 2 h (glass side) or 6 h (hematite side). After UV treatment (30 min at 256 nm) the samples were sintered at 380 °C (4 h) and analyzed by optical microscopy.

Results and discussion (setup 3 and 4)

Stable silver bands/rings were observed on samples when the glass side was covered (not the hematite layer) (Image 5.21).

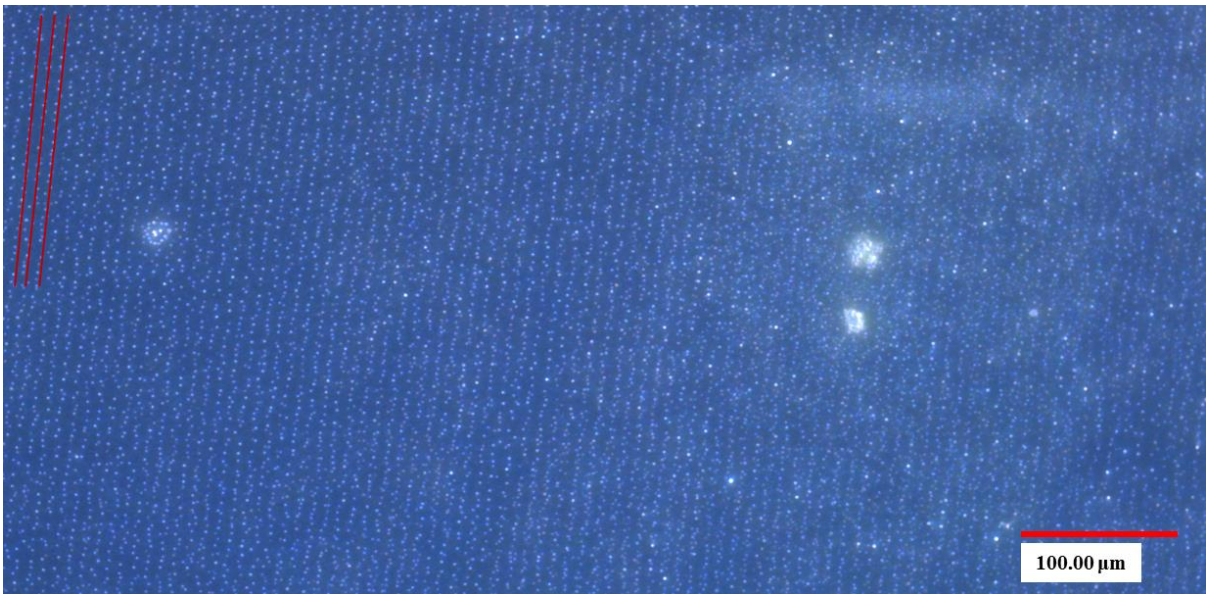

Image 5.21: Optical image of sintered silver bands on the glass side of a hematite PEC anode. The red lines indicate the sintered silver bands.

No precipitation bands were observed for samples prepared in setup 4, when it was tried to implement the fine structured silver bands on top of hematite. In addition, it was found that the precipitation process for this type of samples was very slow. After 6 hours the propagation only occurred up to 2 mm from the stamping center. At the same time the precipitation range on the glass side was up to 1.5 cm from the stamping center. This slowdown of the precipitation propagation speed might be due to interactions of silver ions with the rough hematite surface. The few precipitation bands found before sintering vanished after sintering. For this reason only the samples with the bands on the glass side were measured in PECs.

5.4.3.2.3 Conclusion

It was challenging to implement the silver bands in and onto hematite containing material. Most of the prepared anodes showed minor efficiency improvement after addition of a silver Liesegang bands containing layer. Further PEC measurements are needed.

6. Screening of new precipitation bands forming systems

6.1 Introduction

This chapter is about the development of a simple but efficient strategy for high-throughput screening (HTS) of new materials and electrolyte combinations, to generate new Liesegang type periodic precipitation bands. From previous experiments concerning the classical Liesegang (Chapter 3) and the new silver Liesegang system s(Chapter 4), it was found that a chemical equilibrium with the ability to form insoluble compounds is necessary for the creation of periodic precipitation bands. In case of the classical system it was the chromate/dichromate equilibrium forming two different types of precipitates. In the new silver Liesegang system it was the equilibrium between Ag^+ and Ag^0 under basic conditions which facilitates the periodic precipitation process. It was also found which parameters are crucial for the control of the formation of this process. Keeping in mind the necessity for having a chemical equilibrium generating both soluble and insoluble compounds and the possibility to control the precipitation process, a simple three step protocol for screening new materials, allowing a high throughput of test systems, has been developed. In the first step, precipitation experiments were performed in aqueous solution, by mixing at least two components. Once a precipitate forming system was found the same compound combination was further investigated for precipitation band forming abilities, using a special test plate developed for this purpose. By using this test plate it was possible to optimize/adjust the prerequisites under which precipitation band formation was observed in a hydrogel matrix. In the last step the WETs technique was used to transform the optimized (under HTS-conditions) systems into the micro- and nanoscale. This was done to obtain systems with an increased surface area compared to bulk materials. This increase might lead to an increase in the catalytic efficiency of catalyst materials. For this reason several different metal salts and coordination compound combinations were tested.

6.2 Experimental

6.2.1 Step 1: Precipitation experiments in solution

In the first step the materials/compounds were screened for their ability to form precipitation products if they were combined at given concentrations. For the formation of Liesegang precipitation bands in a hydrogel it is necessary that both compound A and B are water

soluble, but still forming insoluble compounds if combined at different concentrations. The concentration factor is crucial for the control of the later diffusion direction in the WET stamping setup. For this reason simple solution experiments as shown in Figure 6.1 were carried out. The ability of the system forming precipitates at different concentrations was tested by mixing a solution containing compound A with a 10 times less concentrated solution containing compound B and vice versa. Used/tested concentrations: 0.01 M and 0.1 M.

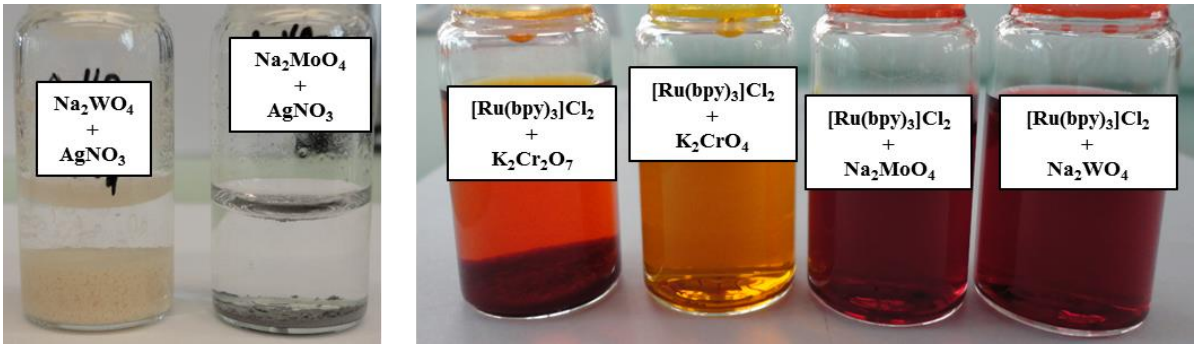

Figure 6.1: Simple solubility-precipitation experiments in water (From left to right): Sodium tungstate + silver nitrate, sodium molybdate + silver nitrate, $[Ru(bpy)_3]Cl_2$ + potassium dichromate, $[Ru(bpy)_3]Cl_2$ + potassium chromate, $[Ru(bpy)_3]Cl_2$ + sodium molybdate and $[Ru(bpy)_3]Cl_2$ + sodium tungstate.

6.2.1.1 Investigated salt/compound (A/B) combinations in aqueous solutions

6.2.1.1.1 Salts

Potassium dichromate ($K_2Cr_2O_7$), potassium chromate (K_2CrO_4), silver nitrate ($AgNO_3$), potassium tetrachloridoplatinate (K_2PtCl_4), palladium(II) chloride ($PdCl_2$), ruthenium(III) chloride hydrate ($RuCl_3 \cdot xH_2O$), iron(II) sulfate hepatahydrate ($FeSO_4 \cdot 7H_2O$), iron nitrate nonahydrate ($Fe(NO_3)_3 \cdot 9H_2O$), sodium tungstate dihydrate ($Na_2WO_4 \cdot 2H_2O$), sodium molybdate dihydrate ($Na_2MoO_4 \cdot 2H_2O$), potassium tetrachloroaurate(III) ($KAuCl_4$), iron(III) chloride hexahydrate ($FeCl_3 \cdot 6H_2O$), sodium oxalate ($Na_2C_2O_4$), copper(II) sulfate pentahydrate ($CuSO_4 \cdot 5H_2O$), ammonium hexafluoridophosphate (NH_4PF_6), silver hexafluoridophosphate ($AgPF_6$) and copper(II) acetate monohydrate ($Cu(CH_3COO)_2 \cdot H_2O$). Detailed description and supplier of the used compounds can be found in Section 2.5.2.

6.2.1.1.2 Coordination compounds

From the literature[234,235] it is known that coordination compounds can be precipitated out of a solution if the counterion is exchanged. Since coordination compounds are used in applications such as catalyst materials, it was decided to study simple $[Fe(bpy)_3]Cl_2$ (tris(2,2'-

bipyridine)iron(II) dichloride), $[Ru(bpy)_3]Cl_2$ (tris(2,2'-bipyridine)ruthenium(II) dichloride) and $[Fe(pytpy)_2]Cl_2$ (bis(4′-(4-pyridyl)-2,2′:6′,2″-terpyridine)iron(II) dichloride) (Figure 6.2) as model systems for other metal coordination compounds. Since in the case of the coordination compounds, an exchange of the counterion was of interest, the following salts were tested in combination with the coordination compounds: $K_2Cr_2O_7$, K_2CrO_4, $AgNO_3$, $FeSO_4$, Na_2WO_4, Na_2MoO_4, $KAuCl_4$, $Na_2C_2O_4$, $CuSO_4$, NH_4PF_6, $AgPF_6$ and $Cu(CH_3COO)_2$. However the pH of the solution can also be a crucial parameter for the formation of precipitates. For this reason all systems where no precipitates were formed were tested again under alkaline and acidic conditions. The pH was adjusted by ammonia or citric acid.

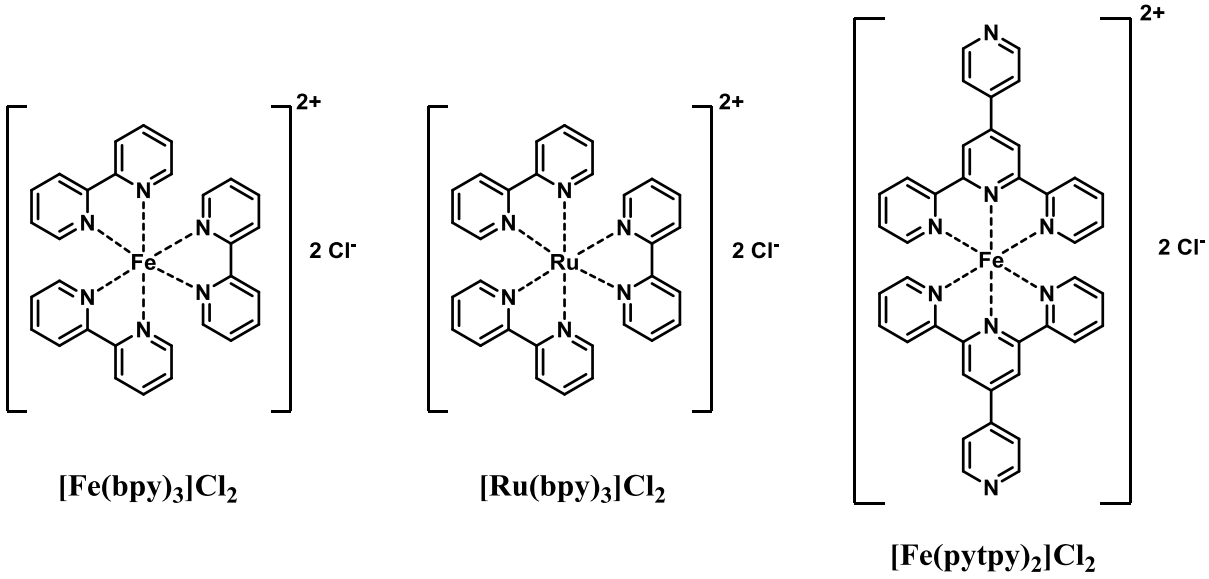

Figure 6.2: Molecular structures of: $[Fe(bpy)_3]Cl_2$ (tris(2,2'-bipyridine)iron(II) dichloride) (left), $[Ru(bpy)_3]Cl_2$ (tris(2,2'-bipyridine)ruthenium(II) dichloride) (middle) and $[Fe(pytpy)_2]Cl_2$ (bis(4′-(1-pyridyl)-2,2′:6′,2″-terpyridine)iron(II) dichloride) (right).

6.2.2 Step 2: Screening for band forming abilities

Once a working, precipitate forming system was found, this system was further investigated for its ability to form precipitation bands in a Liesegang type manner. For this reason a special high throughput screening (HTS)-plate was designed (Figure 6.3 left). Blue prints can be found in the appendix (Appendix B, p. 162). By using this HTS-method, it is possible to compare the results of stepwise changes in the geometry of the system, leading to control over parameters such as the effect of gravity (X, Y, Z-tilt), the amount of material, the use of different salts, ionic liquids or hydrofluids, reaction times and temperatures in parallel.

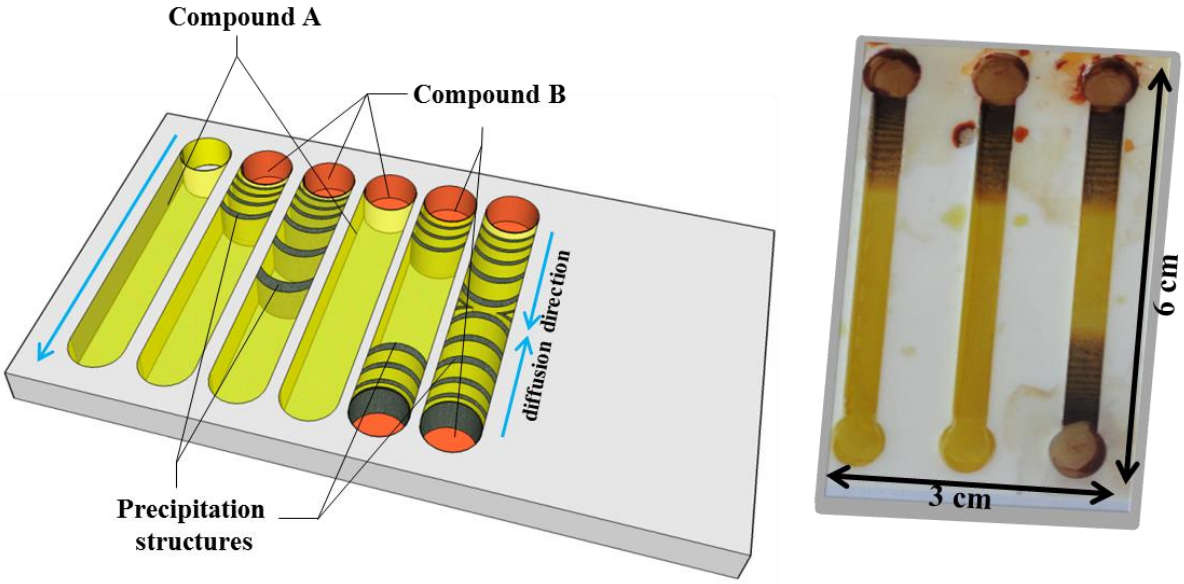

Figure 6.3: Left: scheme of the high throughput screening plate (HTS-plate). Yellow parts indicate gelatin containing the inner electrolyte/compound A. Red parts indicate the outer/invading electrolyte/compound B. The black bands represent the precipitation bands which are formed during the reaction-diffusion process. The blue arrows show the diffusion direction. Right image: photo of an actual HTS-plate showing the reaction-diffusion-precipitation bands found in the classical Liesegang system.

The plate consists of a series of holes which were filled with gelatin containing compound A. After gelation, one end of the hole is hollowed out and replaced by gelatin containing compound B. The system is then closed tightly with a PMMA plate, to be able to monitor the precipitation process and to prevent the system from drying out. In order to control the diffusion direction, compound A must be of lower concentration than B. The precipitation bands containing compound C are formed when a reaction occurs while compound B diffuses into the compound A containing medium. The band formation can be tuned via variations in pH and concentrations of compound A and/or B in the gelatin solutions. In the example (Figure 6.3 right), the classical Liesegang system containing potassium dichromate as compound A and silver nitrate as B, was used. During the reaction-diffusion-process, silver dichromate formed (compound C) as precipitation bands. 5, 10 and 15 w/w% gelatin (*type 0*) solutions were used as hydrogel. The pH of the hydrogel was adjusted by preparation of the gel in either milliQ water (neutral), in alkaline solutions of ammonia (0.3 w/w%) or KOH (0.1 M), or under acidic conditions citric acid (0.1 M) or HCl (0.1 M). After the gelatin solutions were prepared, compound A (0.005 M, 0.01 M, 0.05M, 0.1 M) and compound B (0.1 M, 0.3 M, 0.5 M) were added and the mixtures were heated to 70°C in pressure stable tubes (*BD Falcon*). In the next step the HTS- method was used as described. From the investigations of the silver system (Chapter 4 and 5) it is known that the precipitation bands can be very thin and dense. For this reason all tested systems were analyzed by optical and laser microscopy.

6.2.3 Step 3: Transformation into the micro- and nanoscale

As a control over the pattern formation has been established, the WET-stamping technique (Section 2.4.2) was used to transfer the system into the micro- and nanoscale.

In the first step, a thin gelatin layer containing compound A (0.01 M) was prepared by spin-coating (300 rpm) hot (70°C) compound A-gelatin solution onto a glass substrate. The sample was then allowed to dry at ambient temperature overnight. Along with this a stamp containing compound B (0.1 M) was prepared, according to previous protocols (Section 2.4.2.1). The stamps were loaded with salt B (24 h). In the next step the stamp (pins: Ø 500 µm) was placed on a gelatin-compound A layer and the reaction-diffusion front was allowed to propagate. After 1 hour the process was stopped and the samples were analyzed.

6.3 Results and discussion

6.3.1 Step 1: Precipitation in solution

Table 6.1: Compound A/B combinations part 1. Precipitation was observed for the green highlighted combinations.

	$FeCl_2$	$Fe(NO_3)_3$	$AgNO_3$	K_2CrO_4	$CuSO_4$	$Cu(OAc)_2$	$Na_2(C_2O_4)$	$FeSO_4$
$FeCl_2$		no	yes	yes	no	no	yes	no
$Fe(NO_3)_3$	no		no	no	no	no	no	no
$AgNO_3$	yes	no		yes	yes	no	yes	yes
K_2CrO_4	yes	no	yes		yes	yes	no	yes
$CuSO_4$	no	no	yes	yes		no	no	no
$Cu(OAc)_2$	no	no	no	yes	no		yes	no
$Na_2(C_2O_4)$	yes	no	yes	no	no	yes		no
$FeSO_4$	no	no	yes	yes	no	no	no	
$FeCl_3$	no	no	yes	yes	no	no	no	no
NH_4PF_6	no	no	yes	no	no	yes	no	yes
Na_2MoO_4	yes	yes	yes	no	no	yes	no	yes
K_2PtCl_4	no	no	yes	no	no	no	no	no
$KAuCl_4$	no	no	no	no	no	no	no	no
$PdCl_2$	no	yes	yes	no	no	no	no	no
$RuCl_3$	no	no	yes	no	no	no	no	no
$K_2Cr_2O_7$	yes	no	yes	no	yes	yes	no	yes
Na_2WO_4	yes	yes	yes	no	no	yes	no	yes
$[Fe(bpy)_3]Cl_2$	no	no	yes	no	no	no	no	no
$[Ru(bpy)_3]Cl_2$	no	no	yes	no	no	no	no	no
$[Fe(pytpy)_2]Cl_2$	no	no	yes	no	no	no	no	no

In case of the tested salts and coordination compounds (Table 6.1 and Table 6.2), precipitation products in aqueous solutions have been observed for the following compound A/B combinations (highlighted in green). As mentioned before, acid and/or base were added to the mixtures where no precipitation occurred at the first place. However, no additional precipitation was observed after addition of acid (0.3 M citric acid) or base (0.1 M KOH).

Table 6.2: Compound A/B combinations part 2. Precipitation was observed for the green highlighted combinations.

	$FeCl_3$	NH_4PF_6	Na_2MoO_4	K_2PtCl_4	$KAuCl_4$	$PdCl_2$	$RuCl_3$	$K_2Cr_2O_7$	Na_2WO_4
$FeCl_2$	no	no	yes	no	no	no	no	yes	yes
$Fe(NO_3)_3$	no	no	yes	no	no	yes	no	no	yes
$AgNO_3$	yes	yes	yes	yes	no	yes	yes	yes	yes
K_2CrO_4	yes	no	no	no	no	no	no	no	no
$CuSO_4$	no	no	no	no	no	no	no	yes	no
$Cu(OAc)_2$	no	yes	yes	no	no	no	no	yes	yes
$Na_2(C_2O_4)$	no	no	no	no	no	no	no	no	no
$FeSO_4$	no	yes	yes	no	no	no	no	yes	yes
$FeCl_3$		no	yes	no	no	no	no	yes	yes
NH_4PF_6	no		no	no	no	yes	no	no	no
Na_2MoO_4	yes	no		no	no	yes	no	no	no
K_2PtCl_4	no	no	no		no	yes	no	no	no
$KAuCl_4$	no	no	no	no		yes	no	no	no
$PdCl_2$	no	yes	yes	yes	yes		no	no	yes
$RuCl_3$	no	no	no	no	no	no		no	no
$K_2Cr_2O_7$	yes	no	no	no	no	no	no		no
Na_2WO_4	yes	no	no	no	no	yes	no	no	
$[Fe(bpy)_3]Cl_2$	no	yes	yes	no	yes	no	no	yes	yes
$[Ru(bpy)_3]Cl_2$	no	yes	yes	no	yes	no	no	yes	yes
$[Fe(pytpy)_2]Cl_2$	no	yes	yes	yes	yes	yes	no	yes	yes

6.3.2 Step 2: Band formation under HTS-plate conditions

6.3.2.1 General

After successful precipitation in solution, the same compound A/B combinations were tested with the HTS-method. There, the pH and the amount of hydrogel (gelatin) in the reaction diffusion systems were optimized to facilitate band formation. Nevertheless only a few of the tested systems forming precipitates in solution were found to form precipitation bands in a Liesegang type manner under HTS-conditions. The results are summarized in Table 6.3. The top row represents the invading (outer) electrolyte (B) and the left column represents the stationary (inner) electrolyte (A), which is penetrated by B during the reaction-diffusion

process. Strong and reproducible band formation was observed for the green highlighted systems. In the dark blue highlighted systems, weak band formation was observed. The problem with these two systems was the silver nitrate in the inner electrolyte, which darkened while the structures were analyzed by optical and laser microscopy.

Table 6.3: Working compound A/B combinations under HTS-plate conditions. Precipitation were observed for the green highlighted combinations. Blue highlighted combinations showed weak precipitation bands.

	$AgNO_3$	$FeSO_4$	NH_4PF_6	Na_2MoO_4	Na_2WO_4	$KAuCl_4$	$K_2Cr_2O_7$
$AgNO_3$		yes	no	weak	weak	no	yes
Na_2MoO_4	yes	no	no		no	no	no
Na_2WO_4	yes	no	no	no		no	no
$[Fe(bpy)_3]Cl_2$	no	no	no	no	no	yes	yes
$[Ru(bpy)_3]Cl_2$	no	no	no	no	no	yes	yes
$[Fe(pytpy)_2]Cl_2$	yes	no	no	no	no	no	yes

All reaction diffusion experiments containing silver nitrate were performed in the dark to prevent silver nitrate darkening. This explains why only weak precipitation bands were observed if sodium tungstate or sodium molybdate diffused into the silver nitrate containing system. If the compounds were interchanged and silver nitrate is the invading electrolyte, more precise precipitation bands were observed. The results from the $[Ru(bpy)_3]^{2+}$ and $K_2Cr_2O_7$ system (Figure 6.4) are used to demonstrate how simple the handling of this HTS-setup is.

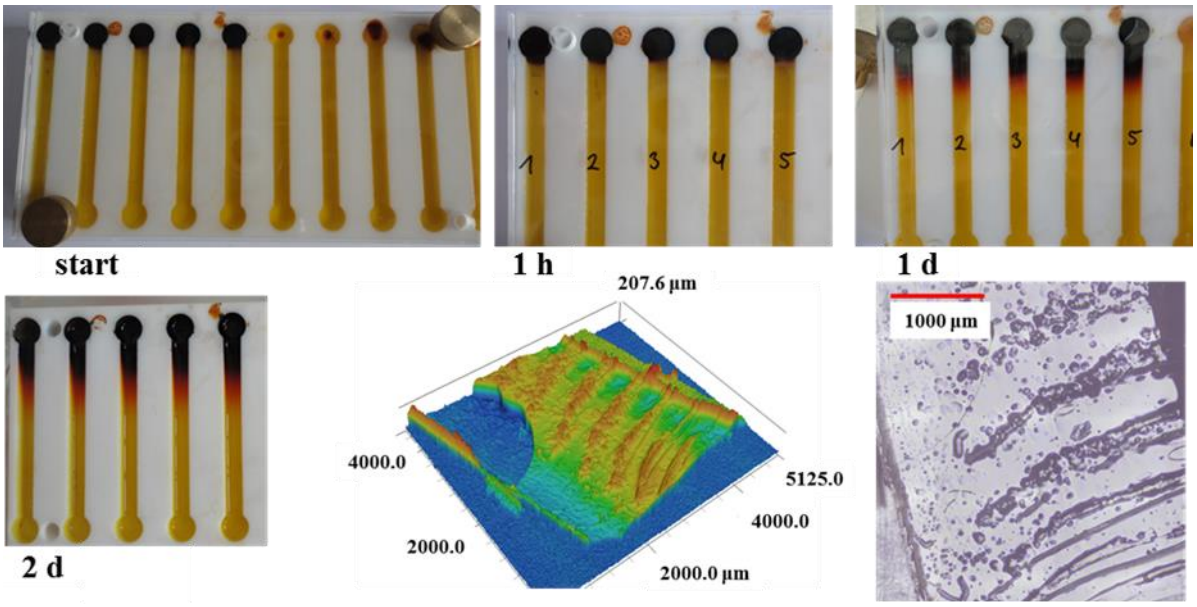

Figure 6.4: Optical images (top and bottom left) and laser profile analysis (bottom middle and right) of the $[Ru(bpy)_3]Cl_2$ / $K_2Cr_2O_7$ system. Optical images were taken at the beginning, after 1 hour, after 1 and 2 days.

6.3.2.2 Optimized parameter

Optimized conditions for all band forming systems can be found in this section. The reaction-diffusion times of all systems performed under HTS-plate conditions were up to 10 times higher compared to those under WETs conditions.

6.3.2.2.1 $FeSO_4$ / $AgNO_3$ system

Inner electrolyte: $FeSO_4$ (0.01 M in 10.0 w/w% gelatin (*type 0*) containing 0.1 w/w% ammonia). Outer electrolyte: $AgNO_3$ (0.3 M in 10 w/w% gelatin or 6 w/w% agarose).

6.3.2.2.2 Na_2MoO_4 / $AgNO_3$ system

Inner electrolyte: Na_2MoO_4 (0.1 M in 10.0 w/w% gelatin (*type 0*) in milliQ water). Outer electrolyte: $AgNO_3$ (0.3 M in 10 w/w% gelatin or 6 w/w% agarose).

6.3.2.2.3 Na_2WO_4 / $AgNO_3$ system

Inner electrolyte: Na_2WO_4 (0.05 M in 10.0 w/w% gelatin (*type 0*) in milliQ water). Outer electrolyte: $AgNO_3$ (0.3 M in 10 w/w% gelatin or 6 w/w% agarose).

6.3.2.2.4 $K_2Cr_2O_7$ / $AgNO_3$ system

Optimized parameters found in Chapter 3.

6.3.2.2.5 $[Fe(bpy)_3]Cl_2$ / $K_2Cr_2O_7$ system

Inner electrolyte: $[Fe(bpy)_3]Cl_2$ (0.005 M in 10.0 w/w% gelatin (*type 0*) in milliQ water). Outer electrolyte: $K_2Cr_2O_7$ (0.5 M in 10 w/w% gelatin or 6 w/w% agarose).

6.3.2.2.6 $[Ru(bpy)_3]Cl_2$ / $K_2Cr_2O_7$ system

Inner electrolyte: $[Ru(bpy)_3]Cl_2$ (0.005 M in 10.0 w/w% gelatin (*type 0*) in 0.1 M citric acid). Outer electrolyte: $K_2Cr_2O_7$ (0.3 M in 10 w/w% gelatin or 6 w/w% agarose).

6.3.2.2.7 $[Fe(pytpy)_2]Cl_2$ / $K_2Cr_2O_7$ system

Inner electrolyte: $[Fe(pytpy)_2]Cl_2$ (0.01 M in 10.0 w/w% gelatin (*type 0*) in milliQ water). Outer electrolyte: $K_2Cr_2O_7$ (0.5 M in 10 w/w% gelatin or 6 w/w% agarose).

6.3.2.2.8 $[Fe(pytpy)_2]Cl_2$ / $AgNO_3$ system

Inner electrolyte: $[Fe(pytpy)_2]Cl_2$ (0.05 M in 10.0 w/w% gelatin (*type 0*) in milliQ water). Outer electrolyte: $AgNO_3$ (0.3 M in 10 w/w% gelatin or 6 w/w% agarose).

6.3.2.2.9 $[Ru(bpy)_3]Cl_2$ / $KAuCl_4$ system

Inner electrolyte: $KAuCl_4$ (0.05 M in 10 w/w% gelatin (*type 0*) in 0.1 M HCl). Outer electrolyte: $[Ru(bpy)_3]Cl_2$ (0.1 M in 6.0 w/w% agarose).

6.3.2.2.10 $[Fe(bpy)_3]Cl_2$ / $KAuCl_4$ system

Inner electrolyte: $[Fe(bpy)_3]Cl_2$ (0.01 M in 10 w/w% gelatin (*type 0*) in 0.1 M HCl). Outer electrolyte: $KAuCl_4$ (0.1 M in 6 w/w% agarose).

6.3.3 Step 3: WETs

6.3.3.1 General

For each system the parameters were optimized under HTS conditions to obtain highly reproducible setups. These conditions were used to transform the working systems into meso- and nanoscales using the WETs technique. Precipitation band formation in a Liesegang type manner under WETs conditions was observed in the following systems (Table 6.4).

Table 6.4: Working compound A/B combinations under WETs conditions. Precipitation bands were observed for the green highlighted combinations.

	$AgNO_3$	$KAuCl_4$	$K_2Cr_2O_7$
Na_2MoO_4	yes	no	no
Na_2WO_4	yes	no	no
$[Fe(bpy)_3]Cl_2$	no	yes	yes
$[Ru(bpy)_3]Cl_2$	no	yes	yes
$[Fe(pytpy)_2]Cl_2$	yes	no	yes

Interestingly, it was not possible to downsize all systems found under HTS-plate conditions. It was not possible to produce band formation in the silver nitrate / iron(II) sulfate system under WETs conditions.

6.3.3.2 $[Ru(bpy)_3]Cl_2$ / $K_2Cr_2O_7$ system

In case of the $[Ru(bpy)_3]Cl_2$ / $K_2Cr_2O_7$ system, the coordination compound was the inner electrolyte and potassium dichromate the invading, outer electrolyte. Nice crystalline precipitation bands were observed (Image 6.1 left).

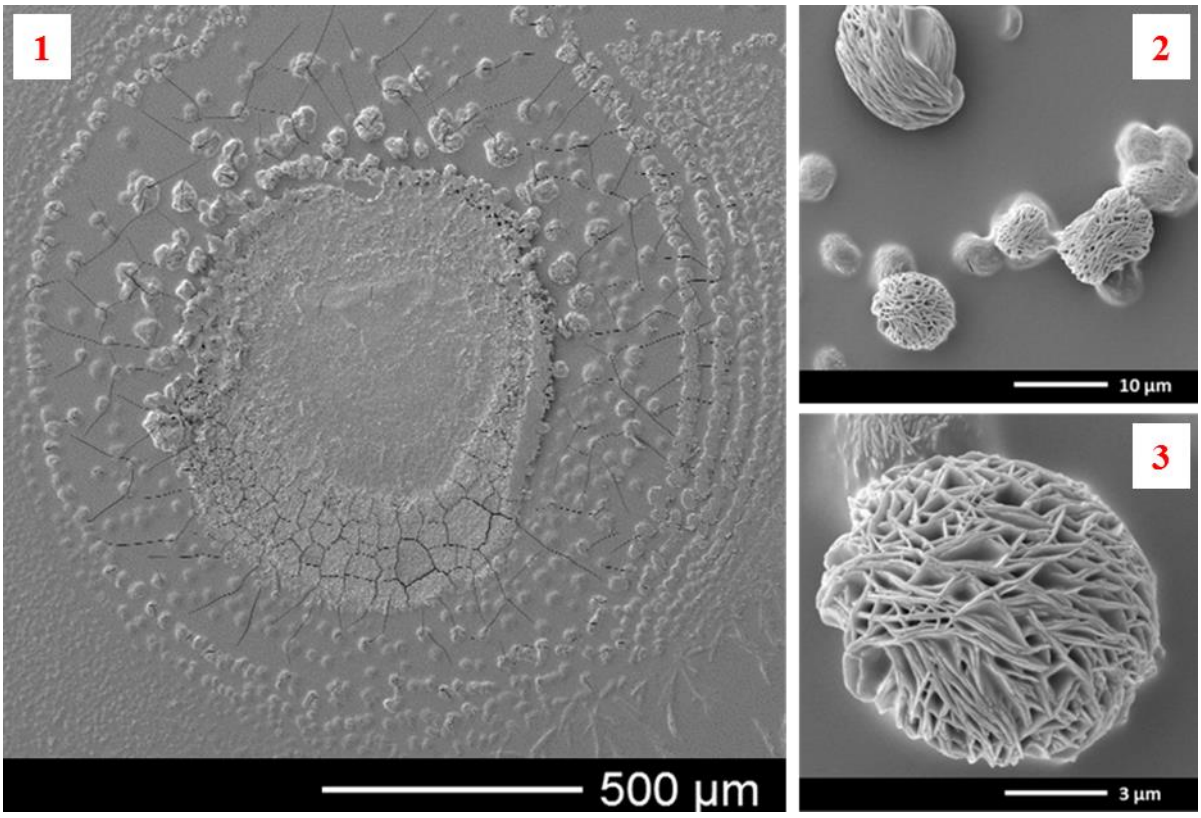

Image 6.1: SEM images of the precipitation bands observed in the $Ru(bpy)_3]Cl_2$ (0.05 M) + citric acid (0.1 M) and $K_2Cr_2O_7$ (0.3 M) system. Image 1: Overview of the observed precipitation bands. Image 2: Overview of the particles forming the bands. Image 3: Porous nano-sheet surface of the particles forming the bands.

In addition, SEM-images (Image 6.1) show that the periodic bands consist of an accumulation of micro- and nanoparticles. These particles offer a very large and porous surface which consists of sharp nano-sheets (Image 6.1 3). Energy dispersive X-ray spectroscopy (EDX) was used to examine the chemical composition of the material forming the bands (cf. Appendix C, p. 168). Therefore measurements were performed on the stamp/gelatin

interaction site, on top of a band, between two bands and on several places outside the precipitation site (background and crystals) (Figure 6.5).

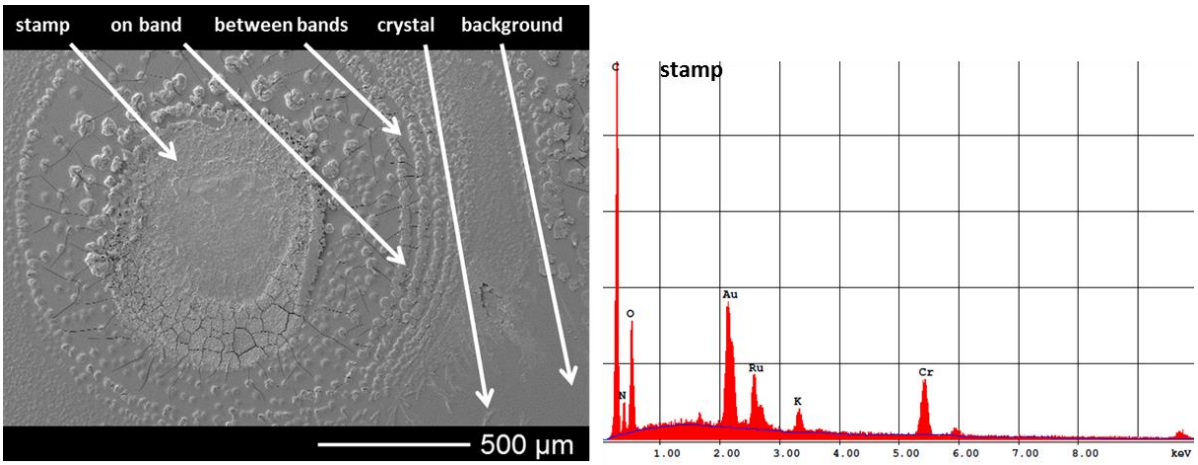

Figure 6.5: SEM image with indicated EDX measurement monitoring points (left) and corresponding EDX spectrum (right).

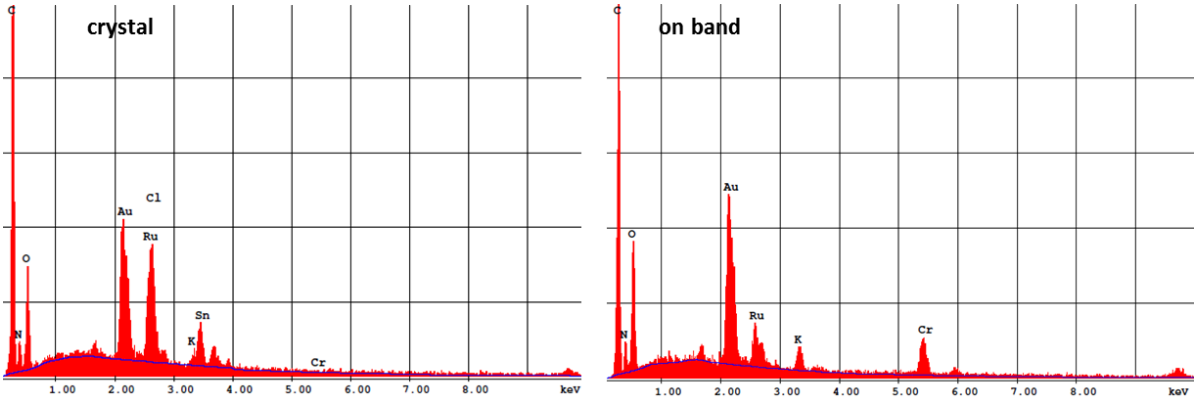

Figure 6.6: EDX spectrum of the crystals in the background where no precipitation bands were formed (left) and EDX spectrum measured on the particles forming the bands (right).

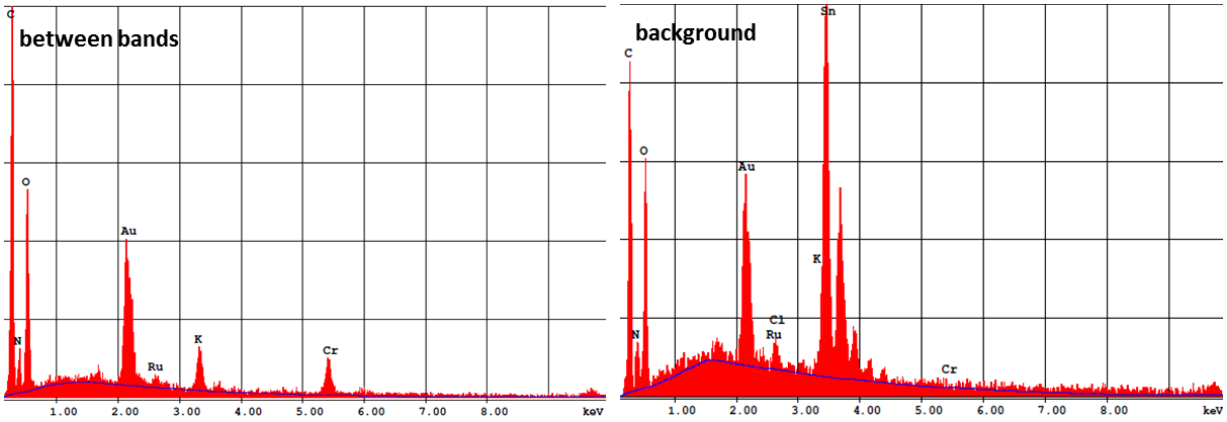

Figure 6.7: EDX spectrum of the material found between adjacent bands (left) and EDX spectrum of the background (right).

From the chemical composition shown in the EDX spectra (Figure 6.5-Figure 6.7) we can see that the material on the stamp interaction site and in the bands consists of ruthenium and

chromium, whereas almost no ruthenium was found between adjacent bands. Background measurements indicate that in the gelatin ruthenium is present but no chromium was found. The gold peak in all spectra comes from the gold sputtering which was used to make the probe conductive for the SEM. Carbon, oxygen, nitrogen and sulfur were neglected because these elements are also present in gelatin. The tin peak is caused from FTO which was used as carrier substrate. If we now focus on the ratios of the chemical elements in the EDX-spectra we can state that the material on the stamp interaction site and in the bands consists of $[Ru(bpy)_3]^{2+}$ which most likely has $[Cr_2O_7]^{2-}$ as the counter ion, since no precipitation was found if K_2CrO_4 was the invading outer electrolyte in the stamp. Since there is almost no ruthenium in the EDX spectrum measured between the bands (Figure 6.7), and due to the fact that this system is based on the postulated chromate/dichromate equilibrium, which is also crucial for the formation of primary bands observed in the classical Liesegang system, it is assumed that the material between the bands consists of potassium chromate. The background and the crystals in the corner of the non-reacted part consist only of $[Ru(bpy)_3]Cl_2$ (Figure 6.6), since no chromium was observed in the EDX measurements of these bands. If the sample is washed with plenty of water only the bands and the stamp interaction parts remain, which is an additional clue for the presence of insoluble $[Ru(bpy)_3][Cr_2O_7]$. A chemical equation can be proposed for the material forming the precipitation bands, which most likely describes our findings (Equation 15).

$$[Ru(bpy)_3]^{2+}(aq) + Cr_2O_7^{2-}(aq) \longrightarrow [Ru(bpy)_3][Cr_2O_7](s) \qquad (15)$$

However, XPS measurements are needed to obtain additional information about the oxidation state of the material in the bands to verify the proposed chemical model.

6.3.3.3 $[Fe(bpy)_3]Cl_2$ / $K_2Cr_2O_7$ system

In case of the $[Fe(bpy)_3]Cl_2$ / $K_2Cr_2O_7$ system, where the coordination compound was the inner electrolyte and potassium dichromate the outer electrolyte in the stamp, nice crystalline precipitation bands were observed (Image 6.2 and Image 6.3). SEM and EDX measurements were performed as in the case of the similar ruthenium system (Section 6.3.3.2). If the sample is washed with plenty of water, the red interband material is washed off, while the material forming the bands remains stable.

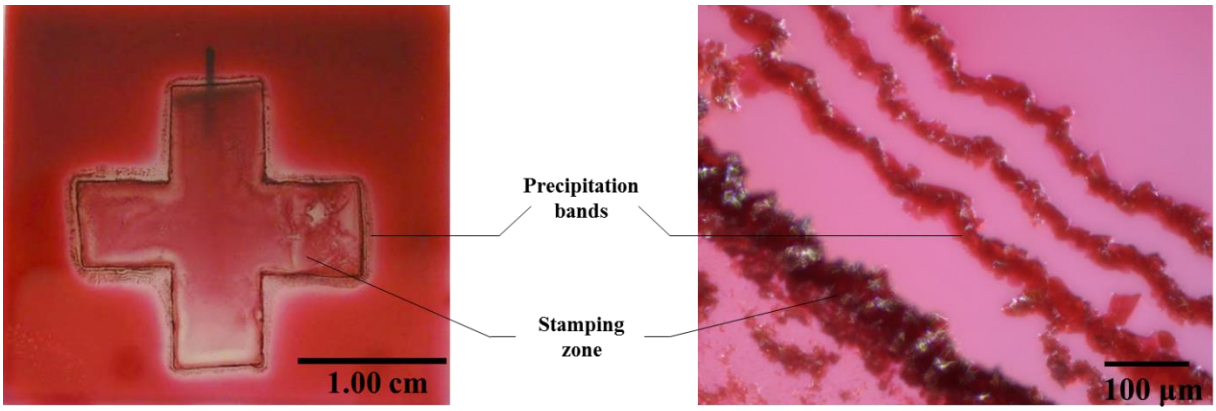

Image 6.2: Labelled images showing the crystalline precipitation bands observed in the $[Fe(bpy)_3]Cl_2$ / $K_2Cr_2O_7$ test system.

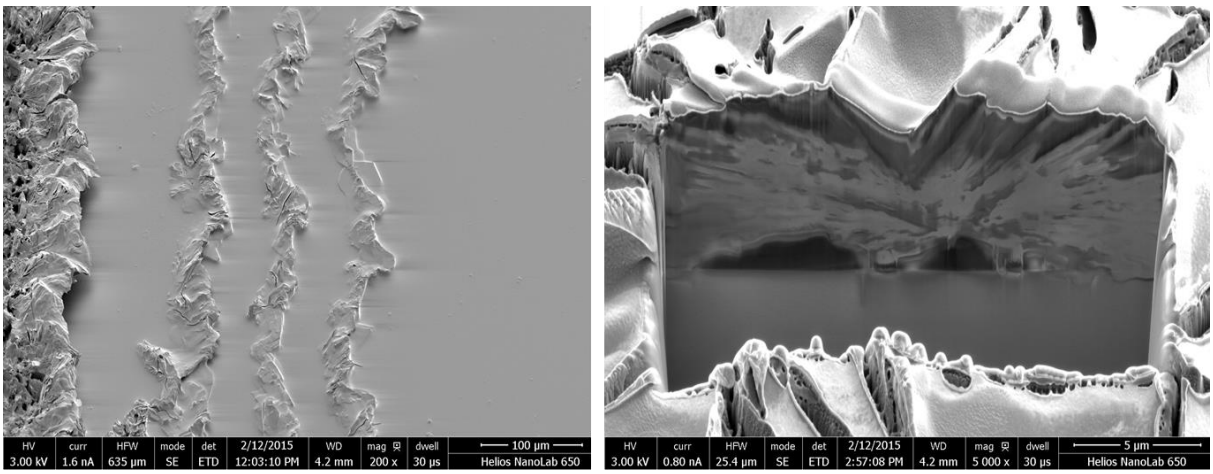

Image 6.3: SEM images showing the crystalline shape of the $[Fe(bpy)_3]Cl_2$ / $K_2Cr_2O_7$ precipitation bands (left) and SEM-FIB cross section image (right) showing how the crystals are structured within the bands.

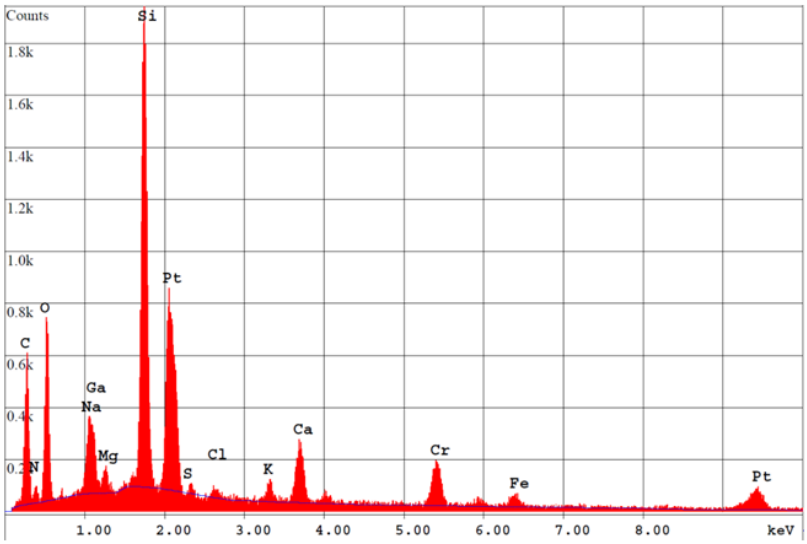

Element	w/w%	At%
C K	22.94	43.16
N K	5.77	9.31
O K	18.29	25.83
Na K	2.41	2.37
Ga L	3.72	1.21
Mg K	0.80	0.74
Si K	12.46	10.00
S K	0.19	0.17
Cl K	0.34	0.21
K K	0.75	0.43
Ca K	2.72	1.54
Cr K	3.82	1.66
Fe K	1.33	0.54
Pt L	24.46	2.83
Total	100.00	100.00

Figure 6.8: EDX measurement and quantitative material analysis of the bands in the $[Fe(bpy)_3]Cl_2$ / $K_2Cr_2O_7$ precipitation system.

From the EDX measurements concerning the $[Fe(bpy)_3]Cl_2$ / $K_2Cr_2O_7$ system (Appendix C, p. 169), the same conclusions can be drawn as for the ruthenium system, since the only difference between both systems is the metal. For this reason the following chemical equation can be proposed which most likely describes our findings of the material forming the bands (Equation 16).

$$[Fe(bpy)_3]^{2+}(aq) + Cr_2O_7^{2-}(aq) \longrightarrow [Fe(bpy)_3][Cr_2O_7](s) \qquad (16)$$

As for the ruthenium system, it is necessary to obtain additional information about the oxidation state of the material, in order to verify the proposed chemical model.

6.3.3.4 $[Fe(pytpy)_2]Cl_2$ / $AgNO_3$ system

Dense precipitation bands (Image 6.4) were observed in the case of the $[Fe(pytpy)_2]Cl_2$ / $AgNO_3$ system, where the WETs samples were prepared according to previous protocols (Section 2.4.2), using the coordination compound as inner, and silver nitrate as outer, electrolyte. SEM and EDX measurements were performed as in the case of the former presented systems (Appendix C, p. 170). If the sample is washed with plenty of water, the purple gelatin containing material between two adjacent bands is washed off, while the greyish purple material forming the bands remains stable.

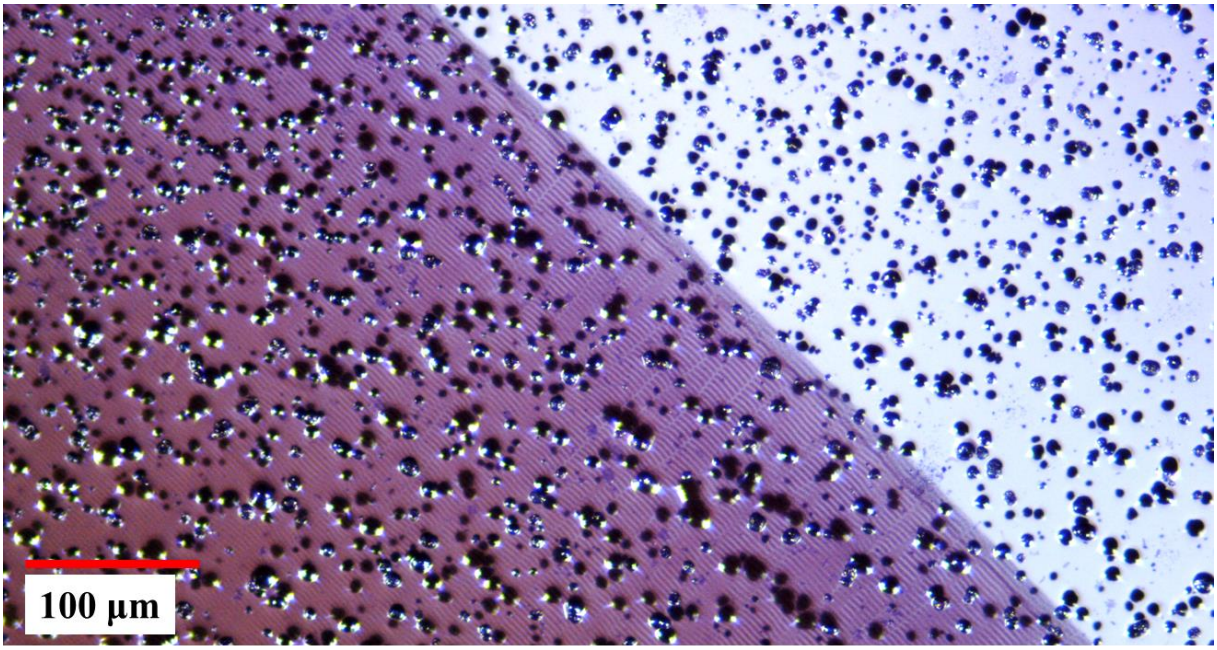

Image 6.4: Optical image of the precipitation bands observed in the $[Fe(pytpy)_2]Cl_2$ / $AgNO_3$ test system.

However, it is difficult to propose a chemical model which describes our findings, since in the repetition experiments no band formation was observed when silver nitrate was replaced by potassium nitrate. For this reason a possible counter ion exchange as observed before can be ruled out as possible explanation for the precipitation. Another additional point why this system has to be seen critical, is the shape of the precipitation bands (band width, space between two bands, average band height), which is very similar to the shape found in the fine structured silver system (Section 5.2). For this reason further investigations concerning the material composition are needed.

6.3.3.5 $[Fe(bpy)_3]Cl_2$ / $KAuCl_4$ system

In the case of the $[Fe(bpy)_3]Cl_2$ / $KAuCl_4$ system, the coordination compound was the inner and $KAuCl_4$ the outer electrolyte in the stamp (Image 6.5). The critical step was the loading of the stamp because when the stamps were loaded longer than 2 hours they lost their consistency. For this reason the best results were obtained if the stamp was loaded for only 45 minutes.

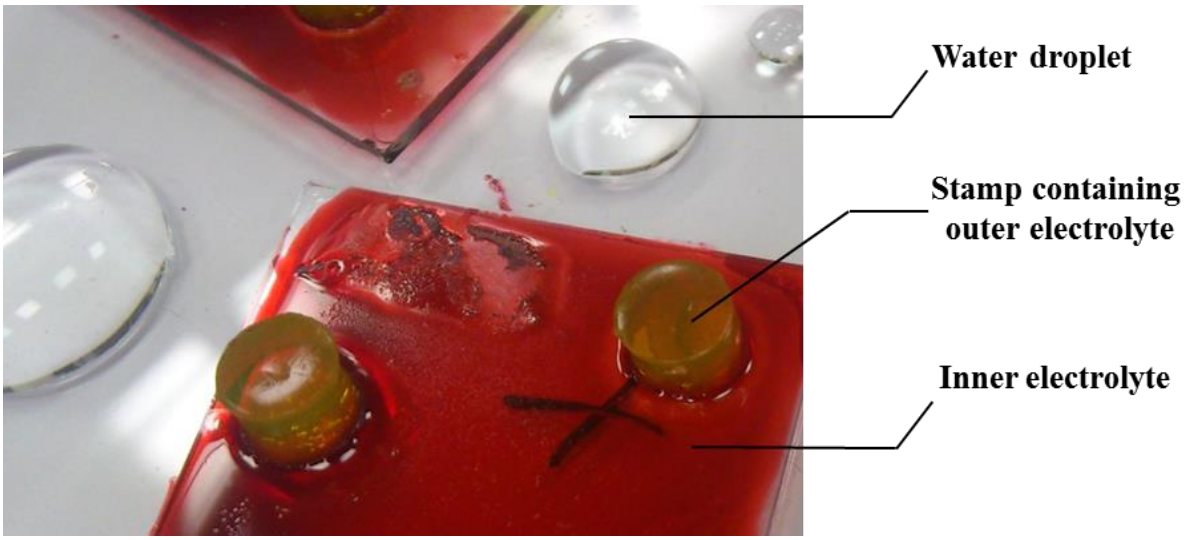

Image 6.5: Labelled optical image of the WETs setup for the $[Fe(bpy)_3]Cl_2$ / $KAuCl_4$ precipitation system.

Periodic precipitation bands were observed after 4 hours stamping/reaction-diffusion time (Figure 6.9).

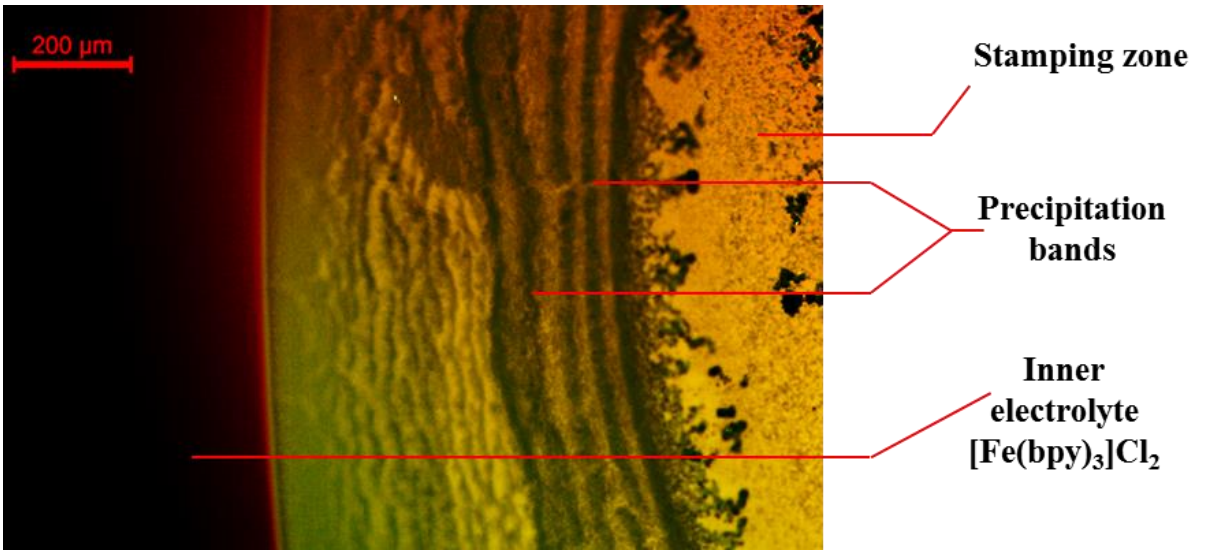

Figure 6.9: Labelled optical image of the precipitation bands, observed in the $[Fe(bpy)_3]Cl_2$ / $KAuCl_4$ system.

From the EDX measurements concerning the $[Fe(bpy)_3]Cl_2$ / $KAuCl_4$ system (Appendix C, p. 171), we can see that the material on the stamp interaction site and in the bands consists of ruthenium, gold and chloride whereas almost no ruthenium was found between adjacent bands. Background measurements indicate that in the gelatin ruthenium is present but no gold or chloride was found. The platinum peak in all spectra comes from the sputtering. Same as for all the other systems, gelatin was used as hydrogel, which explains the occurrence of carbon, oxygen, nitrogen and sulfur. Ruthenium, chloride and gold were found in the material forming the bands. Therefore it is most likely that the precipitation product consists of the coordination compound containing $[AuCl_4]^-$ as counter ion, but since additional analytical measurements are still in progress this has to be proposed rather than proved.

6.3.3.6 $[Ru(bpy)_3]Cl_2$ / $KAuCl_4$ system

In the case of the ruthenium system, the coordination compound was used as outer electrolyte and $KAuCl_4$ as inner electrolyte. Sample preparation was done according to previous protocols (Section 6.3.3.2). Gelatin film: 10 w/w% gelatin (*type 0*) in 0.1 M HCl and 0.05 M $KAuCl_4$ as inner electrolyte. Agarose stamps: 6 w/w agarose, loaded in 0.1 M $[Ru(bpy)_3]Cl_2$ for 24 h. Periodic precipitation bands (Image 6.6) were observed after a reaction diffusion time of 8 hours.

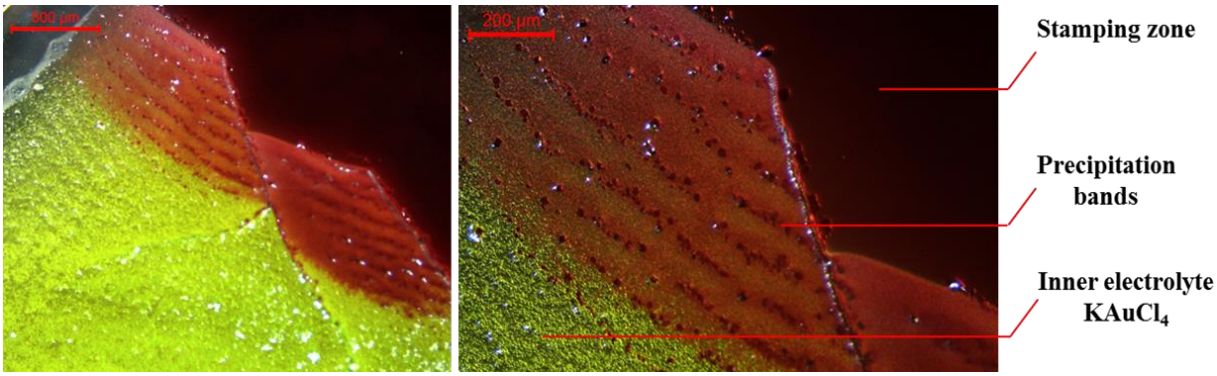

Image 6.6: Optical image (left) of the precipitation bands observed in the $[Ru(bpy)_3]Cl_2$ / $KAuCl_4$ system, where the gold salt was the inner electrolyte and the coordination compound the outer electrolyte. Right image: zoomed in left image. The contrast was increased to highlight the formed precipitation bands.

SEM and EDX measurements from this system fit very well with those from the iron containing system (cf. Appendix C, p. 172). For this reason it is assumed that the coordination compound forms precipitates when its counterion is exchanged. Since an excess of $KAuCl_4$ was present it is also assumed that the counterion of the precipitate forming the bands is $[AuCl_4]^-$. However, for a more detailed characterization additional analyses are required.

6.3.3.7 $AgNO_3$ / Na_2WO_4 precipitation system

In the case of the $AgNO_3$ / Na_2WO_4 precipitation system, WETs samples were prepared according to previous protocols, using Na_2WO_4 as inner and $AgNO_3$ as outer electrolytes. The influence on the shape of the precipitation bands were investigated using time dependent interaction experiments. For this reason each sample was stamped with 4 stamps (Image 6.7), and the reaction diffusion (i.e. interaction between stamp and hydrogel surface) was stopped by removing the stamps after 1, 4, 8 or 24 hours. Afterwards, the samples were analyzed by optical and electron microscopy. After only 1 hour a few bands were formed. After 4 hours, 3 times more bands were formed, in addition to some dispersed particles at the end of the precipitation zone (Image 6.8). Interestingly, the same amount of bands, showing the same dispersed particles at the end of the precipitation zone were observed after 8 and 24 h. Samples prepared at 300 rpm with a reaction diffusion time of 4 hours were further investigated by SEM (Image 6.9) and EDX as in the case of the former presented systems.

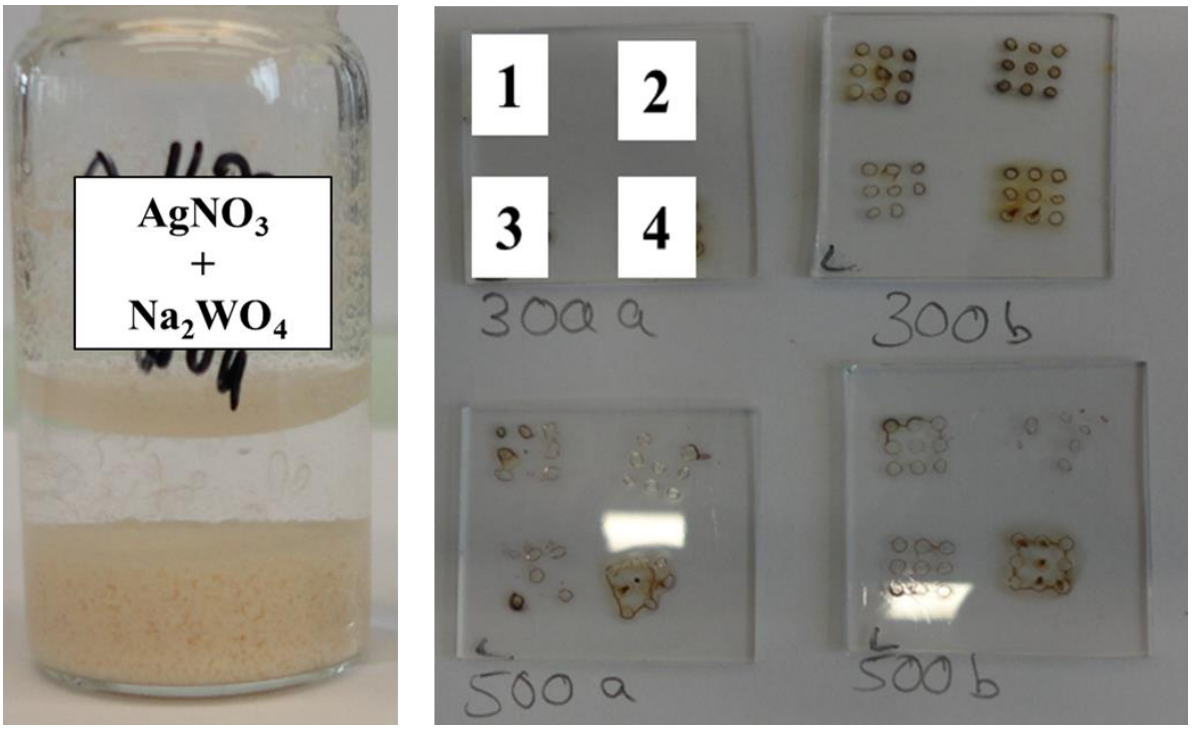

Image 6.7: Labelled optical images of the precipitation observed in solution (left) and under WETs conditions (right) by using the $AgNO_3$ / Na_2WO_4 precipitation system. Number 1-4 indicate the time after which the stamps were removed (1: after 1 h; 2: after 4 h; 3: after 8 h and 4: after 24 h).

Image 6.8: Optical image of the precipitation bands observed in the $AgNO_3$ / Na_2WO_4 WETs system.

EDX measurements (Appendix C, p. 173) were used to examine the chemical composition of the material forming the bands (Image 6.9 A, B).

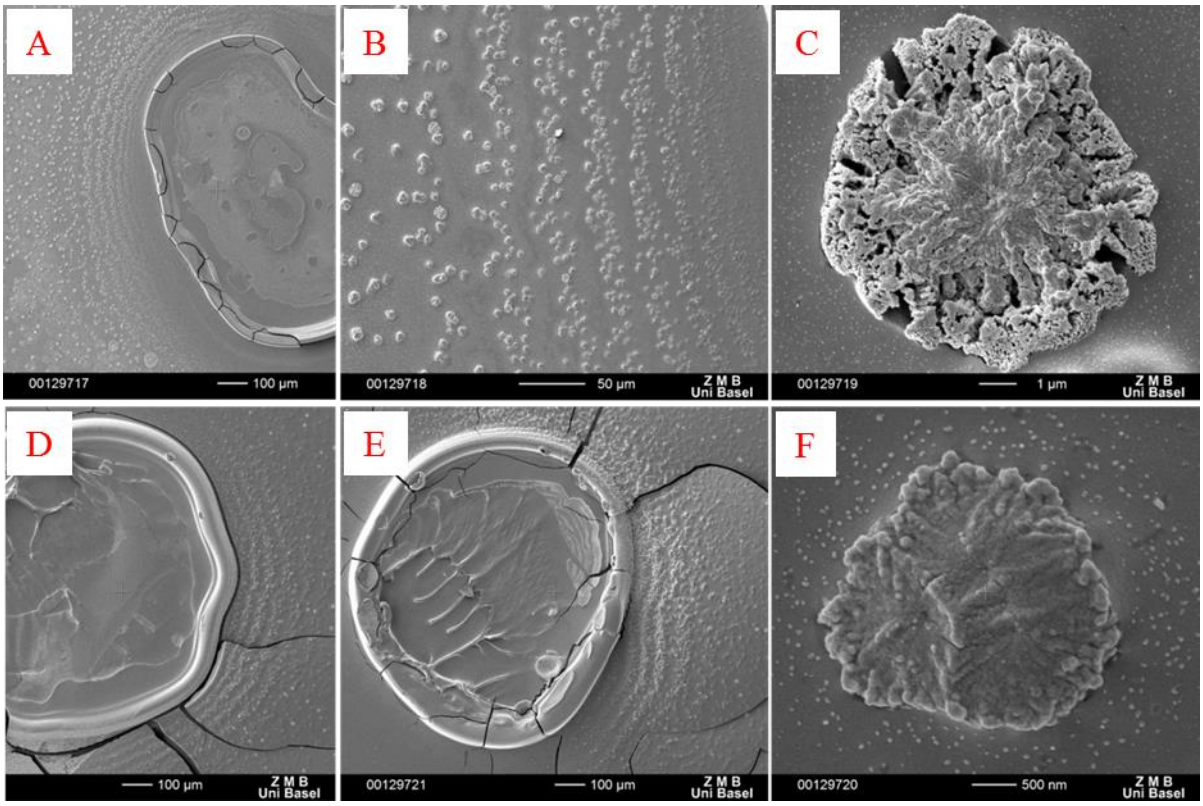

Image 6.9: SEM-Images of the precipitation bands observed in the $AgNO_3$ / Na_2WO_4 system. Image A and D: overview. Images B and E: zoomed overview of A and D. High resolution images of the particles forming the precipitation bands (C and F).

Therefore measurements were performed on the stamp/gelatin interaction site, on top of a band, between two bands and on several places outside the precipitation site (background). The platinum peak in all spectra arises from the sputter layer. Carbon, oxygen, nitrogen and sulfur were neglected, since all are present in gelatin. Silver and tungsten were found to be the main elements in the material forming the bands. Minor silver and tungsten were found between two bands, while only tungsten, but almost no silver was observed in the background measurements. If these findings are combined, a chemical model can be proposed which explains most likely the observations (Equation 17).

$$2Ag^{+}(aq) + WO_4^{2-}(aq) \longrightarrow Ag_2WO_4(s) \qquad (17)$$

This means that the main material forming the precipitation bands in this system is Ag_2WO_4.[236] However, this system is of special interest, since silver tungstate has attracted attention because of its photoluminescence[237] and photocatalytic properties.[238,239] But silver tungstate has three different lattice structures (α,β and γ), leading to different material properties.[240] For this reason additional studies concerning our precipitation system are necessary.

6.3.3.8 $AgNO_3$ / Na_2MoO_4 precipitation system

In the case of the $AgNO_3$ / Na_2MoO_4 precipitation system, the same preparative setups were used as the setup previously described for the tungstate system, with Na_2MoO_4 as inner and $AgNO_3$ as outer electrolytes. Time dependent interaction experiments were carried out in the same way (Image 6.10). At first the precipitates are off-white but they darken after one hour at ambient lab light. Precipitation bands were observed in all systems. Interestingly, band formation stopped after 8 hours because in the samples with 24 h reaction diffusion time, the length of diffusion propagation zone was almost identical with the length found after 8 hours. Also, the number of formed bands was almost identical. Best results were obtained for 4 hours interaction time (Image 6.11), since there the bands to evenly spread micro- and nanoparticles ratio was the highest compared to other reaction diffusion times.

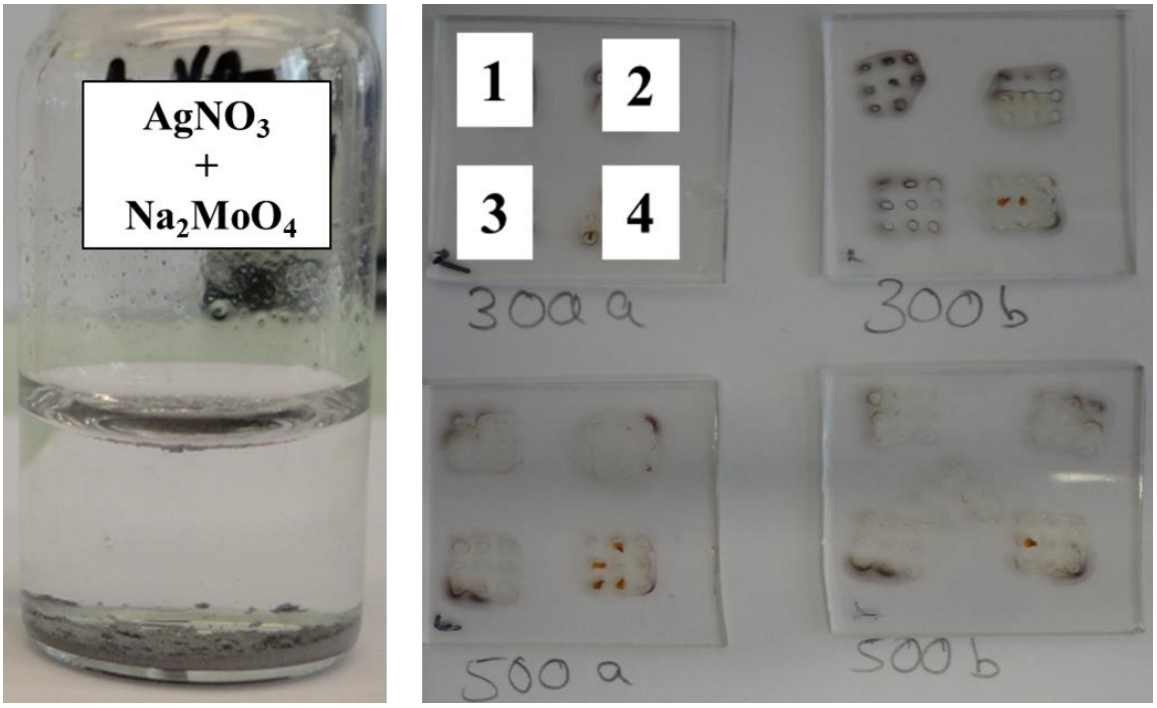

Image 6.10: Labelled optical images of the precipitation observed in solution (left) and under WETs conditions (right) by using the $AgNO_3$ / Na_2MoO_4 precipitation system. The numbering (1-4) indicates the time after which the stamps were removed (1: after 1 h; 2: after 4 h; 3: after 8 h and 4: after 24 h).

EDX measurements were carried out in the same way as for the other systems. From the measurements on the particles forming the bands (cf. Appendix C, p. 174), silver and molybdenum were found, while only molybdenum was found in the analysis between adjacent bands.

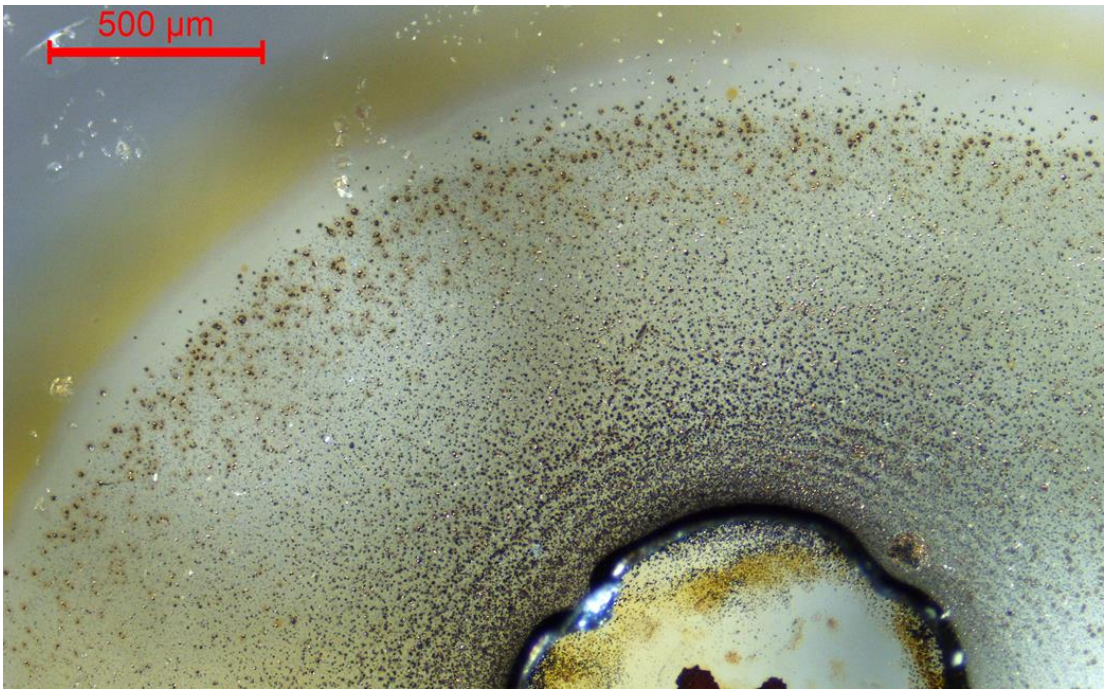

Image 6.11: Optical image of the precipitation bands observed in the $AgNO_3$ / Na_2MoO_4 system after 4 hours.

However, since the bands formed in this system are not well separated, silver contamination was found in the spectra of the measurements between the bands as well. As expected, only molybdenum but almost no silver was found in the background measurements. A possible explanation combining all our findings leads to the following chemical model (Equation 18).

$$2Ag^{+}(aq) + MoO_4^{2-}(aq) \longrightarrow Ag_2MoO_4(s) \qquad (18)$$

This means the main material forming the precipitation bands in this system is Ag_2MoO_4. However, depending on the setup conditions it is possible that polymorph silver molybdate clusters or other cluster like $Ag_2Mo_2O_7$ can form.[241] Nevertheless, this system is also of special interest, since silver molybdate has attracted attention because of its oxygen reduction properties.[240–242] By using the additional surface increase found in every Liesegang system, this makes the new system an ideal candidate to test as an oxygen reduction catalyst in fuel cells. A prerequisite is, however, that this system is further investigated and exact material composition is analyzed by additional methods like XPS.

6.4 Conclusion

Using our new fast screening setup we have developed a cheap, sustainable tool for the screening of band forming systems. These can then be downsized to the nano-scale using the WETs technique. By doing so we found that we can also produce nanostructures and Liesegang-type bands that consist of metal coordination compounds such as $[Fe(bpy)_3][Cr_2O_7]$ and $[Ru(bpy)_3][Cr_2O_7]$. It was also shown that it possible to produce precipitation bands out of the same coordination compound by using $[AuCl_4]$ as counter ions. Based upon these initial test systems we intend to create patterned structures and architectures containing many other catalytically active metal coordination compounds containing increased surface area. In case of the $[Ru(bpy)_3]Cl_2$ / $K_2Cr_2O_7$ system it was found that best reproducibility (80%) was obtained if citric acid was used as additive (pH 5.5*). In case of the $[Fe(bpy)_3]Cl_2$ / $K_2Cr_2O_7$ system best band forming conditions were observed under neutral conditions (pH 6.8-7.3*) (reproducibility 95%). *pH values measured in the 10 w/w% gelatin solution. Weak reproducibility (20% and 50%, respectively) was observed for precipitation bands forming systems containing $[Ru(bpy)_3]Cl_2$ / $KAuCl_4$, $[Fe(bpy)_3]Cl_2$ / $KAuCl_4$ system. Additionally, other precipitation band forming material combinations have been found leading to the formation of silver tungstate and silver molybdate. Both can be used as catalyst materials.

In summary this means that our fast screening setup is a powerful tool for discovering new Liesegang systems. Since in all system a surface increase compared to bulk material has been observed, it can be concluded that Liesegang type structures offer a great potential to be used in future applications.

7. Conclusion and outlook

In this thesis the periodic reaction-diffusion precipitation processes known as the Liesegang phenomenon were investigated. It was assumed that this phenomenon can be transformed and used to increase the active surface area of catalyst materials, without increasing the thickness of the material layer. However, for the controllable use of this phenomenon it was necessary to understand the precipitation process (Chapter 3). Therefore we started our investigations by using high resolution analytical tools such as STXM, NEXFAS and EDX to analyze the precipitation process occurring in the classical Liesegang system, where two different types of precipitation bands can be observed. The information gained from these investigations was used to propose a model, which describes the chemical origin of the precipitation bands in this system. It was found that the main material forming the primary bands was silver dichromate, while the main material forming the secondary bands was found to be silver chromate. By using SEM-FIB it was also possible to show that almost all particles forming the precipitation bands had a core structure, which has a different material composition as its surrounding material. Material analysis using the material contrast of back scattered electrons in electron microscopy (SEM) and energy dispersive X-ray analysis (EDX) showed that this material contains much more silver than the surrounding material. In addition, investigations concerning the origin of the core structures led to the discovery that the fine structured, so-called secondary, bands originate from a different chemical system than the larger primary precipitation bands (Chapter 4). Further investigations resulted in a new Liesegang system containing only fine structured bands. Material analysis using STEM, SEM, SEM-FIB, EDX and XPS showed that the material forming the precipitation bands in the new fine structured Liesegang system mainly consists of elemental silver. Furthermore, we were able to show that the Liesegang phenomenon is not limited to one specific hydrogel matrix, increasing the possibility of possible applications using this system. Although the results obtained from this silver system are very promising, further investigations concerning the model of the precipitation process are needed, because this process is not fully understood yet.

Since silver is known to be the most conductive element and the space between two adjacent bands was less than 10 μm, it was decided to investigate this system further (Chapter 5). Once all necessary parameters were determined and control over the precipitation process occurring in this system had been achieved, application screening was started. Screening experiments showed that these fine structured bands can be used to influence the light absorbing properties of other materials, but further investigations are needed to understand this effect/process.

Nevertheless it was also possible to prepare highly dense mesoscale grid structures, by implementation of a second layer containing fine structured precipitation bands. To increase the range of possible applications further, it was necessary to remove the hydrogel without destroying the precipitation structures. Therefore a simple, but efficient sintering protocol was developed, which allows full removal of the hydrogel and full transformation of the fine structured bands into elemental silver. Since one aim of my project was to increase the surface area of hematite by using the Liesegang phenomenon, it was decided to combine this environmental friendly and sustainable catalyst material with the fine structured silver bands. Four different setups were proposed to investigate the influence of the silver bands on the water oxidation efficiency of the anode used in photo electrochemical cells. However it was challenging to combine both systems (hematite with the silver bands) and most of the prepared anodes showed minor efficiency improvements. Nevertheless we showed that it is possible to combine both systems. For this reason further investigations concerning implementation of both systems and PEC measurements are needed.

By using our high throughput screening setup (Chapter 6), we have developed a simple and cheap method for searching new systems that form patterned structures. While combining the WET-stamping technique with the periodic precipitation process we were able to downsize the structures found in the “fast screening method”. This led to the production of very cheap, extremely porous and highly periodic nano-structures. In addition we have shown that we are able to increase the surface area of the used material by wet-processing simple starting materials. With the implementation of materials that show catalytic properties such as ruthenium(II) or iron(II) coordination compounds as well as silver tungstate and molybdate, we have shown that our technique can increase the active area of these catalysts. This can help to get a step closer to fulfill one of the future hopes of a green and sustainable production of materials and energy. Nevertheless further investigations concerning the material composition of the discovered systems as well as their use as catalysts are necessary.

In summary this research project showed that Liesegang type systems can be used for the simple and cheap production of highly periodic structures which possess a thin layer with a high surface area. Various combinations of different materials, salts and substrates open a very wide field of possible applications. The silver-micro/nanowire system can for example be used as diffraction gratings. The coordination compound systems can be used as a model system for the increase of the catalytic active surface area of other coordination compounds. In case of the hematite containing system the high conductivity of the silver forming the precipitation bands can possibly increase the conductivity of the photo anode, which should

lead to a higher efficiency.

In the future, the systems shown and discussed in this thesis will be tested at the EMPA-functional ceramic materials for energy and environment research. There we have with our collaboration partners *Dr. Rita Tóth* and *Dr. Artur Braun* experienced partners whose research is focused on safe, renewable and sustainable energy sources. In addition we will also continue screening for new materials which have the ability to form self-organized/self-assembled periodic structures, e.g. conducting materials (Ag, Au, Pt, …) or other coordination compounds. They can be used to form nanowires and bands which can for example be used in electronic devices or for catalytic purposes. However, the examples in this thesis represent only a small part of the possibilities which can be reached by using Liesegang type phenomena.

Appendix A: References

(1) BP. BP Statistical Review of World Energy June 2014 www.bp.com/content/dam/bp/excel/Energy-Economics/statistical-review-2014/BP-Statistical_Review_of_world_energy_2014_workbook.xlsx (accessed Mar 31, 2015).

(2) International Energy Agency. 2014 Key World Energy STATISTICS http://www.iea.org/publications/freepublications/publication/KeyWorld2014.pdf (accessed Mar 30, 2015).

(3) International Energy Agency. *Annual Energy Outlook 2014 with projections to 2040*; 2014.

(4) Bp. Energy Outlook 2035 www.bp.com/content/dam/bp/excel/Energy-Economics/energy-outlook-2015/BP-Energy-Outlook-2035-Summary-Tables-2015.xls (accessed Mar 30, 2015).

(5) Naumov, A. The Energy Outlook to 2030: global trends and what can bend them? http://www.bp.com/en/global/corporate/about-bp/energy-economics/energy-outlook.html (accessed Mar 31, 2015).

(6) International Energy Agency. World Energy Outlook 1998.

(7) Bashford, A. *Global population : history, geopolitics, and life on earth*; Columbia studies in international and global history; New York : Columbia University Press: New York, 2014.

(8) World Health Organization. WHO population statistics.

(9) Cincotta, Richard P., Gorenflo, L. J. *Human Population*; Cincotta, Richard P., Gorenflo, L. J., Ed.; Ecological studies,; New York : Springer: New York New York, 2001.

(10) United Nations. *World Population Prospects The 2012 Revision Volume I : Comprehensive Tables*; 2013; Vol. 1.

(11) World Health Organization. Trends in Maternal Mortality : 1990 to 2013 Executive Summary http://apps.who.int/iris/bitstream/10665/112697/1/WHO_RHR_14.13_eng.pdf?ua=1 (accessed Mar 29, 2015).

(12) UNICEF. Levels & Trends in Child Mortality, Report 2014 http://www.who.int/maternal_child_adolescent/documents/levels_trends_child_mortality_2014/en/ (accessed Mar 2, 2015).

(13) Unicef. Child Poverty Report 2014 http://www.unicef.org/media/files/ChildPovertyReport.pdf (accessed Mar 25, 2015).

(14) Murray, W. E. *Geographies of globalization*; Routledge contemporary human geography; 2nd ed.; Abingdon : Routledge: Abingdon, 2015.

(15) *Essential concepts of global environmental governance*; Orsini, A., Ed.; Abingdon : Routledge: Abingdon, 2015.

(16) Kail, R. V. *Essentials of human development : A life-span view*; Cavanaugh, J. C., Ed.; Wadsworth Cengage Learning, 2014.

(17) International Energy Agency. *Policies for renewable heat. An integrated approach*; 2012.

(18) International Energy Agency. Definition: Non-Energy Use http://www.iea.org/interenerstat_v2/definitions/results.asp?id=168&Type=Flows (accessed Mar 15, 2015).

(19) Gurjar, B. R.; Butler, T. M.; Lawrence, M. G.; Lelieveld, J. *Atmos. Environ.* **2008**, *42*, 1593.

(20) Ardebili, L.; Babazadeh, V. M.; Mammadov, M.; Navi, P. *World Appl. Sci. J.* **2011**, *14*, 1141.

(21) Zimmer, L. A.; Asmund, G.; Johansen, P.; Mortensen, J.; Hansen, B. W. *Polar Biol.* **2011**, *34*, 431.

(22) Knuckles, T. L.; Stapleton, P. a.; Minarchick, V. C.; Esch, L.; Mccawley, M.; Hendryx, M.; Nurkiewicz, T. R. *Microcirculation* **2013**, *20*, 158.

(23) International Atomic Energy Agency. *IAEA Bull.* **2013**, *54*, 5.

(24) International Atomic Energy Agency. *IAEA Bull.* **2013**, *54*, 1.

(25) Yoshikawa, H. *Trends Sci.* **2004**, *9*, 10.

(26) United States Nuclear Regulatory Commission. *Chernobyl Nucl. Power Plant Accid.* **2008**.

(27) Rahu, M. *Eur. J. Cancer* **2003**, *39*, 295.

(28) Cardis, E.; Howe, G.; Ron, E.; Bebeshko, V.; Bogdanova, T.; Bouville, A.; Carr, Z.; Chumak, V.; Davis, S.; Demidchik, Y.; Drozdovitch, V.; Gentner, N.; Gudzenko, N.; Hatch, M.; Ivanov, V.; Jacob, P.; Kapitonova, E.; Kenigsberg, Y.; Kesminiene, A.; Kopecky, K. J.; Kryuchkov, V.; Loos, A.; Pinchera, A.; Reiners, C.; Repacholi, M.; Shibata, Y.; Shore, R. E.; Thomas, G.; Tirmarche, M.; Yamashita, S.; Zvonova, I. *J. Radiol. Prot.* **2006**, *26*, 127.

(29) Lindell, M. K.; Perry, R. W. *Risk Anal.* **1990**, *10*, 393.

(30) United Nations Scientific Committee on the Effects of Atomic Radiation. *Sources And Effects Of Ionizing Radiation*; 2008; Vol. I.

(31) Ten Hoeve, J. E.; Jacobson, M. Z. *Energy Environ. Sci.* **2012**, *5*, 8743.

(32) Japan Atomic Energy Agency. *JAEA-Review 2014-051: Remediation of Contaminated Areas in the Aftermath of the Accident at the Fukushima Daiichi Nuclear Power Station: Overview, Analysis and Lessons Learned Part 1: A Report on the "Decontamination Pilot Project";* 2015.

(33) Us Nuclear Regulatory Commission. *Radioact. Waste Prod. Storage, Dispos.* **2002**.

(34) Ewing, R. C.; Lutze, W.; Editors, G. *MRS Bull.* **1994**, 16.

(35) Western, R. *Radiat. Prot. Dosimetry* **1996**, *68*, 143.

(36) Freiesleben, H. *EPJ Web Conf.* **2013**, *54*, 1006.

(37) Radkau, J. *Aufstieg und Fall der deutschen Atomwirtschaft*; Hahn, L., Ed.; München : Oekom: München, 2013.

(38) Wolling, J. *Fukushima und die Folgen : Medienberichterstattung, öffentliche Meinung, politische Konsequenzen*; Wolling, J., Ed.; NEU - Nachhaltigkeits-, Energie- und Umweltkommunikation; Ilmenau : Universitätsverlag: Ilmenau, 2014.

(39) Lundsgaard-Hansen, J. *Energiestrategie 2050 - das Eis ist dünn : die Schweiz und Deutschland auf neuen Wegen*; NZZ Libro; Zürich : Verlag Neue Zürcher Zeitung: Zürich, 2013.

(40) Guggenbühl, H. *Die Energiewende : und wie sie gelingen kann*; Zürich : Rüegger: Zürich, 2013.

(41) Bundesministerium für Umwelt Naturschautz Bau und Reaktorsicherheit. *Gesetz über die friedliche Verwendung der Kernenergie und den Schutz gegen ihre Gefahren (Atomgesetz)*; 2013.

(42) Bundesamt für Energie (Schweiz). *Energieperspektiven 2050* **2013**.

(43) Bundesrepublik Deutschland. *Gesetz für den Ausbau erneuerbarer Energien (Erneuerbare-Energien-Gesetz - EEG)*; 2014.

(44) Eidgenössisches Departement Für Umwelt, Verkehr, E. und K. *Schweizerische Statistik der erneuerbaren Energien. Ausgabe 2013 Vorabzug*; 2014.

(45) Bundesministerium für Energie und Wirtschaft (Deutschland). *Bundesbericht Energieforschung*; 2014.

(46) Umweltbundesamt (Deutschland). Erneuerbare Energien in Zahlen http://www.umweltbundesamt.de/themen/klima-energie/erneuerbare-energien/erneuerbare-energien-in-zahlen (accessed Mar 25, 2015).

(47) Statistisches Bundesamt (Deutschland). Erneuerbare Energieträger https://www.destatis.de/DE/ZahlenFakten/Wirtschaftsbereiche/Energie/Erzeugung/Tabellen/ErneuerbareEnergie.html (accessed Mar 25, 2015).

(48) Statistisches Bundesamt (Deutschland). Bruttostromerzeugung 2013 https://www.destatis.de/DE/ZahlenFakten/ImFokus/Energie/ErneuerbareEnergien2013.html (accessed Mar 15, 2015).

(49) Schiermeier, Q.; Tollefson, J.; Scully, T.; Witze, A.; Morton, O. Energy alternatives: Electricity without carbon. *Nature*, 2008, *454*, 816.

(50) International Energy Agency. *Solar Energy Perspectives*; 2011.

(51) Royal Society of Chemistry. *Solar Fuels and Artificial Photosynthesis*; 2012.

(52) Herrmann, U.; Kearney, D. W. *J. Sol. Energy Eng.* **2002**, *124*, 145.

(53) Michels, H.; Pitz-Paal, R. *Sol. Energy* **2007**, *81*, 829.

(54) Jamel, M. S.; Abd Rahman, A.; Shamsuddin, a. H. *Renew. Sustain. Energy Rev.* **2013**, *20*, 71.

(55) Trainer, T. *Renewable Energy Cannot Sustain A Consumer Society*; Dordrecht : Springer Netherlands: Dordrecht, 2007.

(56) *Photoelectrochemical materials and energy conversion processes*; Alkire, R. C., Ed.; Advances in electrochemical science and engineering; Weinheim : WILEY-VCH Verlag: Weinheim, 2010.

(57) Decoppet, J.-D.; Moehl, T.; Babkair, S. S.; Alzubaydi, R. A.; Ansari, A. A.; Habib, S. S.; Zakeeruddin, S. M.; Schmidt, H.-W.; Grätzel, M. *J. Mater. Chem. A* **2014**, *2*, 15972.

(58) Nuraje, N.; Dang, X.; Qi, J.; Allen, M. a.; Lei, Y.; Belcher, A. M. *Adv. Mater.* **2012**, *24*, 2885.

(59) Grätzel, M. *Nat. Mater.* **2014**, *13*, 838.

(60) National Renewable Energy Laboratory. Best Research-cell efficiencies Chart http://www.nrel.gov/ncpv/images/efficiency_chart.jpg (accessed Mar 29, 2015).

(61) Dimroth, F.; Grave, M.; Beutel, P.; Fiedeler, U.; Karcher, C.; Tibbits, T. N. D.; Oliva, E.; Siefer, G.; Schachtner, M.; Wekkeli, A.; Bett, A. W.; Krause, R.; Piccin, M.; Blanc, N.; Drazek, C.; Guiot, E.; Ghyselen, B.; Salvetat, T.; Tauzin, A.; Signamarcheix, T.; Dobrich, A.; Hannappel, T.; Schwarzburg, K. *Prog. Photovoltaics Res. Appl.* **2014**, *22*, 277.

(62) Richter, A.; Hermle, M.; Glunz, S. W. *IEEE J. Photovoltaics* **2013**, *3*, 1184.

(63) Jungbluth, N.; Jungbluth, N.; Tuchschmid, M.; Tuchschmid, M.; de Wild-Scholten, M.; de Wild-Scholten, M. *Life Cycle Assessment of Photovoltaics: Update of ecoinvent data v2. 0*; 2008.

(64) Jungbluth, N. *Prog. Photovoltaics Res. Appl.* **2005**, *13*, 429.

(65) Stoppato, A. *Energy* **2008**, *33*, 224.

(66) Kannan, R.; Leong, K. C. **2006**, *80*, 555.

(67) Öhrlund Isak. *Future Metal Demand from Photovoltaic Cells and Wind Turbines*; 2012.

(68) Jordan, D. C.; Kurtz, S. R. *Prog. Photovoltaics Res. Appl.* **2013**, *21*, 12.

(69) Gao, F.; Wang, Y.; Zhang, J.; Shi, D.; Wang, M.; Humphry-Baker, R.; Wang, P.; Zakeeruddin, S. M.; Grätzel, M. *Chem. Commun.* **2008**, *7345*, 2635.

(70) Jeon, N. J.; Noh, J. H.; Yang, W. S.; Kim, Y. C.; Ryu, S.; Seo, J.; Seok, S. Il. *Nature* **2015**, *517*, 476.

(71) Li, Z.; Luo, W.; Zhang, M.; Feng, J.; Zou, Z. *Energy Environ. Sci.* **2013**, *6*, 347.

(72) Kim, J. Y.; Magesh, G.; Youn, D. H.; Jang, J.-W.; Kubota, J.; Domen, K.; Lee, J. S. *Sci. Rep.* **2013**, *3*, 2681.

(73) Alexander, B. D.; Kulesza, P.; Rutkowska, I.; Solarska, R.; Augustynski, J. *Jpournal Mater. Chem.* **2008**, *18*, 2298.

(74) Grätzel, M. *Nature* **2001**, *414*, 338.

(75) Van de Krol, R.; Liang, Y.; Schoonman, J. *J. Mater. Chem.* **2008**, *18*, 2311.

(76) Bak, T.; Nowotny, J.; Rekas, M.; Sorrell, C. *Int. J. Hydrogen Energy* **2002**, *27*, 991.

(77) Leygraf, C.; Hendewerk, M.; Somorjai, G. A. *J. Phys. Chem.* **1982**, *86*, 4484.

(78) Sivula, K.; Le Formal, F.; Grätzel, M. *ChemSusChem* **2011**, *4*, 432.

(79) Klahr, B.; Gimenez, S.; Fabregat-Santiago, F.; Hamann, T.; Bisquert, J. *J. Am. Chem. Soc.* **2012**, *134*, 4294.

(80) Bora, D. K.; Braun, A.; Constable, E. C. *Energy Environ. Sci.* **2013**, *6*, 407.

(81) Cesar, I.; Sivula, K.; Kay, A.; Zboril, R.; Grätzel, M. *J. Phys. Chem. C* **2009**, *113*, 772.

(82) Bakhtina, N. a.; Loeffelmann, U.; MacKinnon, N.; Korvink, J. G. *Adv. Funct. Mater.* **2015**, *25*, 1683.

(83) Greener, J.; Li, W.; Ren, J.; Voicu, D.; Pakharenko, V.; Tang, T.; Kumacheva, E. *Lab Chip* **2010**, *10*, 522.

(84) Lee, S. H.; Moon, J. J.; West, J. L. *Biomaterials* **2008**, *29*, 2962.

(85) Demers, L.; Ginger, D.; Park, S.; Li, Z.; Chung, S.; Mirkin, C. *Science* **2002**, *296*, 1836.

(86) Piner, R. D. *Science (80-.).* **1999**, *283*, 661.

(87) Campbell, C. J.; Baker, E.; Fialkowski, M.; Bitner, A.; Smoukov, S. K.; Grzybowski, B. A. *J. Appl. Phys.* **2005**, *97*, 126102.

(88) Smoukov, S. K.; Lagzi, I.; Grzybowski, B. a. *J. Phys. Chem. Lett.* **2011**, *2*, 345.

(89) Grzybowski, B. A.; Bishop, K. J. M.; Campbell, C. J.; Fialkowski, M.; Smoukov, S. K. *Soft Matter* **2005**, *1*, 114.

(90) Walliser, R. M.; Boudoire, F.; Orosz, E.; Tóth, R.; Braun, A.; Constable, E. C.; Rácz, Z.; Lagzi, I. *Langmuir* **2015**, *31*, 1828.

(91) Bensemann, I. T.; Fialkowski, M.; Grzybowski, B. *J. Phys. Chem. B* **2005**, *109*, 2774.

(92) Lagzi, I.; Kowalczyk, B.; Grzybowski, B. *J. Am. Chem. Soc.* **2010**, *132*, 58.

(93) Campbell, C. J.; Baker, E.; Fialkowski, M.; Grzybowski, B. a. *Appl. Phys. Lett.* **2004**, *85*, 1871.

(94) Cho, C.; Valverde, L.; Ozin, G. a.; Zacharia, N. S. *Langmuir* **2010**, *26*, 13637.

(95) Campbell, C. J.; Fialkowski, M.; Bishop, K. J. M.; Grzybowski, B. a. *Langmuir* **2009**, *25*, 9.

(96) Grzybowski, B. A. *Chemistry in Motion: Reaction-Diffusion Systems for Micro- and Nanotechnology*; 2009.

(97) Braun, A.; Toth, R. SNF Project 137868: Reaction-diffusion processes for the growth of patterned structures and architectures: A bottom-up approach for photoelectrochemical electrodes http://p3.snf.ch/Project-137868 (accessed Mar 25, 2015).

(98) Liesegang, R. E. *Naturwissenschaftliche Wochenschrift* **1896**, 353.

(99) Izsák, F.; Lagzi, I. *J. Chem. Phys.* **2005**, *122*, 1.

(100) Sultan, R. F.; Abdel-Rahman, M. *Lat. Am. J. Solids Struct.* **2013**, *10*, 59.

(101) Holba, V. *Colloid Polym. Sci.* **1989**, *267*, 456.

(102) Lexa, D.; Holba, V. *Colloid Polym. Sci.* **1993**, *271*, 884.

(103) Friedeberg, H. *Science (80-.).* **1954**, *119*, 651.

(104) Nabika, H.; Sato, M.; Unoura, K. *Langmuir* **2014**, *30*, 5047.

(105) Lagzi, I. *Langmuir* **2012**, *28*, 3350.

(106) Hantz, P. *Phys. Chem. Chem. Phys.* **2002**, *4*, 1262.

(107) Hantz, P. *J. Phys. Chem. B* **2000**, *104*, 4266.

(108) Chopard, B.; Droz, M.; Magnin, J.; Rácz, Z.; Zrinyi, M. **1998**, 8.

(109) Lagzi, I.; Ueyama, D. *Chem. Phys. Lett.* **2009**, *468*, 188.

(110) Balsamo, F.; Bezerra, F. H. R.; Vieira, M. M.; Storti, F. *Geol. Soc. Am. Bull.* **2013**, *125*, 913.

(111) Allègre, C. J.; Provost, A.; Jaupart, C. *Nature* **1981**, *294*, 223.

(112) Moxon, T. *Agate : microstructure and possible origin*; Terra Publ: Doncaster, 1996.

(113) Katz, L. B. K.; Ehya, H. *Diagn. Cytopathol.* **1990**, *6*, 197.

(114) Pulvertaft, R. J. V.; Greening, J. R.; Haynes, J. A. *J. Pathol. Bacteriol.* **1947**, *59*, 293.

(115) Sneige, N.; Dekmezian, R. H.; Silva, E. G.; Cartwright, J.; Ayala, A. G. *Am. J. Clin. Pathol.* **1988**, *89*, 148.

(116) Misselevich, I.; Zlotnik, M.; Boss, J. H. *Diagn. Cytopathol.* **2004**, *31*, 173.

(117) Tuur, S. M.; Nelson, A. M.; Gibson, D. W.; Neafie, R. C.; Johnson, F. B.; Mostofi, F. K.; Connor, D. H. *Am. J. Surg. Pathol.* **1987**, *11*, 598.

(118) Medvinskiĭ, A. B.; Rusakov, A. V; Tsyganov, M. A.; Kravchenko, V. V. *Biofizika* **2000**, *45*, 525.

(119) Kumar, N.; Jain, S. *Acta Cytol.* **2000**, *44*, 429.

(120) Levy, J.; Ilsar, M.; Deckel, Y.; Pe'er, J. *Clin. Experiment. Ophthalmol.* **2009**, *37*, 313.

(121) Wood, A.; O'Donnell, M.; Casado, A. *Curr. Urol.* **2013**, *7*, 37.

(122) Hein, I. *Am. J. Bot.* **1930**, *17*, 143.

(123) Barge, L. M.; Nealson, K. H.; Petruska, J. *Chem. Phys. Lett.* **2010**, *493*, 340.

(124) Karam, T.; El-Rassy, H.; Sultan, R. *J. Phys. Chem. A* **2011**, *115*, 2994.

(125) Volford, A.; Izsák, F.; Ripszám, M.; Lagzi, I. *Langmuir* **2007**, *23*, 961.

(126) Xie, S.; Zhang, X.; Yang, S.; Paau, M. C.; Xiao, D.; Choi, M. M. F. *RSC Adv.* **2012**, *2*, 4627.

(127) Al-Ghoul, M.; Ammar, M.; Al-Kaysi, R. O. *J. Phys. Chem. A* **2012**, *116*, 4427.

(128) Ramaiah, Subba, K. *Proc. Indian Acad. Sci.* **1939**, *A*, 455.

(129) Brough, H. M. and G. A. *J. Biol. Chem.* **1923**, *58*, 415.

(130) Illo Hein. *Am. J. Bot.* **1930**, *17*, 143.

(131) Smoukov, S. K.; Bitner, A.; Campbell, C. J.; Kandere-Grzybowska, K.; Grzybowski, B. a. *J. Am. Chem. Soc.* **2005**, *127*, 17803.

(132) Petruska, J.; Barge, L. M. *Chem. Phys. Lett.* **2013**, *556*, 315.

(133) Al-Ghoul, M.; Ghaddar, T.; Moukalled, T. *J. Phys. Chem. B* **2009**, *113*, 11594.

(134) Volford, A.; Lagzi, I.; Molnár, F.; Rácz, Z. *Phys. Rev. E* **2009**, *80*, 055102.

(135) Rajurkar, N.; Ambekar, B. *J. Mol. Liq.* **2013**, *180*, 70.

(136) Grzybowski, B. A.; Campbell, C. J. *Mater. Today* **2007**, *10*, 38.

(137) Smith, D. *J. Chem. Phys.* **1984**, *81*, 3102.

(138) Ostwald, W. *Lehrbuch der Allgemeinen Chemie*; Lehrbuch d.; Engelman Leipzig, 1897.

(139) Hantz, P. Pattern formation in a new class of precipitation reactions, University of Geneva, 2006.

(140) Antal, T.; Droz, M.; Magnin, J.; Rácz, Z.; Zrinyi, M. *J. Chem. Phys.* **1998**, *109*, 9478.

(141) Hedges, E. S.; Henley, R. V. *J. Chem. Soc.* **1928**, 2714.

(142) Flicker, M.; Ross, J. *J. Chem. Phys.* **1974**, *60*, 3458.

(143) Venzl, G.; Ross, J. *J. Chem. Phys.* **1982**, *77*, 1302.

(144) Venzl, G.; Ross, J. *J. Chem. Phys.* **1982**, *77*, 1308.

(145) Antal, T.; Droz, M.; Magnin, J.; Rácz, Z. *Phys. Rev. Lett.* **1999**, *83*, 2880.

(146) Venzl, G.; Ross, J. *J. Chem. Phys.* **1986**, *85*, 2006.

(147) Ferenc, I.; Lagzi, I. **2010**, 10.

(148) Krug, H.-J.; Brandtstädter, H. *J. Phys. Chem. A* **1999**, *103*, 7811.

(149) Müller, S. C.; Ross, J. *J. Phys. Chem. A* **2003**, *107*, 7997.

(150) Bena, I.; Droz, M.; Rácz, Z. *J. Chem. Phys.* **2005**, *122*.

(151) Cahn, J. W.; Hilliard, J. E. *J. Chem. Phys.* **1958**, *28*, 258.

(152) Thomas, S.; Lagzi, I.; Molnár, F.; Rácz, Z. *Phys. Rev. Lett.* **2013**, *110*, 078303.

(153) *An introduction to microscopy*; Morris, K., Ed.; Forensics and criminal justice; Boca Raton : CRC Press: Boca Raton, 2010.

(154) Bradbury, S. *An introduction to the optical microscope*; Oxford science publications; Rev. ed.; Oxford [etc.] : Oxford University Press: Oxford etc., 1989.

(155) Keyence VK-X200. Keyence 3D Laser Scanning Microscope http://www.keyence.de/products/measure-sys/3d-measure/vk-x100_x200/index.jsp (accessed Feb 15, 2015).

(156) *Scanning transmission electron microscopy : imaging and analysis*; Pennycook, S. J., Ed.; New York : Springer: New York, 2011.

(157) *Scanning Electron Microscopy*; Kazmiruk Viacheslav, Ed.; [S.l.] : InTech: S.l., 2012.

(158) Marks, L. *Physics (College. Park. Md).* **2013**, *6*, 82.

(159) *Electron microscopy : methods and protocols*; Kuo John, Ed.; Methods in molecular biology,; 2nd ed. / .; Totowa, N.J : Humana Press: Totowa, N.J, 2007.

(160) Entwicklung und Vergleich analytischer Imaging-Methoden zur Mikroanalytik : IR-Imaging und SEM/EDX-Mapping, Muttenz: Muttenz, 2008.

(161) Di Bartolo, B. *Nano-Structures for Optics and Photonics : Optical Strategies for Enhancing Sensing, Imaging, Communication and Energy Conversion*; Silvestri Luciano, Ed.; NATO Science for Peace and Security Series B: Physics and Biophysics,; Dordrecht : Imprint: Springer: Dordrecht, 2015.

(162) Williams, D. B., Ed.; New York [etc.] : Plenum Press: New York etc., 1995.

(163) *Scanning electron microscopy, x-ray microanalysis, and analytical electron microscopy : a laboratory workbook*; Lyman, C. E., Ed.; New York [etc.] : Plenum Press: New York etc., 1990.

(164) JEOL. Jeol periodic table for EDS analysis http://www.jeolusa.com/HOME/Misc/JEOLUSAPeriodicChart/tabid/1185/Default.aspx (accessed Feb 15, 2015).

(165) Utke, I.; Hoffmann, P.; Melngailis, J. *J. Vac. Sci. Technol. B Microelectron. Nanom. Struct.* **2008**, *26*, 1197.

(166) FEI. *Using beam chemistries with SEM , FIB and DualBeam ™ for surface modification*; 2015.

(167) Eaton, P. *Atomic force microscopy*; West, P., Ed.; Oxford : Oxford University Press: Oxford, 2010.

(168) Meyer, E. *Atomic force microscopy*; 1992.

(169) Wäckerlin, C. On-Surface Magnetochemistry, University of Basel, 2013.

(170) Morf, P. Self-assembled monolayers beyond thiols : dithiocarbamates - from pure layers to ternary assembly systems, University_of_Basel, 2007.

(171) Sardela, M. *Practical Materials Characterization*; New York, NY : Imprint: Springer: New York, NY, 2014.

(172) Flechsig, U.; Quitmann, C.; Raabe, J.; Böge, M.; Fink, R.; Ade, H. In *AIP Conference Proceedings*; AIP, 2007; Vol. 879, p. 505.

(173) Frommherz, U.; Raabe, J.; Watts, B.; Stefani, R.; Ellenberger, U.; Garrett, R.; Gentle, I.; Nugent, K.; Wilkins, S. In *AIP Conference Proceedings*; 2010; p. 42.

(174) Raabe, J.; Tzvetkov, G.; Flechsig, U.; Böge, M.; Jaggi, a; Sarafimov, B.; Vernooij, M. G. C.; Huthwelker, T.; Ade, H.; Kilcoyne, D.; Tyliszczak, T.; Fink, R. H.; Quitmann, C. *Rev. Sci. Instrum.* **2008**, *79*, 113704.

(175) Goode, A. E.; Porter, A. E.; Ryan, M. P.; McComb, D. W. *Nanoscale* **2015**, *7*, 1534.

(176) PSI. PolLux Endstation PSI http://www.psi.ch/sls/pollux/endstation (accessed Feb 16, 2015).

(177) Fujishima, a; Honda, K. *Nature* **1972**, *238*, 37.

(178) Morales-Guio, C. G.; Tilley, S. D.; Vrubel, H.; Grätzel, M.; Hu, X. *Nat. Commun.* **2014**, *5*, 3059.

(179) Krol, R. Van De; Grätzel, M. In *Photoelectrochemical Hydrogen Production*; 2012.

(180) Bora, D. K.; Braun, A.; Erni, R.; Müller, U.; Döbeli, M.; Constable, E. C. *Phys. Chem. Chem. Phys.* **2013**, *15*, 12648.

(181) Brillet, J. Solar Energy Stored as Hydrogen: Controlling Inexpensive Oxide-based Nanostructures for Efficient Water Splitting, École polytechnique fédérale de Lausanne, 2012, Vol. 5478.

(182) Gajda-Schrantz, K.; Tymen, S.; Boudoire, F.; Toth, R.; Bora, D. K.; Calvet, W.; Grätzel, M.; Constable, E. C.; Braun, A. *Phys. Chem. Chem. Phys.* **2013**, *15*, 1443.

(183) Li, X.; Yu, J.; Low, J.; Fang, Y.; Xiao, J.; Chen, X. *J. Mater. Chem. A* **2015**, *3*, 2485.

(184) Paracchino, A.; Laporte, V.; Sivula, K.; Grätzel, M.; Thimsen, E. *Nat. Mater.* **2011**, *10*, 456.

(185) Gustav Parmentier GMBH. Wichtige Kennzahlen von Gelatine http://www.parmentier.de/gpfneu/gelatine/deutsch/kennzahl.php (accessed Mar 20, 2015).

(186) Wang, J.; Hanan, G. S. *Synlett* **2005**, 1251.

(187) Beves, J. E. Crystal Engineering with 2,2':6',2"- Terpyridine Derivatives and their Metal Complexes: From simple building blocks to coordination polymers and networks, University of Basel, 2008.

(188) Anderson, T. J.; Scott, J. R.; Millett, F.; Durham, B. *Inorg. Chem.* **2006**, *45*, 3843–3845.

(189) Grolimund, D.; Trainor, T. P.; Fitts, J. P.; Kendelewicz, T.; Liu, P.; Chambers, S. a; Brown, G. E. *J. Synchrotron Radiat.* **1999**, *6*, 612.

(190) Paolucci, G.; Santoni, A.; Comelli, G.; Prince, K.; Agostino, R. *Phys. Rev. B* **1991**, *44*, 10888.

(191) Gorup, L. F.; Longo, E.; Leite, E. R.; Camargo, E. R. *J. Colloid Interface Sci.* **2011**, *360*, 355.

(192) Michel, G.; Machiroux, R. *J. Raman Spectrosc.* **1983**, *14*, 22.

(193) Weast, R. C. *CRC Handbook of Chemistry and Physics 58th Edition 1977-1978*; Weast, R. C., Ed.; 58th ed.; CRC Handbook of Chemistry and Physics 58th Edition, 1977.

(194) Cotton, S. A. *Chemistry of precious metals*; Cotton, S. A., Ed.; London : Blackie Academic & Professional: London, 1997.

(195) Greenwood, N. N. *Chemistry of the elements*; 1995.

(196) Oshitna, K., and Tollens, B. *Ber. Dtsch. Chem. Ges.* **1901**, *34*, 1425.

(197) Dakin, H. *J. Biol. Chem.* **1920**, 499.

(198) Gelatin Manufacturers Association of Asia Pacific. Amino acid composition of gelatin http://www.gmap-gelatin.com/about_gelatin_AminoAcidComp.html (accessed Feb 15, 2015).

(199) Graßmann, W.; Hannig, K.; Schleyer, M. Zur Aminosäuresequenz des Kollagens, II. *Hoppe-Seyler´s Zeitschrift für physiologische Chemie*, 1960, *322*, 71.

(200) Prieto, P.; Nistor, V.; Nouneh, K.; Oyama, M.; Abd-Lefdil, M.; Díaz, R. *Appl. Surf. Sci.* **2012**, *258*, 8807.

(201) Aruna, I.; Mehta, B. R.; Malhotra, L. K.; Shivaprasad, S. M. *J. Appl. Phys.* **2008**, *104*.

(202) Alonso, C.; Salvarezza, R.; Vara, J.; Arvia, A. *Electrochim. Acta* **1990**, 489.

(203) Barnes, P. a.; O'Connor, M. F.; Stone, F. S. *J. Chem. Soc. A Inorganic, Phys. Theor.* **1971**, *1964*, 3395.

(204) Keats, N. G.; Scaife, P. H. *Talanta* **1966**, *13*, 156.

(205) Lowe, T. a.; Hedberg, J.; Lundin, M.; Wold, S.; Wallinder, I. O. *Int. J. Electrochem. Sci.* **2013**, *8*, 3851.

(206) Norby, P.; Dinnebier, R.; Fitch, a. N. *Inorg. Chem.* **2002**, *41*, 3628.

(207) W. J. Culbertson, J. Investigation and design of a regenerable silver oxide system for carbon dioxide control, University of Denver, 1964.

(208) Zanowiak, P.; Zanowiak, P. In *Ullmann's Encyclopedia of Industrial Chemistry*; 2014; Vol. 33, p. 16.

(209) George, B.; Sillen, Lars, G. *Acta Chem. Scand.* **1960**, *14*, 717.

(210) Ajitha, B.; Reddy, P. S. *Int. J. ChemTech Res.* **2014**, *6*, 2123.

(211) Housecroft, C. E.; Sharpe, A. G. *Inorganic chemistry*; 2nd ed.; Pearson Prentice Hall, 2005.

(212) Hollemann, A.; Wiberg, N. *Lehrbuch der Anorganischen Chemie*; 102nd ed.; New York : de Gruyter, 2008.

(213) Mehta, S. K.; Chaudhary, S.; Gradzielski, M. *J. Colloid Interface Sci.* **2010**, *343*, 447.

(214) Darroudi, M.; Ahmad, M. Bin; Abdullah, A. H.; Ibrahim, N. A. *Int. J. Nanomedicine* **2011**, *6*, 569.

(215) Volpe, L.; Peterson, P. J. *Corros. Sci.* **1989**, *29*, 1179–1196.

(216) Pulit, J.; Banach, M. *Dig. J. Nanomater. Biostructures* **2013**, *8*, 787.

(217) Peyser, L. a; Vinson, a E.; Bartko, a P.; Dickson, R. M. *Science* **2001**, *291*, 103.

(218) Gallardo, O. a. D.; Moiraghi, R.; Macchione, M. a.; Godoy, J. a.; Pérez, M. a.; Coronado, E. a.; Macagno, V. a. *RSC Adv.* **2012**, *2*, 2923.

(219) Flores, J. C.; Crespo, D.; Torres, V.; Carmona, J.; Rainforth, W. M.; Zhou, Z.; Calderon-Moreno, J. M. *J. Nanosci. Nanotechnol.* **2012**, *12*, 8158.

(220) OriginLab Corportation. Origin 9.1 User Guide http://cloud.originlab.com/pdfs/Origin91_Documentation/English/Origin_9.1_User_Guide_E.pdf (accessed Feb 19, 2015).

(221) L'Vov, B. V. *Thermochim. Acta* **1999**, *333*, 13.

(222) Jelić, D.; Mentus, S.; Penavin-Škundrić, J.; Bodroža, D.; Antunović, B. *Contemp. Mater.* **2010**, *1*, 144.

(223) Waterhouse, G. I. N.; Bowmaker, G. a.; Metson, J. B. *Phys. Chem. Chem. Phys.* **2001**, *3*, 3838.

(224) Suzuki, R. O.; Ogawa, T.; Ono, K. *J. Am. Ceram. Soc.* **1999**, *82*, 2033.

(225) Wijnhoven, S. W. P.; Peijnenburg, W. J. G. M.; Herberts, C. a; Hagens, W. I.; Oomen, A. G.; Heugens, E. H. W.; Roszek, B.; Bisschops, J.; Gosens, I.; Van De Meent, D.; Dekkers, S.; De Jong, W. H.; van Zijverden, M.; Sips, A. J. a M.; Geertsma, R. E. *Nanotoxicology* **2009**, *3*, 109.

(226) Yung, L. C.; Fei, C. C.; Mandeep, J.; Binti Abdullah, H.; Wee, L. K. *PLoS One* **2014**, *9*, 97484.

(227) Gerhardt, O. *Mater. Corros.* **1951**, *2*, 129.

(228) Chernyshova, I. V; Hochella, M. F.; Madden, a S. *Phys. Chem. Chem. Phys.* **2007**, *9*, 1736.

(229) Cao, H.; Wang, G.; Zhang, L.; Liang, Y.; Zhang, S.; Zhang, X. *ChemPhysChem* **2006**, *7*, 1897.

(230) Souza, F. L.; Lopes, K. P.; Nascente, P. a P.; Leite, E. R. *Sol. Energy Mater. Sol. Cells* **2009**, *93*, 362.

(231) Boudoire, F.; Toth, R.; Heier, J.; Braun, A.; Constable, E. C. *Energy Environ. Sci.* **2014**, 2680.

(232) Mehmet, C.; Yartasi, A.; Kocakerim, M. M. *Ind. Eng. Chem. Res.* **1998**, *37*, 4641.

(233) Cobley, C. M.; Rycenga, M.; Zhou, F.; Li, Z. Y.; Xia, Y. *J. Phys. Chem. C* **2009**, *113*, 16975.

(234) Sulliva, B. P.; Salmon, D. J.; Meyer, T. J. *Inorg. Chem.* **1978**, *17*, 3334.

(235) Broomhead, J. A.; Young, C. G.; Hood, P. *Tris(2,2"-Bipyridine)Ruthenium(II) Dichloride Hexahydrate*; John Wiley & Sons, Inc., 2007.

(236) Jensen, Birger, J.; Lou, J. *Acta Chem. Scand.* **1983**, *A*, 617.

(237) Longo, E.; Volanti, D. P.; Nogueira, C.; Longo, M.; Gracia, L.; Almeida, M. a P.; Pinheiro, A. N.; Ferrer, M. M.; Cavalcante, S.; Luis, R. W. *J. Phys. Chem. C* **2014**, *118*, 1229.

(238) De Santana, Y. V. B.; Gomes, J. E. C.; Matos, L.; Cruvinel, G. H.; Perrin, A.; Perrin, C.; Andres, J.; Varela, J. a.; Longo, E. *Nanomater. Nanotechnol.* **2014**, 1.

(239) Longo, E.; Cavalcante, L. S.; Volanti, D. P.; Gouveia, a F.; Longo, V. M.; Varela, J. a; Orlandi, M. O.; Andrés, J. *Sci. Rep.* **2013**, *3*, 1676.

(240) Bottelberghs, P. H.; Everts, E.; Broers, G. H. J. *Mater. Res. Bull.* **1976**, *11*, 263.

(241) Bhattacharya, S.; Ghosh, A. *Phys. Rev. B - Condens. Matter Mater. Phys.* **2007**, *75*, 2.

(242) Wang, Y.; Liu, Y.; Lu, X.; Li, Z.; Zhang, H.; Cui, X.; Zhang, Y.; Shi, F.; Deng, Y. *Electrochem. commun.* **2012**, *20*, 171.

Appendix B: Data of further investigations

Table: Gelatin properties (Section 3.2.1)

Appendix B, Table 1: Measured values/properties of gelatin containing potassium dichromate or chromate and ammonia as inner electrolytes .

Sample	NH_4OH [w/w%]	pH gelatin solution	0.01M $K_2Cr_2O_7$			0.01M K_2CrO_4		
			pH gelatin solution	gel stiffness	color $K_2Cr_2O_7$/gelatin solution	pH gelatin solution	gel stiffness	color K_2CrO_4/gelatin solution
A	25	13.17	11.82	**liquid**	yellow 	11.90		pale yellow 
B	20	12.88	11.66		yellow 	11.72		pale yellow 
C	15	12.6	11.46		yellow 	11.50		pale yellow 
D	10	12.34	11.24	↓	yellow 	11.28		pale yellow 
E	7	12.14	11.04		yellow 	11.11		pale yellow 
F	5	11.93	10.82		yellow 	10.86		pale yellow 
G	3	11.75	10.62		yellow 	10.66		pale yellow 
H	1.5	11.55	10.31	**jelly like**	yellow 	10.40		pale yellow 
I	1	11.39	10.08		yellow 	10.16		pale yellow 
J	0.7	11.27	9.86		yellow 	9.98		pale yellow 
K	0.5	11.15	9.64		yellow 	9.82	**jelly like**	pale yellow 
L	0.3	11.11	9.32	**soft gel**	yellow 	9.52		pale yellow 
M	0.1	10.89	7.17		yellow - orange 	8.86		pale yellow 
N	0.07	10.76	6.5		yellow - orange 	8.14	**soft gel**	yellow 
O	0.05	10.73	6.23	**soft gel**	orange 	7.51		yellow 
P	0.02	10.49	5.81	↓	orange 	6.81	↓	yellow - orange 
Q	0.01	10.38	5.69		orange 	6.78	**hard gel**	yellow - orange 
R	0	5.26	5.61	**hard gel**	orange 	6.65		orange 

Mathematical Model (Section 3.4.4)

(by *Prof Dr. István Lagzi*)

Knowing the constitution of the bands and the relevant chemical equilibria, we developed a reaction-diffusion model based on the Cahn-Hilliard phase separation scenario[145] to understand the periodic precipitation phenomenon. Our kinetic model contains 5 species, namely $AgNO_3$ (A), K_2CrO_4 (B_1), $K_2Cr_2O_7$ (B_2), and two precipitates, Ag_2CrO_4 (C_1) and $Ag_2Cr_2O_7$ (C_2) (Equations 6-8).

$$B_1 \underset{\kappa_2}{\overset{\kappa_1}{\rightleftharpoons}} B_2 \tag{6}$$

$$A + B_1 \xrightarrow{k_1} C_1 \tag{7}$$

$$A + B_2 \xrightarrow{k_2} C_2 \tag{8}$$

Here κ_1, κ_2 and k_1, k_2 are the chemical rate constants for the equilibrium between chromate and dichromate and for the precipitation reactions, respectively. Pattern formation occurs in the wake of a diffusively moving reaction front resulting from the inhomogeneous initial distribution of the outer and inner electrolytes. The spatiotemporal dynamics (pattern formation) of the system can be summarized in a set of partial differential (reaction-diffusion) equations:

$$\delta_t a = D\Delta a - k_1 a b_1 - k_2 a b_2 \tag{19}$$

$$\delta_t b_1 = D\Delta b_1 - k_1 a b_1 - \kappa_1 b_1 + \kappa_2 b_2 \tag{20}$$

$$\delta_t b_2 = D\Delta b_2 - k_2 a b_2 - \kappa_1 b_1 + \kappa_2 b_2 \tag{21}$$

$$\delta_t m_1 = -\lambda_1 \Delta(\varepsilon_1 m_1 - \gamma m_1^3 + \sigma \Delta m_1) + k_1 a b_1 \tag{22}$$

$$\delta_t m_2 = -\lambda_2 \Delta(\varepsilon_2 m_2 - \gamma m_2^3 + \sigma \Delta m_2) + k_2 a b_2 \tag{23}$$

D is the diffusion constant, and for simplicity, the diffusion constants of the reagents (**A**, $\mathbf{B_1}$, $\mathbf{B_2}$) are taken to be equal. The first three equations 19-21 describe the diffusion and the chemical reactions of the outer and inner electrolytes while equations 22 and 23 describe the precipitation process based on Cahn-Hilliard dynamics in which a moving chemical front produces a homogeneous precipitate behind it.[145] When the local concentration of the precipitate reaches a critical value, the precipitate segregates into high- (c_h) and low- (c_l) concentration regions. In equations 22 and 23 m_1 and m_2 are the concentrations of precipitates shifted by $(c_h + c_l)/2$ and scaled by $\bar{c} = (c_h + c_l)/2$ and $\lambda, \varepsilon, \gamma$ and σ are parameters of the Cahn-Hilliard equation.[134,152] Equations 19-23 were solved numerically using the "method of lines"

technique on a uniform 1D grid with appropriate boundary (no-flux boundary conditions for all species except for A at the junction point of the electrolytes, where for species A a Neumann-type boundary condition was applied: $(a|_{x=0}(t) = a_0)$ and initial conditions $a(t=0,x)=0$, $b_1(t=0,x)=b_{10}$, $b_2(t=0,x)=b_{20}$, $m_1(t=0,x)=m_2(t=0,x)=0$. The equations were integrated in time by the forward Euler method. The grid spacing and the time step were 1.0 and 0.04, respectively.

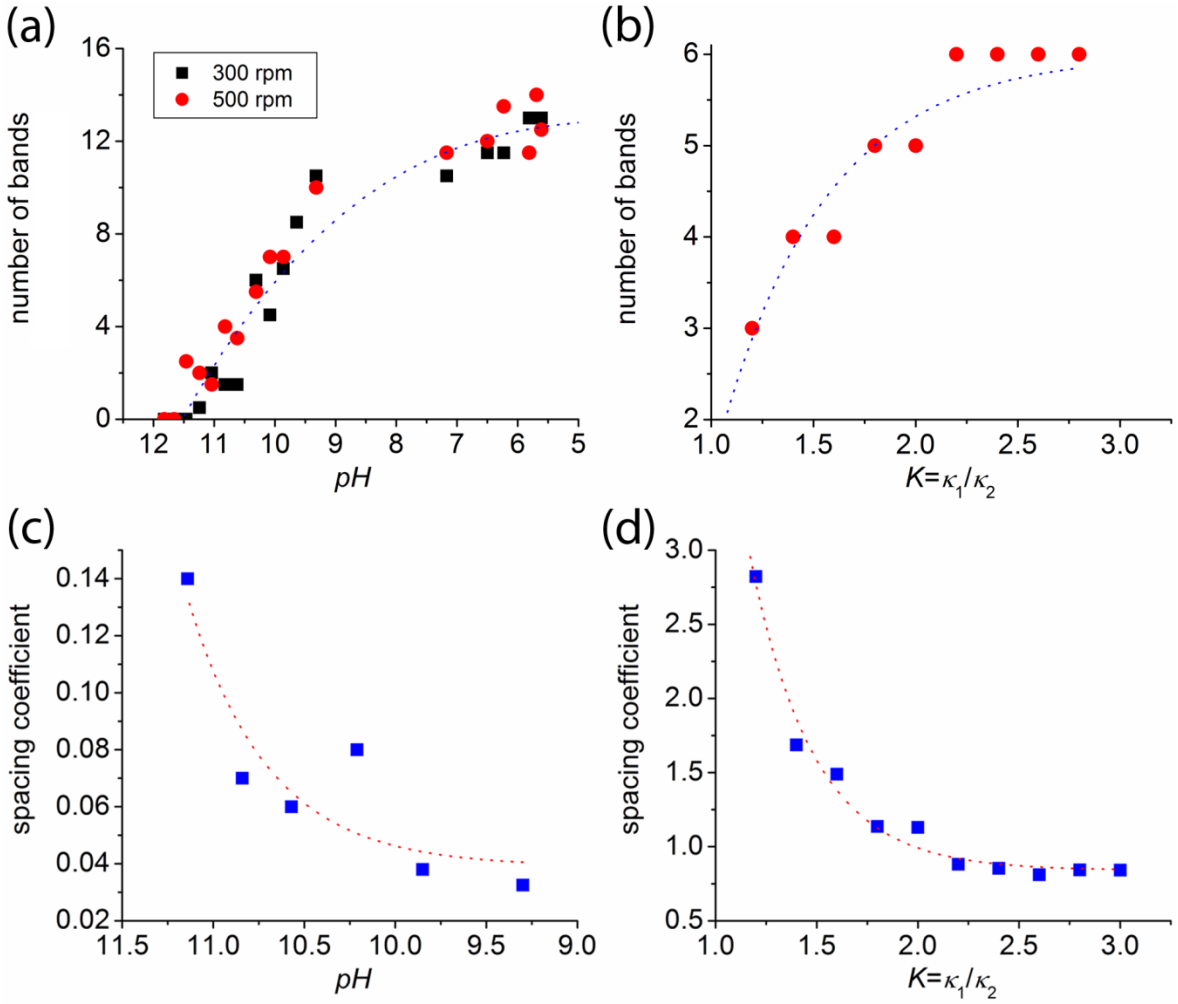

Appendix B, Figure 1: Comparison of the measured (left) and calculated (right) values of the number of formed primary bands (top) and the spacing coefficient (bottom) in the classical Liesegang system.

The results of the model are in very good agreement with te experimental results (Appendix B, Figure 1). At pH = 5.7 only $Ag_2Cr_2O_7$ bands form (very dense bands), while at pH = 10.1 a different type of band can be observed which is an accumulation of many very thin and dense bands. Here, both secondary and primary band formation can be observed as the equilibrium is shifted towards CrO_4^{2-}, a trend accurately reproduced by the model calculation.

Black box (Section 4.3.1.1)

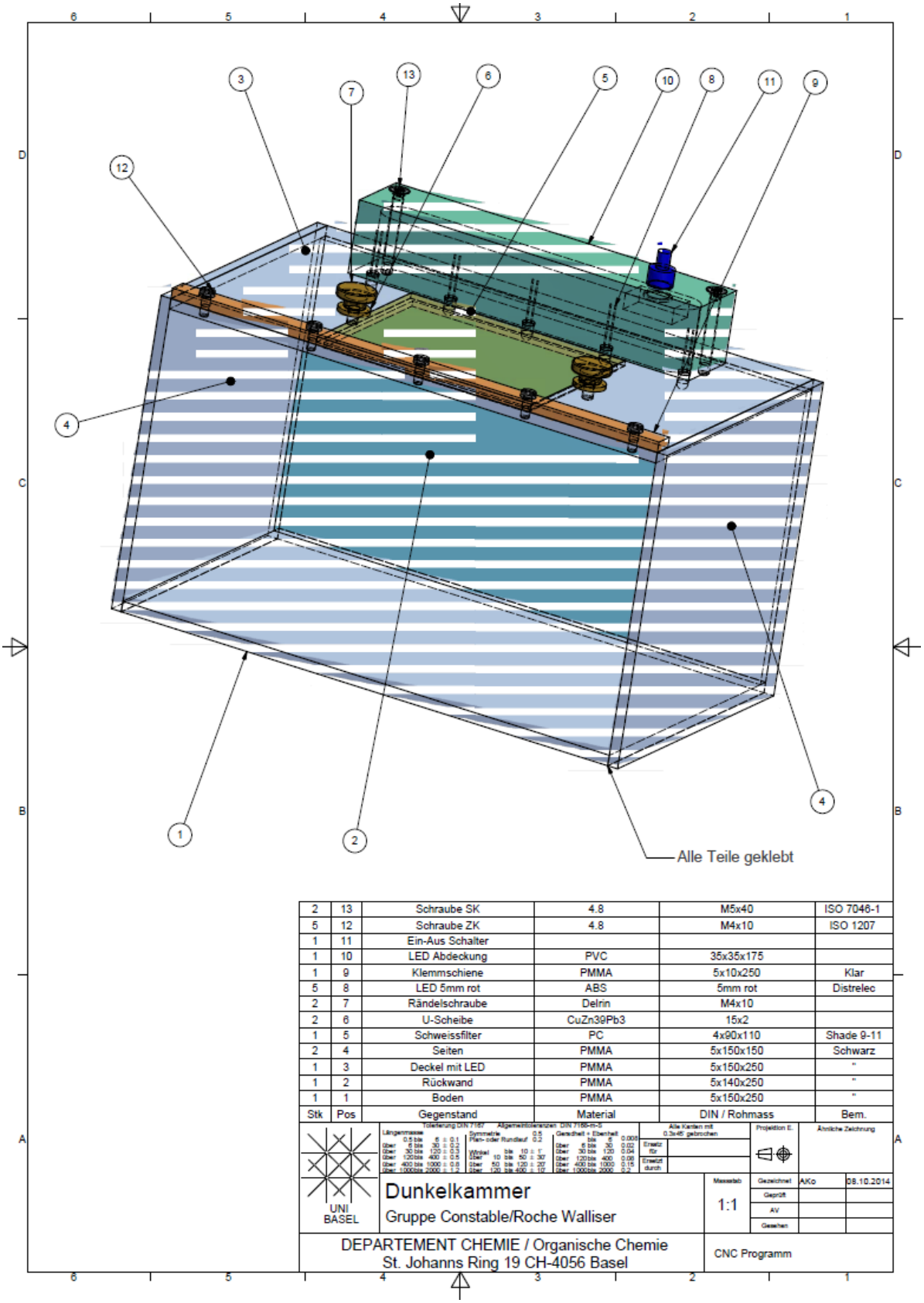

2	13	Schraube SK	4.8	M5x40	ISO 7046-1
5	12	Schraube ZK	4.8	M4x10	ISO 1207
1	11	Ein-Aus Schalter			
1	10	LED Abdeckung	PVC	35x35x175	
1	9	Klemmschiene	PMMA	5x10x250	Klar
5	8	LED 5mm rot	ABS	5mm rot	Distrelec
2	7	Rändelschraube	Delrin	M4x10	
2	6	U-Scheibe	CuZn39Pb3	15x2	
1	5	Schweissfilter	PC	4x90x110	Shade 9-11
2	4	Seiten	PMMA	5x150x150	Schwarz
1	3	Deckel mit LED	PMMA	5x150x250	"
1	2	Rückwand	PMMA	5x140x250	"
1	1	Boden	PMMA	5x150x250	"
Stk	Pos	Gegenstand	Material	DIN / Rohmass	Bem.

Dunkelkammer
Gruppe Constable/Roche Walliser

UNI BASEL

1:1

AKo 08.10.2014

DEPARTEMENT CHEMIE / Organische Chemie
St. Johanns Ring 19 CH-4056 Basel

CNC Programm

Appendix B, Figure 2: Blue print of the black box used in Section 4.3.1.1.

Fine structured bands by varying the used base (Section 4.3.2)

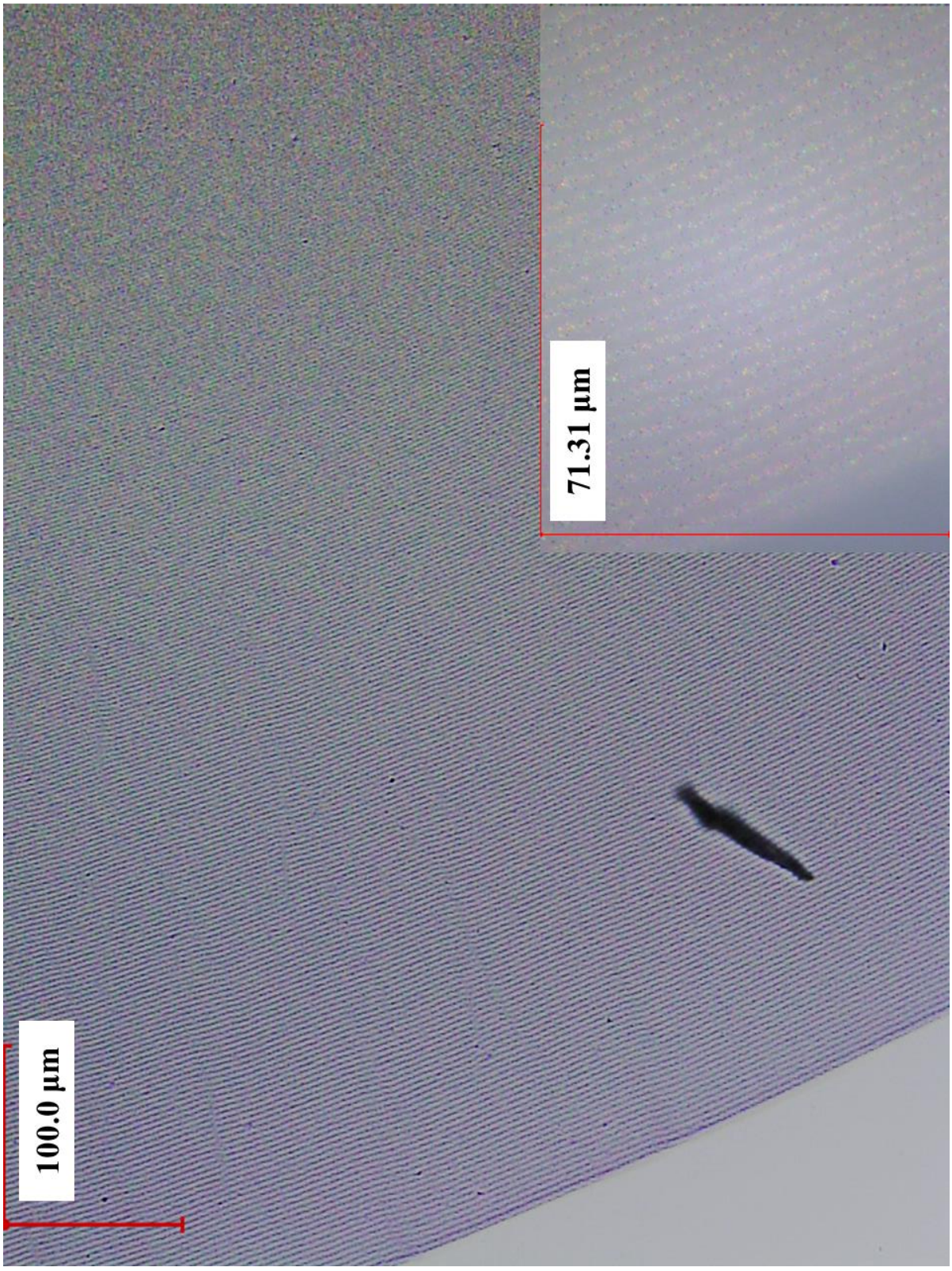

Appendix B, Image 1: Highly periodic precipitation bands found in samples prepared with diethylamine as base (0.3 w/w% Et_2NH). Overview image (100 µm scale bar) and zoomed in image at the end of the precipitation zone (bottom right), with a 71.31 µm scale bar.

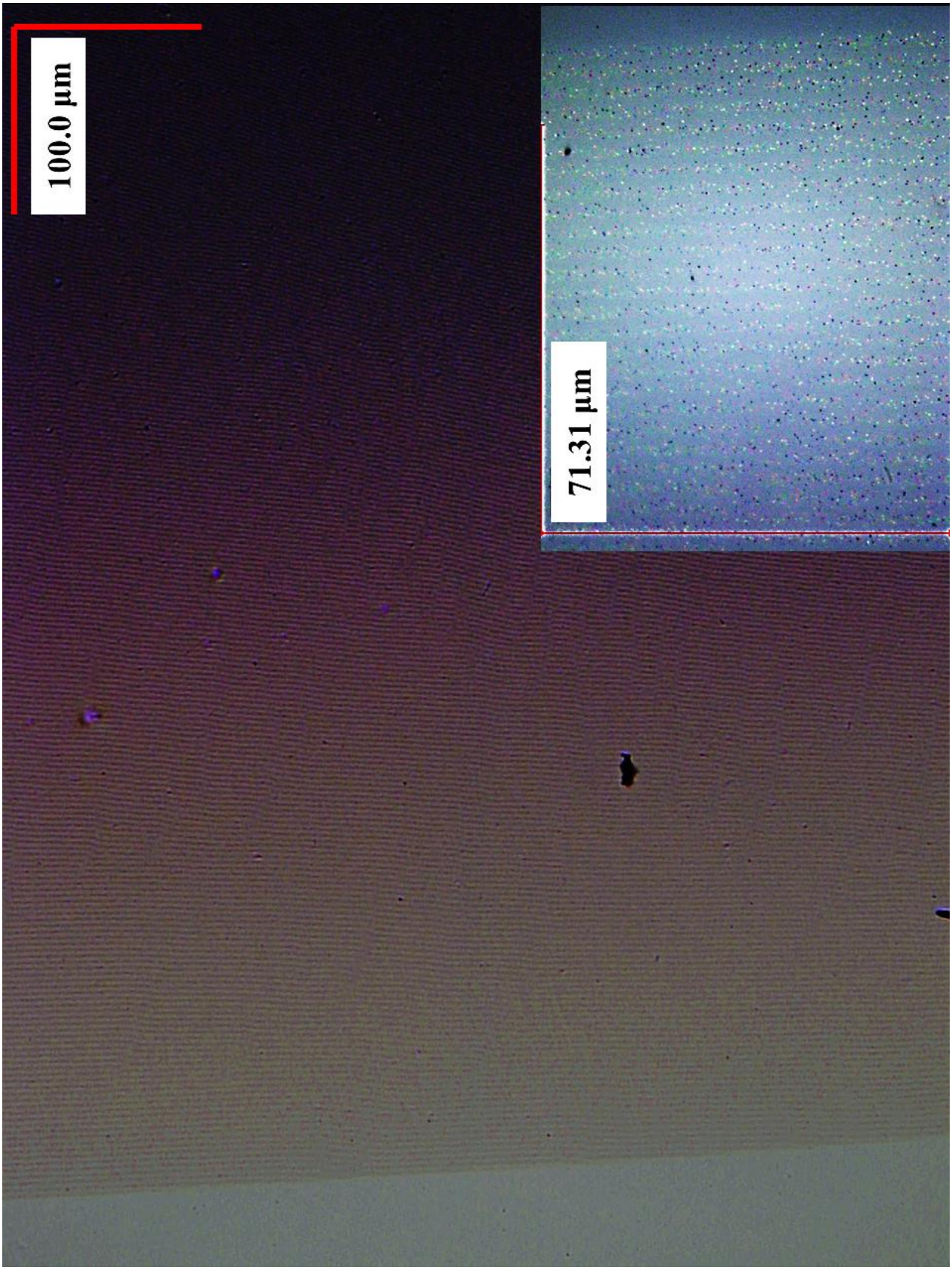

Appendix B, Image 2: Highly periodic precipitation bands found in samples prepared with triethylamine as base (0.3 w/w% Et_3N). Overview image (100 µm scale bar) and zoomed in image at the end of the precipitation zone (bottom right), with a 71.31 µm scale bar.

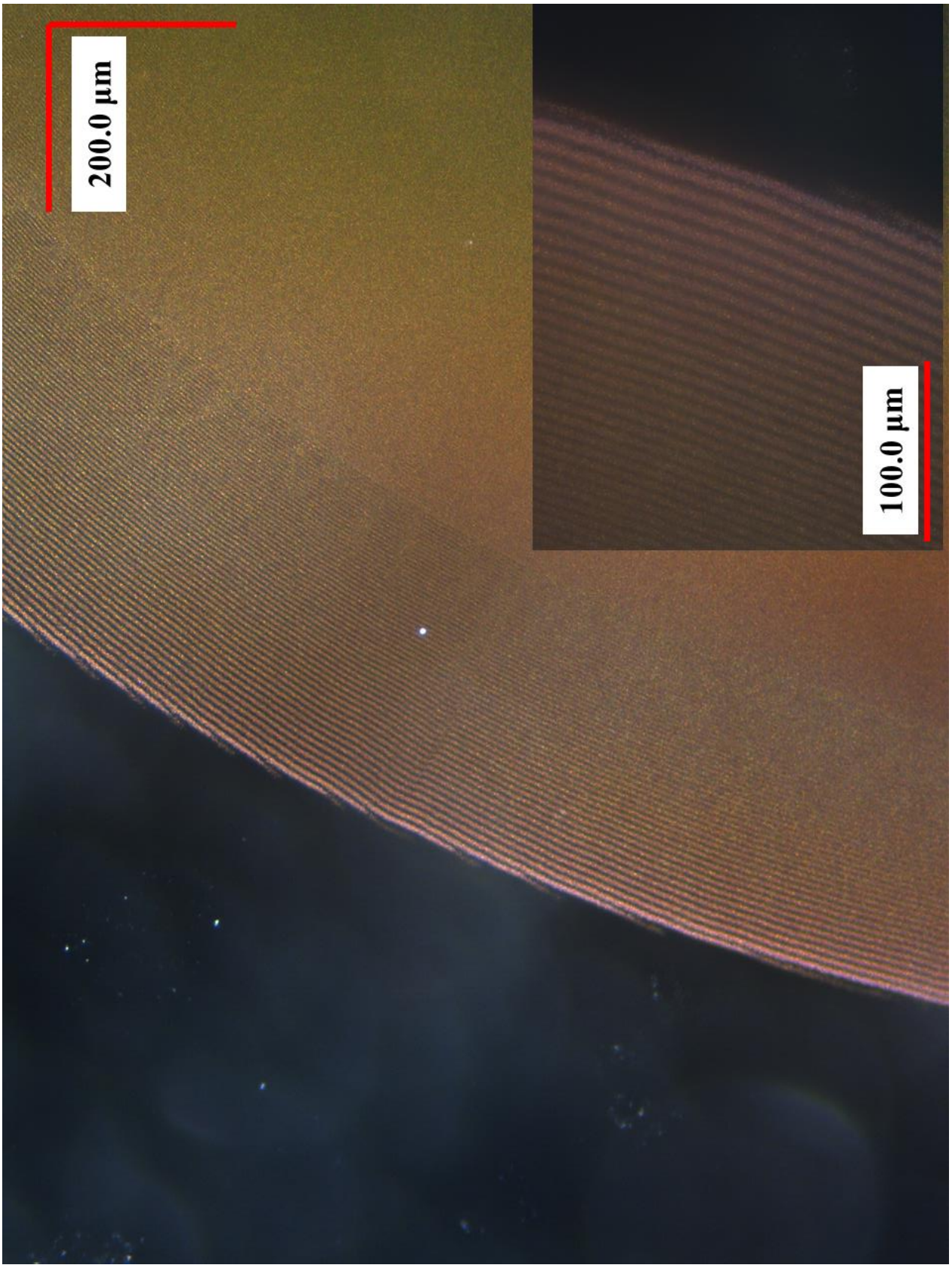

Appendix B, Image 3: Highly periodic precipitation bands found in samples prepared with potassium hydroxide (0.01 M KOH) as base. Overview image (200 µm scale bar) and zoomed in image at the end of the precipitation zone (bottom right), with a 100 µm scale bar.

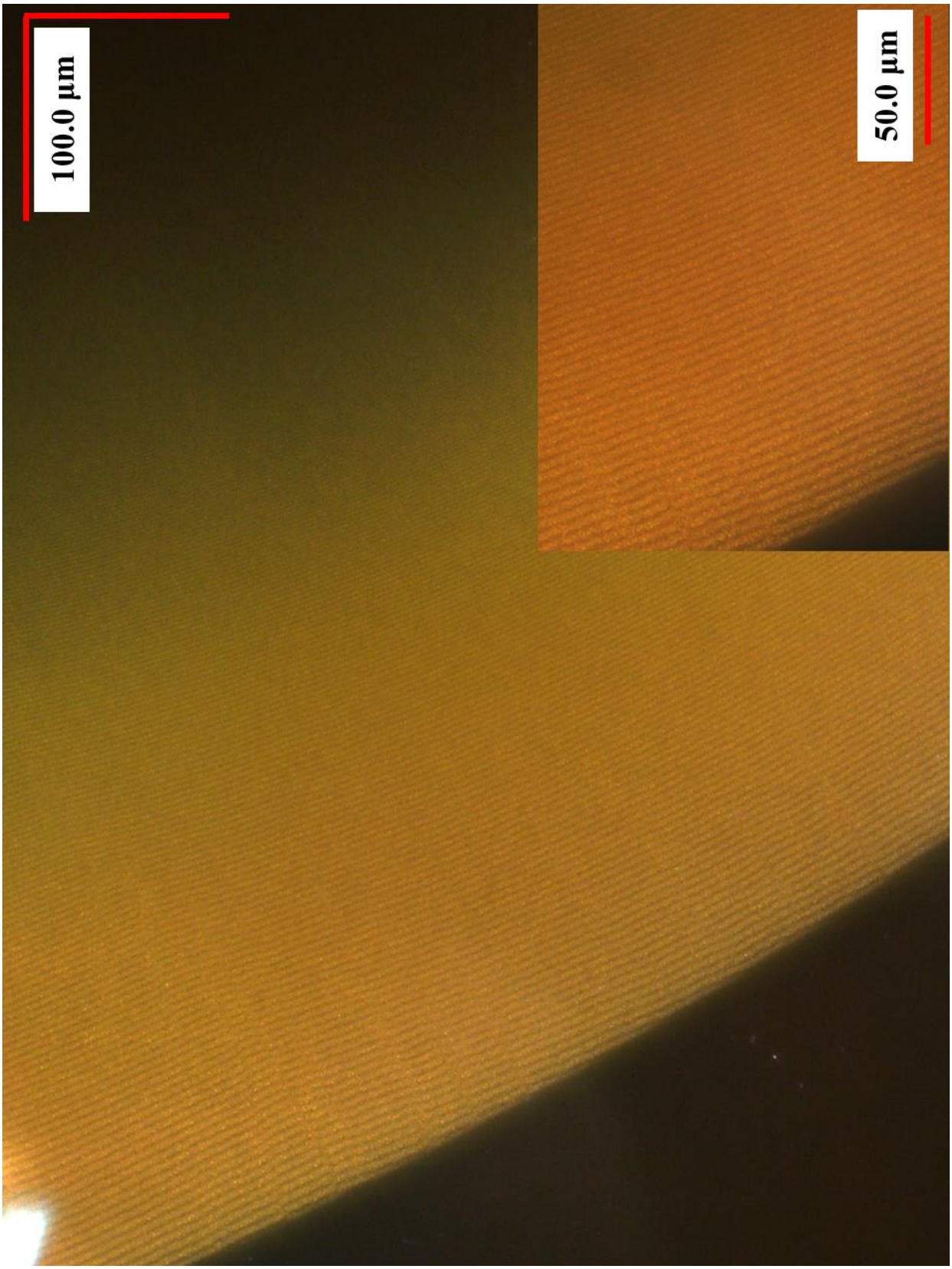

Appendix B, Image 4: Highly periodic precipitation bands found in samples prepared with sodium hydroxide (0.1 M NaOH) as base. Overview image (100 µm scale bar) and zoomed in image at the end of the precipitation zone (bottom right), with a 50 µm scale bar.

Table XPS-measurements (Section 4.3.5)

Appendix B, Table 2 Corrected XPS values silver Liesegang system.

ELEMENT/ORBITAL	O1s			C1s				correction C1s	Ag 3d5/2		Ag 3d3/2		N1s			S2p / S2s	
SAMPLE																	
Sample 2 measured circle1	528.3	526.6	524.0	283.0	281.0	280.0	277.4	280.1	4.2	364.6	363.2	370.4	369.1	367.4			154.8	156.7
Sample 2 corrected circle1	532.5	530.8	528.2	287.2	285.2	284.2	281.6	284.2	3.6	368.8	367.4	374.8	373.3	371.6			159.0	160.9
Sample 2 measured circle2	530.3	528.2	526.3	286.3	283.5	280.9	278.1	283.6	3.0	367.1	364.9	373.0	371.3	367.5			159.2	160.6
Sample 2 corrected circle2	533.3	531.2	529.3	289.3	286.5	283.9	281.1	283.9		370.1	367.9	376.0	374.3	370.5			162.2	163.6
Sample 1 measured circle 1		556.3	554.1	310.9	308.6	306.9		309.3	-24.6	394.7	393.1	401.0	399.3	395.5			188.2	186.4
Sample 1 corrected circle 1		531.7	529.5	286.3	284.0	282.3		284.0		370.1	368.5	376.4	374.7	370.9			163.6	161.8
Gelatin measured	539.1	537.4	535.4	294.1	292.1	290.0		290.0	-5.0						407.3	405.4	403.8	
Gelatin corrected	534.1	532.4	530.4	289.1	287.1	285.0		285.0							402.3	400.4	398.8	
References (lit.)																		
$AgNO_3$		532.3[2]								268.27[2]				406.6[2]				
AgO		528.4-528.6[2]								367.3-368.1[2]								
Ag_2O		529.2-529.8[2]								368.4[4]; 367.9[3]		373.9[2]						
AgOH		-								-								
NH_4OH																		
$[Ag(NH_3)_2]^+$		-								-		-		-				
Ag_2S										367.8*; 368.1[4]		373.8*					162.7*	
Ag_2SO_4										368.3[4]							169.0***	
O_2		533.3[4]																
L-Methionine																	161.1[6]	
L-Cystein																	161.5[6]	
Ag(0)										368.1[1]; 368.2[5]		373.4-374.2[2]						
Ag(I)																		
Alanine**		531.2[2]												400.9-401.1[2]				
Leucine**		530.9[2]												400.9[2]				
Serine **		531.4-532.6[2]			286.2-289.1[2]									399.8[2]				
Proline **					286.8[2]									399.1-400.2[2]				

*Ag-S in nanoparticles: (**S2p at 162.7 and Ag 3d at 373.8, 367.8 eV**) Bull. Korean Chem. Soc. 2012, Vol 33, No 1, pp 60.

**AA: aminoacids in gelatin

*** Metal sulfate ~169 eV [http://xpssimplified.com/elements/sulfur.php]

[1]: Vaccum 86 (2012) 1988-1991

[2]: NIST XPS Database http://srdata.nist.gov/xps

[3]: Chem. Mater., Vol 20, No 4, 2008, pp 1253

[4]: Journal of Chemistry, Volume 2013 (2013), Article ID 987879, 11 pages, http://dx.doi.org/10.1155/2013/987879

[5]http://xpssimplified.com/elements/silver.php

[6]: Journal of Electron Spectroscopy and Related Phenomena, Vol 50, No2, 1990, pp 159.

Structural design experiments (Section 5.2.2)

High resolution images of the precipitation structures observed in the structural design experiments. Top left images: samples prepared with 0.01 M $AgNO_3$ in the stamps. Top right images: samples prepared with 0.06 M $AgNO_3$ in the stamps. Bottom left images: samples prepared with 0.3 M $AgNO_3$ in the stamps and bottom right images: samples prepared with 0.6 M $AgNO_3$ in the stamps

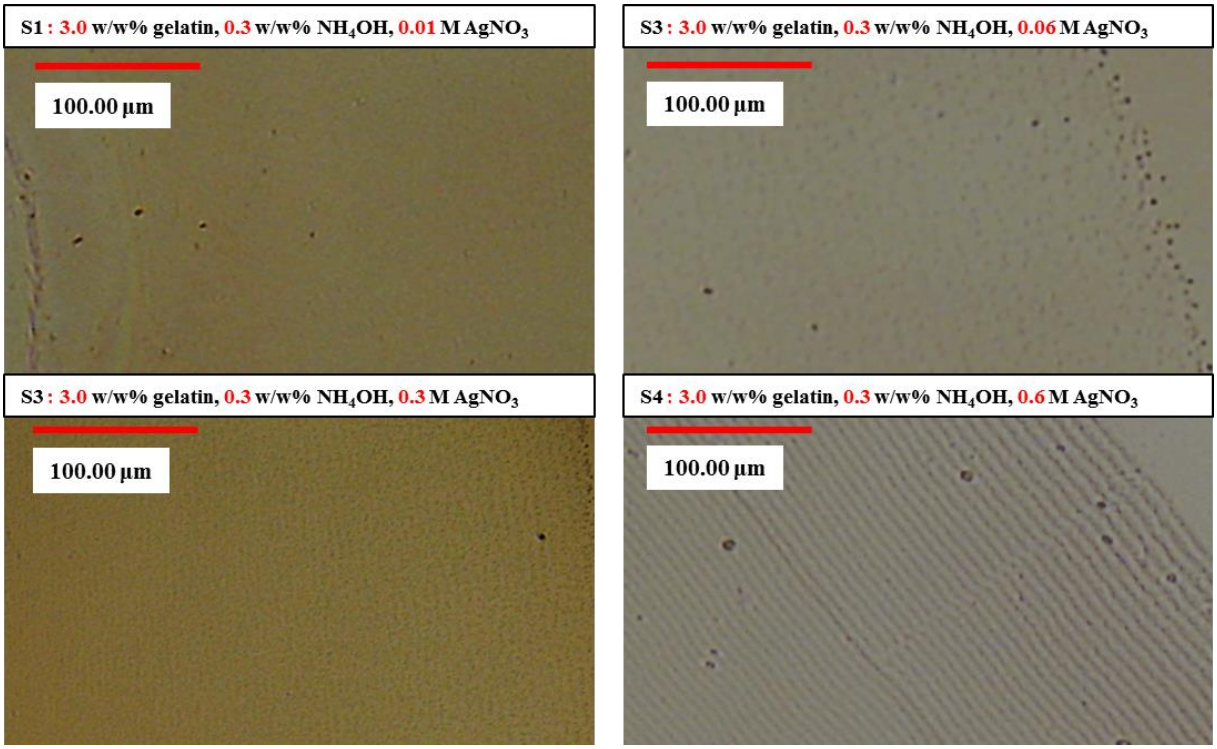

Appendix B, Figure 3: High resolution images for each setup from the structural design experiments. Containing 3.0 w/w% gelatin in 0.3 w/w% ammonia as hydrogel matrix.

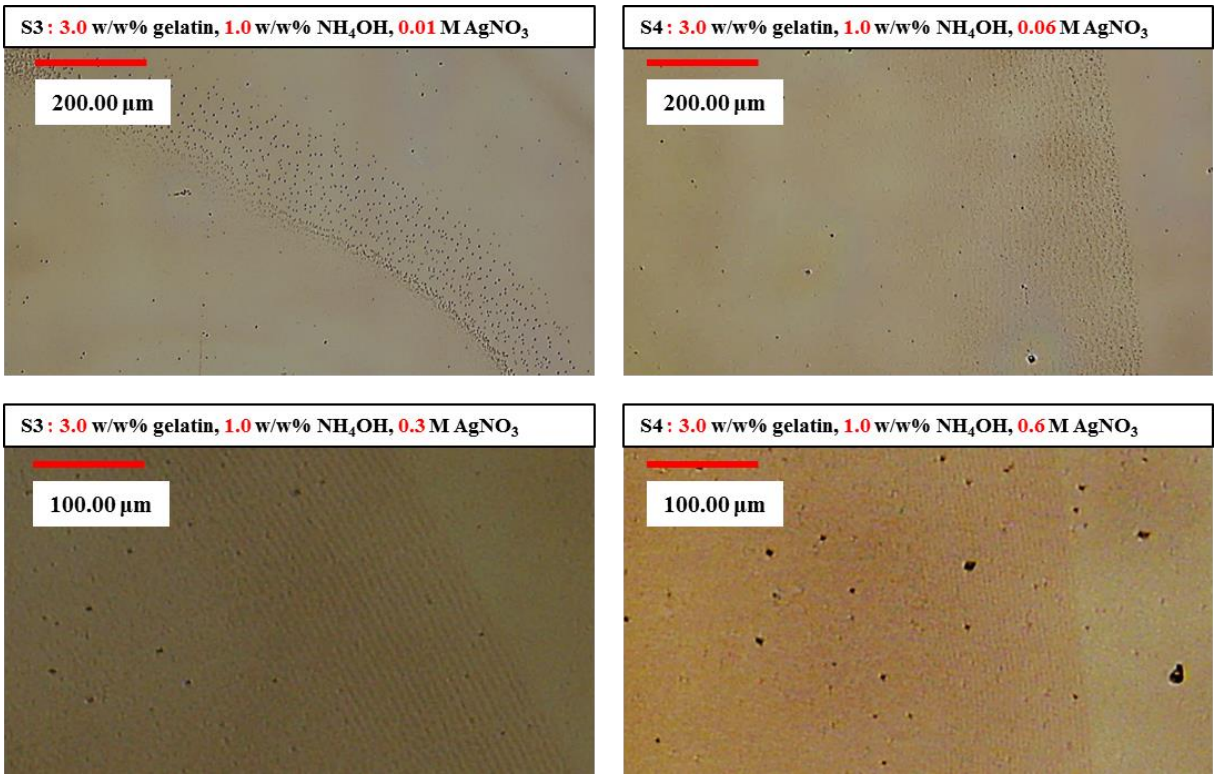

Appendix B, Figure 4: High resolution images for each setup from the structural design experiments. Containing 3.0 w/w% gelatin in 1.0 w/w% ammonia as hydrogel matrix.

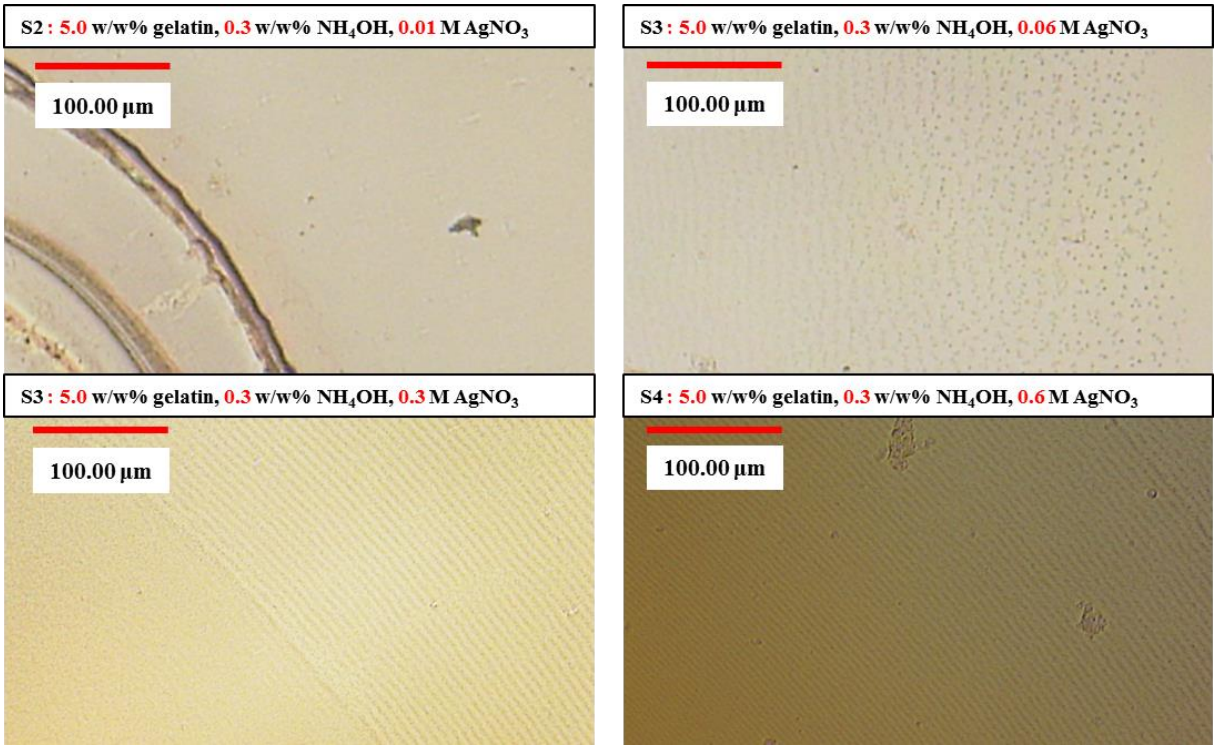

Appendix B, Figure 5: High resolution images for each setup from the structural design experiments. Containing 5.0 w/w% gelatin in 0.3 w/w% ammonia as hydrogel matrix.

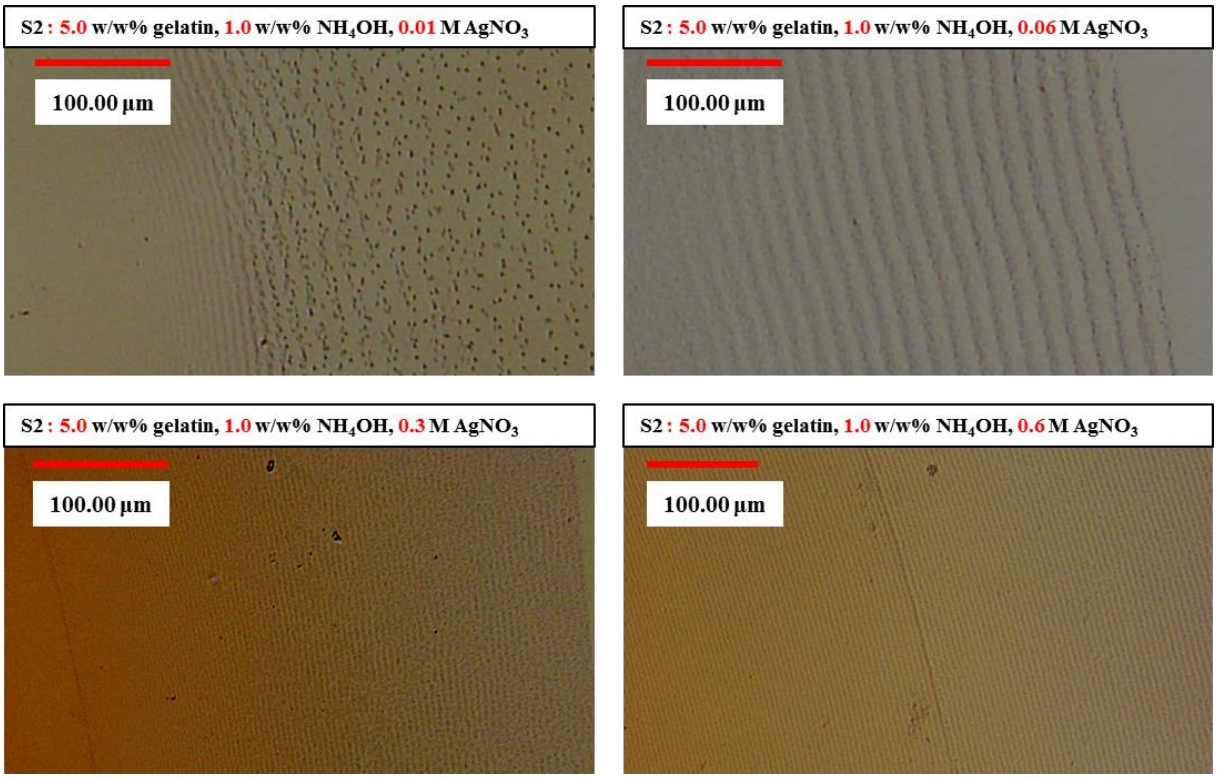

Appendix B, Figure 6: High resolution images for each setup from the structural design experiments. Containing 5.0 w/w% gelatin in 1.0 w/w% ammonia as hydrogel matrix.

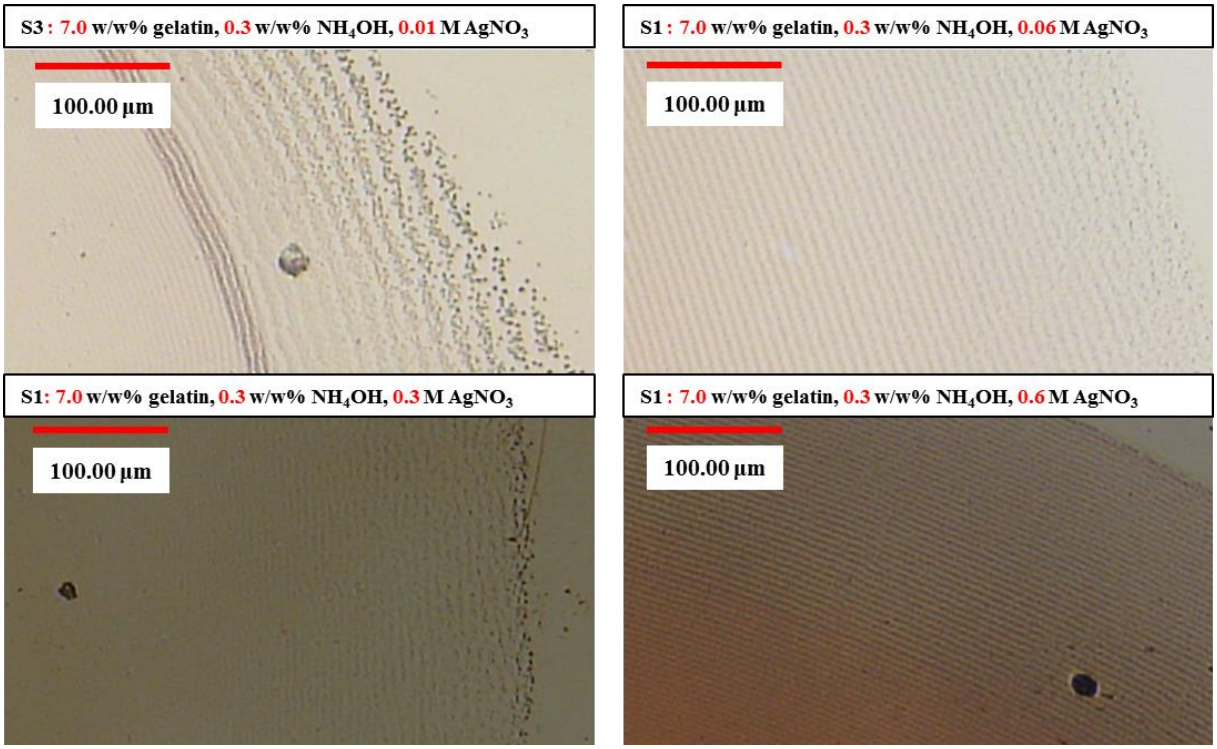

Appendix B, Figure 7: High resolution images for each setup from the structural design experiments. Containing 7.0 w/w% gelatin in 0.3 w/w% ammonia as hydrogel matrix.

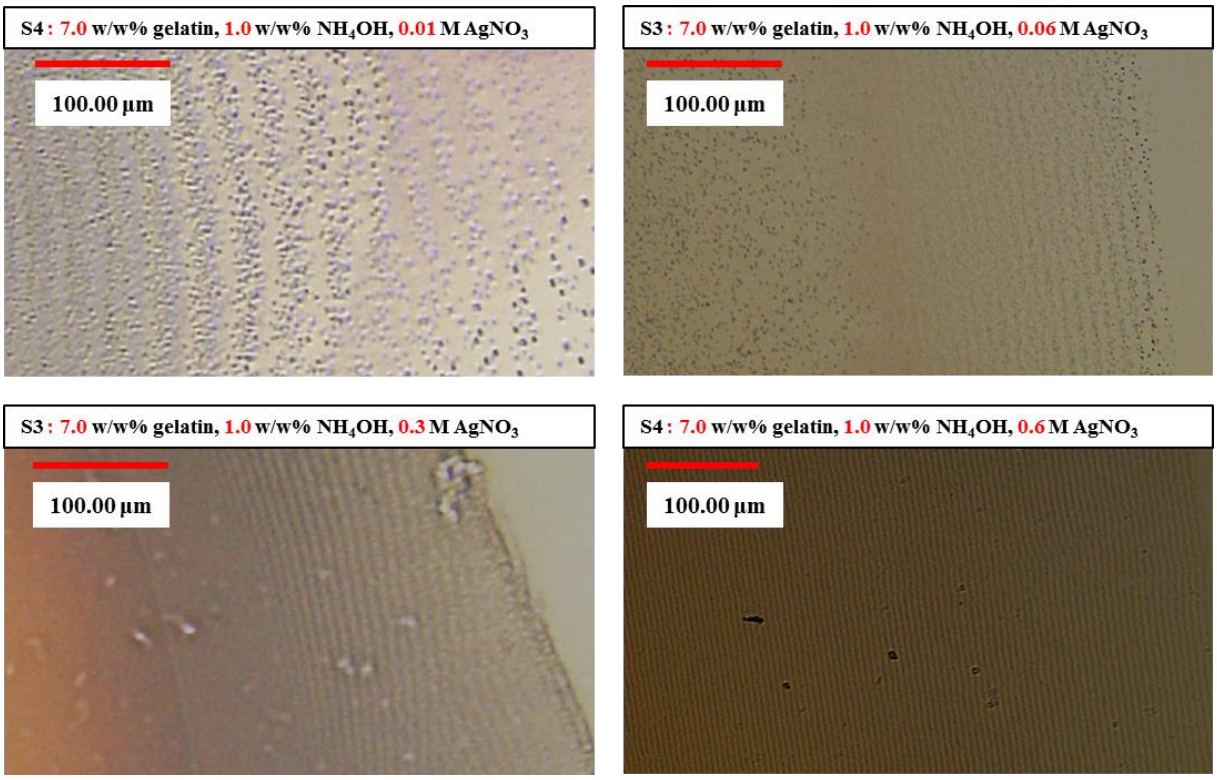

Appendix B, Figure 8: High resolution images for each setup from the structural design experiments. Containing 7.0 w/w% gelatin in 1.0 w/w% ammonia as hydrogel matrix.

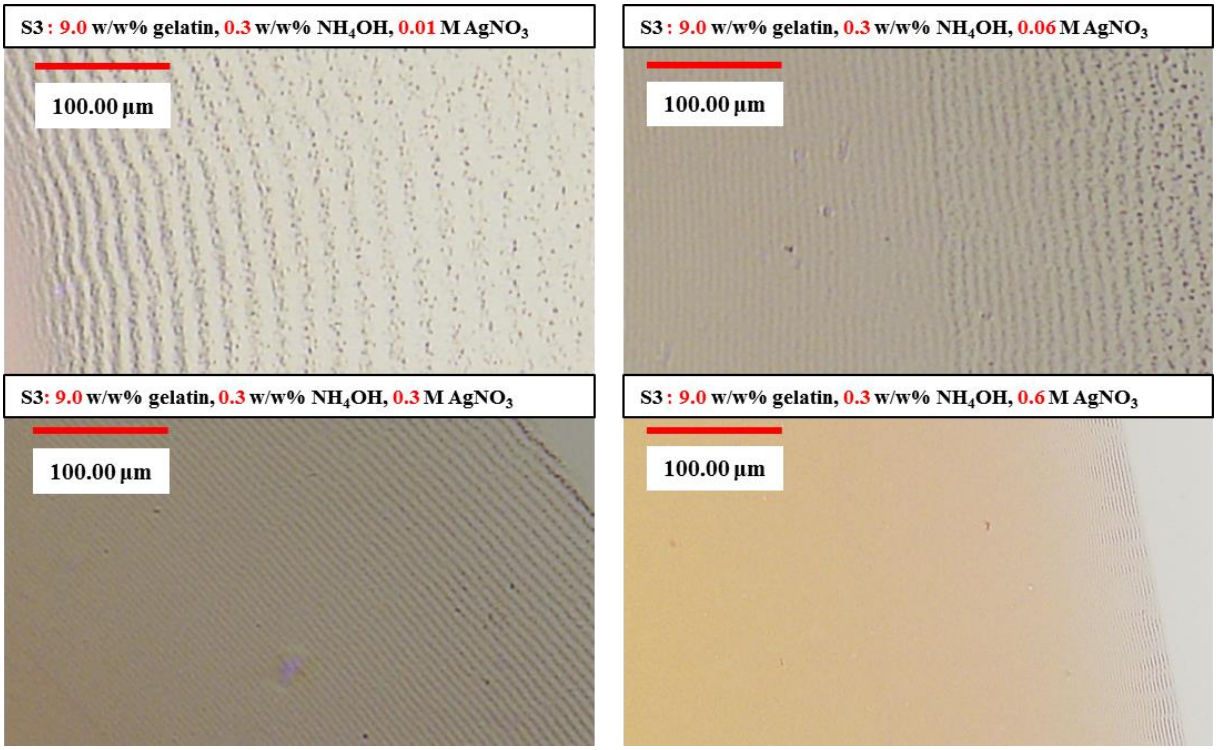

Appendix B, Figure 9: High resolution images for each setup from the structural design experiments. Containing 9.0 w/w% gelatin in 0.3 w/w% ammonia as hydrogel matrix.

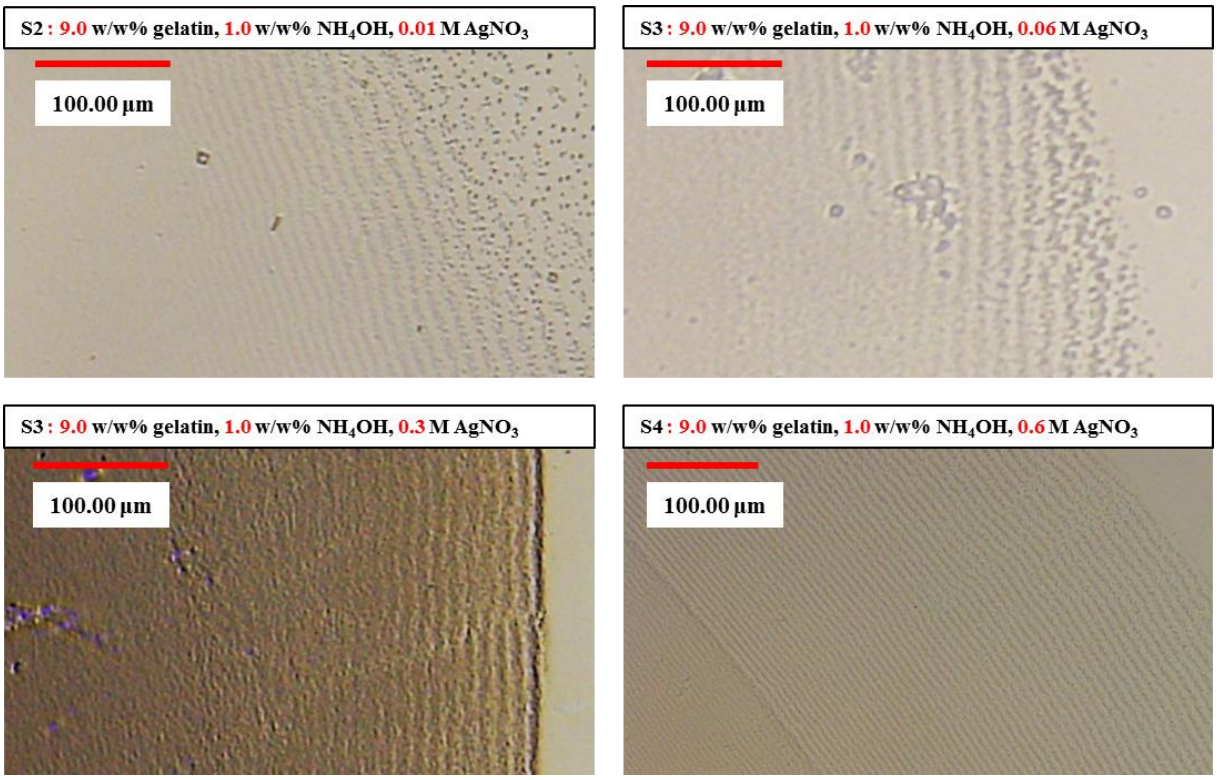

Appendix B, Figure 10: High resolution images for each setup from the structural design experiments. Containing 9.0 w/w% gelatin in 1.0 w/w% ammonia as hydrogel matrix.

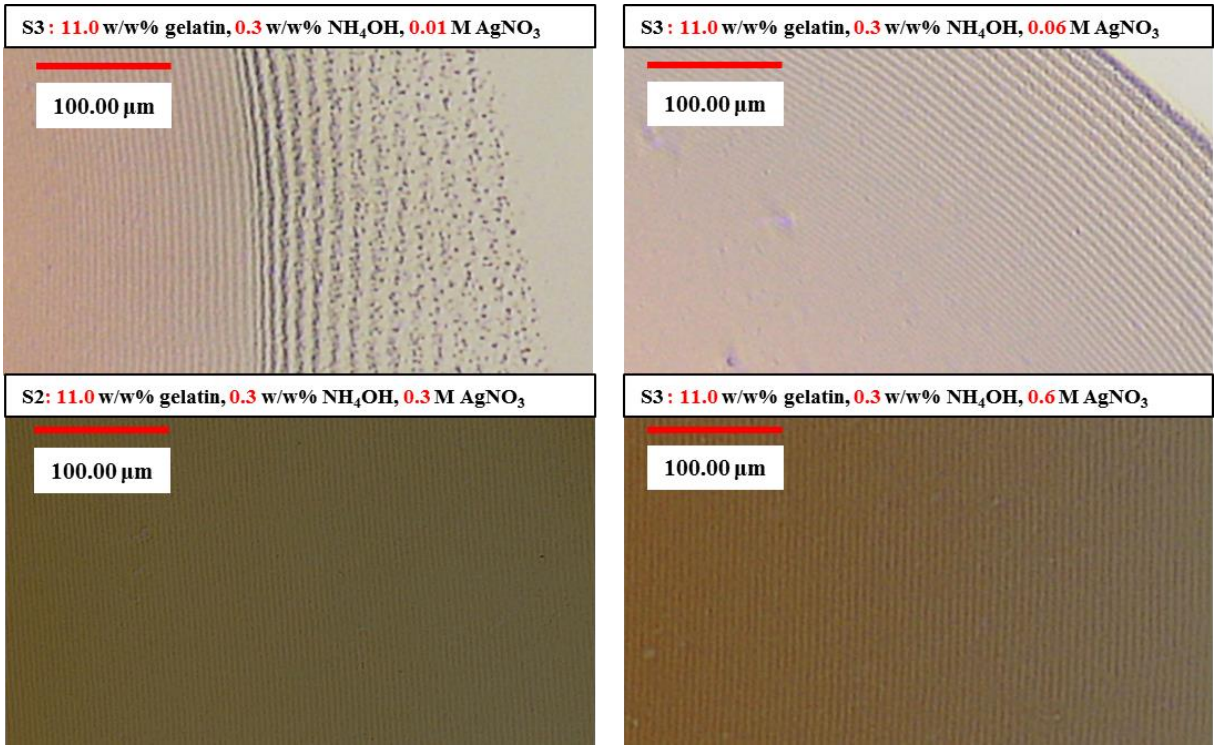

Appendix B, Figure 11: High resolution images for each setup from the structural design experiments. Containing 11.0 w/w% gelatin in 0.3 w/w% ammonia as hydrogel matrix.

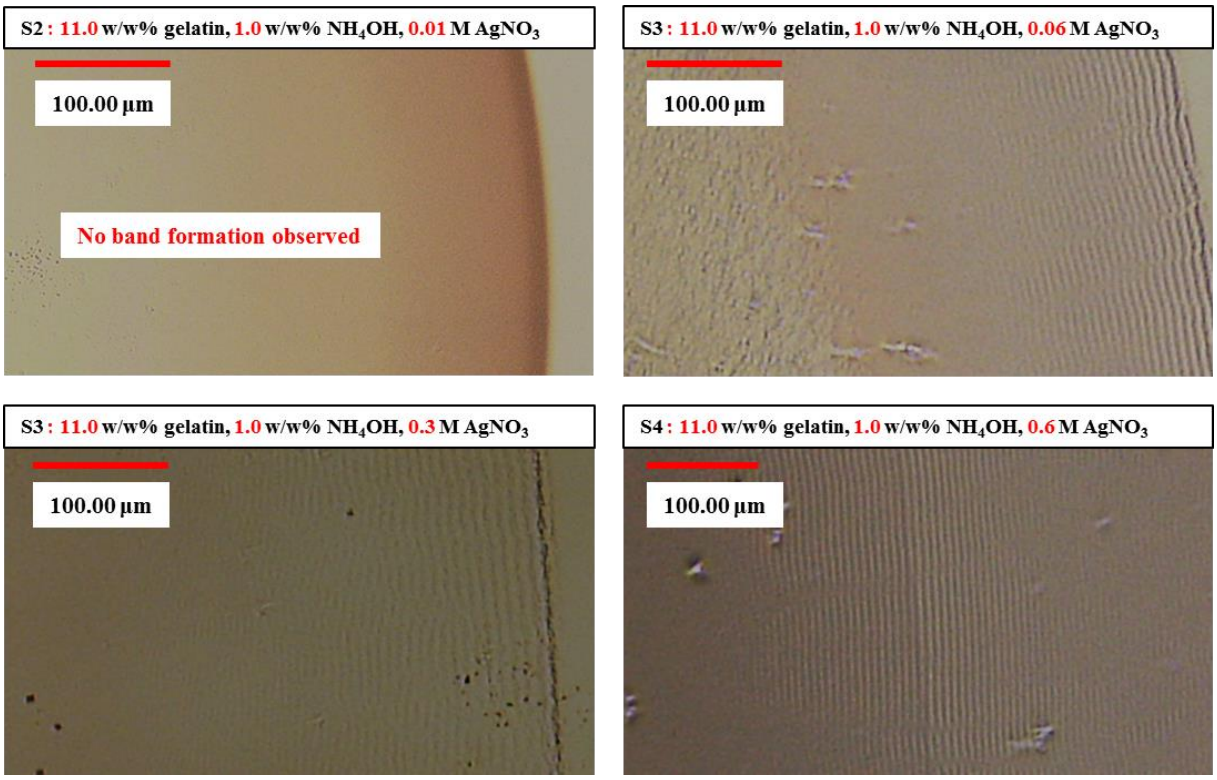

Appendix B, Figure 12: High resolution images for each setup from the structural design experiments. Containing 11.0 w/w% gelatin in 1.0 w/w% ammonia as hydrogel matrix.

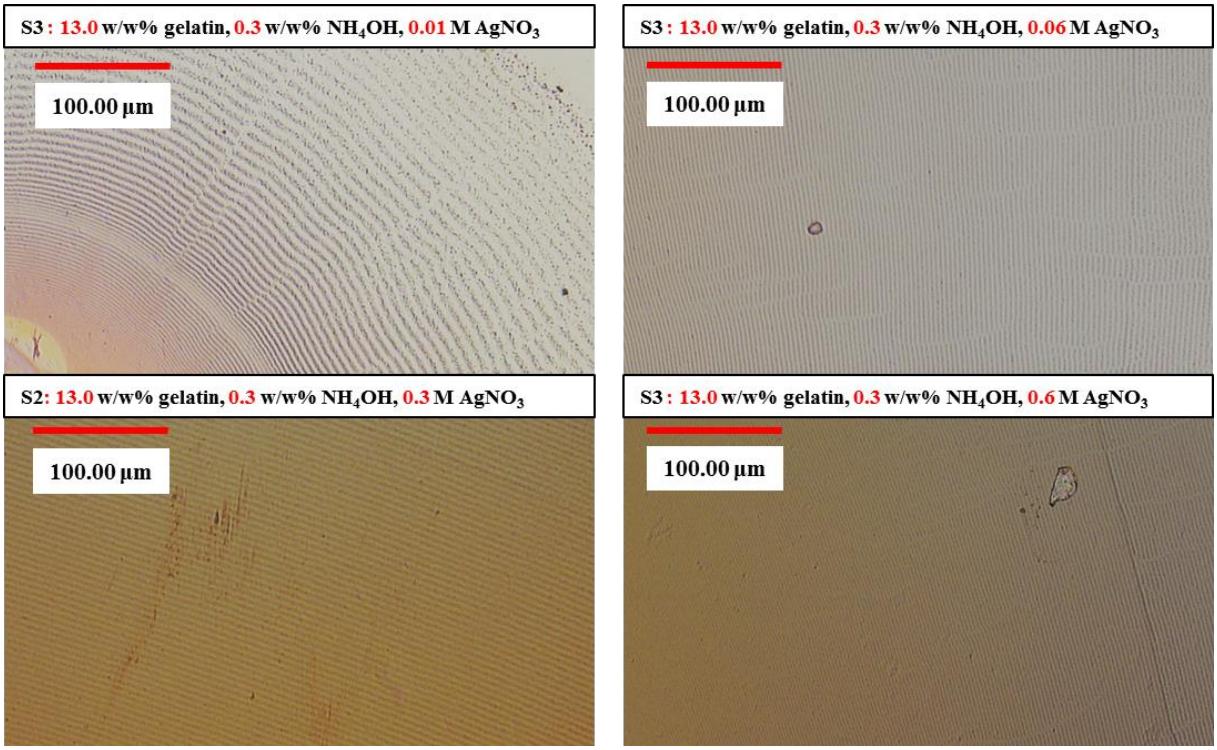

Appendix B, Figure 13: High resolution images for each setup from the structural design experiments. Containing 13.0 w/w% gelatin in 0.3 w/w% ammonia as hydrogel matrix.

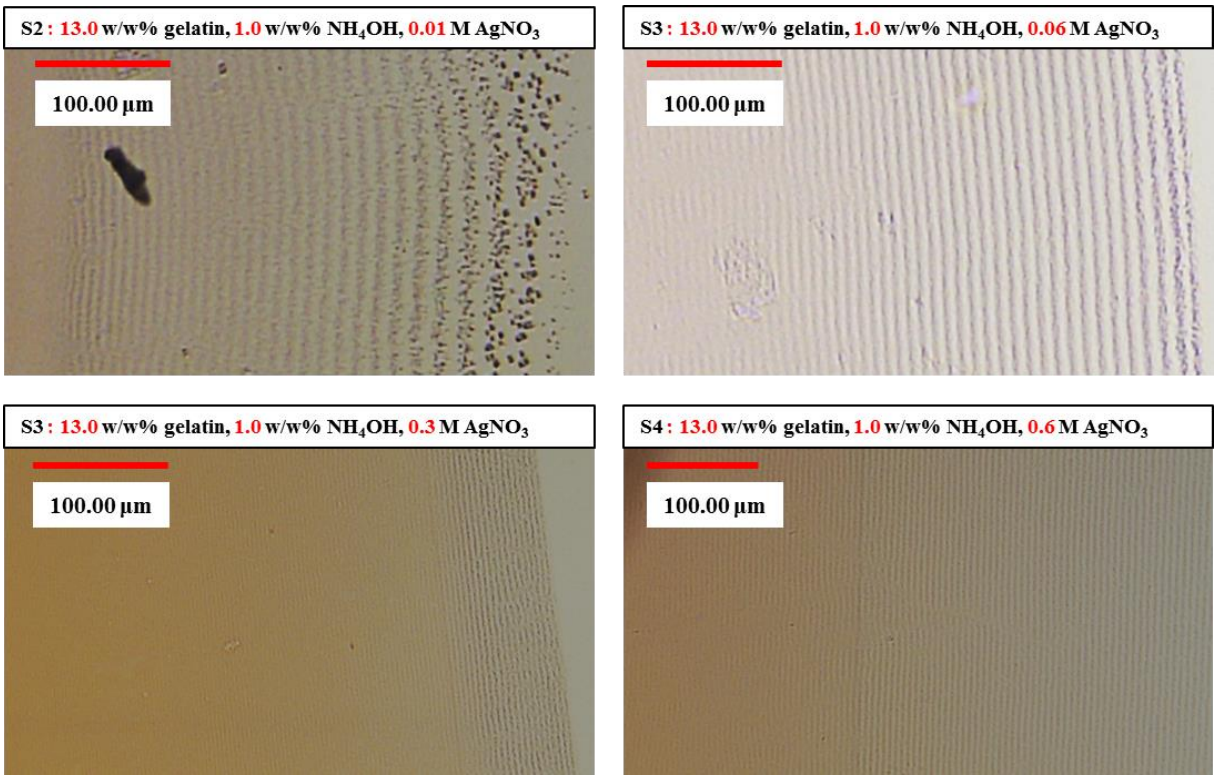

Appendix B, Figure 14: High resolution images for each setup from the structural design experiments. Containing 13.0 w/w% gelatin in 1.0 w/w% ammonia as hydrogel matrix.

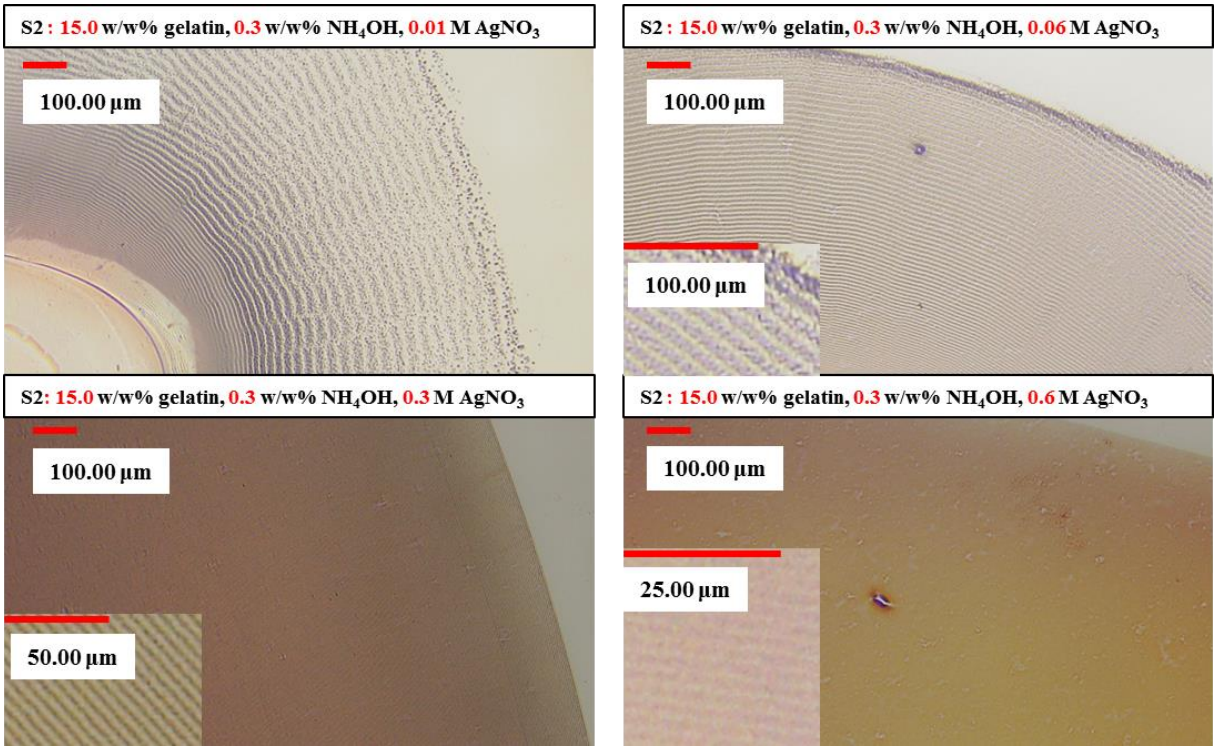

Appendix B, Figure 15: High resolution images for each setup from the structural design experiments. Containing 15.0 w/w% gelatin in 0.3 w/w% ammonia as hydrogel matrix.

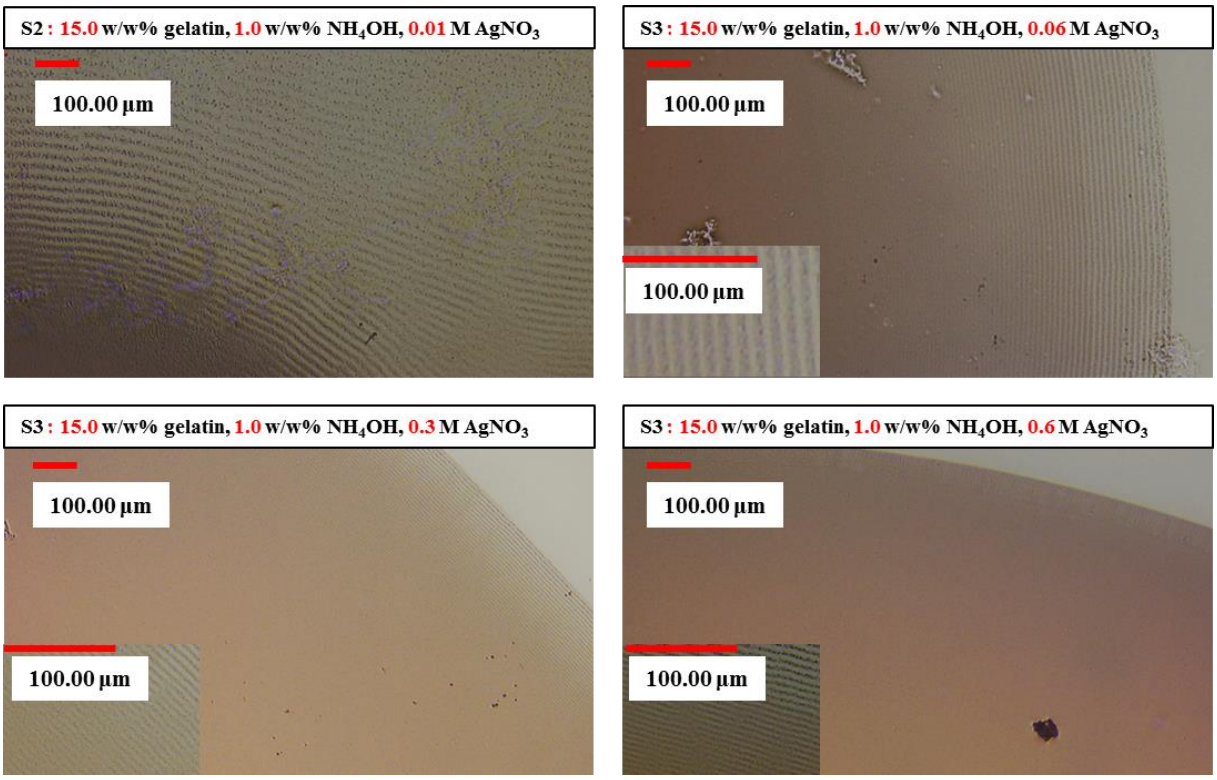

Appendix B, Figure 16: High resolution images for each setup from the structural design experiments. Containing 15.0 w/w% gelatin in 1.0 w/w% ammonia as hydrogel matrix.

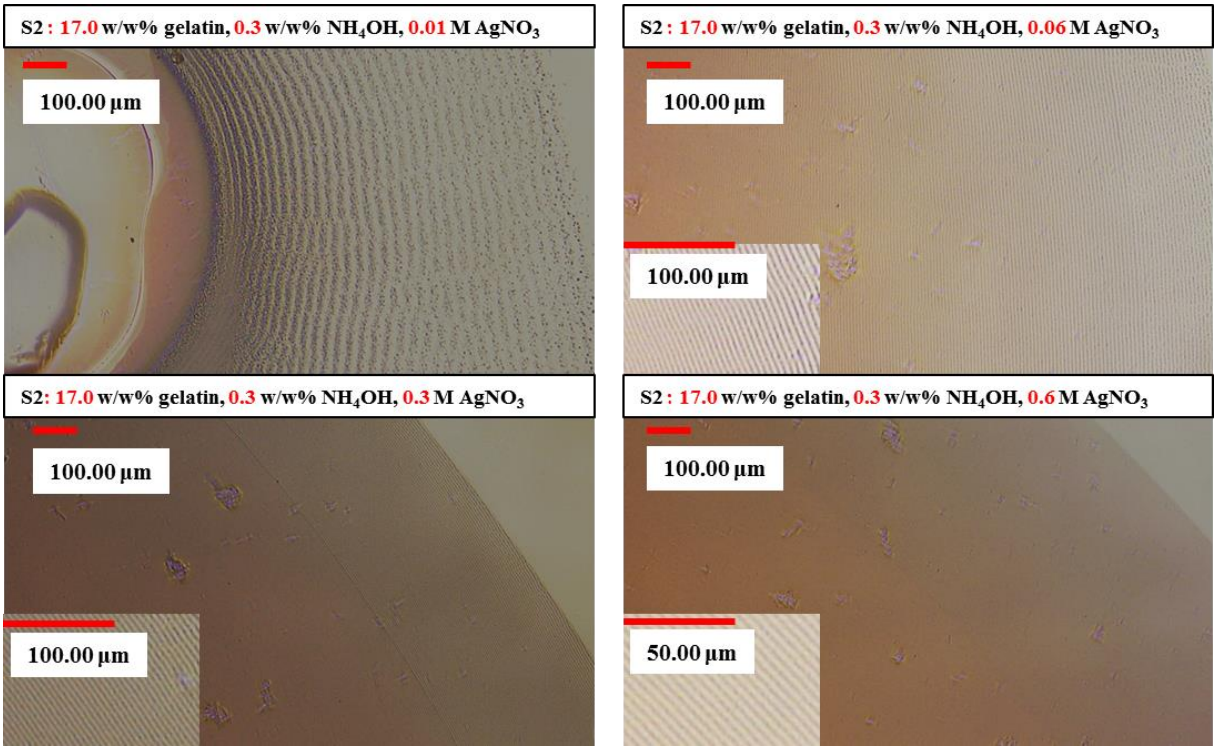

Appendix B, Figure 17: High resolution images for each setup from the structural design experiments. Containing 17.0 w/w% gelatin in 0.3 w/w% ammonia as hydrogel matrix.

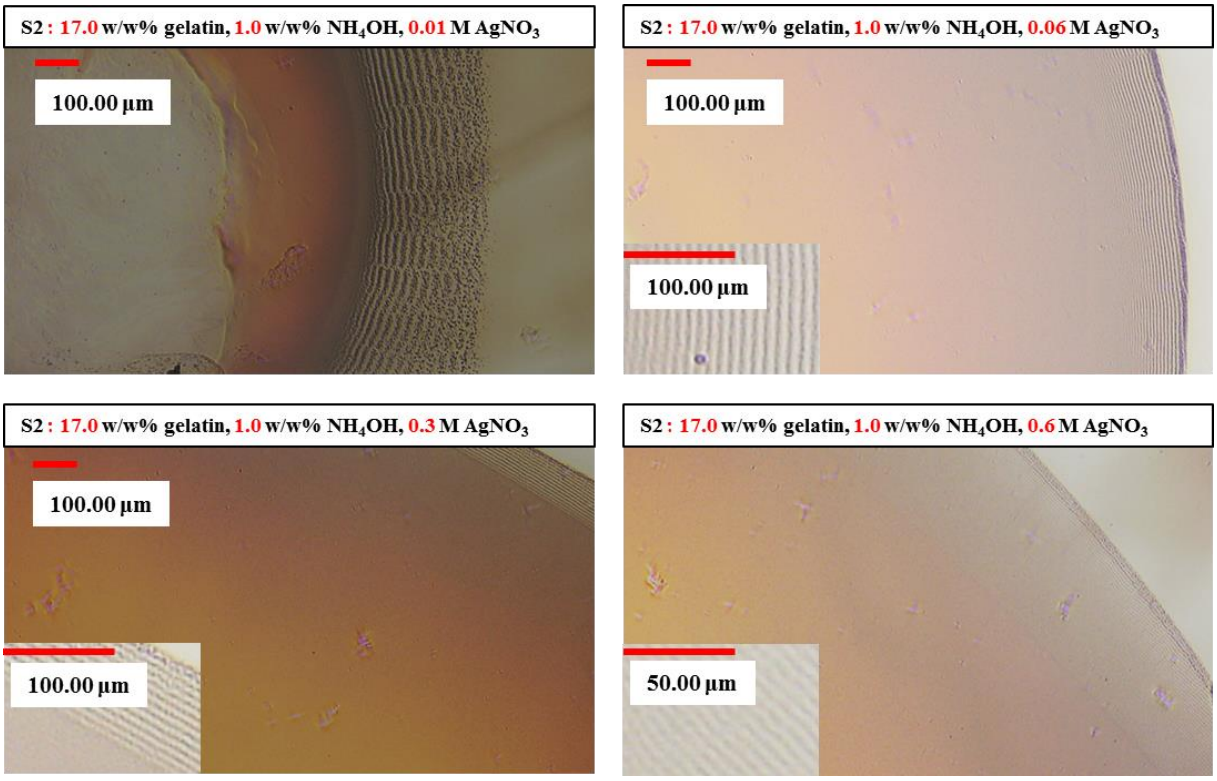

Appendix B, Figure 18: High resolution images for each setup from the structural design experiments. Containing 17.0 w/w% gelatin in 1.0 w/w% ammonia as hydrogel matrix.

Screening for new systems HTS-plate (Section 6.2.2)

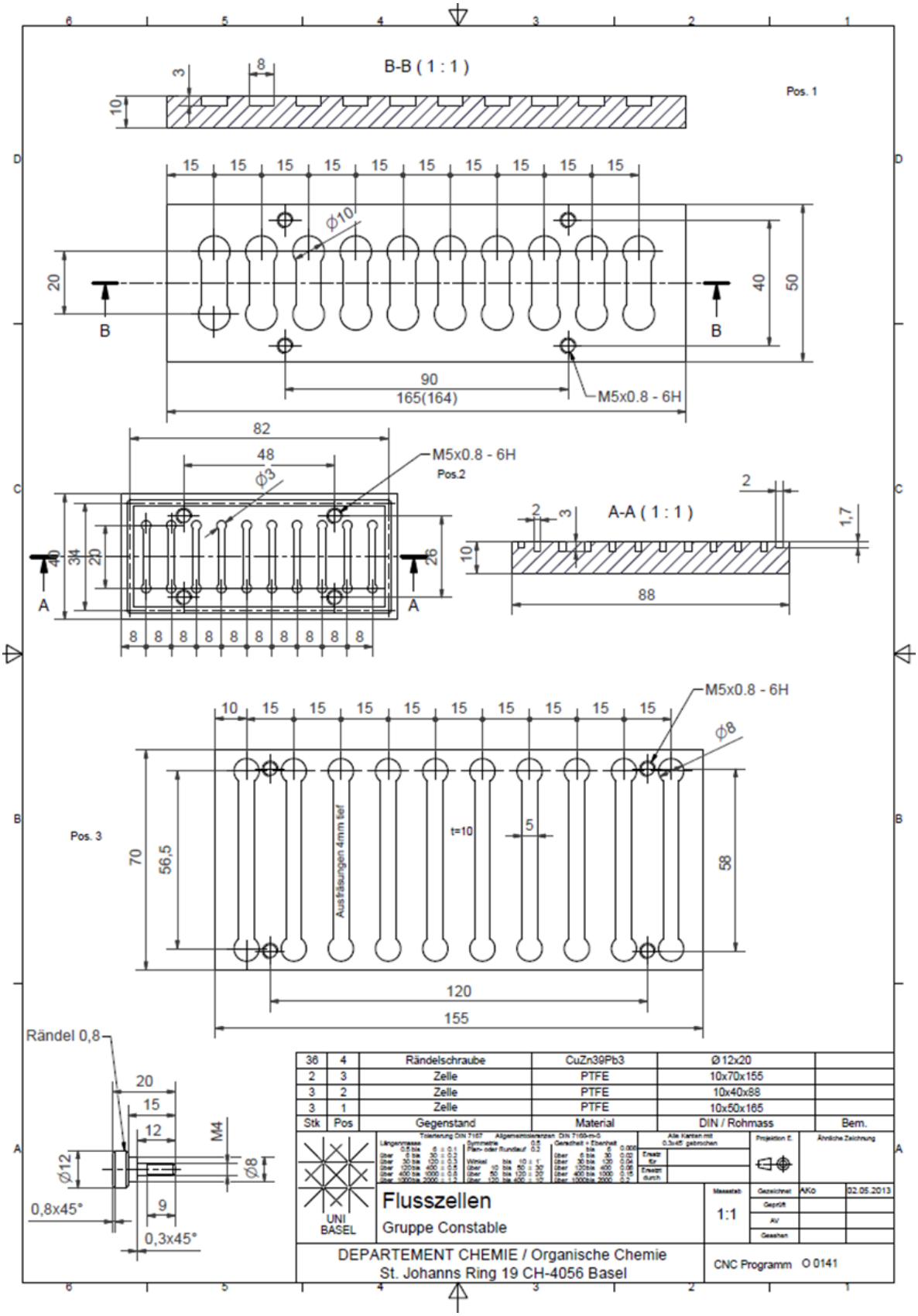

Stk	Pos	Gegenstand	Material	DIN / Rohmass	Bem.
36	4	Rändelschraube	CuZn39Pb3	Ø 12x20	
2	3	Zelle	PTFE	10x70x155	
3	2	Zelle	PTFE	10x40x88	
3	1	Zelle	PTFE	10x50x165	

Appendix B, Figure 19: Blue prints of the HTS-plates used for screening new Liesegang systems.

Appendix C: EDX data

Chapter 3: Classical Liesegang system (part 1)

Background measurement (only gelatin)

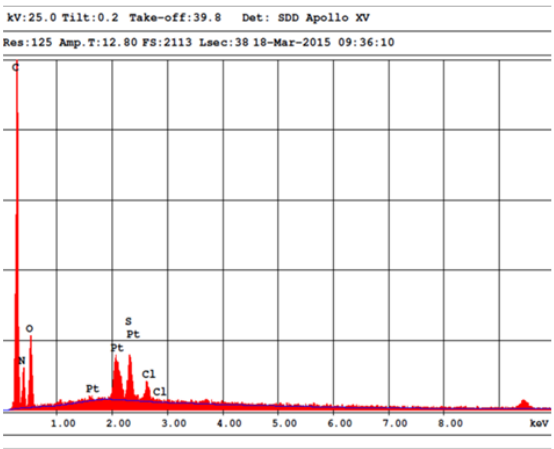

EDAX ZAF Quantification (Standardless)
Element Normalized
SEC Table : User C:\Savecalib18072012\SEC Genesis\BCNOF_19072012.sec

Element	Wt %	At %	K-Ratio	Z	A	F
C K	40.65	48.59	0.1665	1.0171	0.4025	1.0005
N K	27.79	28.49	0.0401	1.0090	0.1429	1.0004
O K	23.83	21.39	0.0320	1.0017	0.1341	1.0000
PtM	5.03	0.37	0.0529	0.7475	1.4070	1.0003
S K	1.79	0.80	0.0150	0.9577	0.8756	1.0011
ClK	0.90	0.37	0.0075	0.9072	0.9173	1.0000
Total	100.00	100.00				

EDX measurement: "white" core particles (primary bands)

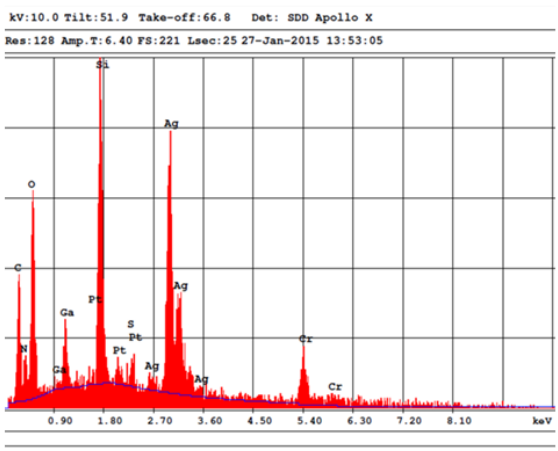

EDAX ZAF Quantification (Standardless)
Element Normalized
SEC Table : User C:\Savecalib18072012\SEC Genesis\BCNOF_19072012.sec

Element	Wt %	At %	K-Ratio	Z	A	F
C K	2.37	8.98	0.0184	1.2562	0.6191	1.0002
N K	2.60	8.46	0.0241	1.2405	0.7481	1.0004
O K	7.99	22.76	0.0548	1.2258	0.5599	1.0006
GaL	2.57	1.68	0.0201	0.9457	0.8258	1.0015
SiK	10.69	17.36	0.1162	1.1659	0.9272	1.0056
PtM	2.23	0.52	0.0170	0.7704	0.9916	1.0004
S K	1.11	1.59	0.0124	1.1479	0.9564	1.0173
AgL	50.94	21.54	0.4477	0.8788	0.9978	1.0023
CrK	19.51	17.11	0.1982	1.0278	0.9887	1.0000
Total	100.00	100.00				

Material surrounding the core structures (primary bands)

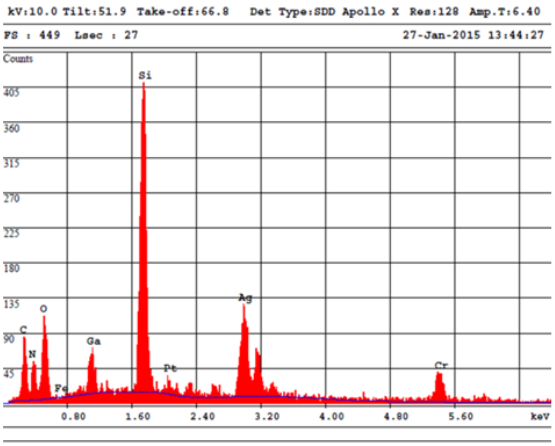

EDAX ZAF Quantification (Standardless)
Element Normalized
SEC Table : User D:\EDAX_Savecalib_21062012_install\SEC Genesis\BCNOF_210620

Element	Wt %	At %	K-Ratio	Z	A	F
C K	3.27	11.03	0.0212	1.2214	0.5300	1.0002
N K	3.93	11.35	0.0325	1.2063	0.6849	1.0004
O K	4.65	11.75	0.0329	1.1922	0.5943	1.0008
FeL	0.00	0.00	0.0000	0.9808	0.6242	1.0005
GaL	4.04	2.34	0.0315	0.9160	0.8490	1.0020
SiK	21.59	31.11	0.2294	1.1321	0.9346	1.0038
PtM	3.07	0.64	0.0226	0.7484	0.9823	1.0002
AgL	35.89	13.46	0.3052	0.8524	0.9946	1.0029
CrK	23.55	18.32	0.2318	0.9929	0.9913	1.0000
Total	100.00	100.00				

Material filling the space between particles (primary bands)

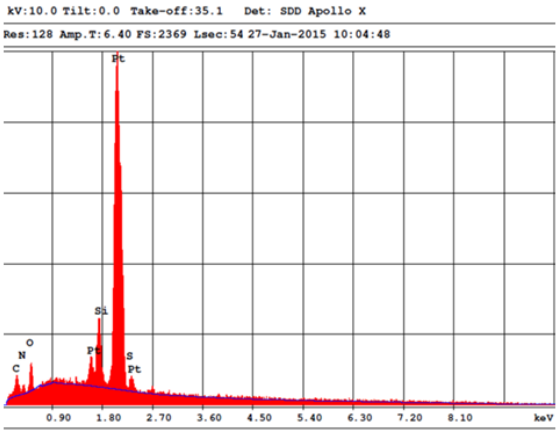

EDAX ZAF Quantification (Standardless)
Element Normalized
SEC Table : User C:\Savecalib18072012\SEC Genesis\BCNOF_19072012.sec

Element	Wt %	At %	K-Ratio	Z	A	F
C K	2.40	16.72	0.0087	1.4714	0.2452	1.0000
N K	2.32	13.82	0.0091	1.4514	0.2710	1.0001
O K	3.27	17.08	0.0150	1.4325	0.3212	1.0000
SiK	4.67	13.90	0.0544	1.3780	0.8458	1.0001
PtM	86.88	37.24	0.7919	0.9065	1.0056	1.0000
S K	0.47	1.24	0.0044	1.3527	0.6845	1.0000
Total	100.00	100.00				

Appendix C, EDX spectrum 1: EDX spectra and quantitative analysis of the classical Liesegang system (Section 3.4.2 part 1)

Chapter 3: Classical Liesegang system (part 2)

Si_3N_4 membrane (background)

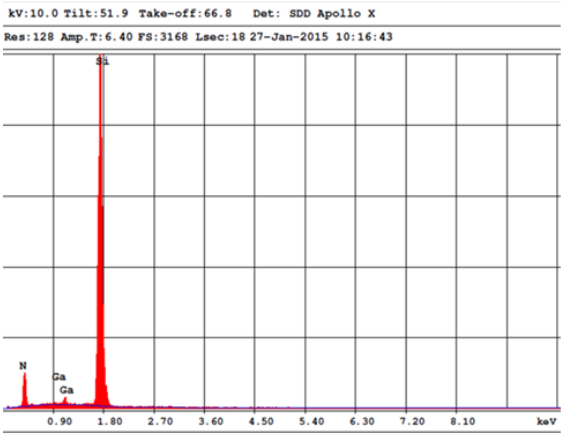

EDAX ZAF Quantification (Standardless)
Element Normalized
SEC Table : User C:\Savecalib18072012\SEC Genesis\BCNOF_19072012.sec

Element	Wt %	At %	K-Ratio	Z	A	F
N K	18.10	30.95	0.0992	1.0603	0.5169	1.0002
GaL	1.61	0.55	0.0129	0.7917	0.9954	1.0139
SiK	80.29	68.49	0.7883	0.9886	0.9931	1.0000
Total	100.00	100.00				

Material forming the core structures (secondary bands)

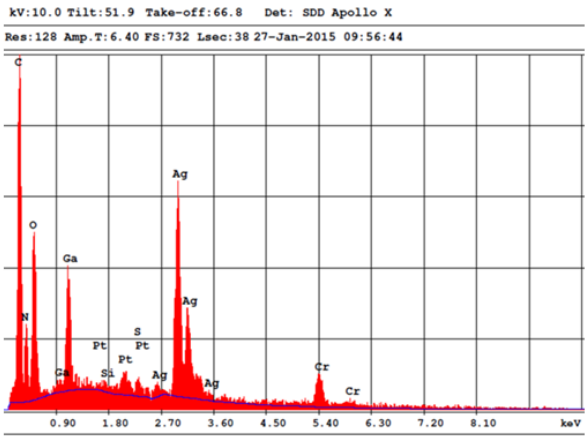

EDAX ZAF Quantification (Standardless)
Element Normalized
SEC Table : User C:\Savecalib18072012\SEC Genesis\BCNOF_19072012.sec

Element	Wt %	At %	K-Ratio	Z	A	F
C K	8.42	27.70	0.0743	1.2500	0.7061	1.0002
N K	5.10	14.38	0.0464	1.2344	0.7364	1.0004
O K	8.28	20.45	0.0559	1.2199	0.5530	1.0005
GaL	6.89	3.90	0.0538	0.9409	0.8303	1.0008
SiK	0.41	0.57	0.0044	1.1602	0.9216	1.0055
PtM	3.65	0.74	0.0280	0.7666	1.0015	1.0004
S K	0.91	1.12	0.0102	1.1423	0.9617	1.0178
AgL	48.95	17.93	0.4293	0.8747	1.0004	1.0021
CrK	17.39	13.21	0.1761	1.0234	0.9895	1.0000
Total	100.00	100.00				

Material surrounding the core structures (secondary bands)

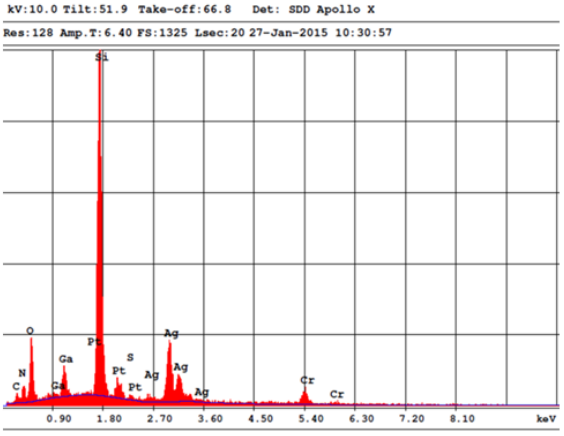

EDAX ZAF Quantification (Standardless)
Element Normalized
SEC Table : User C:\Savecalib18072012\SEC Genesis\BCNOF_19072012.sec

Element	Wt %	At %	K-Ratio	Z	A	F
C K	0.62	2.09	0.0035	1.2112	0.4628	1.0001
N K	3.05	8.81	0.0238	1.1962	0.6528	1.0004
O K	5.95	15.04	0.0417	1.1823	0.5925	1.0006
GaL	3.43	1.99	0.0272	0.9084	0.8698	1.0029
SiK	31.83	45.84	0.3381	1.1227	0.9428	1.0034
PtM	5.87	1.22	0.0424	0.7422	0.9743	1.0002
S K	0.58	0.73	0.0061	1.1058	0.9395	1.0094
AgL	33.70	12.64	0.2823	0.8454	0.9889	1.0017
CrK	14.96	11.64	0.1460	0.9851	0.9907	1.0000
Total	100.00	100.00				

Appendix C, EDX spectrum 2: EDX spectra and quantitative analysis of the classical Liesegang system (Section 3.4.2 part 2)

Chapter 4: New Silver Liesegang system

Section 4.3.4: STEM-EDX measurements

Background (Cu-TEM grid + Thermowax)

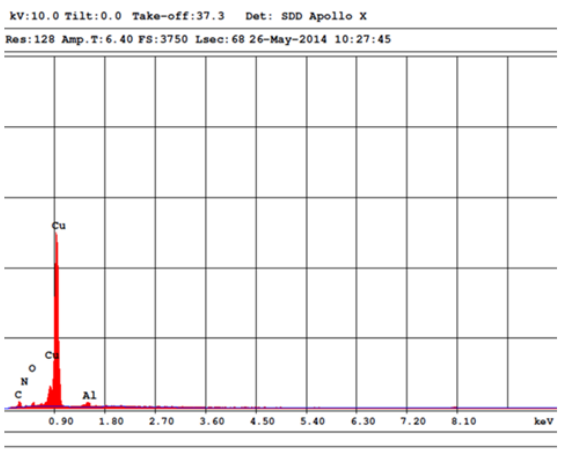

EDAX ZAF Quantification (Standardless)
Element Normalized
SEC Table : User C:\Savecalib18072012\SEC Genesis\BCNOF_19072012.sec

Element	Wt %	At %	K-Ratio	Z	A	F
C K	5.15	20.13	0.0153	1.2480	0.2381	1.0002
N K	1.30	4.36	0.0058	1.2325	0.3639	1.0008
O K	1.75	5.13	0.0116	1.2181	0.5430	1.0021
CuL	89.23	65.92	0.8497	0.9710	0.9807	1.0001
AlK	2.57	4.47	0.0174	1.1321	0.5972	1.0000
Total	100.00	100.00				

STEM-EDX on particles forming the finestructured bands

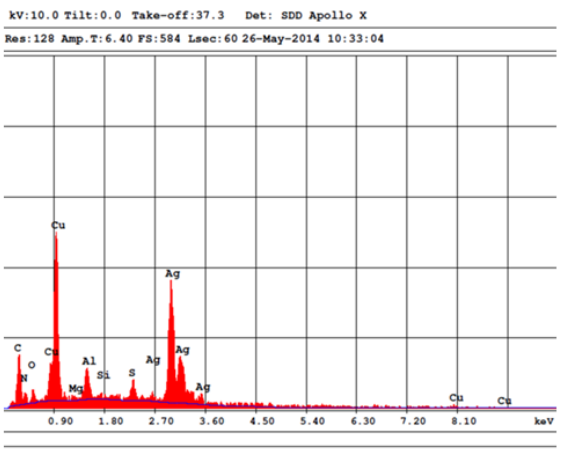

EDAX ZAF Quantification (Standardless)
Element Normalized
SEC Table : User C:\Savecalib18072012\SEC Genesis\BCNOF_19072012.sec

Element	Wt %	At %	K-Ratio	Z	A	F
C K	6.35	26.19	0.0329	1.2862	0.4037	1.0001
N K	2.92	10.34	0.0184	1.2699	0.4952	1.0002
O K	2.42	7.50	0.0088	1.2548	0.2893	1.0003
CuL	25.49	19.89	0.1566	0.9995	0.6145	1.0005
MgK	0.35	0.71	0.0025	1.2253	0.5941	1.0014
AlK	2.75	5.05	0.0228	1.1734	0.7056	1.0024
SiK	0.40	0.71	0.0038	1.1946	0.7854	1.0046
S K	2.17	3.35	0.0233	1.1758	0.8984	1.0150
AgL	57.15	26.26	0.5118	0.9008	0.9942	1.0000
Total	100.00	100.00				

STEM-EDX on particles which changed its structure during observations

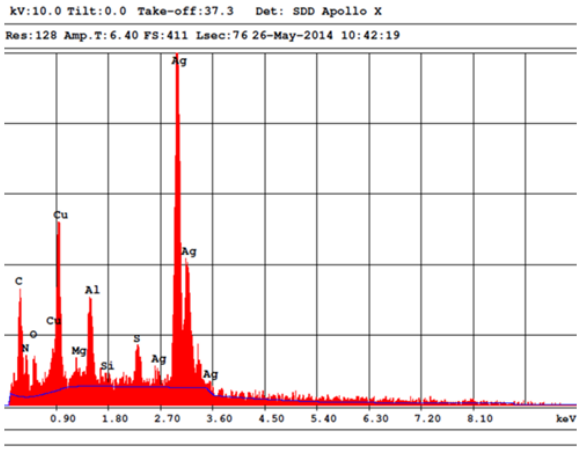

EDAX ZAF Quantification (Standardless)
Element Normalized
SEC Table : User C:\Savecalib18072012\SEC Genesis\BCNOF_19072012.sec

Element	Wt %	At %	K-Ratio	Z	A	F
C K	4.62	22.23	0.0280	1.3183	0.4600	1.0001
N K	3.24	13.37	0.0232	1.3015	0.5507	1.0001
CuL	12.34	11.23	0.0704	1.0236	0.5569	1.0006
MgK	0.85	2.03	0.0067	1.2609	0.6178	1.0018
AlK	3.35	7.17	0.0292	1.2055	0.7226	1.0031
SiK	0.43	0.89	0.0042	1.2257	0.7960	1.0059
S K	2.23	4.02	0.0248	1.2060	0.9038	1.0197
AgL	72.93	39.07	0.6724	0.9252	0.9966	1.0000
Total	100.00	100.00				

SEM-EDX measurement on a particle forming the bands in the silver Liesegang system

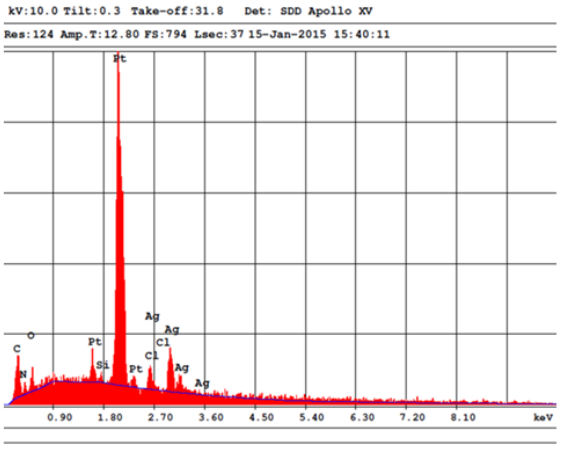

EDAX ZAF Quantification (Standardless)
Element Normalized
SEC Table : User C:\Savecalib18072012\SEC Genesis\BCNOF_19072012.sec

Element	Wt %	At %	K-Ratio	Z	A	F
C K	4.59	29.74	0.0179	1.4540	0.2687	1.0000
N K	2.62	14.58	0.0106	1.4344	0.2805	1.0000
O K	2.12	10.33	0.0082	1.4159	0.2725	1.0000
SiK	0.30	0.82	0.0033	1.3604	0.8243	1.0009
PtM	72.72	29.02	0.6620	0.8954	1.0167	1.0001
ClK	1.88	4.13	0.0189	1.2829	0.7831	1.0033
AgL	15.77	11.38	0.1390	1.0360	0.8505	1.0000
Total	100.00	100.00				

Appendix C, EDX spectrum 3: STEM-EDX spectrum and quantitative material analysis of the new fine structured silver Liesegang system.

Section 4.3.4: New silver Liesegang system

SEM-EDX measurement on a particle found on the Cu-TEM grid used for STEM-EDX analysis

kV:10.0 Tilt:0.0 Take-off:37.3 Det: SDD Apollo X
Res:128 Amp.T:6.40 FS:822 Lsec:76 26-May-2014 10:42:19

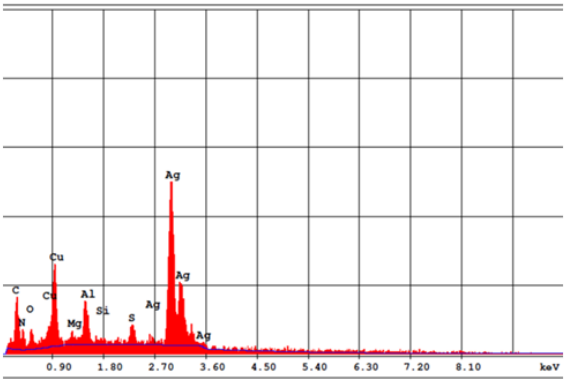

EDAX ZAF Quantification (Standardless)
Element Normalized
SEC Table : User C:\Savecalib18072012\SEC Genesis\BCNOF_19072012.sec

Element	Wt %	At %	K-Ratio	Z	A	F
C K	5.13	22.12	0.0312	1.2992	0.4678	1.0001
N K	3.11	11.48	0.0220	1.2827	0.5524	1.0001
O K	3.44	11.13	0.0115	1.2673	0.2631	1.0002
CuL	11.77	9.59	0.0667	1.0092	0.5612	1.0006
MgK	0.81	1.73	0.0063	1.2407	0.6244	1.0018
AlK	3.19	6.13	0.0277	1.1870	0.7287	1.0030
SiK	0.41	0.76	0.0040	1.2075	0.8015	1.0058
S K	2.14	3.45	0.0235	1.1883	0.9071	1.0193
AgL	70.00	33.60	0.6370	0.9112	0.9987	1.0000
Total	100.00	100.00				

SEM-EDX measurement on a particle forming the bands in the silver Liesegang system

kV:30.0 Tilt:0.0 Take-off:41.7 Det: SDD Apollo XV
Res:125 Amp.T:12.80 FS:2050 Lsec:17 18-Mar-2015 09:24:17

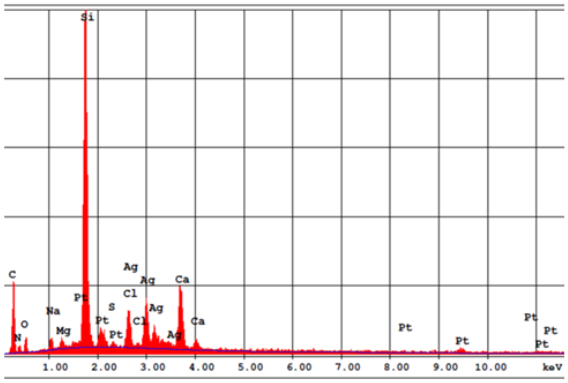

EDAX ZAF Quantification (Standardless)
Element Normalized
SEC Table : User C:\Savecalib18072012\SEC Genesis\BCNOF_19072012.sec

Element	Wt %	At %	K-Ratio	Z	A	F
C K	34.73	53.29	0.0662	1.0449	0.1824	1.0002
N K	11.65	15.33	0.0129	1.0371	0.1070	1.0002
O K	8.96	10.32	0.0108	1.0301	0.1166	1.0003
NaK	1.33	1.07	0.0040	0.9676	0.3081	1.0035
MgK	0.73	0.55	0.0031	0.9930	0.4249	1.0068
SiK	20.37	13.36	0.1425	0.9939	0.7014	1.0038
S K	0.32	0.18	0.0019	0.9877	0.6188	1.0094
ClK	2.66	1.38	0.0183	0.9462	0.7190	1.0118
AgL	9.21	1.57	0.0730	0.8022	0.9828	1.0051
CaK	5.45	2.51	0.0427	0.9681	0.8089	1.0000
PtL	4.59	0.43	0.0354	0.7222	1.0690	1.0000
Total	100.00	100.00				

SEM-FIB-EDX measurement on a particle forming the bands in the silver Liesegang system

kV:15.0 Tilt:51.9 Take-off:66.8 Det: SDD Apollo X
Res:128 Amp.T:6.40 FS:292 Lsec:69 24-Jan-2014 12:05:52

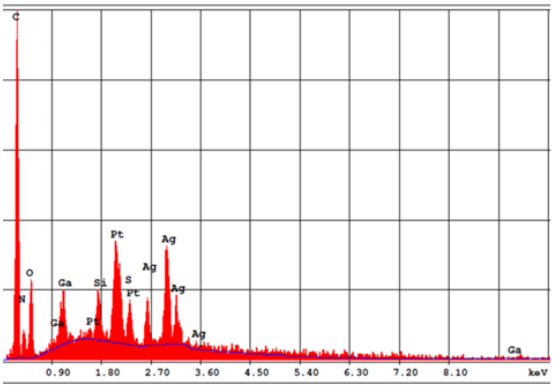

EDAX ZAF Quantification (Standardless)
Element Normalized
SEC Table : User C:\Savecalib18072012\SEC Genesis\BCNOF_19072012.sec

Element	Wt %	At %	K-Ratio	Z	A	F
C K	24.20	54.35	0.1337	1.1577	0.4771	1.0001
N K	6.90	13.29	0.0303	1.1459	0.3835	1.0002
O K	9.20	15.52	0.0379	1.1350	0.3629	1.0001
GaL	4.75	1.84	0.0342	0.9034	0.7963	1.0009
SiK	2.91	2.79	0.0288	1.1044	0.8943	1.0041
PtM	22.35	3.09	0.1701	0.7429	1.0242	1.0003
S K	2.87	2.41	0.0280	1.0801	0.8956	1.0091
AgL	26.84	6.71	0.2243	0.8572	0.9749	1.0000
Total	100.00	100.00				

SEM-FIB-EDX measurement on a particle forming the bands in the silver Liesegang system on FTO-glass

kV:15.0 Tilt:51.9 Take-off:66.8 Det: SDD Apollo X
Res:128 Amp.T:6.40 FS:269 Lsec:47 21-Nov-2014 11:11:41

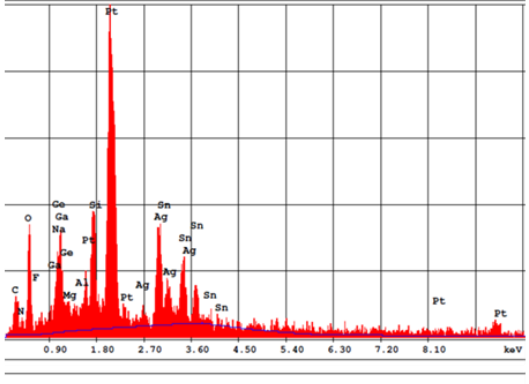

EDAX ZAF Quantification (Standardless)
Element Normalized
SEC Table : User C:\Savecalib18072012\SEC Genesis\BCNOF_19072012.sec

Element	Wt %	At %	K-Ratio	Z	A	F
C K	1.65	8.45	0.0081	1.3017	0.3740	1.0001
N K	1.58	6.91	0.0091	1.2879	0.4493	1.0002
O K	7.20	27.61	0.0346	1.2752	0.3763	1.0002
F K	0.76	2.47	0.0038	1.1961	0.4201	1.0004
NaK	1.88	5.00	0.0142	1.1862	0.6367	1.0015
GaL	4.95	4.35	0.0365	1.0130	0.7271	1.0010
GeL	1.17	0.99	0.0087	1.0019	0.7444	1.0012
MgK	0.73	1.84	0.0062	1.2135	0.7043	1.0014
AlK	0.63	1.43	0.0059	1.2020	0.7833	1.0024
SiK	4.62	10.09	0.0498	1.2696	0.8473	1.0023
PtM	43.23	13.59	0.3607	0.8504	0.9809	1.0001
AgL	18.05	10.26	0.1626	0.9685	0.9271	1.0036
SnL	13.56	7.01	0.1177	0.9331	0.9303	1.0000
Total	100.00	100.00				

Appendix C, EDX spectrum 4: SEM-EDX spectra and quantitative material analysis of the new fine structured silver Liesegang system.

Chapter 5: Applications of the silver Liesegang system

Section 5.3.2.1.2: SEM-FIB-EDX: Sintered silver Liesegang bands on FTO

SEM-FIB-EDX on sintered silver Liesegang bands on FTO

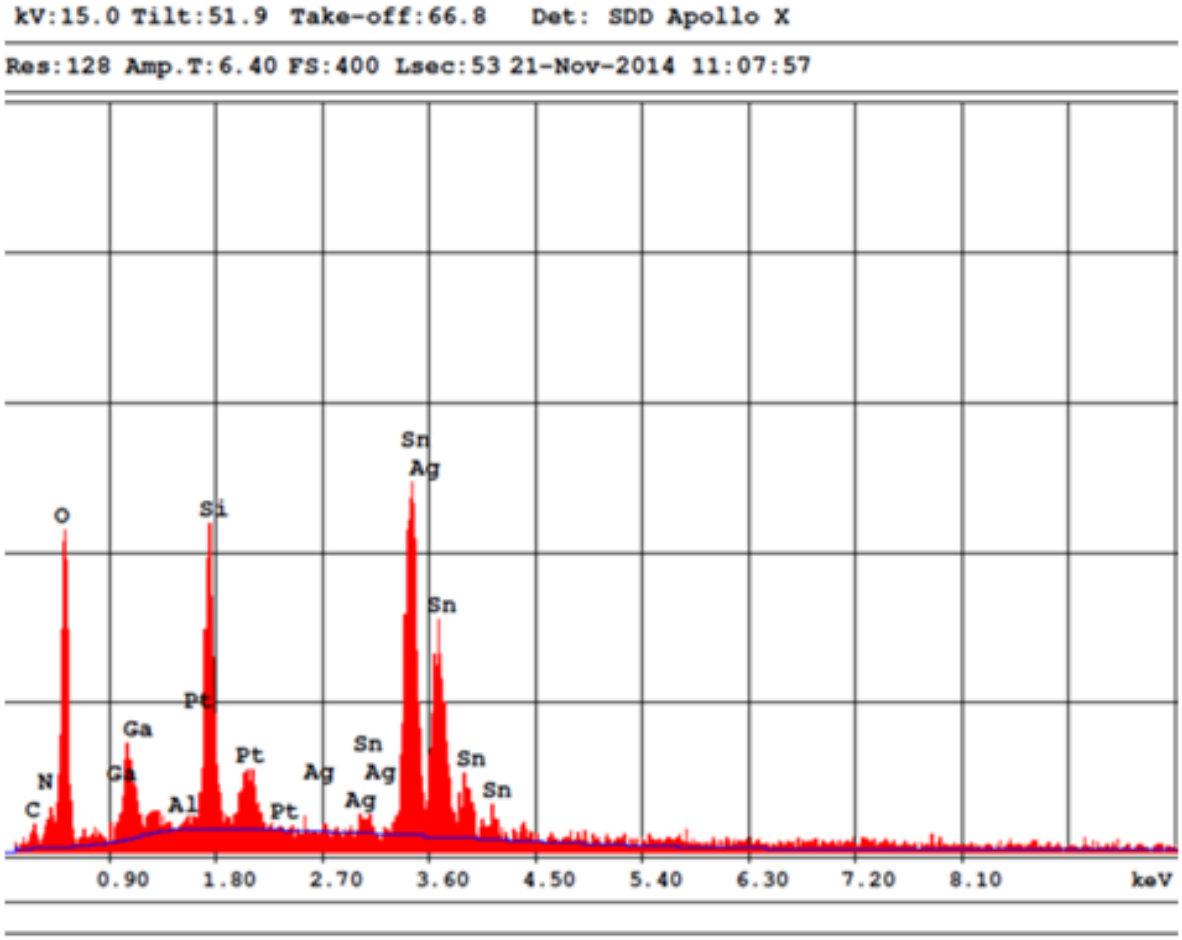

EDAX ZAF Quantification (Standardless)
Element Normalized
SEC Table : User C:\Savecalib18072012\SEC Genesis\BCNOF_19072012.sec

Element	Wt %	At %	K-Ratio	Z	A	F
C K	0.54	2.03	0.0031	1.2431	0.4664	1.0002
N K	2.49	8.02	0.0186	1.2302	0.6088	1.0003
O K	17.36	49.02	0.0775	1.2183	0.3664	1.0001
GaL	3.25	2.10	0.0211	0.9688	0.6683	1.0014
AlK	0.00	0.00	0.0000	1.1418	0.7641	1.0047
SiK	8.70	13.99	0.0873	1.1950	0.8358	1.0051
PtM	6.26	1.45	0.0484	0.8028	0.9630	1.0003
AgL	0.00	0.00	0.0000	0.9223	0.9826	1.0303
SnL	61.41	23.38	0.5427	0.8872	0.9961	1.0000
Total	100.00	100.00				

Appendix C, EDX spectrum 5: SEM-FIB-EDX spectra and quantitative material analysis of sintered fine structured silver Liesegang system precipitation bands.

Chapter 6: Screening for new systems

Section 6.3.3.2: [Ru(bpy)$_3$]Cr$_2$O$_7$ system

Background (gelatin containing the inner electrolyte)

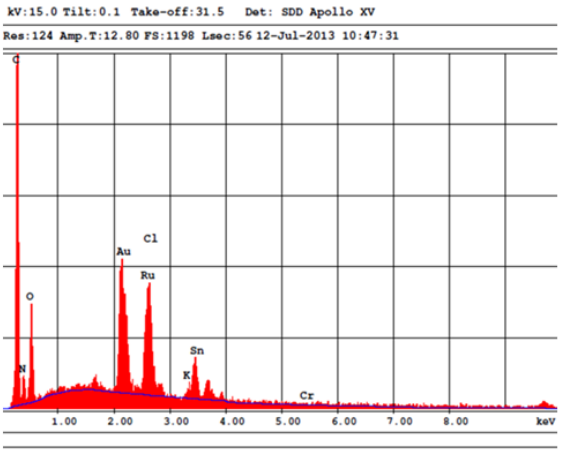

EDAX ZAF Quantification (Standardless)
Element Normalized
SEC Table : User C:\Savecalib18072012\SEC Genesis\BCNOF_19072012.sec

Element	Wt %	At %	K-Ratio	Z	A	F
RuL	28.96	20.21	0.2759	0.9578	0.9835	1.0113
ClK	23.97	47.71	0.2461	1.1464	0.8846	1.0123
K K	2.84	5.12	0.0252	1.1485	0.7732	1.0001
SnL	43.35	25.77	0.3450	0.9185	0.8665	1.0002
CrK	0.88	1.19	0.0083	1.0790	0.8808	1.0000
Total	100.00	100.00				

EDX measurements at the stamping zone

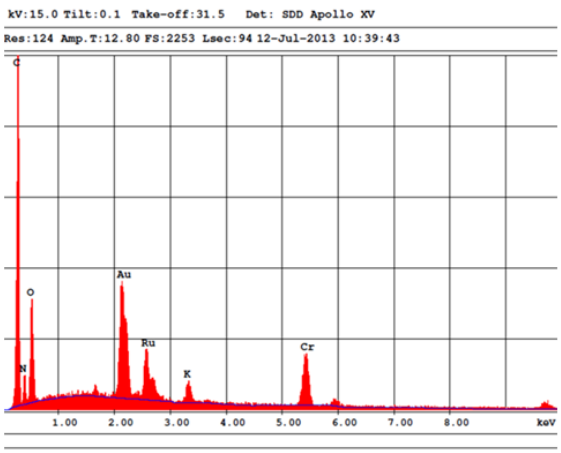

EDAX ZAF Quantification (Standardless)
Element Normalized
SEC Table : User C:\Savecalib18072012\SEC Genesis\BCNOF_19072012.sec

Element	Wt %	At %	K-Ratio	Z	A	F
RuL	35.33	21.18	0.3245	0.9214	0.9885	1.0087
K K	8.97	13.90	0.0814	1.1050	0.8116	1.0117
CrK	55.70	64.92	0.5460	1.0317	0.9500	1.0000
Total	100.00	100.00				

EDX measurements on the particles forming the bands

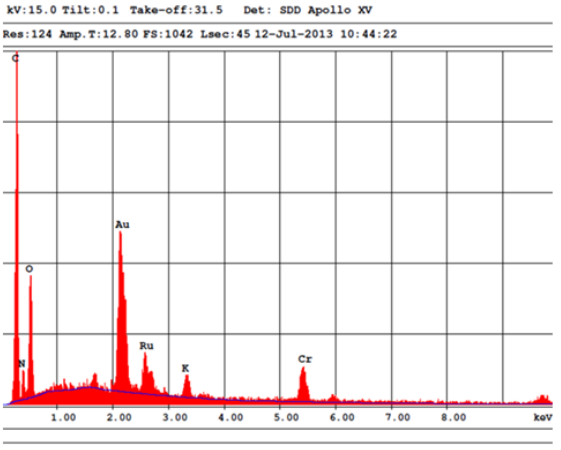

EDAX ZAF Quantification (Standardless)
Element Normalized
SEC Table : User C:\Savecalib18072012\SEC Genesis\BCNOF_19072012.sec

Element	Wt %	At %	K-Ratio	Z	A	F
RuL	35.37	20.91	0.3257	0.9186	0.9927	1.0097
K K	12.74	19.46	0.1153	1.1016	0.8132	1.0107
CrK	51.89	59.63	0.5052	1.0284	0.9466	1.0000
Total	100.00	100.00				

EDX measurements between two adjacent bands

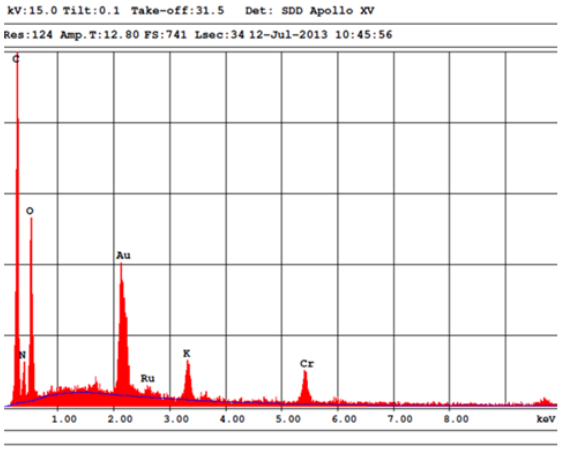

EDAX ZAF Quantification (Standardless)
Element Normalized
SEC Table : User C:\Savecalib18072012\SEC Genesis\BCNOF_19072012.sec

Element	Wt %	At %	K-Ratio	Z	A	F
RuL	9.00	4.41	0.0814	0.8848	1.0005	1.0223
K K	28.26	35.81	0.2814	1.0612	0.9212	1.0184
CrK	62.74	59.78	0.5958	0.9867	0.9624	1.0000
Total	100.00	100.00				

Appendix C, EDX spectrum 6: SEM-EDX spectra and quantitative material analysis of the [Ru(bpy)$_3$]Cr$_2$O$_7$ Liesegang system

Section 6.3.3.3: $[Fe(bpy)_3]Cr_2O_7$ system

Background (gelatin containing the inner electrolyte)

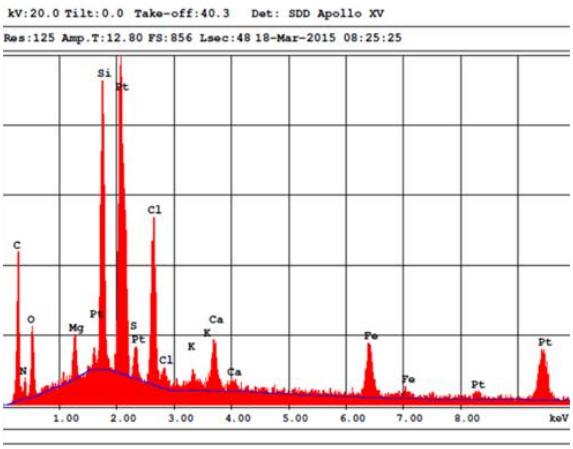

EDAX ZAF Quantification (Standardless)
Element Normalized
SEC Table : User C:\Savecalib18072012\SEC Genesis\BCNOF_19072012.sec

Element	Wt %	At %	K-Ratio	Z	A	F
C K	14.94	41.92	0.0288	1.1719	0.1645	1.0001
N K	5.60	13.48	0.0093	1.1613	0.1425	1.0002
O K	7.29	15.36	0.0146	1.1516	0.1742	1.0002
MgK	1.03	1.43	0.0055	1.1029	0.4859	1.0014
SiK	5.93	7.12	0.0465	1.1005	0.7117	1.0013
S K	0.81	0.85	0.0049	1.1262	0.5352	1.0028
ClK	5.74	5.46	0.0392	1.0710	0.6369	1.0012
K K	0.70	0.60	0.0051	1.0618	0.6914	1.0022
CaK	2.24	1.88	0.0183	1.0833	0.7532	1.0012
FeK	5.30	3.20	0.0514	1.0015	0.9464	1.0223
PtL	50.43	8.71	0.3932	0.7675	1.0158	1.0000
Total	100.00	100.00				

EDX measurements at the stamping zone

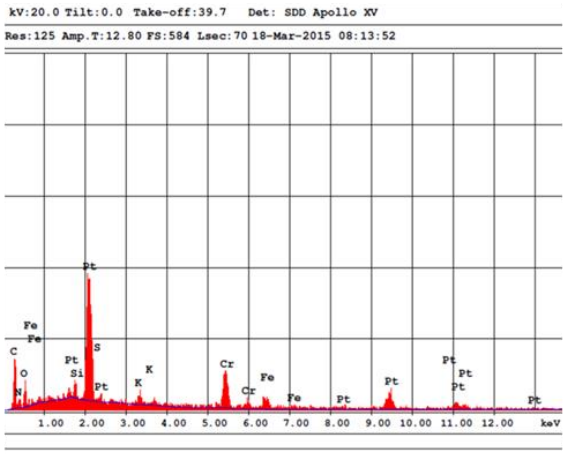

EDAX ZAF Quantification (Standardless)
Element Normalized
SEC Table : User C:\Savecalib18072012\SEC Genesis\BCNOF_19072012.sec

Element	Wt %	At %	K-Ratio	Z	A	F
C K	14.16	41.89	0.0372	1.1923	0.2202	1.0002
N K	7.91	20.07	0.0158	1.1815	0.1686	1.0003
O K	7.41	16.45	0.0162	1.1716	0.1866	1.0004
SiK	1.14	1.44	0.0086	1.1192	0.6789	1.0004
S K	0.00	0.00	0.0000	1.1503	0.5201	1.0009
K K	1.36	1.24	0.0102	1.0819	0.6931	1.0028
CrK	9.35	6.39	0.0875	1.0133	0.9101	1.0148
FeK	4.05	2.58	0.0396	1.0220	0.9346	1.0218
PtL	54.62	9.95	0.4350	0.7861	1.0130	1.0000
Total	100.00	100.00				

EDX measurements on the particles forming the bands

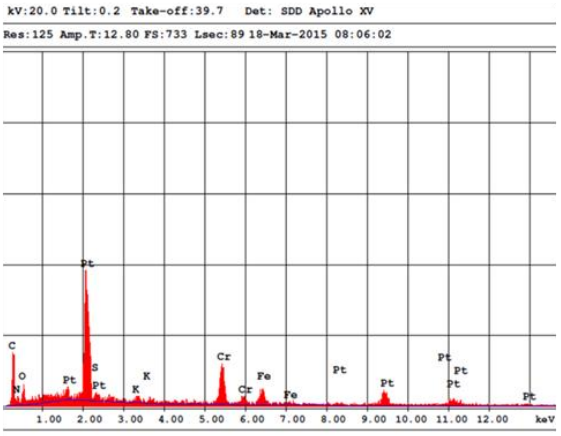

EDAX ZAF Quantification (Standardless)
Element Normalized
SEC Table : User C:\Savecalib18072012\SEC Genesis\BCNOF_19072012.sec

Element	Wt %	At %	K-Ratio	Z	A	F
C K	16.11	46.03	0.0429	1.1856	0.2246	1.0002
N K	6.93	16.97	0.0137	1.1749	0.1678	1.0003
O K	7.21	15.47	0.0161	1.1650	0.1916	1.0005
S K	0.53	0.57	0.0032	1.1412	0.5365	1.0010
K K	1.04	0.92	0.0080	1.0749	0.7070	1.0037
CrK	11.39	7.52	0.1067	1.0064	0.9164	1.0166
FeK	5.78	3.55	0.0560	1.0144	0.9359	1.0203
PtL	51.01	8.97	0.4020	0.7784	1.0125	1.0000
Total	100.00	100.00				

EDX measurements between two adjacent bands

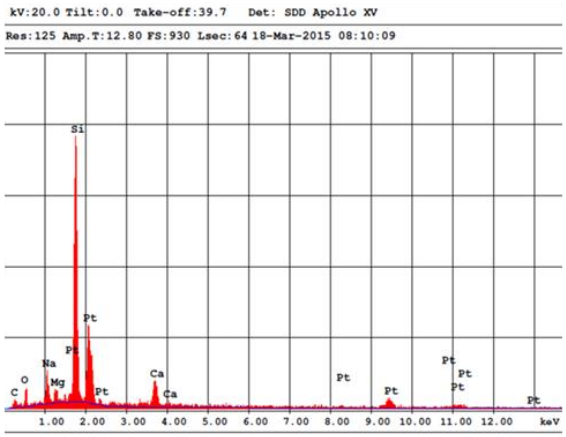

EDAX ZAF Quantification (Standardless)
Element Normalized
SEC Table : User C:\Savecalib18072012\SEC Genesis\BCNOF_19072012.sec

Element	Wt %	At %	K-Ratio	Z	A	F
C K	4.90	15.57	0.0077	1.1619	0.1343	1.0001
O K	9.05	21.57	0.0196	1.1418	0.1894	1.0003
NaK	4.41	7.31	0.0196	1.0673	0.4163	1.0029
MgK	1.52	2.38	0.0085	1.0936	0.5104	1.0053
SiK	28.45	38.62	0.2264	1.0913	0.7290	1.0004
CaK	5.88	5.59	0.0473	1.0733	0.7505	1.0000
PtL	45.80	8.95	0.3528	0.7566	1.0183	1.0000
Total	100.00	100.00				

Appendix C, EDX spectrum 7: EDX spectrum and quantitative analysis of the $[Fe(bpy)_3]Cr_2O_7$ Liesegang system.

Section 6.3.3.4: [Fe(pytpy)$_2$]Cl$_2$ / AgNO$_3$ system

Background (gelatin containing the inner electrolyte)

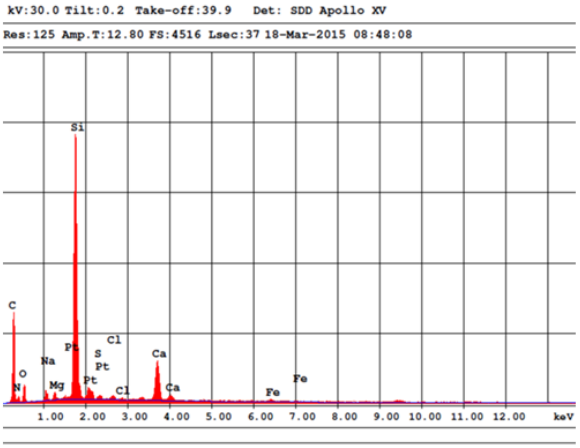

EDAX ZAF Quantification (Standardless)
Element Normalized
SEC Table : User C:\Savecalib18072012\SEC Genesis\BCNOF_19072012.sec

Element	Wt %	At %	K-Ratio	Z	A	F
C K	45.77	59.03	0.1046	1.0215	0.2236	1.0003
N K	13.73	15.18	0.0139	1.0139	0.1001	1.0003
O K	13.12	12.70	0.0162	1.0071	0.1229	1.0003
NaK	1.35	0.91	0.0043	0.9461	0.3359	1.0031
MgK	0.69	0.44	0.0031	0.9710	0.4671	1.0059
SiK	17.34	9.56	0.1285	0.9721	0.7615	1.0011
PtM	3.04	0.24	0.0258	0.7673	1.1076	1.0002
S K	0.33	0.16	0.0022	0.9662	0.6820	1.0025
ClK	0.34	0.15	0.0025	0.9256	0.7770	1.0037
CaK	3.90	1.51	0.0343	0.9410	0.9359	1.0004
FeK	0.40	0.11	0.0036	0.8712	1.0109	1.0075
Total	100.00	100.00				

EDX measurements at the stamping zone

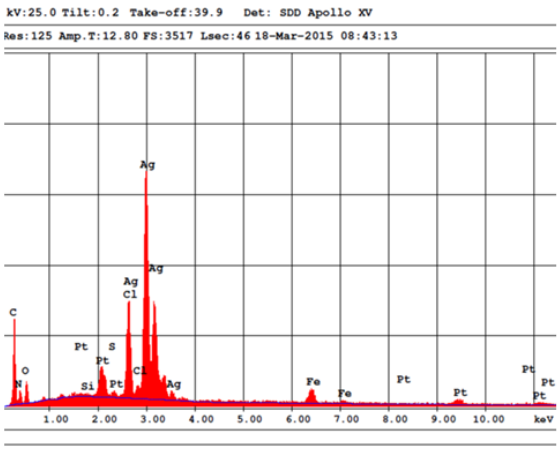

EDAX ZAF Quantification (Standardless)
Element Normalized
SEC Table : User C:\Savecalib18072012\SEC Genesis\BCNOF_19072012.sec

Element	Wt %	At %	K-Ratio	Z	A	F
C K	19.44	45.31	0.0592	1.1298	0.2697	1.0002
N K	9.00	18.00	0.0196	1.1206	0.1946	1.0002
O K	9.86	17.25	0.0127	1.1123	0.1154	1.0001
SiK	0.18	0.18	0.0011	1.0686	0.5718	1.0090
S K	0.35	0.30	0.0027	1.0605	0.7060	1.0257
ClK	6.05	4.78	0.0510	1.0293	0.7908	1.0347
AgL	44.47	11.54	0.3751	0.8673	0.9723	1.0005
FeK	3.12	1.56	0.0276	0.9648	0.9155	1.0046
PtL	7.55	1.08	0.0591	0.7632	1.0264	1.0000
Total	100.00	100.00				

EDX measurements on the particles forming the bands

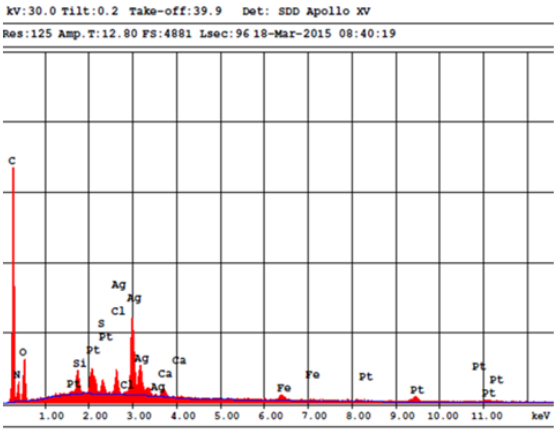

EDAX ZAF Quantification (Standardless)
Element Normalized
SEC Table : User C:\Savecalib18072012\SEC Genesis\BCNOF_19072012.sec

Element	Wt %	At %	K-Ratio	Z	A	F
C K	40.54	53.10	0.1698	1.0323	0.4055	1.0004
N K	20.05	22.52	0.0281	1.0246	0.1367	1.0004
O K	21.14	20.79	0.0260	1.0177	0.1210	1.0001
SiK	1.12	0.63	0.0073	0.9822	0.6613	1.0037
S K	0.61	0.30	0.0048	0.9762	0.7934	1.0098
ClK	1.02	0.45	0.0084	0.9352	0.8694	1.0142
AgL	10.13	1.48	0.0933	0.7906	1.1639	1.0009
CaK	0.46	0.18	0.0039	0.9539	0.8779	1.0005
FeK	0.75	0.21	0.0066	0.8815	0.9967	1.0080
PtL	4.17	0.34	0.0320	0.7118	1.0807	1.0000
Total	100.00	100.00				

EDX measurements between two adjacent bands

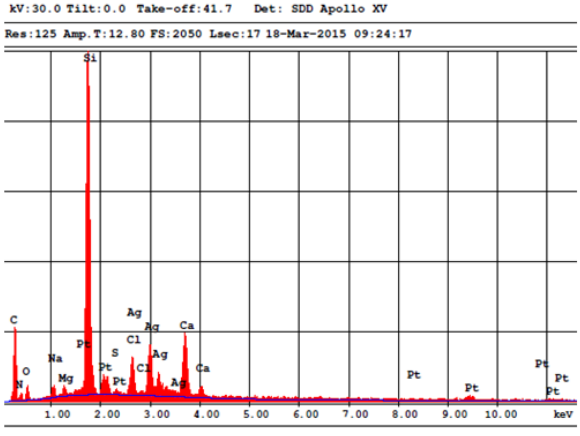

EDAX ZAF Quantification (Standardless)
Element Normalized
SEC Table : User C:\Savecalib18072012\SEC Genesis\BCNOF_19072012.sec

Element	Wt %	At %	K-Ratio	Z	A	F
C K	34.73	53.29	0.0662	1.0449	0.1824	1.0002
N K	11.65	15.33	0.0129	1.0371	0.1070	1.0002
O K	8.96	10.32	0.0108	1.0301	0.1166	1.0003
NaK	1.33	1.07	0.0040	0.9676	0.3081	1.0035
MgK	0.73	0.55	0.0031	0.9930	0.4249	1.0068
SiK	20.37	13.36	0.1425	0.9939	0.7014	1.0038
S K	0.32	0.18	0.0019	0.9877	0.6188	1.0094
ClK	2.66	1.38	0.0183	0.9462	0.7190	1.0118
AgL	9.21	1.57	0.0730	0.8022	0.9828	1.0051
CaK	5.45	2.51	0.0427	0.9681	0.8089	1.0000
PtL	4.59	0.43	0.0354	0.7222	1.0690	1.0000
Total	100.00	100.00				

Appendix C, EDX spectrum 8: EDX spectrum and quantitative analysis of the [Fe(pytpy)$_2$]Cl$_2$ / AgNO$_3$ Liesegang system.

Section 6.3.3.5: $[Fe(bpy)_3]Cl_2$ / $KAuCl_4$ system

Background (gelatin containing the inner electrolyte)

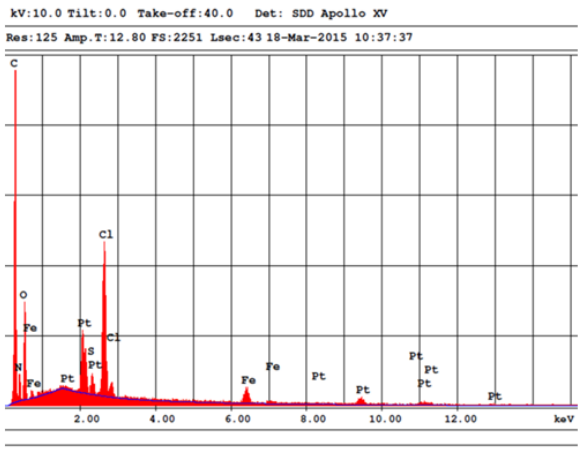

EDAX ZAF Quantification (Standardless)
Element Normalized
SEC Table : User C:\Savecalib18072012\SEC Genesis\BCNOF_19072012.sec

Element	Wt %	At %	K-Ratio	Z	A	F
C K	39.09	59.66	0.1137	1.0825	0.2686	1.0001
N K	9.51	12.44	0.0239	1.0696	0.2348	1.0002
O K	12.75	14.61	0.0472	1.0578	0.3502	1.0001
FeL	2.04	0.67	0.0102	0.8709	0.5735	1.0001
PtM	15.15	1.42	0.1096	0.6613	1.0931	1.0009
S K	1.83	1.04	0.0171	0.9849	0.9416	1.0115
ClK	19.63	10.15	0.1773	0.9403	0.9605	1.0001
Total	100.00	100.00				

EDX measurements at the stamping zone

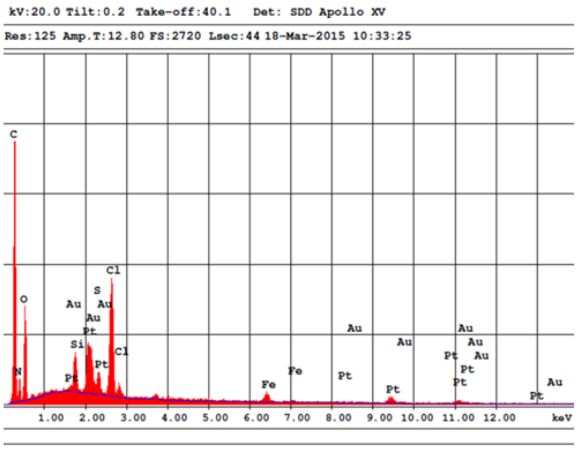

EDAX ZAF Quantification (Standardless)
Element Normalized
SEC Table : User C:\Savecalib18072012\SEC Genesis\BCNOF_19072012.sec

Element	Wt %	At %	K-Ratio	Z	A	F
C K	38.68	54.34	0.0978	1.0496	0.2408	1.0003
N K	14.46	17.42	0.0208	1.0403	0.1380	1.0004
O K	20.51	21.64	0.0361	1.0320	0.1705	1.0001
SiK	1.46	0.88	0.0118	0.9890	0.8142	1.0024
S K	1.07	0.57	0.0084	0.9789	0.7979	1.0054
ClK	6.92	3.30	0.0557	0.9354	0.8598	1.0002
FeK	1.83	0.55	0.0162	0.8766	0.9953	1.0154
PtL	12.51	1.08	0.0843	0.6525	1.0324	1.0000
AuL	2.54	0.22	0.0170	0.6496	1.0308	1.0000
Total	100.00	100.00				

EDX measurements on the particles forming the bands

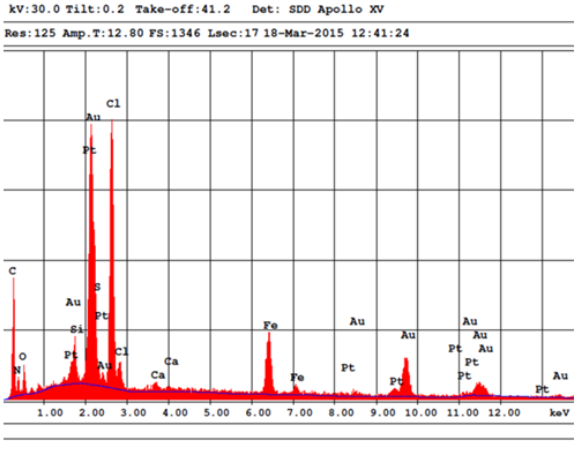

EDAX ZAF Quantification (Standardless)
Element Normalized
SEC Table : User C:\Savecalib18072012\SEC Genesis\BCNOF_19072012.sec

Element	Wt %	At %	K-Ratio	Z	A	F
C K	31.08	55.10	0.0543	1.0799	0.1617	1.0002
N K	13.62	20.71	0.0164	1.0718	0.1121	1.0002
O K	7.54	10.04	0.0101	1.0645	0.1252	1.0002
SiK	1.30	0.99	0.0084	1.0266	0.6238	1.0036
S K	0.71	0.47	0.0037	1.0200	0.5038	1.0083
ClK	12.39	7.44	0.0739	0.9770	0.6095	1.0008
CaK	0.46	0.25	0.0033	1.0122	0.7020	1.0023
FeK	5.33	2.03	0.0478	0.9273	0.9432	1.0260
PtL	4.28	0.47	0.0341	0.7561	1.0531	1.0000
AuL	23.28	2.52	0.1852	0.7559	1.0524	1.0000
Total	100.00	100.00				

EDX measurements between two adjacent bands

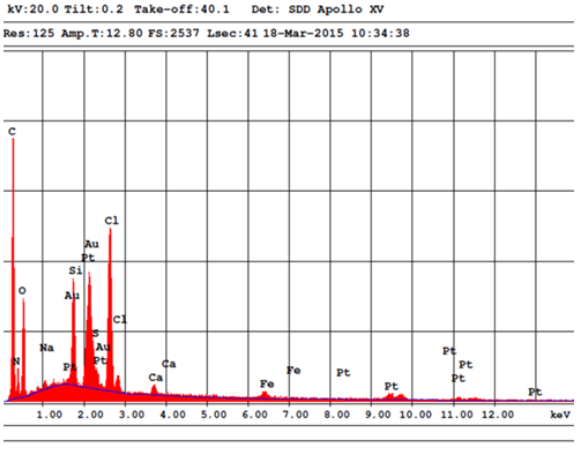

EDAX ZAF Quantification (Standardless)
Element Normalized
SEC Table : User C:\Savecalib18072012\SEC Genesis\BCNOF_19072012.sec

Element	Wt %	At %	K-Ratio	Z	A	F
C K	34.56	51.22	0.0789	1.0579	0.2159	1.0003
N K	14.81	18.83	0.0215	1.0485	0.1386	1.0003
O K	18.86	20.99	0.0329	1.0401	0.1678	1.0001
NaK	0.39	0.30	0.0016	0.9733	0.4170	1.0007
SiK	3.17	2.01	0.0256	0.9965	0.8071	1.0024
AuM	8.52	0.77	0.0734	0.7046	1.2222	1.0005
S K	0.76	0.42	0.0057	0.9888	0.7615	1.0056
ClK	7.89	3.96	0.0620	0.9445	0.8324	1.0004
CaK	0.59	0.26	0.0051	0.9698	0.8942	1.0005
FeK	1.21	0.38	0.0107	0.8850	0.9896	1.0153
PtL	9.24	0.84	0.0629	0.6603	1.0311	1.0000
Total	100.00	100.00				

Appendix C, EDX spectrum 9: EDX spectrum and quantitative analysis of the $[Fe(bpy)_3]Cl_2$ / $KAuCl_4$ Liesegang system.

Section 6.3.3.6: [Ru(bpy)$_3$]Cl$_2$ / KAuCl$_4$ system

Background (gelatin containing the inner electrolyte)

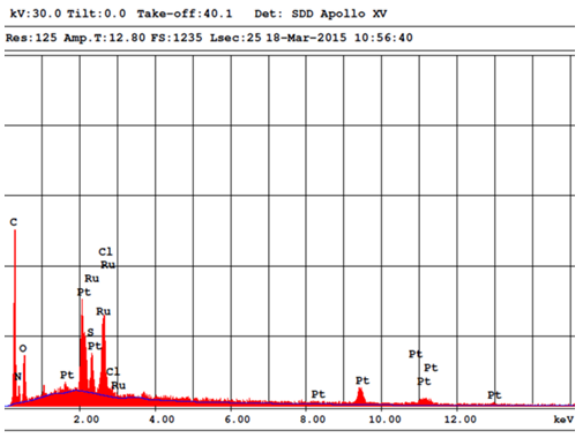

EDAX ZAF Quantification (Standardless)
Element Normalized
SEC Table : User C:\Savecalib18072012\SEC Genesis\BCNOF_19072012.sec

Element	Wt %	At %	K-Ratio	Z	A	F
C K	41.41	54.00	0.1229	1.0315	0.2875	1.0003
N K	18.87	21.10	0.0232	1.0238	0.1199	1.0004
O K	21.67	21.22	0.0280	1.0170	0.1271	1.0000
PtM	10.77	0.86	0.1229	0.7747	1.4723	1.0005
S K	1.63	0.80	0.0117	0.9755	0.7289	1.0057
RuL	1.62	0.25	0.0140	0.8256	1.0440	1.0000
ClK	4.03	1.78	0.0303	0.9345	0.8043	1.0000
Total	100.00	100.00				

EDX measurements at the stamping zone

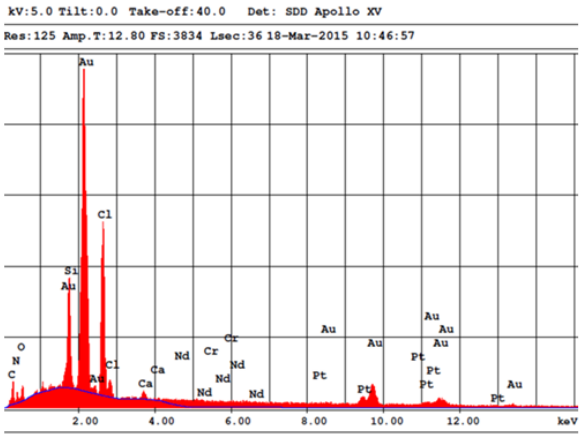

EDAX ZAF Quantification (Standardless)
Element Normalized
SEC Table : User C:\Savecalib18072012\SEC Genesis\BCNOF_19072012.sec

Element	Wt %	At %	K-Ratio	Z	A	F
C K	0.56	3.50	0.0034	1.5733	0.3827	1.0000
N K	0.63	3.36	0.0050	1.5413	0.5145	1.0000
O K	0.41	1.92	0.0041	1.5672	0.6291	1.0000
SiK	4.80	12.73	0.0661	1.4330	0.9601	1.0013
AuM	68.64	25.99	0.5406	0.7804	1.0087	1.0003
ClK	24.95	52.49	0.3253	1.3735	0.9491	1.0000
Total	100.00	100.00				

EDX measurements on the particles forming the bands

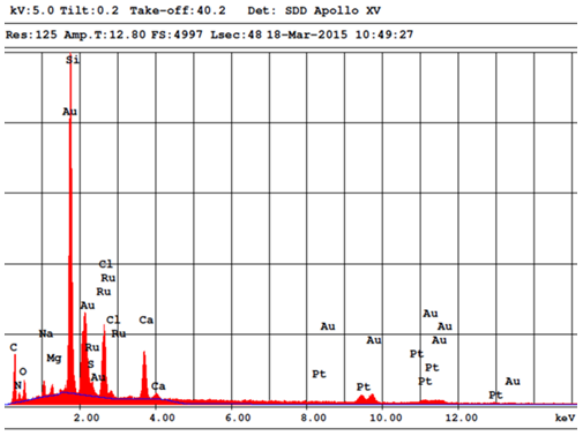

EDAX ZAF Quantification (Standardless)
Element Normalized
SEC Table : User C:\Savecalib18072012\SEC Genesis\BCNOF_19072012.sec

Element	Wt %	At %	K-Ratio	Z	A	F
C K	2.66	9.34	0.0129	1.3169	0.3668	1.0000
N K	1.10	3.30	0.0075	1.2930	0.5259	1.0000
O K	1.05	2.77	0.0091	1.2981	0.6678	1.0001
NaK	0.69	1.26	0.0073	1.1759	0.9021	1.0015
MgK	0.51	0.88	0.0057	1.1993	0.9378	1.0034
SiK	30.39	45.61	0.3546	1.1936	0.9760	1.0016
AuM	38.47	8.23	0.2489	0.6472	0.9993	1.0003
S K	1.94	2.55	0.0217	1.1813	0.9434	1.0040
RuL	1.98	0.82	0.0160	0.8315	0.9721	1.0000
ClK	21.23	25.24	0.2308	1.1301	0.9624	1.0000
Total	100.00	100.00				

EDX measurements between two adjacent bands

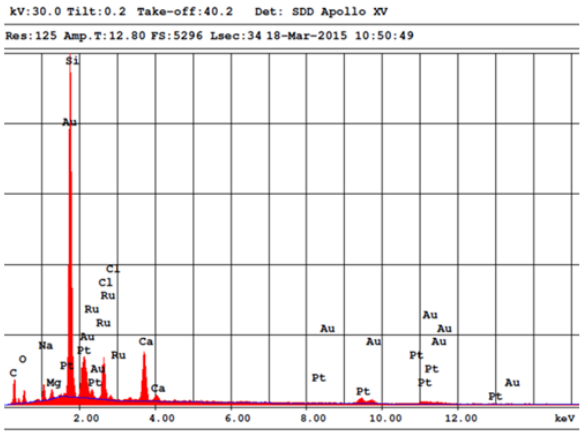

EDAX ZAF Quantification (Standardless)
Element Normalized
SEC Table : User C:\Savecalib18072012\SEC Genesis\BCNOF_19072012.sec

Element	Wt %	At %	K-Ratio	Z	A	F
C K	27.88	50.18	0.0370	1.0597	0.1252	1.0002
O K	10.94	14.79	0.0155	1.0447	0.1355	1.0004
NaK	2.34	2.20	0.0076	0.9812	0.3316	1.0047
MgK	1.05	0.94	0.0047	1.0069	0.4383	1.0090
SiK	29.39	22.63	0.2086	1.0077	0.7027	1.0025
RuL	0.00	0.00	0.0000	0.8473	0.7300	1.0035
ClK	6.02	3.67	0.0331	0.9591	0.5718	1.0037
CaK	7.29	3.93	0.0534	0.9866	0.7423	1.0000
PtL	8.71	0.96	0.0682	0.7361	1.0644	1.0000
AuL	6.39	0.70	0.0499	0.7356	1.0629	1.0000
Total	100.00	100.00				

Appendix C, EDX spectrum 10: EDX spectrum and quantitative analysis of the [Ru(bpy)$_3$]Cl$_2$ / KAuCl$_4$ Liesegang system.

Section 6.3.3.7: $AgNO_3$ / Na_2WO_4 system

Background (gelatin containing the inner electrolyte)

kV:5.0 Tilt:0.0 Take-off:40.0 Det: SDD Apollo XV

Res:125 Amp.T:12.80 FS:5156 Lsec:34 18-Mar-2015 10:15:16

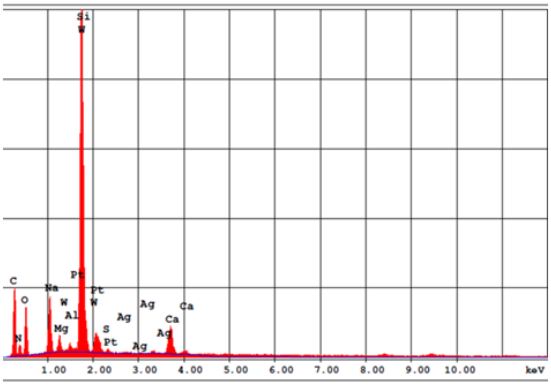

EDAX ZAF Quantification (Standardless)
Element Normalized
SEC Table : User C:\Savecalib18072012\SEC Genesis\BCNOF_19072012.sec

Element	Wt %	At %	K-Ratio	Z	A	F
C K	2.07	6.40	0.0146	1.2267	0.5739	1.0004
N K	1.40	3.71	0.0074	1.2052	0.4376	1.0000
O K	2.36	5.48	0.0166	1.2028	0.5832	1.0001
NaK	2.04	3.30	0.0201	1.0944	0.8956	1.0012
MgK	0.64	0.98	0.0067	1.1154	0.9343	1.0027
AlK	0.48	0.67	0.0050	1.0782	0.9601	1.0057
SiK	25.92	34.26	0.2798	1.1054	0.9760	1.0006
W M	13.83	2.79	0.0872	0.6190	1.0188	1.0001
PtM	6.76	1.29	0.0401	0.5997	0.9889	1.0001
S K	0.45	0.52	0.0047	1.0885	0.9615	1.0015
AgL	0.28	0.09	0.0021	0.7448	0.9936	1.0081
CaK	43.76	40.53	0.4596	1.0565	0.9939	1.0000
Total	100.00	100.00				

EDX measurements at the stamping zone

kV:15.0 Tilt:0.0 Take-off:40.0 Det: SDD Apollo XV

Res:125 Amp.T:12.80 FS:1809 Lsec:28 18-Mar-2015 10:12:00

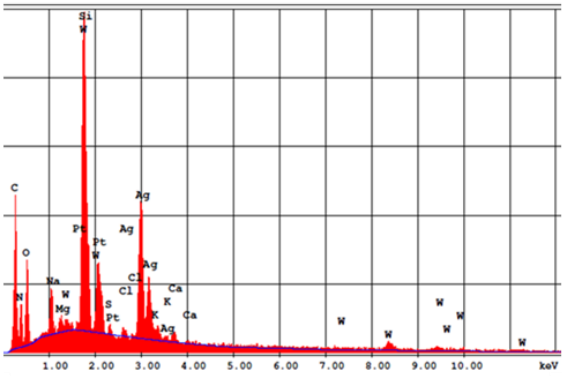

EDAX ZAF Quantification (Standardless)
Element Normalized
SEC Table : User C:\Savecalib18072012\SEC Genesis\BCNOF_19072012.sec

Element	Wt %	At %	K-Ratio	Z	A	F
C K	12.35	32.44	0.0403	1.1815	0.2763	1.0002
N K	9.16	20.61	0.0275	1.1694	0.2572	1.0002
O K	10.99	21.66	0.0267	1.1582	0.2095	1.0001
NaK	1.98	2.71	0.0102	1.0790	0.4770	1.0009
MgK	0.57	0.74	0.0038	1.1044	0.5963	1.0018
SiK	7.66	8.60	0.0694	1.1329	0.7985	1.0023
W M	21.84	3.75	0.1715	0.7630	1.0291	1.0001
PtM	10.79	1.74	0.0739	0.7614	0.8996	1.0001
S K	0.28	0.27	0.0022	1.1052	0.7218	1.0057
ClK	0.05	0.04	0.0004	1.0511	0.7868	1.0096
AgL	23.69	6.92	0.1877	0.8759	0.9043	1.0003
K K	0.00	0.00	0.0000	1.0535	0.8666	1.0008
CaK	0.65	0.52	0.0060	1.0788	0.8470	1.0006
Total	100.00	100.00				

EDX measurements on the particles forming the bands

kV:15.0 Tilt:0.0 Take-off:40.0 Det: SDD Apollo XV

Res:125 Amp.T:12.80 FS:1809 Lsec:28 18-Mar-2015 10:12:00

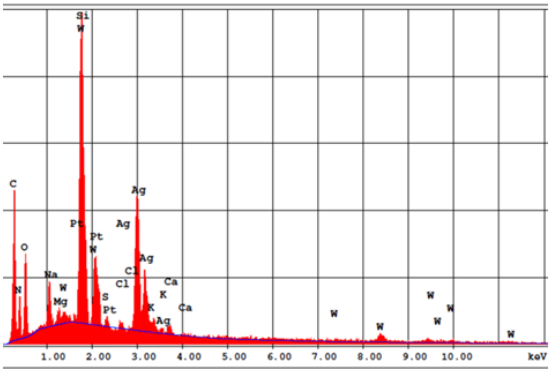

EDAX ZAF Quantification (Standardless)
Element Normalized
SEC Table : User C:\Savecalib18072012\SEC Genesis\BCNOF_19072012.sec

Element	Wt %	At %	K-Ratio	Z	A	F
C K	12.35	32.44	0.0403	1.1815	0.2763	1.0002
N K	9.16	20.61	0.0275	1.1694	0.2572	1.0002
O K	10.99	21.66	0.0267	1.1582	0.2095	1.0001
NaK	1.98	2.71	0.0102	1.0790	0.4770	1.0009
MgK	0.57	0.74	0.0038	1.1044	0.5963	1.0018
SiK	7.66	8.60	0.0694	1.1329	0.7985	1.0023
W M	21.84	3.75	0.1715	0.7630	1.0291	1.0001
PtM	10.79	1.74	0.0739	0.7614	0.8996	1.0001
S K	0.28	0.27	0.0022	1.1052	0.7218	1.0057
ClK	0.05	0.04	0.0004	1.0511	0.7868	1.0096
AgL	23.69	6.92	0.1877	0.8759	0.9043	1.0003
K K	0.00	0.00	0.0000	1.0535	0.8666	1.0008
CaK	0.65	0.52	0.0060	1.0788	0.8470	1.0006
Total	100.00	100.00				

EDX measurements between two adjacent bands

kV:15.0 Tilt:0.0 Take-off:40.0 Det: SDD Apollo XV

Res:125 Amp.T:12.80 FS:6407 Lsec:35 18-Mar-2015 10:13:52

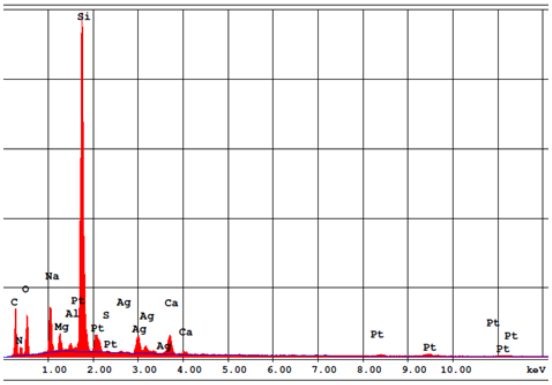

EDAX ZAF Quantification (Standardless)
Element Normalized
SEC Table : User C:\Savecalib18072012\SEC Genesis\BCNOF_19072012.sec

Element	Wt %	At %	K-Ratio	Z	A	F
C K	16.54	30.15	0.0321	1.0773	0.1802	1.0002
N K	8.13	12.71	0.0164	1.0666	0.1894	1.0004
O K	14.47	19.79	0.0362	1.0567	0.2365	1.0003
NaK	4.69	4.47	0.0273	0.9857	0.5882	1.0036
MgK	1.58	1.42	0.0110	1.0094	0.6870	1.0068
AlK	0.76	0.62	0.0059	0.9811	0.7851	1.0129
SiK	33.05	25.76	0.2879	1.0102	0.8610	1.0014
PtM	8.02	0.90	0.0512	0.6816	0.9376	1.0001
S K	0.07	0.05	0.0005	0.9962	0.7790	1.0034
AgL	8.14	1.65	0.0624	0.7939	0.9637	1.0026
CaK	4.55	2.49	0.0408	0.9752	0.9200	1.0000
Total	100.00	100.00				

Appendix C, EDX spectrum 11: EDX spectrum and quantitative analysis of the $AgNO_3$ / Na_2WO_4 Liesegang system.

Section 6.3.3.8: $AgNO_3$ / Na_2MoO_4 system

Background (gelatin containing the inner electrolyte)

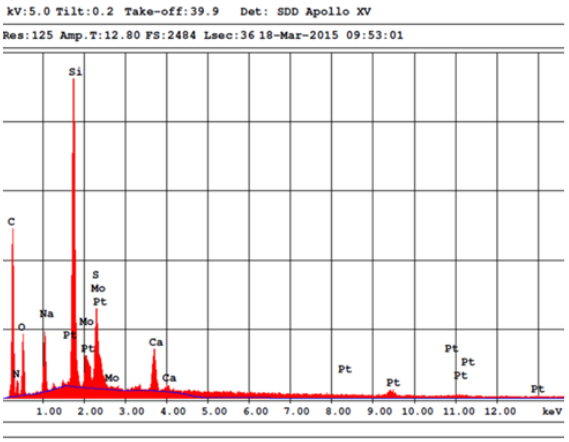

EDAX ZAF Quantification (Standardless)
Element Normalized
SEC Table : User C:\Savecalib18072012\SEC Genesis\BCNOF_19072012.sec

Element	Wt %	At %	K-Ratio	Z	A	F
C K	8.82	25.37	0.0490	1.2691	0.4376	1.0000
N K	2.30	5.67	0.0154	1.2467	0.5370	1.0001
O K	3.64	7.87	0.0296	1.2466	0.6521	1.0001
NaK	2.84	4.26	0.0292	1.1329	0.9056	1.0017
SiK	31.08	38.23	0.3496	1.1464	0.9779	1.0035
PtM	16.51	2.92	0.1026	0.6224	0.9982	1.0002
MoL	30.43	10.96	0.2408	0.8100	0.9770	1.0000
S K	4.38	4.72	0.0477	1.1307	0.9627	1.0000
Total	100.00	100.00				

EDX measurements at the stamping zone

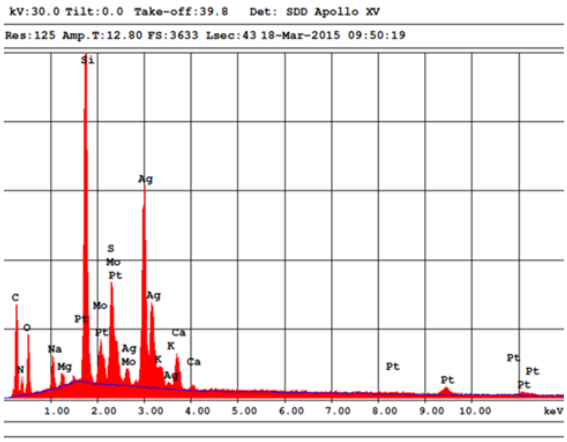

EDAX ZAF Quantification (Standardless)
Element Normalized
SEC Table : User C:\Savecalib18072012\SEC Genesis\BCNOF_19072012.sec

Element	Wt %	At %	K-Ratio	Z	A	F
C K	20.36	37.29	0.0464	1.0751	0.2120	1.0003
N K	10.22	16.05	0.0164	1.0671	0.1506	1.0004
O K	19.00	26.12	0.0246	1.0598	0.1220	1.0002
NaK	2.44	2.33	0.0059	0.9954	0.2411	1.0024
MgK	0.71	0.64	0.0024	1.0214	0.3254	1.0046
SiK	12.16	9.52	0.0718	1.0222	0.5735	1.0069
MoL	7.79	1.79	0.0582	0.8637	0.8552	1.0107
S K	0.77	0.53	0.0050	1.0157	0.6304	1.0110
AgL	20.92	4.27	0.1604	0.8305	0.9218	1.0012
K K	0.16	0.09	0.0013	0.9804	0.7825	1.0020
CaK	1.74	0.95	0.0122	1.0027	0.6974	1.0000
PtL	3.73	0.42	0.0296	0.7482	1.0601	1.0000
Total	100.00	100.00				

EDX measurements on the particles forming the bands

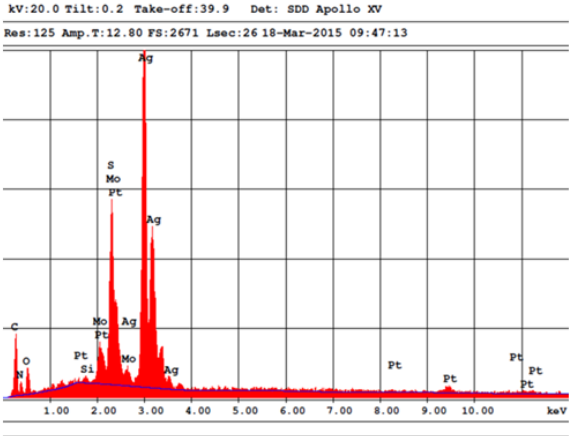

EDAX ZAF Quantification (Standardless)
Element Normalized
SEC Table : User C:\Savecalib18072012\SEC Genesis\BCNOF_19072012.sec

Element	Wt %	At %	K-Ratio	Z	A	F
C K	7.03	28.19	0.0220	1.2253	0.2550	1.0001
N K	3.96	13.62	0.0109	1.2141	0.2269	1.0001
O K	7.08	21.31	0.0104	1.2038	0.1221	1.0001
SiK	0.23	0.39	0.0016	1.1495	0.6232	1.0100
MoL	17.49	8.78	0.1457	0.9449	0.8677	1.0161
S K	0.96	1.44	0.0085	1.1781	0.7361	1.0166
AgL	53.34	23.82	0.4323	0.9365	0.8655	1.0000
PtL	9.92	2.45	0.0801	0.7989	1.0102	1.0000
Total	100.00	100.00				

EDX measurements between two adjacent bands

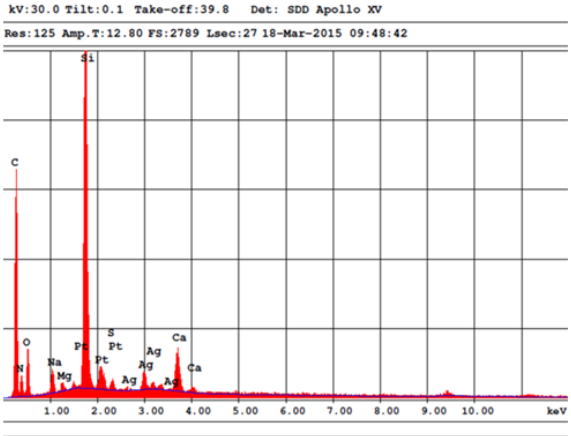

EDAX ZAF Quantification (Standardless)
Element Normalized
SEC Table : User C:\Savecalib18072012\SEC Genesis\BCNOF_19072012.sec

Element	Wt %	At %	K-Ratio	Z	A	F
C K	42.94	53.78	0.1211	1.0194	0.2765	1.0004
N K	19.72	21.18	0.0231	1.0119	0.1158	1.0004
O K	17.15	16.13	0.0212	1.0051	0.1230	1.0002
NaK	1.63	1.06	0.0049	0.9443	0.3153	1.0020
MgK	0.39	0.24	0.0016	0.9691	0.4380	1.0039
SiK	11.81	6.33	0.0845	0.9702	0.7364	1.0011
PtM	2.45	0.19	0.0226	0.7658	1.2048	1.0002
S K	0.37	0.17	0.0026	0.9643	0.7378	1.0024
AgL	1.73	0.24	0.0154	0.7781	1.1419	1.0028
CaK	1.83	0.69	0.0163	0.9386	0.9493	1.0000
Total	100.00	100.00				

Appendix C, EDX spectrum 12: EDX spectrum and quantitative analysis of the $AgNO_3$ / Na_2MoO_4 Liesegang system.